1-28-2015

Structural Influences on the Photochemistry and Photophysical Properties of p-Phenylene Ethynylenes: Aggregation Effects and Solvent Interactions

Eric Harris Hill

Eric Harris Hill

Candidate

Nanoscience and Microsystems Engineering

Department

This dissertation is approved, and it is acceptable in quality and form for publication:

Approved by the Dissertation Committee:

David G. Whitten , Chairperson

Deborah G. Evans

Kirk S. Schanze

Andrew P. Shreve

Structural Influences on the Photochemistry and Photophysical Properties of *p*-Phenylene Ethynylenes: Aggregation Effects and Solvent Interactions

by

Eric Harris Hill
B.S. Chemistry, Southern Oregon University, 2009

Dissertation

Submitted in Partial Fulfillment of the
Requirements for the Degree of

Doctor of Philosophy
Nanoscience and Microsystems Engineering

The University of New Mexico
Albuquerque, New Mexico

December 2014

Acknowledgements

I consider the path my life has taken to reach this point to be a combination of serendipity and an intense interest in science and technology spurred by the influential people in my life. By this measure, my pursuit of a doctorate would not have been possible without the contributions of many others. My heartfelt thanks go to my advisors David Whitten and Debi Evans for all that they have taught me in my time as a graduate student. When I arrived at UNM, I had not selected a graduate advisor, but after a brief period of frustration after several unproductive interviews I was taken on by Professors Evans and Whitten for a collaborative project involving computational work with the OPEs. After five years since arriving in Albuquerque, NM in August 2009, I feel lucky to have been graced with the opportunity to work under Debi and David. They have different styles of mentoring, and work in completely separate areas, but their combined mentorship has given a really well-rounded experience. I truly appreciate all that they have done for me, both as a student and as a friend. I also sincerely appreciate the great conversations and support of their respective spouses, Mark Ondrias and Jo Whitten.

There are several people who must be acknowledged for their particular advice and tutelage during my time at UNM. Ken Sherrell and Professor Charlotte Mobarak took me on as an intern at the UNM Mass Spectrometry Facility for two years and taught me a great deal about the different types of mass spectrometry instrumentation and methods. This was an awesome experience, and gave me the knowledge and experience using the mass spectrometers needed for elucidating photochemical products and mechanisms. Professor Kirk Schanze has been a collaborator of the group since I have joined and has been a great mentor, friend, and is always a pleasure to see at a conference. Professor Andrew Shreve began advising me a few years into my work, and our discussions about potential experiments and spectral deconvolution were very useful. I would like to also thank Professor John Grey for providing advice and training on his instrumentation for potential experiments, though I was not able to complete any experiments with him. I am also grateful to Professor Ying-Bing Jiang for training me to use the transmission electron microscope in the Earth and Planetary Sciences department at UNM, and providing assistance with his easygoing nature as needed. Finally, Heather Armstrong, the former Nanoscience and microsystems program coordinator, deserves heaping praise for all her help with everything related to the PhD program since before I even arrived in Albuquerque. She truly

cares about her students, and is always keen to have an interesting conversation.

Much of the work that I have done relies heavily on the previous work of the members of the Whitten and Schanze group, to whom I am extremely grateful for their mentorship and camaraderie. Dr. Yanli Tang, Dr. Ying Wang, Dr. Anand Parthasarathy, Dr. Tom Corbitt, Dr. Zhijun Zhou, and Dr. Eunkyung Ji provided a great deal of help with settling into the lab when I first arrived to UNM. Yanli Tang and Zhijun Zhou introduced me to the synthesis of the OPEs, which I did not pursue for research but still found interesting. Tom Corbitt was also a great coworker and mentor, training me to do bactericidal testing, open-minded enough to humor me in a few pilot experiments, and always great to discuss Sci-fi novels with. Though Anand Parthasarathy was a postdoc in Professor Kirk Schanzes group at the University of Florida, we have had many meetings through our groups' collaborations, and his friendly manner and advice are always welcome. Ying Wang, being the graduate student a year ahead of me, deserves special praise for his unending friendliness and mentorship up until he was awarded his PhD in Fall 2013.

I thank the entire Whitten and Schanze and Evans groups, past and present, students and coworkers, for their participation in my experience at UNM. Subhadip Goswami, Linnea Ista, Jeremiah Anderson, Jasper Thompson, Tye Martin, Yue (Phoeby) Zhang, Patrick Donabedian, Harry Pappas, and Taylor Canady. In addition, several students from other research groups deserve thanks: Gregory Soliz, Lance Edens, Melissa Hernandez, Alex Leonard, Mark Fleharty, Dr. Christina Salas, Dr. Adam Wise, and Dr. Arjun Thapa. I thank my Chinese collaborators at Tsinghua University, particularly Prof. Xu Huaping, Prof. Zhang Xi, Kai Liu, Han Peng, Ma Ning, Ren Huifeng, Pengbo Wan, and Wu Guanglu. Of course, the office staff of the Center for Biomedical Engineering at UNM receive huge thanks for all of their help; Thank you Stephanie Sanchez, Isela Roeder, Fernando Santillanes, and Travis Woods for everything.

I have to acknowledge the UNM Nanoscience and Microsystems REU program for bringing me into contact with some of my best students during my time at UNM. Dominic Sanchez (California Polytechnic University) and Kelly Stratton (currently in the Biomedical Engineering PhD program at University of Connecticut) were a thrill to have as students, and their dedication and energy led to great interactions which made for an excellent teaching experience.

I have to thank former teachers throughout my education for their guidance. The Chemistry professors at Southern Oregon University are amazing teachers, and they directly prepared me for graduate school. I would like to give particular thanks to Professors Doug Chapman, Hala Schepmann, and Steven Petrovic at SOU for their guidance throughout my undergraduate education. Stepping further back in time, I owe profound thanks to Michael J. McDonough, the current Principal of Bellaire High School in Bellaire, TX. At the time when I was in highschool at Bellaire (2000-2004), he was the one assistant principal who kept me on the path to staying on track in school, despite my best friend at that time dropping out. He was able to give me personal counseling that I needed and was a strong role-model for my future development.

I should thank the funding agencies which supported me and my work during my time at UNM. U.S. Defense Threat Reduction Agency for support through Grants W911NF07-1-0079 and HDTRA1-08-1-0053. The U.S. National Science Foundation for support through grant DMR-1207362. The U.S. Department of Education for support through the Graduate Assistance in Areas of National Need (GAANN) grant P200A090028. The University of New Mexico Office of Graduate Studies for multiple Research Project and Travel Grants and support through an Excellence Fellowship. The Chemistry Department at UNM for funds to design and build two high-performance computing clusters. Special thanks to all the software developers who provide free or open-source software.

Last in the list but far from last in importance, I thank my family and friends for their unending support. My Dad's enthusiasm for cars, video games, and computers has from an early age contributed to my ongoing interest in computers and technology, while my Mom's career as a Physicians Assistant led to frequent discussions about medicine and anatomy, leading to my interest in biochemistry. While thanking my parents, I should probably also thank the LEGO corporation, as those blocks were a toy of choice which undoubtedly helped foster my interest in science and engineering. Thanks to my sister Leah and brother-in-law Jody for their support. Special thanks to all my Cousins, Uncles, Aunts, Nieces, Nephews, In-laws, and of course my Great-uncle Wiley. Thanks to my friends both here and abroad for all the great times, with special thanks to W.P. for getting me through the last few years.

Structural Influences on the Photochemistry and Photophysical Properties of *p*-Phenylene Ethynylenes: Aggregation Effects and Solvent Interactions

by

Eric Harris Hill

B.S. Chemistry, Southern Oregon University, 2009

Ph.D. Nanoscience and Microsystems Engineering, University of New Mexico, 2014

Compounds based on the *p*-phenylene ethynylene backbone with pendant charged groups, known as conjugated polyelectrolytes, have been of particular interest in recent years due to their solubility in water, sensing properties, and biocidal activity against bacteria, viruses, and fungi. A series of oligomers based on these polymers were synthesized (OPEs), and several interesting questions about their photophysical and biocidal properties were raised by earlier experimental observations, which are addressed by this dissertation. The study initially focuses on the influence of the backbone length and presence of carboxyester substituents on the photophysical properties of the OPEs. Next, the photochemistry of the OPEs is explored as the products and mechanisms are elucidated through isotopic studies with mass spectrometry, revealing that photo-protonation by water and addition of oxygen across the triple bond are the two dominant initial mechanisms of all major pathways in aqueous solution. Finally, the aggregation of OPEs with is studied in two systems: surfactants and model bacterial membranes. The placement of the ionic alkyl substituents played a dominant role in determining the outcome of molecular interactions and type of aggregates which resulted between OPEs and both systems. Biophysical simulations of the interactions between OPEs and these two systems provided mechanistic insight into the mechanism of bacterial membrane disruption and the attenuation of photodegradation observed with OPE-surfactant complexes. In addition to determining the OPEs could be protected from photolysis and the structural basis for aggregate type, surfactant complexation was used to form a biocidal complex from a non-biocidal anionic OPE. The work presented will be of great use for future developments in sensors, biocides, photo-resistant materials, and drug delivery applications.

Table of Contents

Chapter I: Introduction

1.1 The Early Days of OPEs: from LEDs to Biocides

The first synthesis of an oligo-*p*-Phenylene ethynylene is reported in 1983 by Lakmikantham and coworkers.[1] In this study, cuprous acetylide and iodobenzene were heated to form a yellow-brown powder with 10-12 repeat units of OPE. Since then, the use of palladium-catalyzed alkyne coupling reactions have enabled synthetic routes to a variety of different OPEs.[2] The first Pd/Cu cross-coupling reaction of OPEs was reported by J. M. Tour and coworkers in 1994, in which an iterative approach was used to double the length of the molecules.[3] Moroni and coworkers followed this work in 1996 and 1997 as they discussed a series of *p*-phenylene-ethynylene oligomers made using palladium cross-coupling reactions.[4,5] In the first studies seen in the literature, derivatives with this backbone had been studied as "molecular wires" due to their conductive backbone from extended conjugation.[3,7] Prior to the existence of any body of research about the OPEs, the poly-phenylene ethynylenes (PPEs) were primarily explored for purposes involving photoluminescence and electroluminescence with high thermal or electric stability.[5-7] While these molecules are of great interest as molecular wires due to the tunability of their radiative recombination and carrier transport characteristics, the development of water-soluble PPEs and OPEs led to the exploration of their sensing properties.[8-16]

The primary synthetic method used for the synthesis of OPEs in recent years is the specific cross-coupling reaction known as Sonogashira coupling.[17] In this method, a haloarene (generally an iodoarene), is mixed with an alkyne in a polar aprotic solvent and an amine with Pd(II) and CuI. The reaction is given below in Scheme 1.1.

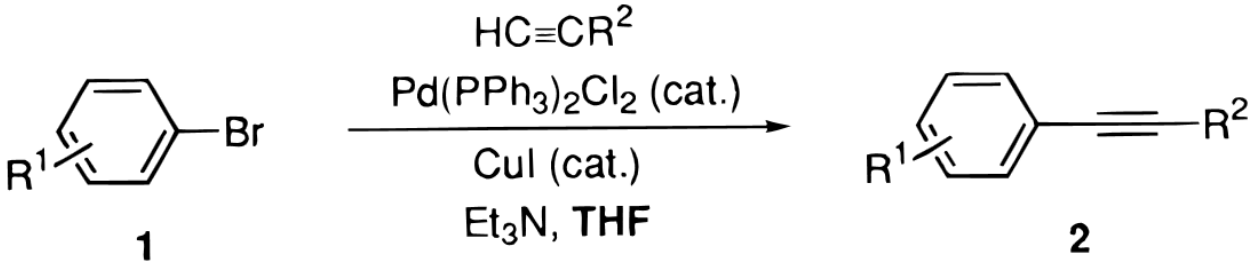

Scheme 1.1. Formation of a *p*-phenylene ethynylene with Sonogashira coupling; Reprinted with

Chen and coworkers reported in 1999 a study of reversible fluorescence quenching in a water-soluble conjugated poly-phenylene vinylene, which closely preceded numerous studies of PPEs as fluorescence quenching and unquenching sensors.[8] The Schanze group at the University of Florida embarked on numerous studies of fluorescence sensors that were used to detect compounds such as pyrophosphate, boronic acid, saccharides, and enzymes such as proteases.[11-15] The significant fluorescence quenching effect observed with PPEs led to significant interest in their use to detect chemo- and biosensors. The first studies of the biocidal activity of PPEs was carried out with a water-soluble polymer with cationic pendants on aliphatic sidechains.[18] Bacillus anthracis and Escherichia coli were exposed to the polymer in under white light and significant killing was observed, heralding the beginning of research of these molecules as biocides. This study was followed in the work between the Whitten and Schanze groups, which further explored the biocidal activity of cationic PPEs in a variety of colloidal and interfacial applications.[19-22] While the PPEs exhibited good sensing and biocidal properties, the characterization of biocidal and sensing characteristics as a function of structure is hindered by the effects of intra- and inter-chain aggregation, polydispersity of size, and general poor water solubility. These disadvantages of the PPEs led to recent work by the Whitten group at the University of New Mexico and Schanze group at the University of Florida which led to the development of a series of OPEs which exhibit good water solubility and interesting sensing and biocidal properties.[23-25] The structures of several different types of PPEs and OPEs are shown in the scheme below.

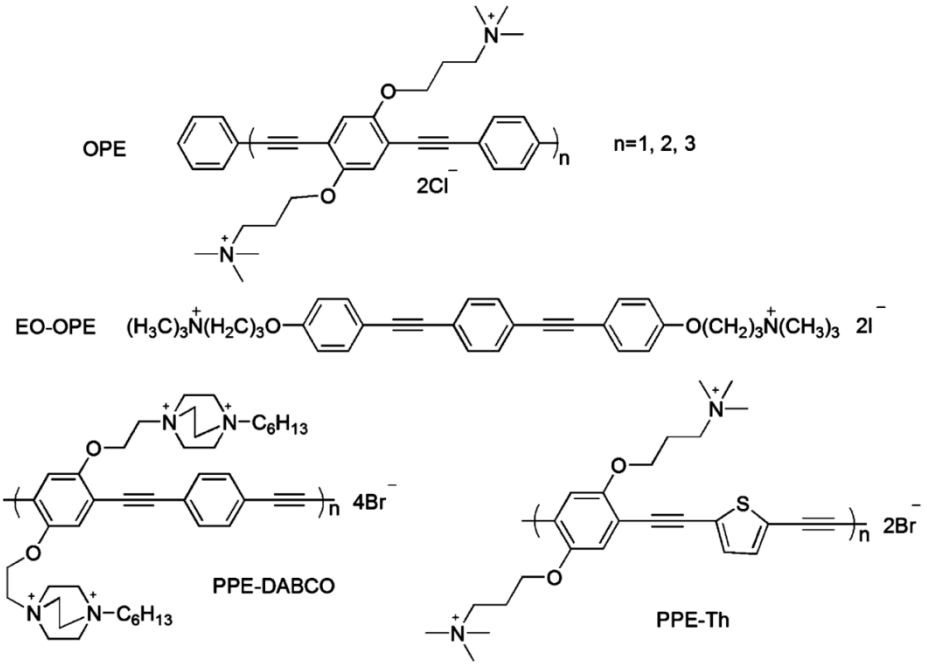

Scheme 1.2. Different OPEs and PPEs showing the various backbones and charged moieties of the PPEs and OPEs. Modified from figure in ref. 29

The work by Tang and coworkers explored the synthesis of a series of model compounds of 1 to 3 repeat units which have the same general structure as the PPEs which were previously explored. These cationic OPEs were shown to have good sensing properties through their induced circular dichroism and changes in absorbance and fluorescence upon binding to anionic scaffolds.[23] The figure below shows the changes in UV-Vis and CD spectra after binding to anionic cellulose scaffolds. The changes upon assembly upon an anionic cellulose molecule, CMC, are shown below, in Figure 1.1. In this figure, the red-shifted absorbance maximum and enhanced fluorescence common to J-aggregates is shown.

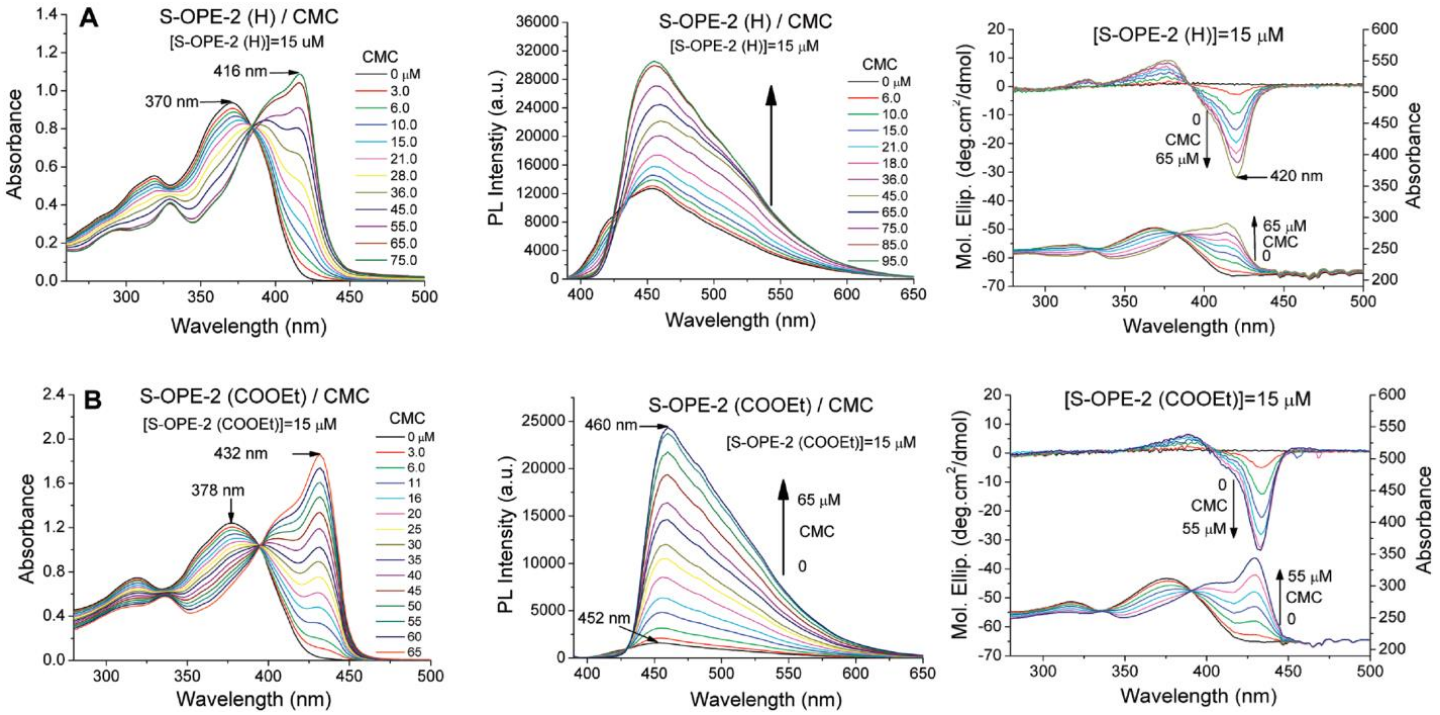

Fig 1.1 Changes in UV-vis absorbance, fluorescence, and circular dichroism, from left to right, upon binding to the anionic scaffold CMC by an n=2 OPE with (A) No terminal groups, (B) Terminal carboxyester groups. Figure reprinted from reference 23.

In addition, the compounds showed good biocidal activity against both Gram-positive and Gram-negative strains of bacteria.[24] A series of "end-only" OPEs with only one repeat unit of length and cationic end-groups was made by Zhou and coworkers and this series of compounds, while not as desirable for fluorescence sensing or stimulated emission, exhibits effective activity against viruses, bacteria, and biofilms.[25] In the same period of time (2008-2011), a series of PPEs similar to the OPEs made by Tang et al, but with larger sizes in a range of n=7 to 49, were synthesized by Ji and coworkers.[26] The synthesis of these different series of OPEs with a variety of lengths and structural features provided a novel platform to explore the relationship between structure and activity to relate to the larger polymers, the PPEs.

Prior to the development of the OPEs, Ding and coworkers reported an *in vitro* study of the effects of the PPEs on liposomes to determine the mechanism of interaction.[27] Detailed experimental studies of the mechanisms of biocidal activity of the OPEs against Gram-negative and Gram-positive bacteria, *S. cerivisiae* spores and cells, and of the inactivation of viruses were meticulously carried out by Ying Wang and coworkers.[28,29] In their work, numerous effects of the

compounds on cells were elucidated, and the effects that were observed in the dark were able to be tested independently from those biocidal processes that occur when OPEs are exposed to light in the presence of cells or other pathogens. In the light, the sensitization of singlet-oxygen by the OPEs leads to the generation of reactive oxygen species (ROS) which induce a cascade of damaging effects to cellular components including proteins and nucleic acids. This was well established in studied by Wang and coworkers, but the effects of the OPEs on cells in the dark were less clear. The effects on the cell membranes were observed through different microscopy techniques, and several *in vitro* techniques were performed in order to further examine the differences in lipid reorganization and membrane disruption that the different types of OPE induce in an effort to determine a general mechanism.[28] Wang and coworkers were able to give relative abilities of different OPEs to induce dye-leakage in vesicles of different lipid composition, and the change in ^{31}P NMR spectra and small-angle X-ray scattering (SAXS) profiles for lipid vesicles that were induced by the OPEs. In these studies, a small cationic peptide which results in pore-formation and a surfactant which leads to carpet-model disruption of bilayers were also studied and the results of the different molecules against various bilayer compositions mimicking bacterial or mammalian cell membranes were qualitatively compared.[29] A figure summarizing the results from this work is given below.

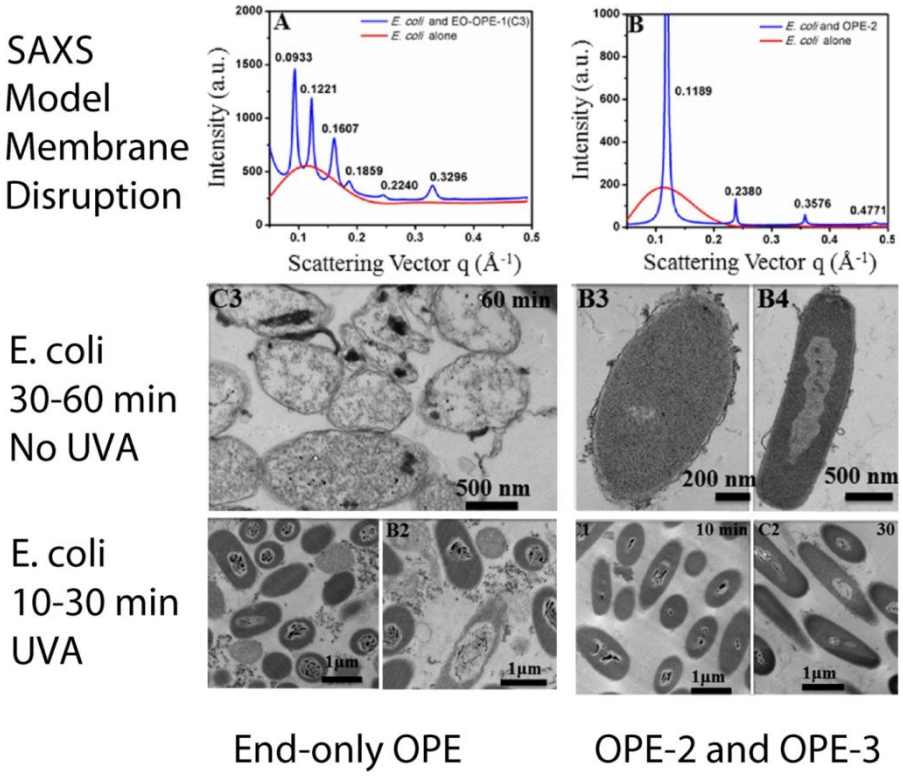

Figure 1.2 Damage induced by the EO-OPEs and OPEs with sidechains leads to different resulting cell damage in the dark, and different resulting lipid phases are formed. Figures reprinted from reference 29.

As shown in the figure above, there were significant differences between the effects of the EO-OPEs and the OPEs in the dark. In particular, the lipid phases as shown by SAXS gave rise to different structural profiles, and the appearance of the cell and cellular envelope after exposure to OPEs in the dark are affected differently between the two types of molecules. While these studies were informative and shed light on the outcomes which were observed, no clear molecular-level mechanism had been established for the different types of OPEs and their biocidal action against membranes.

1.2 A brief history of antibiotics and antibiotic resistance

Historically, all cultures have remedies which are generally concocted from some type of local plant or fungus, and even in the great apes self-medication gives insight into the early origins of Human herbal medicine.[30,31] Many of these "traditional" medicines have longtime anecdotal usage, and may or may not have real efficacy, but with modern instrumentation longtime folk-

remedies can be tested for active compounds.[32,33] In antiquity, crude knowledge of antibiotics was utilized by the ancient Egyptians and Greeks in the form of specially selected mold and plant extracts.[34-37] The first modern instance of antibiotic effects was observed by Louis Pasteur and Robert Kock in 1877, where an airborne bacillus was able to inhibit growth of Bacillus anthracis.[38] This was shortly followed by synthetic efforts to produce antibiotics by Paul Ehrlich in the 1880s, who screened hundreds of dyes in order to discover the medically useful drug Arsphenamine, then called Salvarsan.[39] His discovery was aided by the observation that the dyes would selectively color different types of cells (animal, bacterial, etc.), leading to the idea that different molecules have different species selectivity. This pioneering achievement led to his receiving the Nobel Prize in Physiology or Medicine in 1908, 20 years before the discovery of penicillin. A similar research approach led the team at Bayer (IG Farben at the time) under Gerhard Domagk to discover Prontosil, a prodrug, after testing some hundreds of coal-tar dyes against bacteria, leading to a Nobel Prize in Medicine or Physiology in 1939.[40] However, the awarding of the Nobel Peace Prize to Carl von Ossietzky in 1935 had angered the German government, who would not allow German nationals to receive the prize, and this gave Domagk some trouble with the Gestapo upon the announcement of his award. The discovery of Prontosil did not yield a useful drug in itself, however a team at the Pasteur Institute found in 1935 that Prontosil is metabolized in the body, and that one of the two metabolites that is produced is sulfanilamide, the active component.[41] The discovery of sulfanilamide led to a "sulfa-craze" in the late 1930s in which millions of tons of different sulfa drugs were produced by different companies. The long-term usage of the sulfa drugs was limited by their variety of unpleasant side-effects, and they were replaced in common healthcare settings by penicillin upon its characterization.

Alexander Fleming was able to deduce that the Penicilium mold must secrete an active substance and concentrate it, but the Penicilium mold had been used in traditional medicine since the dawn of the history of medicine. In 1945, 17 years after penicillin was first concentrated, the chemical structure was elucidated by Dorothy Hodgkin, a talented scientist who also discovered the structures for vitamin B12 and insulin. However, the results which revealed the β-lactam ring were contrary to current scientific opinion (which had favored a thiazolidine-oxazolone moiety), and the results were not published until 1949.[42,43] The first clinical usage of penicillin was for streptococcal septicemia in March of 1942, and this amount used roughly half the total U.S.

supply at the time.[44] The U.S. War Production Board drew up a plan to increase the stocks of penicillin to supply troops in Europe, leading to the production of 2.3 million doses in time for the Normandy invasion. Meanwhile back at home, a moldy cantaloupe in Peoria, Illinois was found to have the best strain of Penicillium for production. While penicillin and sulfa drugs provided an excellent means to counter infections, the organisms that it targeted quickly developed resistance.[45,46]

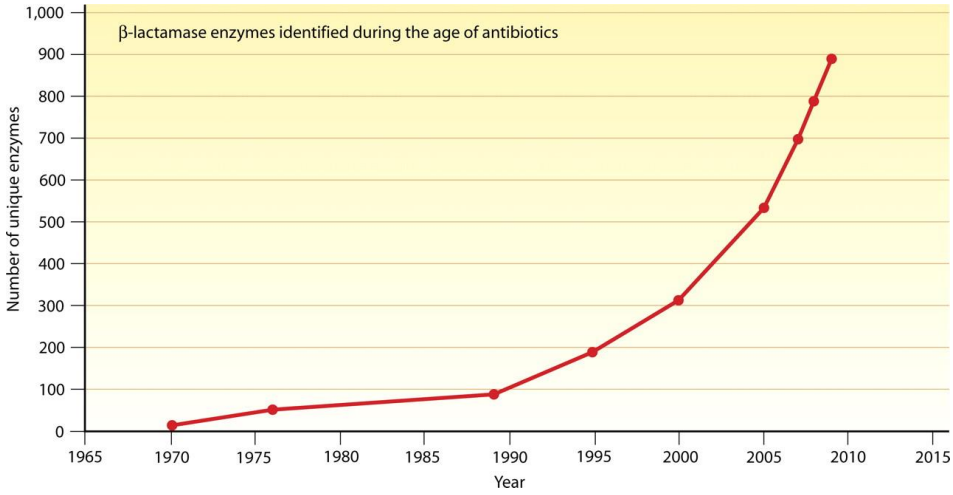

Figure 1.3 The number of new β-lactam enzymes found over time, representative of overall antibiotic-resistance proliferation. Reprinted with permission from Davies et al.[45] © American Society for Microbiology

Antibiotic resistance is a process by which bacteria can develop a resistance to specific drugs and families of compounds with similar chemical structures.[45] There are two general types of antibiotic resistance that can be developed by cells, from chromosomal and non-chromosomal changes. In chromosomal antibiotic resistance, changes (mutations) in the bacterial chromosomes affect the expression of proteins such as efflux pumps, altering metabolic pathways, changing chromosomal binding sites of drug molecules, and possible production of enzymes which break down drugs.[46-53] The earliest studies of antibiotic-resistance focused on chromosomal changes, particularly those inducing resistance to β-lactam antibiotics such as penicillin. In the normal antibiotic mechanism of penicillin, the four-membered β-lactam ring binds to the enzyme DD-transpeptidase, inhibiting its ability to cross-link the peptidoglycan in the bacterial cell wall. Resistance to this class of antibiotics is conferred through the transfer of

genes which promote the expression of β-lactamases by the bacteria.[54] These enzymes hydrolyze the lactam ring, breaking it open and preventing further inhibition of DD-transpeptidase. In recent years, many other chromosomal changes have been shown to lead to bacteria acquiring antibiotic resistance.[46-53] Changes to the expression levels of efflux pumps have been shown in recent work to be particularly important for antibiotic resistance levels of Gram-negative bacteria E. coli and P. aeruginosa, as certain pumps are more effective at efflux of certain drugs such as tetracycline, chloramphenicol, and other common antibiotics.[49,50] Early studies of antibiotic resistance showed that sulfonamide-resistant S. aureus do not require para-aminobenzoic acid for folic and nucleic acid synthesis, avoiding the inhibition of this process induced by sulfonamide drugs.[53] Instead, these Gram-positive microbes used preformed folic acid as is done in mammals.

Non-chromosomal antibiotic resistance has been primarily observed in the form of autonomously replicating units of non-chromosomal DNA which is covalently closed and circular, or attached to the chromosomal DNA as a heteroduplex.[55-64] In the acquiring of non-chromosomal antibiotic resistance, the expression of resistance traits is almost immediate after the bacteria obtain certain "R-factor" plasmids. While in some cases the R-factor plasmids can transform the host genome, some plasmids independently replicate within the cell, and are not incorporated into the chromosome. The transmission of these plasmids between different populations is known as lateral transfer, and is illustrated in a diagram below.

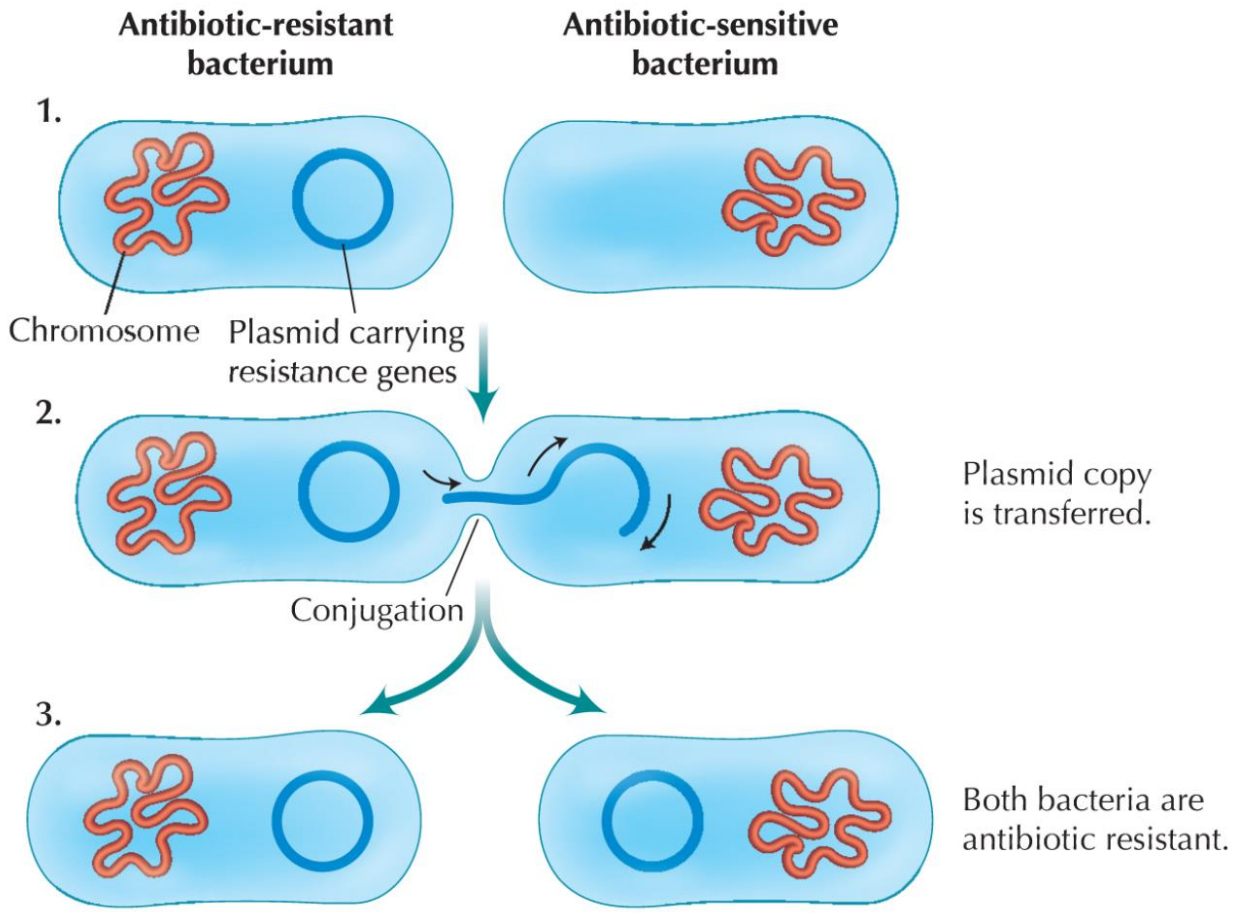

Figure 1.4. The process of lateral gene transfer of antibiotic-resistance plasmids © 2007 Cold Spring Harbor Laboratory Press

These non-chromosomal antibiotic-resistance plasmids are particularly frightening from a healthcare perspective, as they replicate and proliferate independently in the cell, and cannot be targeted through tampering with chromosomal factors. In one of the original studies of non-chromosomal factors of antibiotic resistance, Gillham found with Chlamydomonas reinhardi that streptomycin resistance was transferred through non-chromosomal factors.[55] While the non-chromosomal plasmids are not always transferable to other organisms, they can be made transmissible through incorporation of other genetic material from other plasmids, or by the presence of genes on different R-factor plasmids. In one study, it was found that virulent strains of Shigella sonnei always had a 120-megadalton plasmid which was not present in the avirulent forms, though streptomycin and sulfonamide-resistance was not dependant on this plasmid.[63] Similarly to the transmission dynamics of antibiotic-resistance, the virulence factor plasmid itself

was not transmissible, but could be mobilized by the plasmid R386. The influence of these non-chromosomal "R-factors" may indeed be significant for antibiotic-resistance in bacteria; a study of Enterobacteria with those that were preserved from before the "antibiotic era" revealed the insertion of genes in the modern strains which were not present in the legacy strains.[64] While the genetic factors that contribute to antibiotic resistance are numerous, antibiotic resistance can be countered by using "broad-spectrum" antibiotics which can induce damage that cannot be defended against by the cell.

1.3 Proliferation of Antibiotic-resistant Bacteria in the Healthcare Setting

The problem of antibiotic-resistant bacteria has become a substantial burden for healthcare providers in the last few decades. Hospitals in the United States have seen a drastic increase in cases of patients acquiring infections of antibiotic-resistant bacteria such as Gram-negative *Pseudomonas Aeruginosa* and *E. coli*, as well as Gram-positive *Staphylococcus aureus*, to the extent of 1.7 million hospital-acquired infections, annually.[65] A large number of nosocomial (hospital-acquired) infections are caused by a methicillin-resistant strain of *S. aureus*, which can survive most conventional antibiotic treatments. Several large-scale studies have shown that exposure to antibiotics can increase the chances of acquiring such an infection in a hospital environment, as the antibiotics kill most of the natural flora of the body while allowing the antibiotic-resistant bacteria to thrive.[65-68] The development of novel antibiotics or bactericides that do not induce resistance in targeted pathogens is essential for effective treatment of many types of nosocomial infections. Greater numbers of hospital-acquired infections in the U. S. from antibiotic-resistant strains of bacteria have led to an increased need for broad-spectrum antimicrobial compounds which are capable of eliminating bacteria on surfaces and medical tools. Recently, the proliferation of antibiotic-resistant pathogens has been seen as a critical global threat, which calls for an increased pace of research in this area.[65-68] To date, bacteria from genuses staphylococci, enterococci, gonococci, streptococci, salmonella, several other Gram-negative bacteria, and Mycobacterium tuberculosis have been found to exhibit resistance to multiple types of antibiotics.

The term "broad-spectrum" antibiotics generally designates that the damage caused by the agent is not specific to a single species of bacteria and can act on a wide range of organisms. This can be the result of biochemical means, such as the inhibition of synthesis of enzymes

responsible for crucial cellular processes such as cell wall or protein synthesis, or of physical means. The most prominent physical means of broad-spectrum antibiotic activity are the disruption of the bacterial membranes or the production of singlet oxygen, which subsequently generates reactive oxygen species which further damage the cell. Recent studies by the Whitten and Schanze groups have focused on cationic biocides based on the *p*-phenylene ethynylene repeat unit. Studies have shown that polymers based on this backbone are highly effective light-activated biocides at low concentrations, and the mechanism of their biocidal activity was shown to be the result of both membrane disruption and singlet oxygen generation upon irradiation to UV or visible light. In the following sections of this introduction, the physical means of broad-spectrum antimicrobial activity are discussed.

1.4 Mechanisms of Antimicrobial Activity of Different Broad-spectrum Biocides

1.4.1 Singlet-oxygen Sensitization

One useful method of sterilization is the use of a light-activated biocide in combination with UV or visible light.[18,69,70] This is particularly useful for the decontamination of surfaces, which are prone to propagation of catheter-associated infections.[71,72] One mechanism of inducing microbial killing is the use of a light-activated singlet-oxygen sensitizer which is localized in or on the cell prior to irradiation. In its lowest energy excited state, O_2 has singlet degeneracy, while in the ground state it exists as a triplet. The energy difference between the triplet ground state and singlet oxygen corresponds to 94.2 kJ/mol, which gives singlet oxygen an IR transition at ~1270 nm. Molecules that have significant intersystem crossing between excited singlet states and triplet states are able to transfer energy to O2 in the environment, exciting it to singlet oxygen.[73] When a molecule with a high yield of triplet excited states undergoes photoexcitation, the process that follows which leads to generation of singlet oxygen is given in the equations below.

1 $S + h\nu \rightarrow {}^1S^* \rightarrow {}^3S^*$

2 ${}^3S^* + {}^3O_2 \rightarrow {}^1O_2^*({}^1\Sigma_g^+) + S$

3 ${}^1O_2^*({}^1\Sigma_g^+) \rightarrow {}^1O_2^*({}^1\Delta_g)$

Where S is a sensitizing molecule, h is Plancks constant and ν is the frequency of light. Equation 1 shows the excitation of a sensitizer molecule S to the singlet excited state, which then decays to a triplet excited state through inner system crossing. When introduced to ground state

oxygen in equation 2, the oxygen is excited by the sensitizer, and the sensitizer returns to the ground state.As shown in equations 2 and 3 above, there are two low-lying singlet excited states, $^1\Sigma_g^+$ and $^1\Delta_g$, where oxygen quickly relaxes from the $^1\Sigma_g^+$ to the $^1\Delta_g$ state which is generally referred to as singlet oxygen. While the lifetime of singlet oxygen is long in the gas phase (> 1 hr), it has an extremely short lifetime in liquids. The lifetime of singlet oxygen in water is very short at around 3 μs, and when compared with other solvents it is extremely short-lived.[73,75] The figure below from Wilkinson and Brummer shows the differences in disappearance rate constant of singlet oxygen in various solvents.[74]

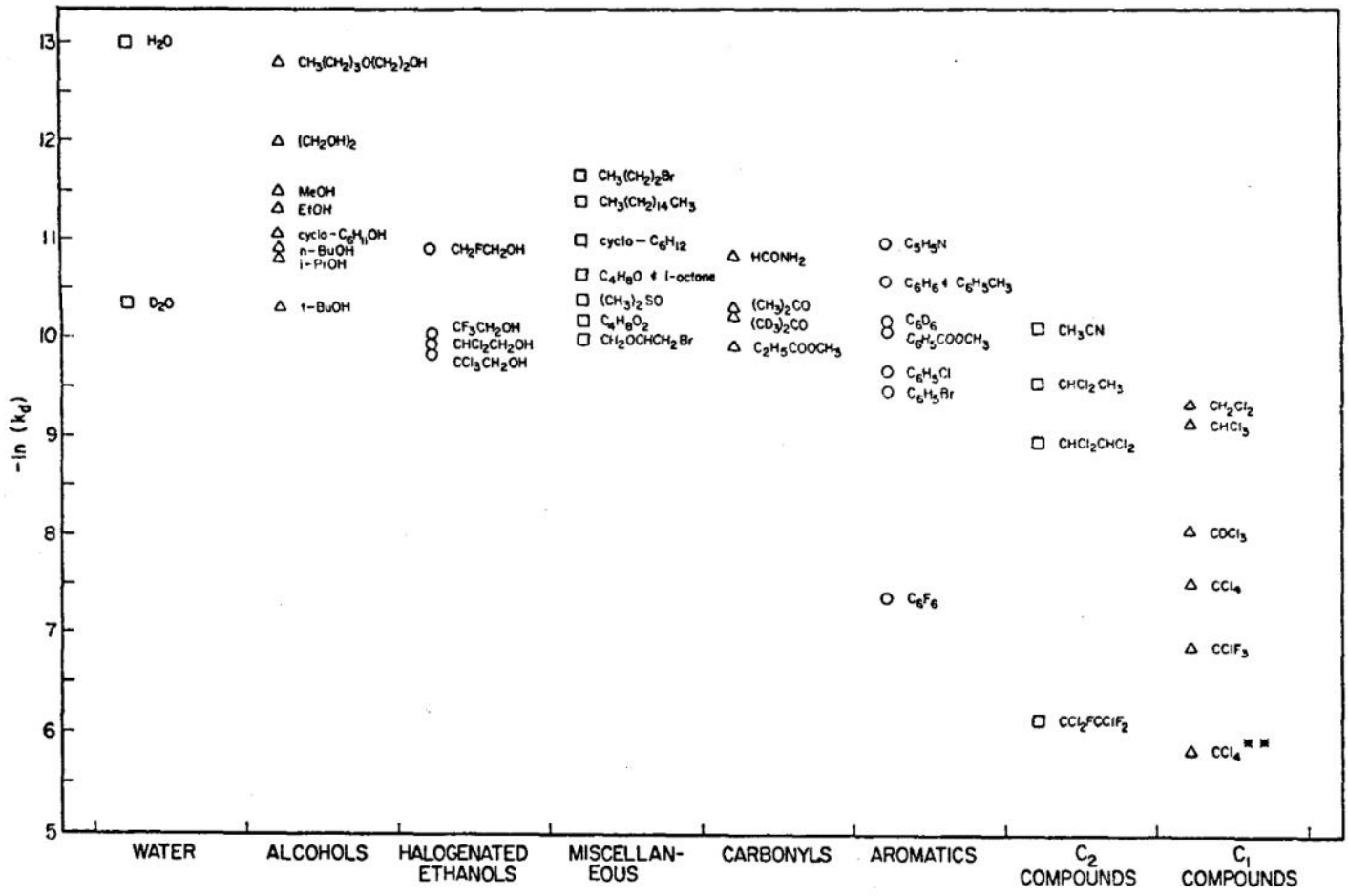

Figure 1.5. The rate of constant of dissappearance of singlet oxygen in different solvents. © AIP Publishing LLC, Ref. 74

As part of the short lifetime of singlet oxygen in aqueous solvent, a cascade of reactive oxygen species (ROS) are produced through successive reactions between H_2O and $^1O_2^*$. These reactive species have considerable lifetimes, and readily react with different cell components. The ROS

produced by singlet-oxygen sensitizers serve as broad-spectrum antimicrobials, but due to the short lifetime of singlet oxygen it is crucial that the sensitizer be in close proximity to the microbe. The different reactive species that are produced by singlet oxygen in water are shown below.

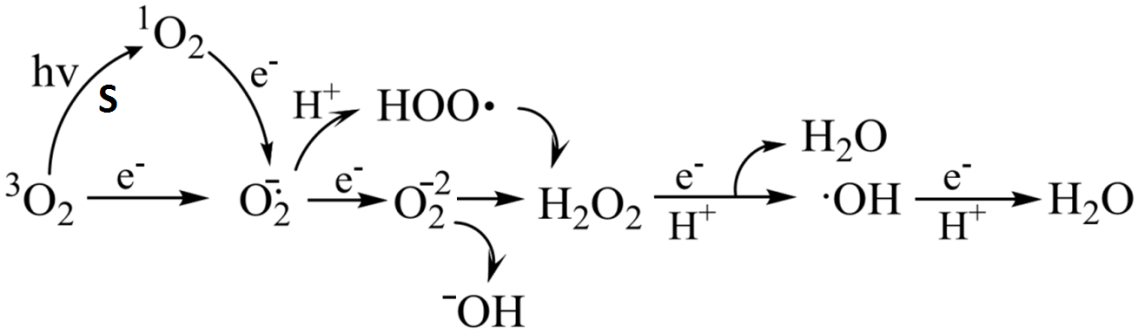

Scheme 1.3. Singlet-oxygen reactions with water to produce various reactive oxygen species.

The scheme above shows that a multitude of reactive species are produced by singlet oxygen in aqueous solution. Following the products in scheme 1.3 the formation of a superoxide radical precedes the formation of hydrogen peroxide, followed by a hydroxyl radical. The damage to phospholipids, proteins, and nucleic acids by these ROS is broad-spectrum, and serves as a primary means of antimicrobial activity for the OPEs and other biocides.[77] Another important antimicrobial mechanism by which OPEs kill bacteria is the disruption of bacterial membranes, which is discussed in the next section.

1.4.2 *Membrane Disruption*

The bacterial membrane is a feature in both Gram-positive and Gram-negative bacteria, which is composed of a phospholipid bilayer with embedded proteins. The major difference between Gram-negative and Gram-positive bacteria is in their cell wall structure.[78] Gram-negative bacteria have an inner bilayer and an outer bilayer rich in lipopolysaccharides, with only a thin peptidoglycan cell wall between the two layers. In Gram-positive bacteria, there is only a single plasma membrane which is beneath a thick layer of peptidoglycan. The differences between the two types of bacteria are shown below.

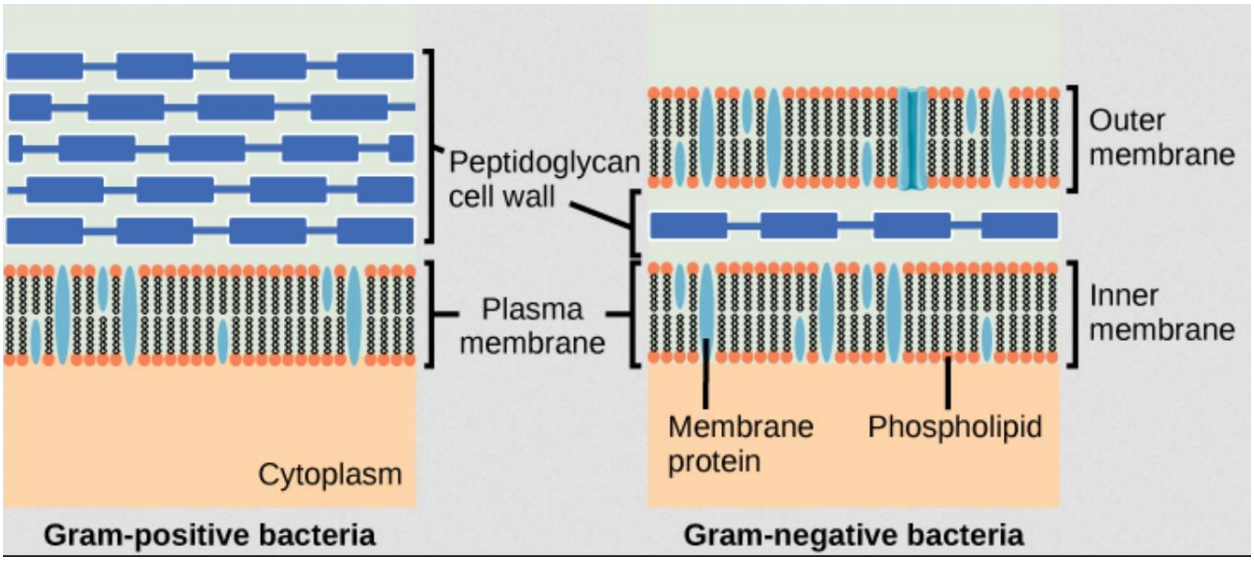

Figure 1.6. Illustration of the differences in cell wall structure between Gram-positive and Gram-negative strains of bacteria

The disruption of cell membranes has been seen in nature through various cellular processes. One common instance of cell disruption which is easily observed is the damage associated with apoptosis, which can be observed through the degradation of membrane proteins and changes in membrane potential prior to apoptosis.[79-81] In mammalian cells, mitochondria can serve as a model cell for the changes preceding apoptosis, as has been shown in prior studies. The process of membrane disruption is aided in part by the structure of the peptides involved, which have similar structural characteristics. Most natural peptides used as venom or by the body for defense against pathogens are small and contain many cationic residues. One example of natural peptides of this nature are defensins, a class of peptides which are produced in mammals and in some plants.[82-84] These β-sheet containing peptides are biocidally active against both Gram-positive and Gram-negative strains of bacteria, and also promote immune response. There are several different models which are used to describe the mechanism of disruption of the membrane by different types of antimicrobial peptides. An illustration of the different models from Melo et al is shown in the scheme below.[85]

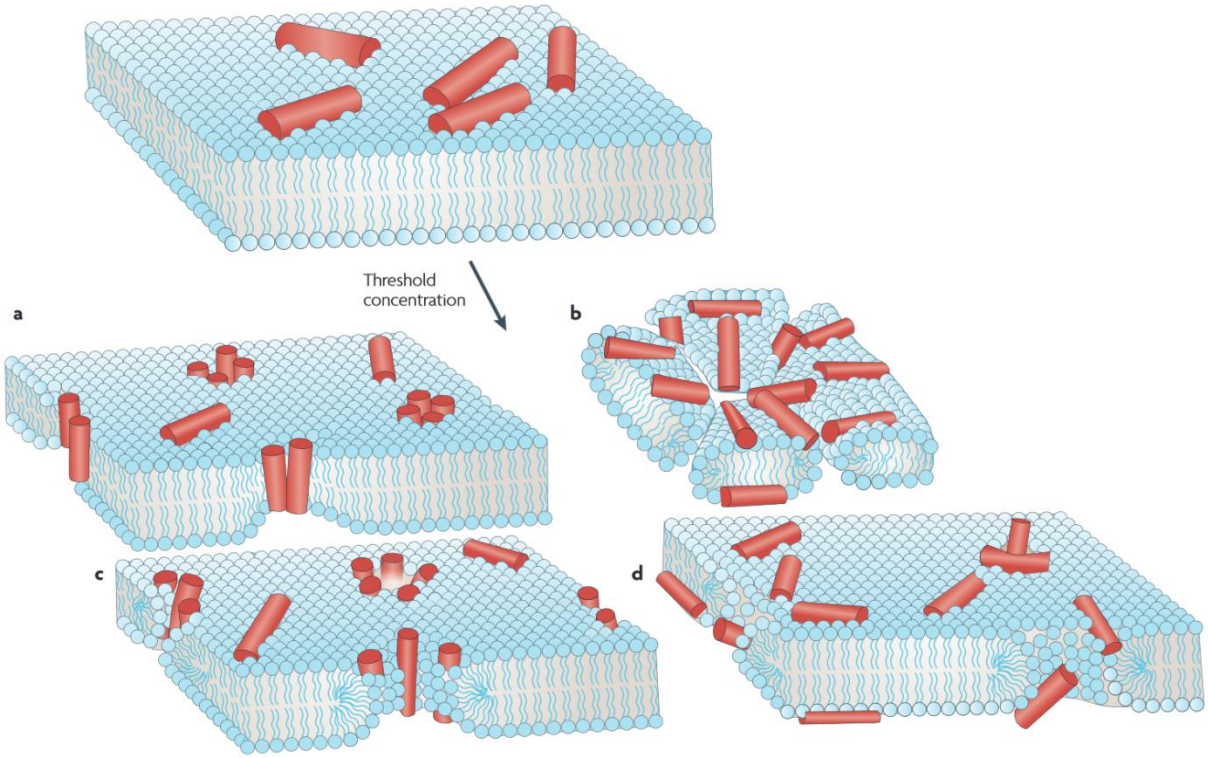

Figure 1.7. The different proposed membrane-disruption mechanisms of antimicrobial peptides: (A) Barrel-stave pore[86]; (B) Carpet Model[87]; (C) Ordered Toroidal Pore[88]; (D) Disordered Toroidal Pore[89]. Reprinted from Melo et al.[85] © Nature Publishing Group

In the scheme above, we can see the different mechanisms of membrane disruption by antimicrobial peptides. In all cases, a sufficient concentration of the peptide must be reached prior to the disruption of the membrane. The two primary modes of disruption are the carpet model and the formation of water pores of different structure. The carpet mechanism involves biocidal agents adsorbing onto the membrane surface and inducing dissociation in a detergent-like manner. This occurs after sufficient coverage is reached, and its success is dependent on a high peptide to lipid ratio.[85,86] Peptides such as alamethicin insert into the membrane perpendicular to the membrane surface and then induce an ordered pore, known as barrel-stave pore.[86,90] Most other antimicrobial peptides, including magainins, melittin, and protegrins, form water pores which contact both lipid headgroups and peptides, and have a more toroidal shape.[88,89,91] In the case of the pore forming peptides, their structure is generally composed of α-helices. The scheme below illustrates some of the cationic antimicrobial peptides and membrane-

active small organic molecules with different structural motifs.

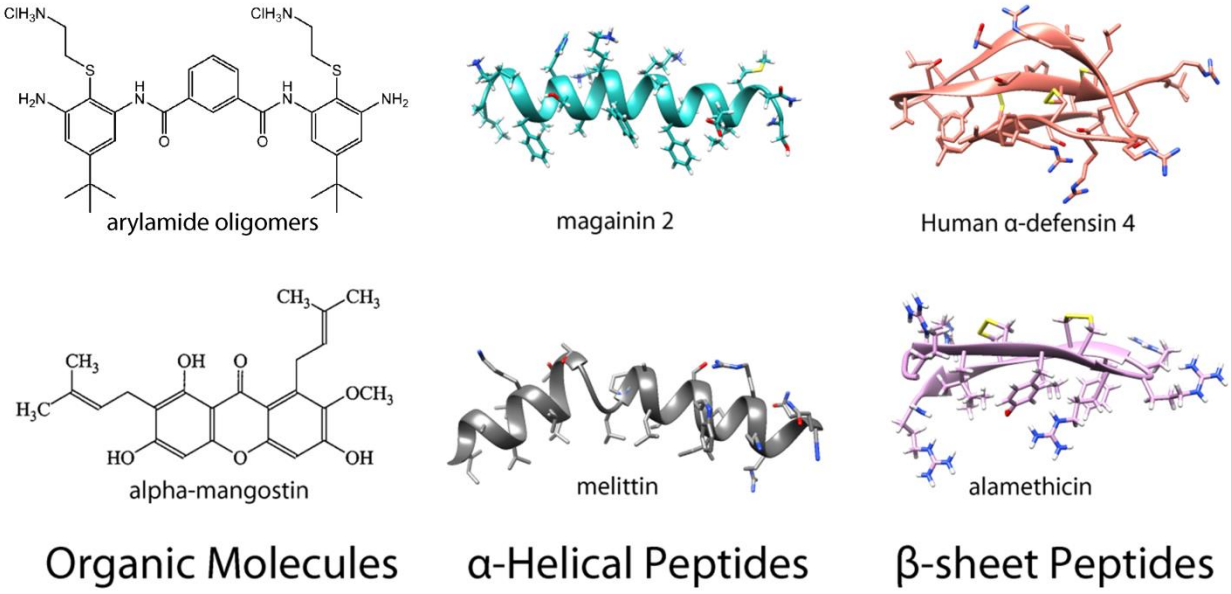

Scheme 1.4. Antimicrobial peptides and organic molecules[92,93] with membrane activity.

The cationic peptides 2-magainin and melittin have been extensively studied both experimentally and through molecular dynamics (MD) simulations as toroidal pore-forming peptides.[88,89] One drug which is currently undergoing phase II clinical trials, Brilacidin, is one example of a molecule which acts as a broad-spectrum antibiotic, mimicking the behavior of defensins which induce cell membrane disruption.[94] The antibiotic Colistin behaves in a similar manner, disrupting the cell membrane by the carpet model, but has been shown to induce an antibiotic-resistance response in A. baumanii.[95] There are several different models of membrane disruption that have been shown to occur for antimicrobial peptides or other detergents. In addition, water-soluble organic molecules such as the cationic OPEs have been shown to effectively disrupt the bacterial membrane. While some resistance can be evolved that changes membrane composition or charge, the disruption of the bacterial membrane is broad-spectrum and would be difficult to evolve resistance to. It has been shown that singlet-oxygen sensitizers such as methylene blue can induce membrane disruption upon photoirradiation.[96] In addition to activity against structure of the membranes themselves, the membrane-bound proteins of bacteria have been shown to be displaced by antimicrobial peptides.[97,98] Membrane activity in combination with another broad-spectrum biocidal method such as singlet-oxygen production leads to strong broad-spectrum

antimicrobial activity, and should be further exploited for surface decontamination applications.

1.5 Motivation

The motivation behind this work can be divided into a few points of interest:

1. The changes in photophysical properties of the OPEs from solvent interactions and self-assembly on different types molecules and scaffolds beckoned further study.
2. The photochemistry of the different series of OPEs was unknown and suspected to have an impact on the performance of the molecules as light-activated biocides.
3. The effects of aggregation of OPEs on their ability to interact with lipids and induce damage was shown experimentally but not mechanistically elucidated.

The combined experimental and computational work was carried out with the initial aim of addressing these points, and many offshoots of related work were formed along the way. In the course of this work, many of these concepts were intertwined and an understanding of the interconnectivity between the photochemistry, photophysical properties, and molecular-level interactions at play in the different processes involved in sensing or biocidal activity was sought.

1.6 References

(1) Lakshmikantham, M. V.; Vartikar, J.; Jen, K.-Y.; Cava, M. P.; Huang, W. S.; MacDiarmid, A.G. *Polym. Prepr.* **1983,** *24*(2),75.
(2) Thorand, S.; Krause, N. Improved procedures for the palladium-catalyzed coupling of terminal alkynes with aryl bromides (Sonogashira coupling). *The Journal of Organic Chemistry* **1998,** *63*(23), 8551-8553.
(3) Schumm, J. S.; Pearson, D. L.; Tour, J. M. Iterative Divergent/Convergent Approach to Linear Conjugated Oligomers by Successive Doubling of the Molecular Length: A Rapid Route to a 128Å-Long Potential Molecular Wire. *Angew. Chem. Int. Ed. Engl.* **1994,** *33,* 1360–1363.
(4) Wautelet, P.; Moroni, M.; Oswald, L.; Le Moigne, J.; Pham, A.; Bigot, J.-Y. Rigid rod conjugated polymers for nonlinear optics. 2. Synthesis and characterization of phenylene-ethynylene oligomers. *Macromolecules* **1996,** *29*(1), 446-455.
(5) Moroni, M. L.; Le Moigne, J.; Pham, T.A.; Bigot, J.-Y. Rigid rod conjugated polymers for nonlinear optics. 3. Intramolecular H bond effects on poly (phenyleneethynylene) chains. *Macromolecules* **1997,** *30*(7), 1964-1972.
(6) Weder, C.; Wrighton, M.S. Efficient solid-state photoluminescence in new poly (2, 5-dialkoxy-p-phenyleneethynylene) s. *Macromolecules* **1996,** *29*(15), 5157-5165.
(7) Grem, G.; Leditzky, G.; Ullrich, B.; Leising, G. Realization of a blue-light-emitting device using poly(*p*-phenylene). *Adv. Mater.* **1992,** *4*, 36–37.

(8) Chen, L., McBranch, D. W., Wang, H. L., Helgeson, R., Wudl, F.; Whitten, D. G. Highly sensitive biological and chemical sensors based on reversible fluorescence quenching in a conjugated polymer. *Proc. Nat. Acad. Sci.* **1999,** *96*(22), 12287-12292.
(9) Bunz, U. H. Poly(aryleneethynylene)s: Syntheses, Properties, Structures, and Applications. *Chem. Rev.* **2000**, *100*, 1605-44.
(10) McQuade, D. T.; Pullen, A. E.; T. M. Swager. Conjugated polymer-based chemical sensors. *Chemical Reviews* **2000,** *100*(7), 2537-2574.
(11) Pinto, M. R.; Schanze, K. S. Conjugated Polyelectrolytes: Synthesis and Applications. *Synthesis* **2002,** *09*, 1293-1309.
(12) Tan, C.; Pinto, M. R.; Schanze, K. S. Photophysics, aggregation and amplified quenching of a water-soluble poly(phenylene ethynylene) ***Chem. Commun.*** **2002,** 446-447
(13) DiCesare, N.; Pinto, M. R.; Schanze, K. S.; Lakowicz, J. R. Saccharide Detection Based on the Amplified Fluorescence Quenching of a Water-Soluble Poly(phenylene ethynylene) by a Boronic Acid Functionalized Benzyl Viologen Derivative. *Langmuir* **2002,** *18,*7785–7.
(14) Pinto, M. R.; Schanze, K. S. Amplified Fluorescence Sensing of Protease Activity with Conjugated Polyelectrolytes. *Proc. Nat. Acad. Sci.* **2004**, *101*, 7505-10.
(15) Zhao, X.; Liu, Y.; Schanze, K. S. A Conjugated Polyelectrolyte-based Fluorescence Sensor for Pyrophosphate. *Chem. Comm.* **2007**, 2914-2916.
(16) Achyuthan, K. E.; Bergstedt, T. S.; Chen, L.; Jones, R. M.; Kumaraswamy, S.; Kushon, S. A.; Ley, K. D.; Lu, L.; McBranch, D.; Mukundan, H. et al. Fluorescence Superquenching of Conjugated Polyelectrolytes: Applications for Biosensing and Drug Discovery. *J. Mat. Chem.* **2005**, *15*, 2648-2656
(17) Sonogashira, K.; Tohda, Y.; Hagihara, N. A convenient synthesis of acetylenes: catalytic substitutions of acetylenic hydrogen with bromoalkenes, iodoarenes and bromopyridines. *Tetrahedron Letters* **1975,** *16*(50), 4467-4470.
(18) Lu, L.; Rininsland, F. H.; Wittenburg, S. K.; Achyuthan, K. E.; McBranch, D. W.; Whitten, D. G. Biocidal activity of a light-absorbing fluorescent conjugated polyelectrolyte. *Langmuir* **2005,** *21*(22), 10154-10159.
(19) Corbitt, T. S.; Sommer, J. R.; Chemburu, S.; Ogawa, K.; Ista, L. K.; Lopez, G. P.; Whitten, D. G.; Schanze, K. S. Conjugated Polyelectrolyte Capsules: Light-Activated Antimicrobial Micro "Roach Motels" *ACS Applied Materials & Interfaces* **2008,** *1*(1), 48-52.
(20) Chemburu, S.; Corbitt, T. S.; Ista, L. K.; Ji, E.; Fulghum, J.; Lopez, G. P.; Ogawa, K.; Schanze, K.S.; Whitten, D. G. Light-induced biocidal action of conjugated polyelectrolytes supported on colloids. *Langmuir* **2008,** *24*(19), 11053-11062.
(21) Corbitt, T. S.; Ding, L.; Ji, E.; Ista, L. K.; Ogawa, K.; Lopez, G. P.; Schanze, K. S.; Whitten, D. G. Light and dark biocidal activity of cationic poly (arylene ethynylene) conjugated polyelectrolytes. *Photochemical & Photobiological Sciences* **2009,** *8*(7), 998-1005.
(22) Ista, L. K.; Dascier, D.; Ji, E.; Parthasarathy, A.; Corbitt, T. S.; Schanze, K. S.; Whitten, D. G. Conjugated-Polyelectrolyte-Grafted Cotton Fibers Act as "Micro Flypaper" for the Removal and Destruction of Bacteria. *ACS Applied Materials & Interfaces* **2011,** *3*(8), 2932-2937.
(23) Tang, Y.; Hill, E. H.; Zhou, Z.; Evans, D. G.; Schanze, K. S.; Whitten, D. G. Synthesis, Self-assembly, and Photophysical Properties of Cationic Oligo(p-phenyleneethynylene)s. *Langmuir* **2011**, *27*, 4945-55.
(24) Tang, Y.; Corbitt, T. S.; Parthasarathy, A.; Zhou, Z.; Schanze, K. S.; Whitten, D. G. Light-induced antibacterial activity of symmetrical and asymmetrical oligophenylene

ethynylenes. *Langmuir* **2011,** *27*(8), 4956-4962.
(25) Zhou, Z.; Corbitt, T. S.; Parthasarathy, A.; Tang, Y.; Ista, L. K.; Schanze, K. S.; Whitten, D. G. "End-only" functionalized oligo (phenylene ethynylene) s: Synthesis, photophysical and biocidal activity. *The Journal of Physical Chemistry Letters* **2010,** *1*(21), 3207-3212.
(26) Ji, E.; Parthasarathy, A.; Corbitt, T. S.; Schanze, K. S.; Whitten, D. G. Antibacterial activity of conjugated polyelectrolytes with variable chain lengths. *Langmuir* **2011,** *27*(17), 10763-10769.
(27) Ding, L.; Chi, E. Y.; Chemburu, S.; Ji, E.; Schanze, K. S.; Lopez, G. P.; Whitten, D. G. Insight into the Mechanism of Antimicrobial Poly (phenylene ethynylene) Polyelectrolytes: Interactions with Phosphatidylglycerol Lipid Membranes *Langmuir* **2009,** *25*(24), 13742-13751.
(28) Wang, Y.; Zhou, Z.; Zhu, J.; Tang, Y.; Canady, T. D.; Chi, E. Y.; Schanze, K. S.; Whitten, D. G. Dark antimicrobial mechanisms of cationic phenylene ethynylene polymers and oligomers against Escherichia coli. *Polymers* **2011,** *3*(3), 1199-1214.
(29) Wang, Y.; Jett, S. D.; Crum, J.; Schanze, K. S.; Chi, E. Y.; Whitten, D. G. Understanding the Dark and Light-enhanced Bactericidal Action of Cationic Conjugated Polyelectrolytes and Oligomers. *Langmuir* **2013,** *29*(2), 781–792.
(30) Huffman, M. A. Self-Medicative Behavior in the African Great Apes: An Evolutionary Perspective into the Origins of Human Traditional Medicine *BioScience* **2001,** *51*(8), 651-661.
(31) Huffman, M. A. Animal self-medication and ethno-medicine: exploration and exploitation of the medicinal properties of plants. *Proceedings of the Nutrition Society* **2003,** *62*(02), 371-381.
(32) Ojewole, J. A. Antinociceptive, anti-inflammatory and antidiabetic properties of *Hypoxis hemerocallidea* Fisch. & CA Mey.(Hypoxidaceae) corm ['African Potato'] aqueous extract in mice and rats. *Journal of Ethnopharmacology*, **2006,** *103*(1), 126-134.
(33) Cakilcioglu, U.; Khatun, S.; Turkoglu, I.; Hayta, S. Ethnopharmacological survey of medicinal plants in Maden (Elazig-Turkey). *Journal of Ethnopharmacology* **2011,** *137*(1), 469-486.
(34) Sullivan, R. The identity and work of the ancient Egyptian surgeon. *Journal of the Royal Society of Medicine* **1996,** *89*(8), 467-473.
(35) Sipos, P.; Gyõry, H.; Hagymási, K.; Ondrejka, P.; Blázovics, A. Special wound healing methods used in ancient Egypt and the mythological background. *World Journal of Surgery* **2004,** *28*(2), 211-216.
(36) Wainwright, M. Moulds in ancient and more recent medicine. *Mycologist* **1989,** *3*(1), 21-23.
(37) Forrest, R. D. Early history of wound treatment. *Journal of the Royal Society of Medicine* **1982,** *75*(3), 198.
(38) Landsberg, H. Prelude to the discovery of penicillin. *Isis* **1949,** 225-227.
(39) Bosch, F.; Rosich, L. The contributions of Paul Ehrlich to pharmacology: a tribute on the occasion of the centenary of his Nobel Prize. *Pharmacology* **2008,** *82*(3), 171-179.
(40) Otten, H. Domagk and the development of the sulphonamides. *Journal of Antimicrobial Chemotherapy* **1986,** *17*(6), 689-690.
(41) J. et Th. Tréfouël; F. Nitti et D. Bovet, Activité du p.aminophénylsulfamide sur l'infection streptococcique expérimentale de la souris et du lapin *C. R. Soc. Biol.* **1935**, *120*, 756.
(42) Crowfoot, D.; Bunn, Charles W.; Rogers-Low, Barbara W.; Turner-Jones, A. "X-ray crystallographic investigation of the structure of penicillin". In Clarke, H. T.; Johnson, J. R.; Robinson, R. (ed). Chemistry of Penicillin. (1949) Princeton University Press. pp. 310–367.

(43) Curtis, R.; Jones, J. Robert Robinson and penicillin: an unnoticed document in the saga of its structure. *Journal of Peptide Science* **2007,** *13*(12), 769-775.
(44) Grossman, C. M. The first use of penicillin in the United States. *Annals of Internal Medicine* **2008,** *149*(2), 135-136.
(45) Massova, I.; Mobashery, S. Kinship and diversification of bacterial penicillin-binding proteins and β-lactamases. *Antimicrobial Agents and Chemotherapy* **1998,** *42*(1), 1-17.
(46) Davies, J.; Davies, D. Origins and evolution of antibiotic resistance. *Microbiology and Molecular Biology Reviews* **2010,** *74*(3), 417-433.
(47) Levin, B. R.; Lipsitch, M.; Perrot, V.; Schrag, S.; Antia, R.; Simonsen, L.; Walker, N. M.; Stewart, F. M. The population genetics of antibiotic resistance. *Clinical Infectious Diseases* **1997,** *24*(S1), S9-S16.
(48) Herrero, M.; de Lorenzo, V.; Timmis, K. N. Transposon vectors containing non-antibiotic resistance selection markers for cloning and stable chromosomal insertion of foreign genes in gram-negative bacteria. *Journal of Bacteriology* **1990,** *172*(11), 6557-6567.
(49) Okusu, H.; Ma, D.; Nikaido, H. AcrAB efflux pump plays a major role in the antibiotic resistance phenotype of Escherichia coli multiple-antibiotic-resistance (Mar) mutants. *Journal of Bacteriology* **1996,** *178*(1), 306-308.
(50) Poole, K.; Krebes, K.; McNally, C.; Neshat, S. Multiple antibiotic resistance in Pseudomonas aeruginosa: evidence for involvement of an efflux operon. *Journal of Bacteriology*, **1993,** *175*(22), 7363-7372.
(51) Singer, M.; Baker, T. A.; Schnitzler, G.; Deischel, S. M.; Goel, M.; Dove, W.; Jaacks, K. J.; Grossman, A. D.; Erickson, J. W.; Gross, C. A. A collection of strains containing genetically linked alternating antibiotic resistance elements for genetic mapping of Escherichia coli. *Microbiological Reviews* **1989,** *53*(1), 1-24.
(52) Ito, T.; Okuma, K.; Ma, X. X.; Yuzawa, H.; Hiramatsu, K. Insights on antibiotic resistance of *Staphylococcus aureus* from its whole genome: genomic island SCC. *Drug Resistance Updates* **2003,** *6*(1), 41-52.
(53) Landy, M.; Larkum, N. W.; Oswald, E. J.; Streightoff, F. Increased synthesis of p-aminobenzoic acid associated with the development of sulfonamide resistance in Staphylococcus aureus. *Science* **1943,** *97*(2516), 265-267.
(54) Li, X. Z.; Mehrotra, M.; Ghimire, S.; Adewoye, L. β-Lactam resistance and β-lactamases in bacteria of animal origin. *Veterinary Microbiology* **2007,** *121*(3), 197-214.
(55) Gillham, Nicholas W. Transmission and segregation of a non-chromosomal factor controlling streptomycin resistance in diploid Chlamydomonas. *Nature* **1963,** 294-294.
(56) Thomas, D. Y.; Wilkie, D. Recombination of mitochondrial drug-resistance factors in Saccharomyces, cerevisiae. *Biochemical and Biophysical Research Communications* **1968,** *30*(4), 368-372.
(57) Cohen, S. N.; Chang, A. C.; Hsu, L. Nonchromosomal antibiotic resistance in bacteria: genetic transformation of Escherichia coli by R-factor DNA. *Proc. Nat. Acad. Sci.* **1972,** *69*(8), 2110-2114.
(58) Cohen, S. N.; Miller, C. A. Non-chromosomal antibiotic resistance in bacteria: II. Molecular nature of R-factors isolated from Proteus mirabilis and Escherichia coli. *Journal of Molecular Biology* **1970,** *50*(3), 671-687.
(59) Cohen, S. N.; Miller, C. A. Non-chromosomal antibiotic resistance in bacteria, III: Isolation of the discrete transfer unit of the R-factor R1. *Proc. Nat. Acad. Sci.* **1970,** *67*(2), 510-516.

(60) Jacob, A. E.; Hobbs, S. J. Conjugal transfer of plasmid-borne multiple antibiotic resistance in Streptococcus faecalis var. zymogenes. *Journal of Bacteriology* **1974,** *117*(2), 360-372.
(61) Brefort, G.; Magot, M.; Ionesco, H.; & Sebald, M. Characterization and transferability of *Clostridium perfringens* plasmids. *Plasmid* **1977,** *1*(1), 52-66.
(62) Guerry, P.; Van Embden, J.; Falkow, S. Molecular nature of two nonconjugative plasmids carrying drug resistance genes. *Journal of Bacteriology* **1974,** *117*(2), 619-630.
(63) Sansonetti, P. J.; Kopecko, D. J.; Formal, S. B. Shigella sonnei plasmids: evidence that a large plasmid is necessary for virulence. *Infection and Immunity* **1981,** *34*(1), 75-83.
(64) Datta, N.; Hughes, V. M. Plasmids of the same Inc groups in Enterobacteria before and after the medical use of antibiotics. *Nature* **1983,** 616-617.
(65) Laxminarayan, R.; Duse, A.; Wattal, C.; Zaidi, A. K.; Wertheim, H. F.; Sumpradit, N.; Vlieghe, E.; Hara, G. L.; Gould, I.M.; Goossens, H. *et al* Antibiotic resistance—the need for global solutions. *The Lancet* **2013,** *13*(12), 1057-1098.
(66) Neu, H. C. The crisis in antibiotic resistance. *Science* **1992,** *257*(5073), 1064-1073.
(67) Tenover, F. C.; Hughes, J. M. The challenges of emerging infectious diseases: development and spread of multiply-resistant bacterial pathogens. *Jama* **1996,** *275*(4), 300-304.
(68) Bonomo, R. A. Multiple antibiotic-resistant bacteria in long-term-care facilities: an emerging problem in the practice of infectious diseases. *Clinical Infectious Diseases* **2000,** *31*(6), 1414-1422.
(69) Bozja, J.; Sherrill, J.; Michielsen, S.; Stojiljkovic, I. Porphyrin-based, light-activated antimicrobial materials. *Journal of Polymer Science Part A: Polymer Chemistry*, **2003,** *41*(15), 2297-2303.
(70) Perni, S.; Piccirillo, C.; Pratten, J.; Prokopovich, P.; Chrzanowski, W.; Parkin, I. P.; Wilson, M. The antimicrobial properties of light-activated polymers containing methylene blue and gold nanoparticles. *Biomaterials* **2009,** *30*(1), 89-93.
(71) Wilson, M. Light-activated antimicrobial coating for the continuous disinfection of surfaces. *Infection Control and Hospital Epidemiology* **2003,** *24*(10), 782-784.
(72) Noimark, S.; Dunnill, C. W.; Wilson, M.; Parkin, I. P. The role of surfaces in catheter-associated infections. *Chemical Society Reviews* **2009,** *38*(12), 3435-3448.
(73) Schweitzer, C.; Schmidt, R. Physical Mechanisms of Generation and Deactivation of Singlet Oxygen *Chemical Reviews* **2003,** 103(5), 1685–1757.
(74) Lindig, B. A.; Rodgers, M. A.; Schaap, A. P. Determination of the lifetime of singlet oxygen in water-d2 using 9, 10-anthracenedipropionic acid, a water-soluble probe. *Journal of the American Chemical Society* **1980,** *102*(17), 5590-5593.
(75) Wilkinson, F.; Brummer, J. G. Rate constants for the decay and reactions of the lowest electronically excited singlet state of molecular oxygen in solution. *Journal of Physical and Chemical Reference Data* **1981,** *10*(4), 809-999.
(76) Wilkinson, F.; Helman, W. P.; Ross, A. B. Rate constants for the decay and reactions of the lowest electronically excited singlet state of molecular oxygen in solution. An expanded and revised compilation *Journal of Physical and Chemical Reference Data* **1995,** *24*(2), 663-677
(77) Proctor, P. H.; Reynolds, E. S. Free radicals and disease in man. *Physiological Chemistry and Physics and Medical NMR* **1983,** *16*(3), 175-195.
(78) Schleifer, K. H.; Kandler, O. Peptidoglycan types of bacterial cell walls and their taxonomic implications. *Bacteriological Reviews* **1972,** *36*(4), 407.
(79) Kihlmark, M.; Imreh, G.; Hallberg, E. Sequential degradation of proteins from the

nuclear envelope during apoptosis. *Journal of Cell Science* **2001,** *114*(20), 3643-3653.
(80) Lemasters, J. J.; DiGuiseppi, J.; Nieminen, A. L.; Herman, B. Blebbing, free Ca2+ and mitochondrial membrane potential preceding cell death in hepatocytes. *Nature* **1987,** *325*(6099), 78-81
(81) Ly, J. D.; Grubb, D. R.; Lawen, A. The mitochondrial membrane potential (Δψm) in apoptosis; an update. *Apoptosis* **2003,** *8*(2), 115-128.
(82) Ganz, T. Defensins: antimicrobial peptides of innate immunity. *Nature Reviews Immunology* **2003,** *3*(9), 710-720.
(83) Kim, C.; Gajendran, N.; Mittrücker, H.; Weiwad, M.; Song, Y.; Hurwitz, R.; Wilmanns, M.; Fischer, G.; Kaufmann, S. Human alpha-defensins neutralize anthrax lethal toxin and protect against its fatal consequences. *Proc. Nat. Acad. Sci.* **2005,** 102(13), 4830–5.
(84) Thomma, B. P.; Cammue, B. P.; Thevissen, K. Plant defensins. *Planta* **2002,** *216*(2), 193-202.
(85) Melo, M. N.; Ferre, R.; Castanho, M. A. Antimicrobial peptides: linking partition, activity and high membrane-bound concentrations. *Nature Reviews Microbiology* **2009,** *7*(3), 245-250.
(86) Baumann, G.; Mueller, P. A molecular model of membrane excitability. *J. Supramol. Struct.* **1974,** *2*, 538–557.
(87) Pouny, Y.; Rapaport, D.; Mor, A.; Nicolas, P.; Shai, Y. Interaction of antimicrobial dermaseptin and its fluorescently labeled analogues with phospholipid membranes. *Biochemistry* **1992,** *31*, 12416–12423
(88) Ludtke, S. J.; He, K.; Heller, W.T.; Harroun, T.A.; Yang, L.; Huang, H.W. Membrane pores induced by magainin. *Biochemistry* **1996,** *35*, 13723–13728.
(89) Leontiadou, H.; Mark, A. E.; Marrink, S. J. Antimicrobial peptides in action. *J. Am. Chem. Soc.* **2006,** *128*, 12156–12161
(90) Boheim, G. Statistical Analysis of Alamethicin Channels in Black Lipid Membranes. *J. Membr. Bio.* **1974,** *19*, 277-303.
(91) Sokolov, Y.; Mirzabekov, T.; Martin, D. W.; Lehrer, R. I.; Kagan, B. L. Membrane channel formation by antimicrobial protegrins. *Biochimica et Biophysica Acta (BBA)-Biomembranes* **1999,** *1420*(1), 23-29.
(92) Koh, J. J.; Qiu, S.; Zou, H.; Lakshminarayanan, R.; Li, J.; Zhou, X.; Beuerman, R. W. Rapid bactericidal action of alpha-mangostin against MRSA as an outcome of membrane targeting. *Biochimica et Biophysica Acta (BBA)-Biomembranes* **2013,** *1828*(2), 834-844.
(93) Tang, H.; Doerksen, R. J.; Jones, T. V.; Klein, M. L.; Tew, G. N. Biomimetic facially amphiphilic antibacterial oligomers with conformationally stiff backbones. *Chemistry & Biology* **2006,** *13*(4), 427-435.
(94) Butler, M. S.; Cooper, M. A. Antibiotics in the clinical pipeline in 2011. *The Journal of Antibiotics* **2011,** 64 (6), 413–425.
(95) Napier, B. A.; Burd, E. M.; Satola, S. W.; Cagle, S. M.; Ray, S. M.; McGann, P.; Weiss, D. S. Clinical use of colistin induces cross-resistance to host antimicrobials in *Acinetobacter baumannii*. *MBio* **2013,** *4*(3), e00021-13.
(96) Mertins, O.; Bacellar, I. O.; Thalmann, F.; Marques, C. M.; Baptista, M. S.; Itri, R. Physical damage on giant vesicles membrane as a result of methylene blue photoirradiation. *Biophysical Journal* **2014,** *106*(1), 162-171.
(97) Brogden, K. A. Antimicrobial peptides: pore formers or metabolic inhibitors in bacteria?. *Nature Reviews Microbiology* **2005,** *3*(3), 238-250.

(98) Wenzel, M.; Chiriac, A. I.; Otto, A.; Zweytick, D.; May, C.; Schumacher, C.; Bandow, J. E. Small cationic antimicrobial peptides delocalize peripheral membrane proteins. *Proc. Nat. Acad. Sci.* **2014,** *111*(14), E1409-E1418.

Chapter II: Photophysical Properties of Oligo-p-Phenylene Ethynylenes

2.1 Introduction

2.1.1 Theoretical Explanations of Chromophore Aggregation

The aggregation of chromophores has been of great interest to researchers for decades, as the resulting changes in the photophysical properties of the chromophore can be harnessed for various purposes, such as sensing[1-5], solar cells[6], organic LEDs[7], and tunable lasers[8-10]. Organic dyes, which have large, permanent, electric dipole moments, have been thoroughly researched for their aggregation properties.[11-20]The photophysical changes that are observed can be explained through geometry-dependent interactions of two molecules with strong dipoles. Based on Frenkel's exciton theory, this theory was first developed by Davydov [21], and shortly adapted for dimers by Kasha.[22,23] The framework as constructed by Kasha *et al* in 1965 gives a model by which the orientation of the transitions dictates the change to the electronics of the system which can result in a blue-shift or red-shift in the absorbance, among other properties.[24] When the transition dipoles of the two molecules are parallel in orientation, the transition from the ground state to the higher-energy exciton level is allowed, while the lower-energy one is forbidden. Dubbed an "H-aggregate", this results in a blue-shifted absorbance spectrum[14-16], as first reported with Thiazine dyes by Rabinowitch and Epstein in 1941.[14] The formation of an H-aggregate may also result from an edge-face orientation, giving rise to an aggregate which resembles a herringbone shape[20]. When transition dipoles are in-line, the higher-energy transition is forbidden, and the lower is allowed, leading to a red-shifted absorbance spectrum. Referred to as a "J-aggregate", this was first reported to occur with cyanine dyes in 1936 by Jelley[17], and cyanine dyes have since become a model system for the study of J-aggregation.[18,19]

Chromophore aggregation can also result in significant changes to the ability of the system to fluoresce or phosphoresce.[25] Fluorescence quenching and unquenching plays an important role in molecular sensors, with a large representation of medical and biochemical sensing technologies such as FRET bioassays [26-29], optical contrast agents [30,31], and dissolved oxygen sensors.[32,33] Conjugated polyelectrolytes, polymers with a conjugated backbone and pendant charged groups for solubility, have been of particular interest for biosensing [1-5,34-38]. Polymers based on the phenylene-ethynylene (PPE) backbone have been shown by the Whitten and Schanze groups to be effective sensors as they are water soluble and undergo fluorescence

enhancement or quenching when bound to a biomolecule of interest. [1-5,36-38] The importance of molecules based on this backbone, particularly as sensors, highlights the usefulness of determining mechanisms by which photophysical changes are induced, and if a structural or chemical basis for these effects can be established. Furthermore, these experimental effects can be explored with theoretical calculations to determine the geometry and predict photophysical properties at the quantum-mechanical level.[1]

2.1.2 *Density Functional Theory Calculations of Conjugated Organic Molecules*

Density functional theory (DFT) is a quantum mechanical theory which finds its original roots in the Thomas-Fermi model of electronic structure of many-body systems.[39,40] While the Thomas-Fermi model failed to approximate real systems and only worked in the limit as atomic number goes to infinity, it nevertheless served as an important step in the development of a model of electronic structure. DFT was first put on a firm theoretical footing when Hohenberg and Kohn developed their theorems in 1964, which stated that the ground state properties of a many-electron system are uniquely determined by an electron density that depends only on 3 spatial coordinates.[41] This allows one to determine the ground-state density of a many-particle system via direct variation with respect to the density of the system. This work was extended by Kohn and Sham in 1965, where the direct variation is replaced with an intermediate orbital calculation.[42] The Kohn-Sham framework of the Hohenberg-Kohn theorem implies that for any interacting system the single-particle orbitals are unique functionals of the density. As modeling many-body electron exchange and correlation is difficult in the K-S framework, a local density approximation based off of the homogeneous electron gas model is used as the basis for all modern DFT calculations.[43] This simplifies non-interacting systems so that they can be solved using a Slater determinant of the orbitals, and allows kinetic energy of a system to be solved exactly. DFT has been successfully used to predict structural and electronic properties of molecules for decades, and in recent years has been of great impact to the study of chromophores. A particular development which has lent great support in the study of chromophores is the extension of DFT to Time-dependent DFT (TD-DFT), allowing for the exploration of electronic properties in the presence of an electric or magnetic field.[44] This allows the prediction of electronic spectra and excited state geometries for direct comparison to experimental measurements.

2.1.3 Previous work with PPEs and OPEs

There has been growing interest in the synthesis of well-defined conjugated oligomers that have well-defined chemical and physical properties and serve as important model systems to provide a basis for determining the structure-property relationships of the larger polymers.[38,45-49] Conjugated polymers and polyelectrolytes have been the subject of much investigation for their sensing and antimicrobial activities,[34,50-55] but have a drawback in that they consist of a mixture of molecules with a broad range of molecular weights due to the statistical nature of the polymerization processes.[45,56-61] Polymers and oligomers utilizing a backbone of *p*-phenylene ethynylenes have been previously studied by multiple research groups for their sensing properties.[1-5,35,45-49,62] The Whitten and Schanze groups have reported that cationic oligomers based on this structure are effective at sensing enzymatic activity[2,3,37,38], conjugating with bio-scaffolds[1,34-36], and inducing strong antimicrobial activity.[63-65] Throughout the studies of larger water-soluble oligomers, the changes observed upon complexation with a host molecule have suggested that planarization of the backbone may lead to a chromophore with a lower excitation energy.[1]

Three series of well-defined cationic oligomers with different chain lengths and different end groups on the main chain were synthesized to investigate structure-reactivity relationships through photophysical and antimicrobial properties.[1] In addition, a series of "end-only" OPEs were synthesized by Zhou *et al* which have cationic groups on their ends and are only three phenyl rings long.[65] The structure of these oligomeric *p*-phenylene-ethynylenes[1,65] (OPEs) are shown in Scheme 2.1. The OPE-n (n = 1, 2, 3) oligomers with carboxyester endgroups on one end and terminal hydrogen on the other end were synthesized first and studied both in solution, and attached onto solid surfaces by covalent linkages.[1] To investigate the effect of carboxyester end-groups on the photophysical, self-assembly, and antimicrobial properties, the other two sets of oligomers +*n*H (with a hydrogen on both ends) and +*n*C (with a carboxyester group on both ends) were synthesized. Preliminary reports of photophysical properties and complexation with anionic scaffolds of smaller oligomer raised two major questions that could not be completely resolved.[1] The first question centered around the presence of carboxyester end-groups greatly decreasing the fluorescence of OPEs in water, but complexation with anionic scaffolds resulting in shifting of the absorption and fluorescence and increase of fluorescence. A second unresolved

issue was whether the shifts in fluorescence upon complex formation could be attributed to J-aggregate formation or to planarization. Both of these questions were addressed in separate studies, and are discussed in this dissertation chapter.[1,66]

The general structure which describes the different OPEs studied in this dissertation are given below, in Scheme 2.1.

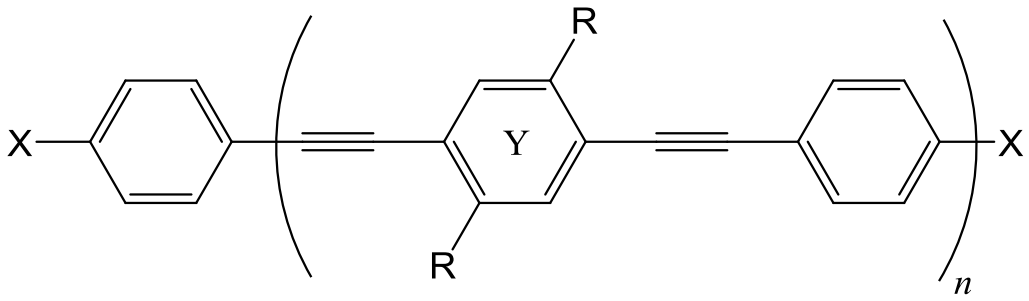

^{+}nC series: X = COOEt, R = $O(CH_2)_3N^{+}(CH_3)_3$
^{+}nH series: X=H, R = $O(CH_2)_3N^{+}(CH_3)_3$
^{-}nC series: X = COOEt, R = $O(CH_2)_3SO_3^{-}$
^{-}nH series: X=H, R = $O(CH_2)_3SO_3^{-}$
$^{+}$EO: n=1, X = $O(CH_2)_3N^{+}(CH_3)_3$, R = H
$^{-}$EO: n=1, X=$O(CH_2)_3SO_3^{-}$, R = H

Scheme 2.1. *p*-Phenylene ethynylene oligomers used in this study

As can be seen in the scheme above, the OPEs with charged groups coming off opposite ends have the title EO designating "end-only", while those with charged groups coming off the side are named based on their number of repeat units and end-group functionality. A class of end-only OPEs with a thiophene central ring (EOT, in Scheme 2.1 Y is thiophene ring with no sidechains) is also briefly discussed.

As discussed in the previous chapter, the oligo-*p*-phenylene ethynylynes (OPEs) were first synthesized by Yanli Tang and Zhijun Zhou in the Whitten Group at the University of New Mexico. The initial preparation of the OPEs by Yanli Tang was followed by a study of the photophysical properties of the series of compounds, including their photophysical changes upon intercalation with or adsorption onto an oppositely-charged scaffolds such as carboxymethylcellulose and DNA.[1,67] At first, these changes were attributed solely to the formation of J-aggregates, as they showed the red-shifted absorbance and some enhanced

fluorescence common to these aggregates. These changes are shown in Figure 1.1 of Chapter 1. Despite the similarity to J-aggregates, changes induced by interfacial solvent and enhanced conjugation from an increase of planarity could also be reasons for the changes in photophysical properties observed.

As it was not sufficient to simply assume that a J-aggregate was formed, a computational study was carried out using density functional theory to calculate electronic structure of the OPEs of various lengths with the goal of determining whether molecular geometry, particularly of the PPE backbone, plays a role in the photophysical properties separate from aggregate formation.[1] Computational studies using Density Functional Theory (DFT) calculations have previously shown reliable results with similar oligo-phenylenethynylenes.[68-71] In order to further understand the relationship between structure and photophysical properties, DFT calculations were performed using the Gaussian 03 software package.[72] The results of the computational study, taken together with the experimental results provide a consistent explanation for the structure, self-assembly and photophysics of this interesting series of cationic conjugated oligomers.

Recent explorations into the photochemistry of a class of notably photoreactive OPEs in water led to the idea of complexation with the anionic surfactant sodium dodecyl sulfate (SDS) to reduce photodegradation.[73] This was shown to allow sustained biocidal activity of the OPE-SDS complexes throughout long-term irradiations which would normally render the compound inactive, and the photophysical changes observed upon surfactant complexation suggested formation of a molecular aggregate.[74] In an effort to determine the structure of the aggregates formed with OPEs based on orientation of charged groups and hydrogen-bonding ability, a study of OPEs with both charged end-groups and sidechains was carried out, and the influence of COOEt endgroups on photophysical changes was assessed.

2.2 *Density Functional Theory Study of OPE Geometry*

Electronic structure calculations were performed using DFT, and the methods for the calculations are given in Chapter 7. A variety of different properties were examined at different levels of theory, and many interesting and insightful conclusions were made.

2.2.1 Optimized Geometries and Barriers to Rotation about the Backbone

The structures of the S-OPE-n (H) series optimized by the DFT:B3LYP/6-31g** basis set are shown below, in Figure 2.2.

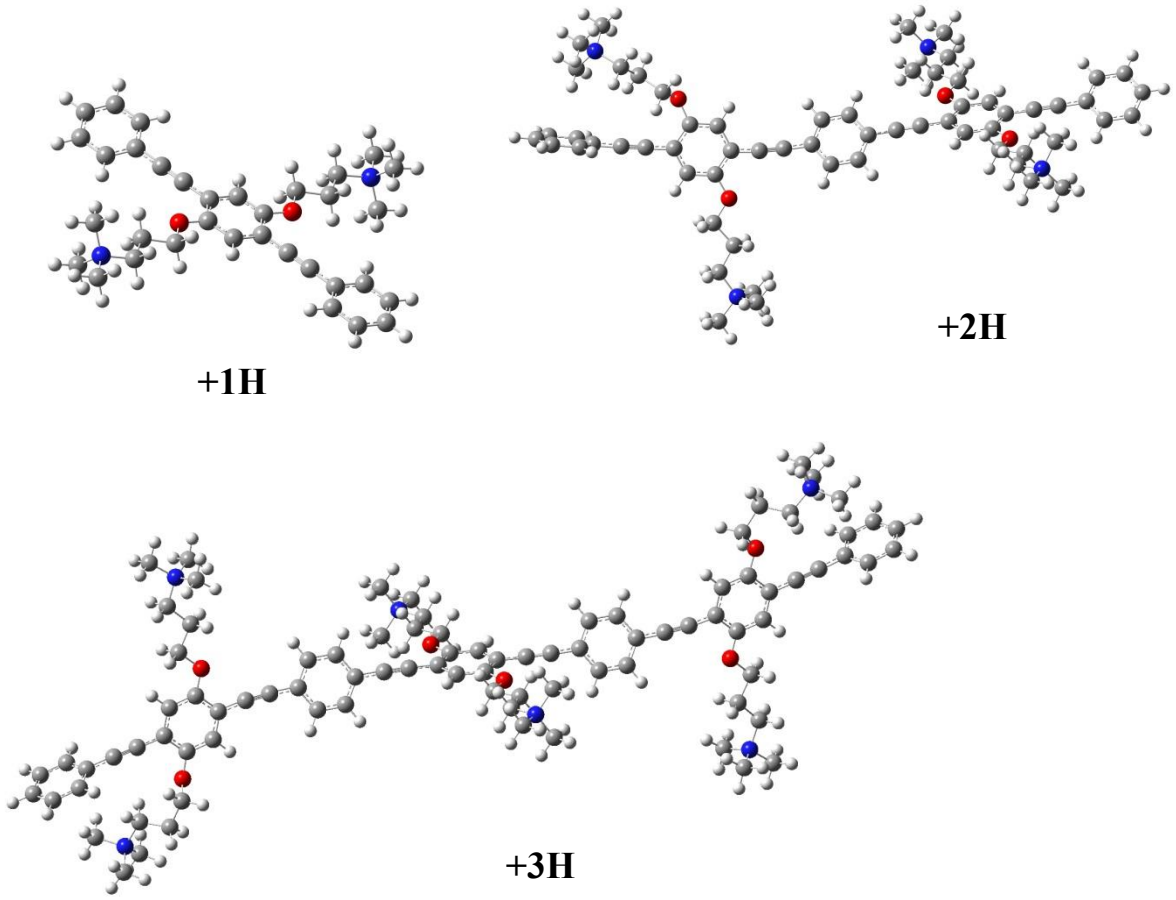

Figure 2.2. The DFT:B3LYP/6-31g** optimized structures for the ^{+}nH series.[1]

The frequencies of the vibrational movements of optimized structures were calculated to ensure that a global minimum had been reached, and the resulting calculated frequencies are given in Figure 7.11 in the methods section. The optimized structures in Figure 2.2 show decreased planarity in the ground state as the number of subunits increases. **+1H**, the smallest molecule, is nearly planar. The larger oligomers have much larger rotations about the ethynyl group which break the planarity of the backbone. It has been previously shown in the aforementioned computational study by James et al.[68] that the energy difference between a fully planar and

perpendicular torsional angle between phenyl rings is 0.5 kcal/mol, while kT at room temp (298K) is 0.59 kcal/mol. This suggests that the oligomers have a non-planar geometry in the ground state, as is clearly shown in the optimized structures of the OPEs where n=2 and 3 deviate from planarity. It would seem that these deviations from planarity would cause discrete "segment chromophores." The energy of the coordinates for **+1H** shown in Figure 2.2 were calculated as the two dihedral angles about the ethynyl group, which dictate co-planarity, were changed by 10º increments for a total of 360º, as discussed in the methods section (Ch. 7). The ΔE of the OPE with sidechains **+1H** and the end-only OPE **+EO** are shown below, in Figure 2.3.

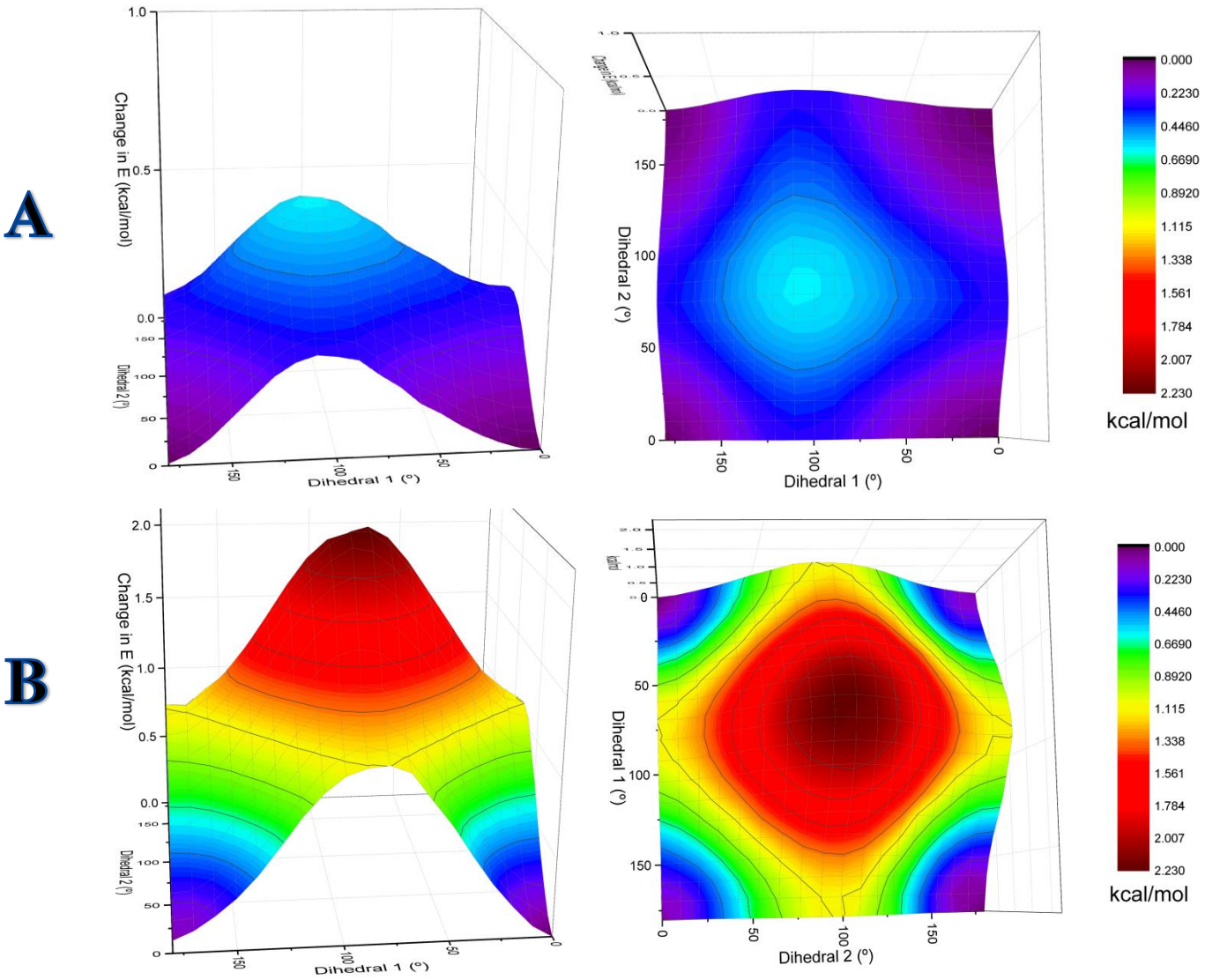

Figure 2.3. Dihedral angle scan across both ethynyl groups in (A) **+1H**; (B) **+EO**; Both energy scans were performed at the B3LYP/6-31g** level of theory as discussed in the methods (Ch.2.)

The energy scans clearly demonstrate a lower energy barrier to rotation for the OPE with sidechains (< 0.5 kcal/mol), than that of the end-only OPE which has a barrier to orthogonality (both dihedrals at ~90º) above 2 kcal/mol. As previously mentioned, kT at room temperature is 0.59 kcal/mol, suggesting that the OPEs with sidechains are able to rotate around the ethynyl groups at room temperature. The breaks in planarity induced by this likely contribute to the electronic properties of the molecules, particularly when at an increased number of repeat units.

2.2.2 *Electronic structure and influence of planarization on calculated absorption energy*

The λ_{max} of OPEs red shift with increasing number of repeat units from 1 to 3 in both solvents; however, the change of λ_{max} between n=1 and n=3 is much larger than that between n=2 and n=3 for all series of compounds. The shape of the absorption spectra and location of the absorbance maximum show negligible changes on going from n=3 to a similarly structured polymer with 49 repeat units. Therefore we conclude that there is a limiting "segment chromophore" reached perhaps already with the n=2 compounds and certainly with the n=3 compounds. The present results may be compared with those of Pearson and Tour for oligo(2,5-thiophene ethynylenes) where a saturation of the optical absorption was noted between the oligomers having 8 and 16 thiophene rings.[49] For the OPEs a similar saturation is already evident between the oligomers (n=2 and n=3) having 5 and 7 phenyl rings.

The frontier orbitals of the +*n*H series optimized by the DFT:B3LYP/6-31g** basis set are shown below, in Figure 2.4.

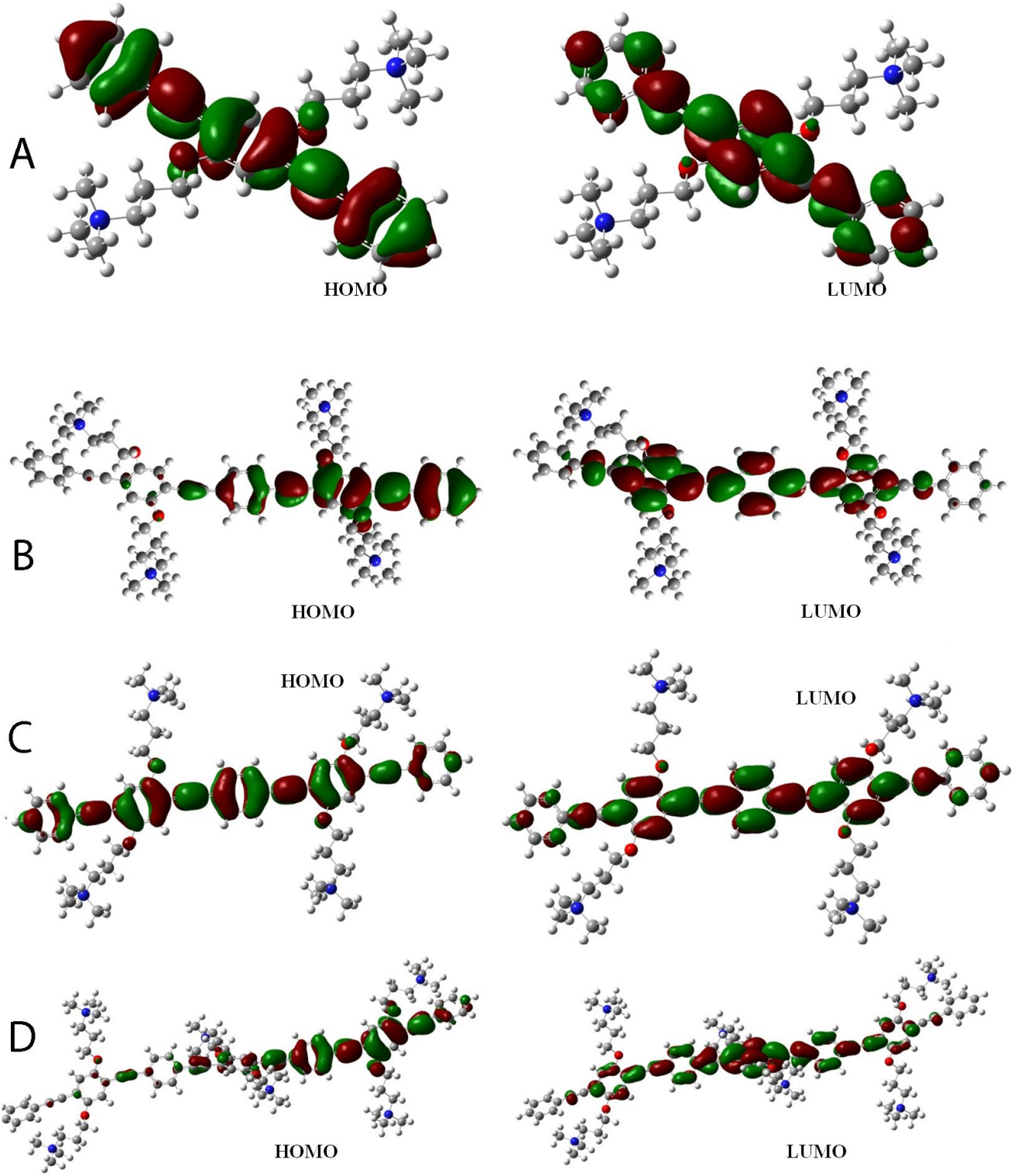

Figure 2.4. Molecular Orbitals of (A)+**1H**; (B)+**2H**; (C) +**2H** with planar backbone; (D) +**3H**, calculated using the DFT:B3LYP/6-31g** method and basis set.[1]

It is shown in the orbitals in Figure 2.4 that as the length of the oligomer increases, the effective length of the π-conjugated chromophore is limited. In the smallest oligomer there is complete conjugation, but in the larger oligomers breaks in the π-conjugation are seen. It is shown in Figure 2.4C that the Molecular Orbitals of **+2H**, when optimized with constrained rotation around the triple-bond, that the conjugation extends much further than seen with the optimized ground state structure for **+2H** seen in Figure 2.4. It has been shown by Li and coworkers[69] that fully planar OPEs have more extended π-conjugation than OPEs with orthogonal segments that break conjugation. This is seen in Figure 2.4, where the breaks in π-conjugation in the larger oligomers result from the twisted phenylene backbone.

The frontier molecular orbitals for the optimized +*n*H structures are shown in Figure 2.4. From these molecular orbitals, it is evident that as the length of the oligomer increases, the effective length of the π-conjugated chromophore becomes finite. The DFT calculations demonstrate that **+1H** is not only planar but the HOMO and LUMO orbitals are also fully conjugated. A combined experimental and computational study by James *et al*[68] of a structurally related but non-charged OPE-1 suggests that this compound is planar in the ground state, but that there is little barrier to rotation along the long axis. In contrast, the optimized structures for **+2H** and **+3H** shown in Figure 2.2, are decidedly non-planar and the frontier orbitals for both compounds are largely confined to a partially planar region that extends over little more than three phenyl rings. We suggest that this unit is likely the "segment chromophore" that is responsible for the absorption maximum and that larger polymers may likely consist of several of these "segment chromophores" where π-conjugation is effectively broken between segments.

The results shown in Figure 2.4 suggest that such a chromophore may be 3-4 phenyl rings in length, including the ethynyl groups in between. It is also observed when comparing Figures 2.4B and 2.4C that when **+2H** is forced into a planar state, the extent of conjugation in along the backbone increases by at least one phenyleneethynylene unit. Semiempirical calculations by Miteva and coworkers have also shown that there is a decrease in the HOMO/LUMO gap as the planarity of the backbone is increased[70], which correlates to the red-shifting of absorption upon complexation. We suggest that complexation may likely result in planarization of the "segment chromophores" described above or some other mode of extension of the "segment chromophore" during the complexation process. The electronic (Absorption) spectra that were calculated for n=1 and 2 OPEs are shown below, in Figure 2.5.

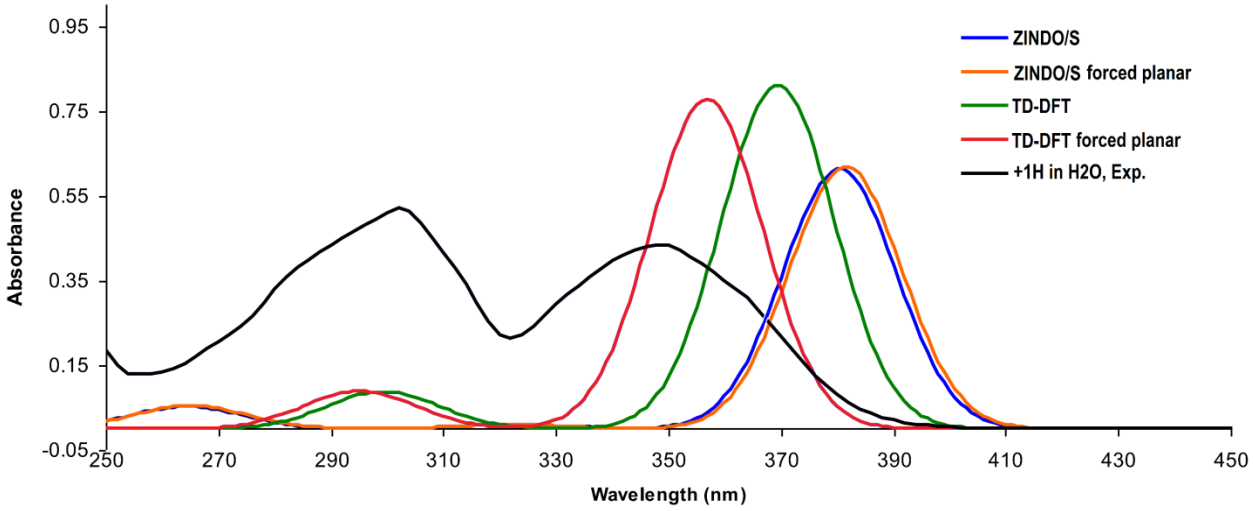

Figure 2.5 Calculated absorbance spectra of **+1H** using the ZINDO/S semi-empirical method and TD-DFT at the B3LYP/6-31g** level of theory compared with experimental values. "forced planar" in the legend designates backbone geometry where phenyl rings are forced to be coplanar.

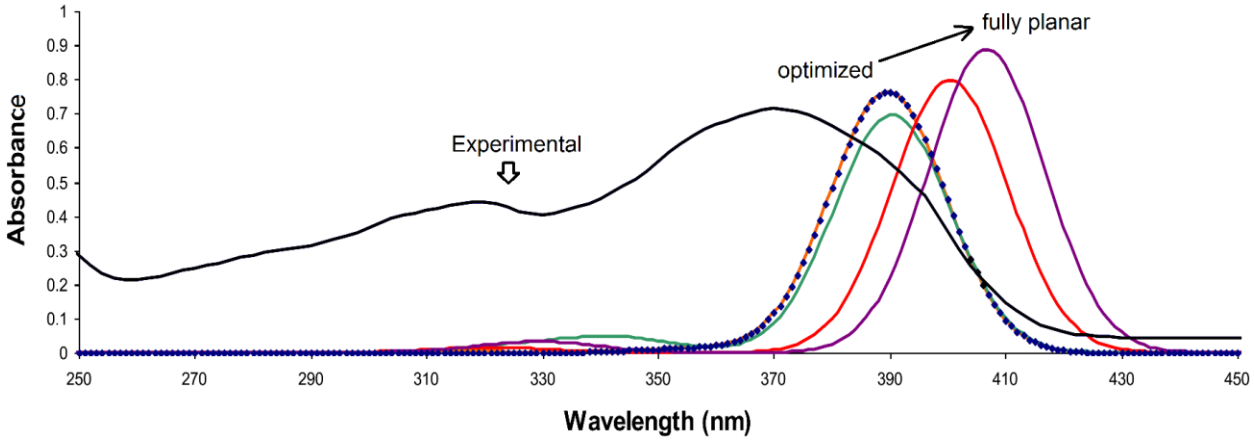

Figure 2.6 Calculated absorbance spectra of **+2H** at the semi-empirical ZINDO/S level of theory compared with experimental spectra. "fp*n*" The dotted line indicates the ground-state optimized geometry at the B3LYP/6-31g** level of theory, and the black arrow indicates the progression as each of the dihedral angles are forced into coplanarity.

The calculated spectra in Figure 2.5 show reasonable agreement in the calculated absorbances compared with measured values, despite grossly underestimated oscillator strength for the minor band near 300 nm.The calculated electronic spectra in Figure 2.6 suggest that planarization of the backbone for the larger oligomers can have a significant effect on the HOMO-LUMO gap. This is in agreement with the HOMO and LUMO electron density plots shown in Figures 2.3 and 2.4, where the planarized OPE in Figure 2.4 has a clearly increased MO density along the length of the molecule. That change is also reflected in Figure 2.6., where the λ_{max} of the main absorption band redshifts about 30 nm when entirely planarized. Pearson and Tour found for oligo(2,5-thiophene ethynlene)s that saturation of optical absorption spectra occurs between 8 and 16 thiophene rings and their simulations suggest an extended planar zig-zag conformation for the oligomer having 16 thiophene rings.[49] Experimental work by Godt and coworkers has also shown that little redshift of λ_{max} occurs after 4-5 phenyl rings is reached[60], which we would attribute to reaching the limit of chromophore length. In a computational study by Na Li and coworkers, it was shown in calculated molecular orbitals and electronic spectra that the extent of the chromophore in dimethoxy-p-phenylene-ethynylene oligomers in a fully planar configuration was reached at around 8-10 repeat units[69]. In addition the length of a conjugated unit seen in this study was found to be highly dependent on the planarity of the phenylene-ethynylene backbone. In a DFT-level study by Magyar and coworkers the electronic excitation energy of phenylene–acetylene oligomers were calculated with various conformational arrangements[71]. This research showed that most conformations resulted in reaching a limiting chromophore length, around 4 to 6 units for the planar configurations and 3 units for the twisted conformations. These results lend support to the hypothesis that the predominant cause of photophysical changes from complex formation is segment planarization, especially in the larger oligomers.

A closer inspection of the variation of absorption spectral changes between complexes of the oligomers with carboxymethylcellulose (CMC) and carboxymethylamylose (CMA) across the series is instructive. For example when the absorption spectra of complexes for **+2H** and CMC (Figure 2.1) and CMA are compared, it is clear that the absorption spectrum for **+2H**/CMC is sharper, more red-shifted and more intense than that for **+2H**/CMA. In contrast when **+2C** assembles with the same scaffolds, (Figure 2.1) both spectra are sharp, strongly red-shifted and intense. We believe this trend is consistent with different extents of "segment planarization"

among the complexes that can be attributed to the environment provided by the different scaffolds. In general the strength of complex formation and apparent degree of "segment planarization" increases from CMA to CMC; this can be attributed to the fact that CMA consists of interrupted helices and random coils in water while CMC exists as a more sheet-like structure.[74-76] The greater strength of complex formation and segment planarization also increases as a function of the number of electrophilic (COOEt) end groups that could be attributed in part to favorable ion-dipole interactions between the end groups and the scaffold. The contribution of the COOEt endgroups to the photophysical properties of the OPEs was further studied, with focus on the influence of interfacial solvent on the fluorescence intensity.[66]

2.3 Influence of Interfacial Solvent on Photophysical Properties of OPEs

One of the series of OPEs that were synthesized by Tang et al. were capped with carboxyester terminal groups, and the fluorescence quantum yields were much lower in water for OPEs with carboxyester endgroups (n=1, 0.023) compared to those without (n=1, 0.64).[1] The fluorescence quantum yields of the COOEt-terminated OPEs in methanol were higher than water (n=1, 0.75). This suggested the quenching effects of water and the structural relevance of the carboxyester group in this process, and has led us to further study. In this section we present an investigation of the quenching of an OPE with carboxyester end-groups by water followed by examination of the system by classical molecular dynamics simulations. In order to assess the isotope effect on the interaction of water with the fluorescence of the OPEs, absorbance and fluorescence spectra of 20 μM (repeat unit concentration) OPEs were obtained as described above.

Quenching of fluorescence by water has been previously reported for other organic molecules, but the mechanism behind the quenching by solvent in this case was not clear. [78-80] Interfacial water has been shown to have a strong effect on the photochemistry of OPEs. Studies of the photochemistry of two structural isomers of a model OPE in water suggested that structured interfacial water plays a significant role in two major pathways involving the photo-addition of water along the triple-bond of the backbone.[73,81] Further investigation into the effects of water on photochemistry revealed that an OPE could be protected upon complexation with an ionic surfactant, removing the interfacial water and preventing the photoaddition of water.[73] These studies highlighted the effects of interfacial water on photochemistry of the backbone, but a complete understanding of the relationship between solvent and photophysical properties of the

OPEs has not yet been reached. A study of the deuterium isotope effect on the fluorescence intensity and lifetime was carried out in order to further investigate solvent quenching.The UV-Visible absorbance and fluorescence spectra for the series of carboxyester- terminated OPEs with repeat unit numbers of n=1, 2, and 3 in D_2O and H_2O are shown in Figure 2.7.

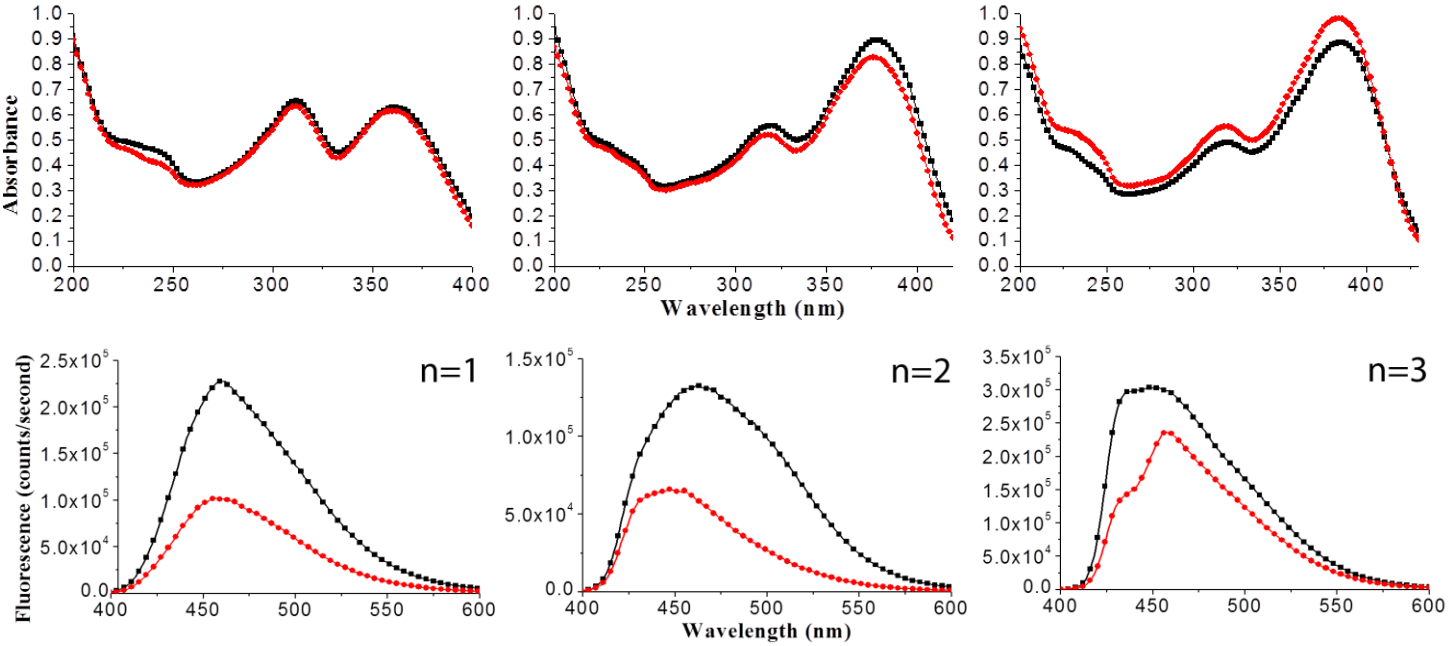

Figure 2.7. Absorbance and Fluorescence of **+1C**, **+2C**, and **+3C**. Samples in D_2O are in black and H_2O are in red.[66]

In the top row of Figure 2.7, the absorbance spectra of all three compounds show little variation in D2O compared with H_2O. The fluorescence is enhanced for all three compounds in D2O relative to H_2O. Using the integrated fluorescence from the bottom row of Figure 2.7, the enhancement was calculated to be a factor of 2.25, 2.5, and 1.5 for n=1, 2 and 3, respectively. The relative fluorescence quantum yields for the OPEs in H_2O and D_2O are shown in Table 2.1. Values for compounds in H_2O obtained from a previous study. [1]

Table 2.1.Relative fluorescence quantum yields of the compounds studied in D_2O and H_2O.

Sample	**Solvent**	Φ_f
+1C	H_2O	0.023
+1C	D_2O	0.050
+2C	H_2O	0.039
+2C	D_2O	0.090
+3C	H_2O	0.069
+3C	D_2O	0.113

Table 2.1 shows fluorescence quantum yields increase in D_2O by a factor of 2.2, 2.3, and 1.6 for OPEs 1, 2 and 3, respectively.[66] In order to determine the effect of interfacial water on the photophysical properties of the OPEs shown in Scheme 2.1, several experimental approaches were taken. Since carboxyester groups are prone to hydrogen bond with water, it was logical to examine the effect of replacing hydrogen with deuterium. We explored the fluorescence quantum yields and intensities of the OPEs in D_2O and compared them with H_2O. The fluorescence change induced by complexation with an ionic surfactant was followed and classical molecular dynamics simulations of the OPEs with surfactants were performed to shed light on the aggregate structure and displacement of interfacial water. The influence of backbone length was studied through comparison of the photophysical properties across the series of OPEs studied. The results of this study will provide knowledge about solvent interactions with OPEs and will be useful for the design of fluorescent sensors.

The results given above provide a picture of the relationship between interfacial water and the photophysical properties of the series of oligomeric *p*-phenylene ethynylenes with carboxyester endgroups. In the original study which discusses the photophysical properties of this class of molecules and their synthesis, it is observed that these OPEs have very high fluorescence in methanol, but very low fluorescence in water.[1] As OPEs without carboxyester endgroups have high fluorescence in water, comparable to those in methanol, we decided to investigate the mechanism of this quenching. Determination of the reason for quenching and unquenching may allow for the design of other molecules based on this backbone for sensing purposes where strong fluorescence enhancements and wavelength shifts are needed.

The experimental studies conducted revealed how the interactions of the OPE with water

strongly influence the photophysical properties, particularly fluorescence intensity. Since the presence of carboxyester groups was a critical factor in the reduced fluorescence intensities, hydrogen-bonding was expected to play some factor in the formation of a layer of structured interfacial water. To establish the quenching effect of water on the fluorescence, H_2O was replaced with D_2O and fluorescence spectra and quantum yields were obtained. In Figure 2.7, we can see a significant isotope effect on the fluorescence of all three oligomers. Compound $^{+1C}$ and $^{+2C}$ have more than double the fluorescence in D_2O relative to H_2O. The reduced fluorescence quenching of the pure compounds by D_2O relative to H_2O is likely the result of partial protonation of the excited state, as the acidity of a H in H_2O is 0.44 pH more acidic than a deuterium in D_2O.[82,83] Compound 3 exhibits less fluorescence quenching by water than the two smaller oligomers, as the increase of fluorescence when switching to D_2O is only slight.

2.4 Photophysical Changes upon OPE Self-Aggregation is Dictated by Molecular Structure and Presence of Interfacial Water

2.4.1 Formation of an H-aggregate with "end-only" OPEs

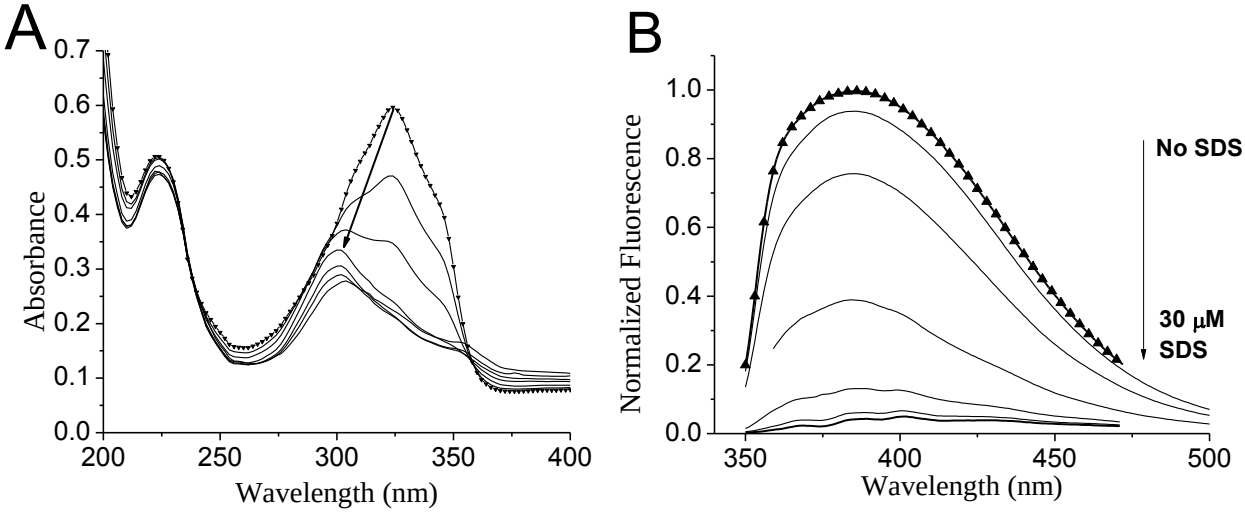

Figure 2.8. A. UV-Visible absorbance, and **B.** Fluorescence spectrum of 15 μM **+EO** upon consecutive 1 μL additions of 15 mM SDS. The compound in pure water is marked with black triangles, followed by OPE to SDS ratios of 3:1, 3:2, 1:1, 3:4, 3:5, and 1:2. The spectral changes upon addition of surfactant are indicated by the black arrows.[74]

The absorbance spectrum in Figure 2.8A shows a decrease in absorbance and a blueshifted λ_{max}.

The fluorescence spectrum in Figure 2.8B shows a sharp drop in absorbance as the ratio of surfactant to OPE increases. The changes in absorbance and fluorescence spectra of the anionic **-EO** upon addition of cationic surfactant TTAB are similar to those observed with **+EO** and SDS in Figure 2.8, and are shown in Figure A1 in the Appendix.[74] The changes in UV-visible absorbance and fluorescence anionic OPE with side-chains, **2,** are given in Figure 2.10 in the following section.

In the case of the end-only OPEs **+EO** and **-EO**, clear evidence of an H-aggregate is seen in Figure 2.8**.** The aggregated state of both **+EO** and **-EO** shows a blue-shift in the main absorbance band from 325 nm to 300 nm. The peak shape of the absorbance band also changes significantly. Prior to addition of surfactant, the main absorbance band of both **+EO** and **-EO** extends from 300 to 350 nm with a symmetrical triangular shape to the peak. Upon complex formation (at > 1:1 OPE to surfactant ratio), the peak which was shifted to 300 has a large tail leading off into the red. There is also a sharp drop in fluorescence, as seen in Figure 2.8B. The fluorescence quantum yields in Table 2.2 also show a reduced quantum yield for both **+EO** and **-EO.** Fluorescence loss is a common effect in H-aggregation, resulting from rapid internal conversion between singlet states which prevents the relaxation from the allowed excitonic state back to the ground state. This fluorescence quenching effect is ubiquitous in almost all H-aggregates, with a few exceptions.[84] These aggregates likely take on a parallel conformation where π-stacking and release of interfacial water strongly contributes to the strength of the aggregate. The aggregation between the two OPE monomers is induced by the presence of an oppositely-charged surfactant, which enables the two OPEs to stack atop one another without significant repulsion between charged side-chains. In the initial photochemical study of these complexes, classical Molecular Dynamics simulations were performed which suggested a likely structure of the H-aggregate formed by the end-only OPE **+EO**.[73] The structure of this aggregate obtained from this study is shown below, in Figure 2.9

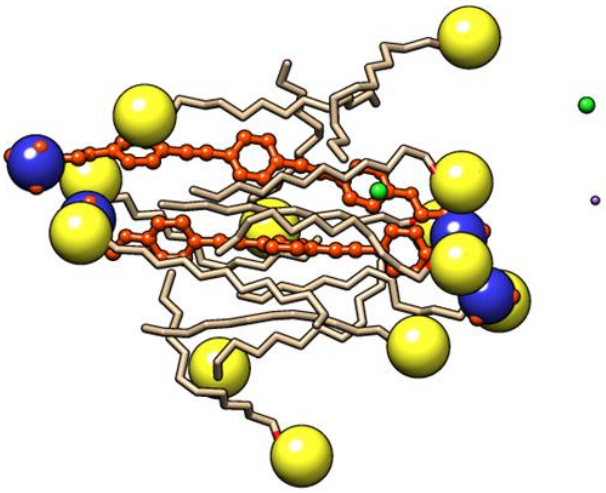

Figure 2.9. Snapshot of aggregate of end-only OPE +**EO** and SDS obtained through all-atom molecular dynamics. The OPE is shown in orange, and the lipid tails are shown in tan. The lipid headgroups are shown in yellow, and the OPE charged groups are shown in blue.[73]

2.4.2 Formation of a red-shifted aggregate with OPE-ns

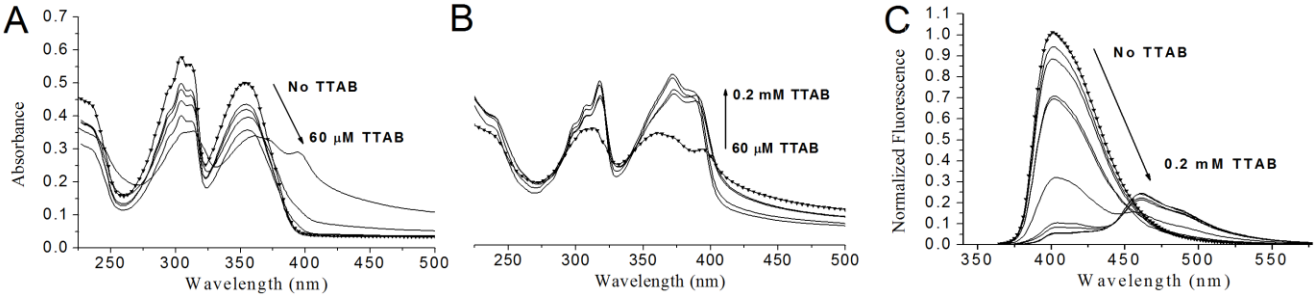

Figure 2.10 A. UV-visible absorbance spectra of 20 μM **-1H** in water with 0, 10, 20, 30, 40, and 60 μM TTAB (OPE:TTAB ratios of 2:1, 1:1, 2:3, 1:2, and 1:3); **B.** Absorbance spectra at 60, 80, 100, 150 and 200 μM TTAB (OPE:TTAB ratios of 1:3, 1:4, 1:5, 1:7.5, and 1:10); **C.** Fluorescence spectra at all concentrations listed for A and B. The compound in pure water is marked with black triangles. The spectral changes upon addition of surfactant are indicated by the black arrows.[74]

A drop in absorbance can be observed in Figure 2.10A as the concentration of TTAB is increased to the ratio of 1:3 OPE to TTAB. Precipitate formation in solution was concurrent with this drop in absorbance, and the resulting precipitate was insoluble in aqueous media but soluble in organic media such as methanol and acetonitrile. No precipitate formation is observed for

concentrations above a 1:3 ratio, though the solution takes on a slight turbidity with a weak blue coloration. A strong red-shift is clear in Figure 2.10B and is present in the last trace of Figure 2.10A. While the end-only OPEs clearly formed H-aggregates, it was thought that the steric hindrance of the two charged sidechains of the OPEs **+1H** and **-1H** would not allow the π-stacking necessary to form an H-aggregate. Indeed, the OPEs with sidechains form an aggregate with strongly red-shifted absorbance when complexed with an oppositely-charged surfactant. Compound **-1H** clearly forms a molecular aggregate, with pronounced red-shifted absorbance and fluorescence, as can be seen in Figure 2.10. In addition to a 50 nm red-shift in absorbance and fluorescence bands, the absorbance bands exhibit changes to the fine structure upon aggregate formation. The fluorescence quantum yields in Table 2.2 show that **-1H** had a lower quantum yield (0.4) when aggregated than in pure water (0.65).

As with the "end-only" OPEs **+EO** and **-EO**, the OPE **-1H** also formed complexes at and above a 1:1 OPE to surfactant ratio. However, the complex formed near a 1:1 OPE to surfactant ratio yielded a precipitate which was formed up to a 1:3 OPE to TTAB ratio. The precipitate formation can be seen in the drop in optical density in Figure 2.10 A. The formation of solid precipitate could be further induced if surfactant was added very slowly or if the solution was brought to a low temperature (~14 ºC). When removed from the solution and dissolved in organic solvent such as ethanol, acetonitrile, or acetone, a clear, light-blue solution is formed. The precipitate was formed from a 1:1 to a 1:3 ratio of OPE to surfactant, which suggests this is a charge-neutral aggregate of surfactant and OPEs, which lost solubility in water due to charge neutrality. The red-shifted aggregate is formed above the 1:3 OPE to TTAB ratio, suggesting that the aggregate involves atleast 2 OPEs and 6 surfactant molecules. The structure of this aggregate is not known, however it is thought that the backbones align in a staggered conformation to avoid the repulsion between OPEs due to the ionic sidechains.

2.4.3 *Deaggregation of OPEs with Surfactants above the CMC*

The change in UV-visible absorbance and fluorescence of the two different types of anionic OPEs and the cationic surfactant TTAB when surfactant concentration is brought above the critical micelle concentration (CMC) is shown below in Figures 2.11 and 2.12**.** Both of the end-only OPEs **+EO** and **-EO** had a slow spectral change in micellar surfactant solution. The absorbance and fluorescence spectra are similar to those of the premicellar aggregate upon

solution preparation, but after 12-24 hours the spectra are stable.

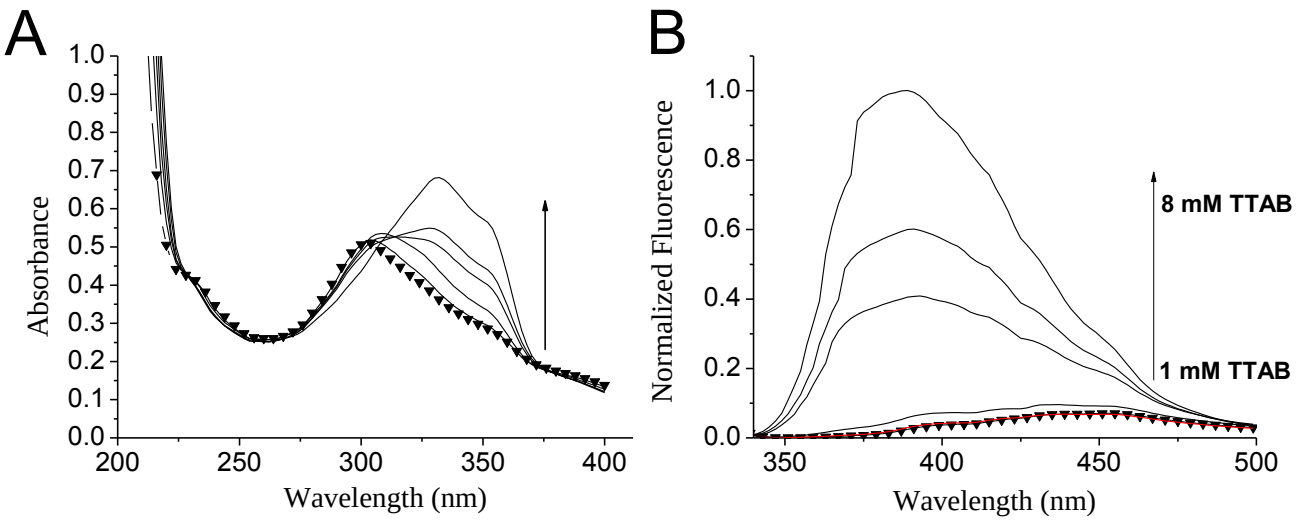

Figure 2.11. A. UV-visible absorbance and **B.** fluorescence spectra of 15 μM **-EO** in 1, 2, 3, 4, 6 and 8 mM TTAB. The 1 mM trace is marked with black triangles.[74] The spectral changes upon addition of surfactant are indicated by the black arrows.[74]

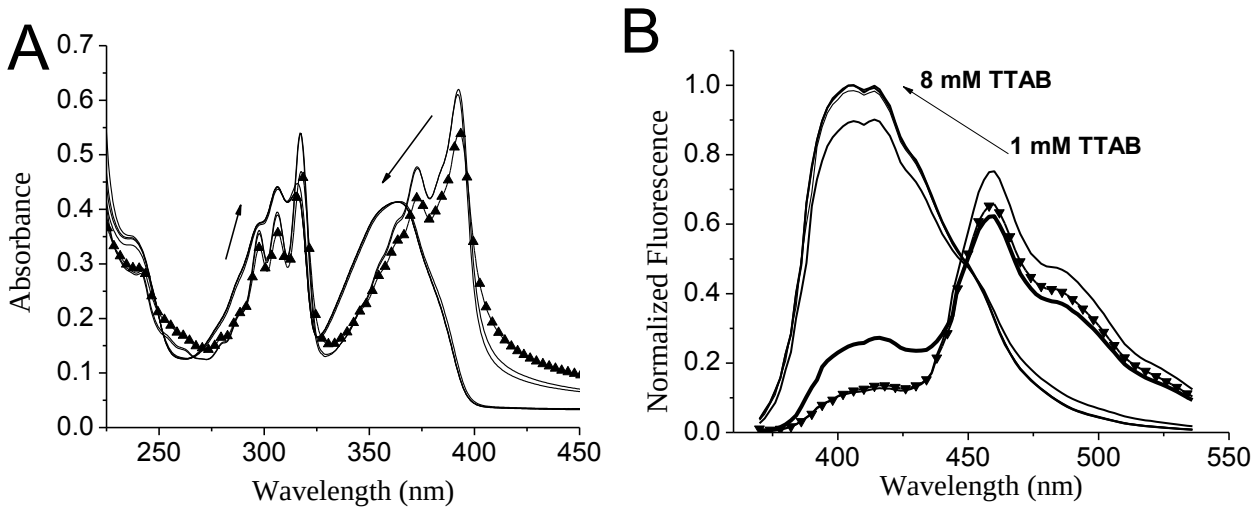

Figure 2.12. A. UV-visible absorbance and **B.** fluorescence spectra of 15 μM **-1H** in 1, 2, 3, 4, 6 and 8 mM TTAB. The 1 mM trace is marked with black triangles. The sharp transition between the two spectral profiles occurs between 3 and 4 mM TTAB, as the CMC of TTAB is 3.79 mM. The 3 mM line in the fluorescence spectrum is bolded to indicate the blue-shifted fluorescence that appears near 410 nm. [74]

The complexes formed by the two types of OPEs are quite different, yet as the surfactant concentration reaches the CMC both display a similar effect. As the CMC is approached, the

wavelength of maximum absorbance and spectral profile mostly returns to that of the compound alone in water with no surfactant. This can be seen for the "end-only" OPE **-EO**, in Figure 2.11, and for the OPE with sidechains, **-1H**, in Figure 2.12. A clear example of the de-aggregation of the "end-only" OPEs as the surfactant concentration approaches the CMC is seen in Figure 2.11. The absorbance peak was originally blue-shifted from 325 nm to 300 nm as the ratio of surfactant to OPE approached 1:1, similar to Figure 2.9A, but upon approaching the CMC this absorbance band was then red-shifted back to 325 nm. The fluorescence was also drastically enhanced as the compound **-EO** was de-aggregated, with fluorescence changes observed in Figure 2.11B reveal the reverse trend of what was observed in Figure 2.9B. In the case of **-1H** and TTAB, there is a sharp change in both absorbance and fluorescence spectra above the CMC (Figure 2.12). The large red-shift that was observed had already been blue-shifted from the maximum extent of its influence that was observed in Figure 2.10A to ~10 nm red-shifted compared to in pure water. Despite this, the increase of TTAB concentration towards the CMC still induced **-1H** to blue-shift 40 nm to return to 355 nm. In Figure 2.12B the onset of the monomer fluorescence is apparent at ~410 nm in 3 mM TTAB**.** This deaggregation is likely a result of the intermolecular forces between the surfactants overwhelming the weakly binding forces behind aggregation of the OPEs, in addition to there being a significantly larger number of SDS molecules.

There is generally a fluorescence increase for the OPEs when in an aqueous solution of surfactant micelles relative to pure water which is attributed to reduced quenching of fluorescence by interfacial water. The fluorescence quantum yields, however, are only increased in the case of **-EO.** Table 2.2 shows that the quantum yields of the OPEs in micellar solutions are slightly lower, which is possibly a result of a population of OPEs that have not been deaggregated entirely by the formation of micelles. A recent study of the photochemistry of end-only OPEs in micellar solution used classical molecular dynamics to predict that the end-only OPEs would bury their backbone in the nonpolar micelle core, spanning the width of the micelle. [73] The OPE **1**, however, only associates with the micelle at the interface with water, and does not bury deeply in the micelle. It is important to note the general aggregation behavior that is observed for both types of molecules; aggregation occurs above a 1:2 ratio of surfactant and OPE and the same aggregate is observed in this entire range of surfactant concentrations leading up to the critical micelle concentration. Once the CMC of surfactant is near, the OPEs begin to

deaggregate and gain a similar UV-Vis absorbance and fluorescence profile to that of the compound in pure water, albeit with slightly enhanced fluorescence. Regardless of which aggregate is formed, the aggregate maintains a consistent structure through a range of concentrations from a 1:2 OPE to SDS ratio to the millimolar range just below the CMC.

2.4.4 Fluorescence Quantum Yields

Table 2.2. The relative fluorescence quantum yields for each of the OPEs in pure water, with 1 mM surfactant (below CMC), and with 10 mM surfactant (above CMC).[74]

Compound	**Solvent**	Φ_f	σ_Φ
	water	0.64	0.02
	premicellar	0.07	0.01
+1H	micellar	0.59	0.07
	water	0.65	0.01
	premicellar	0.40	0.01
-1H	micellar	0.51	0.01
	water	0.66	0.02
	premicellar	0.12	0.01
+EO	micellar	0.63	0.08
	water	0.35	0.01
	premicellar	0.10	0.01
-EO	micellar	0.77	0.01

2.4.5 The role of H-bonding in Aggregate Formation

2.4.5.1 Aggregation of COOEt OPEs and Isotope Effects on Fluorescence

Both anionic and cationic end-only OPEs were able to form a strong aggregate with a simple oppositely-charged surfactant. However, there was a discrepancy in the strength of the aggregate between cationic and anionic *n*=1 OPEs compounds **+1H** and **-1H**. In Figure 2.13 we can clearly see that there is little change to the absorbance of fluorescence spectrum of **+1H** upon addition of SDS. This suggests that there is a very weak association of SDS molecules with **+1H**, leading to a weak and tenuous aggregate. The changes in UV-visible absorbance and fluorescence of the cationic OPE, **+1H,** with sequential additions of 5 μM SDS are shown below, in Figure 2.13.

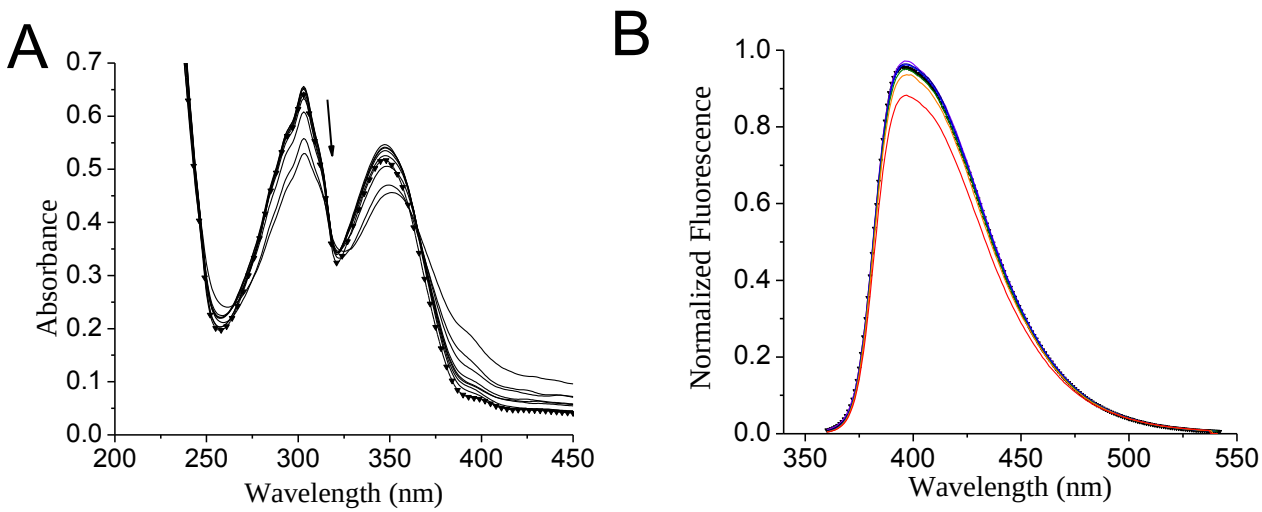

Figure 2.13. A. UV-visible absorbance, and **B.** Fluorescence spectrum of **+1H** upon consecutive additions of 15 mM SDS [74] The change upon addition of surfactant is indicated by the black arrow.[74]

It was not initially clear why the anionic compound **-1H** formed a strong aggregate with TTAB, when the cationic analog **+1H** formed a very weak aggregate with SDS. However, when comparing the structures of **+1H** and **-1H** given in Scheme 2.1, it is apparent that compound **+1H** has no hydrogen bond acceptors while **-1H** has sulfonate groups which are strong H-bond acceptors. A recent study of the fluorescence quenching by water of a molecule similar to **+1H** but with carboxyester end-groups also shows similar strong red-shifted aggregate formation with surfactant**.**[30] As the carboxyester groups behave as H-bond acceptors, we suggest that the lack of aggregate formation seen between **+1H** and SDS results from the inability of **+1H** to accept H-bonds from water. The red-shifted aggregates likely belong to a layer of structured interfacial water that allow a stable aggregate. In order to further explore the effects of solvent interaction on complex formation, the COOEt series of cationic OPEs with n=1, 2, and 3 were complexed with the anionic surfactant SDS in D_2O and H_2O and their photophysical properties were assessed. The Figure 2.14 below shows an image of the samples before and after complexation with SDS.

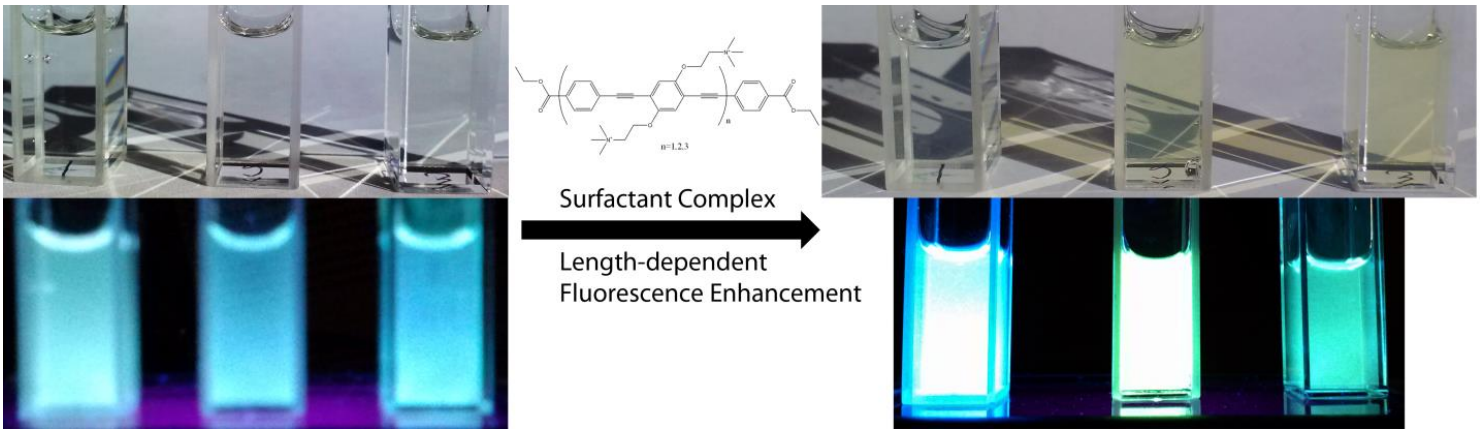

Figure 2.14. Change in 20 μM cationic OPE absorbance and fluorescence upon complexation with 75 μM SDS. OPE repeat unit number increases from 1 to 3 from left to right.[66]

The interactions between the n=1,2, and 3 OPEs with COOEt endgroups and water and the subsequent changes in photophysical properties were further studied by forming a pre-micellar complex between the OPE and an oppositely charged surfactant, SDS. Prior to this study, the effects of surfactant complexation on the photochemistry of an "end-only" OPE with alkylammonium chains on the ends of the molecule had been examined, and a surfactant complex was observed to prevent photolysis of the compound due to removal of interfacial water.[73] Based off of this result, we sought to explore the effect of removal of interfacial water from the series of OPEs with COOEt endgroups on their fluorescence, which is highly quenched in water. By examining **+1C**, we are able to observe the effect of aggregation that cannot be a result of planarization, as the n=1 oligomers were shown in part 2 of this chapter are shown to be planar in the ground state. Furthermore, the comparison of aggregates formed in D_2O vs H_2O reveals the importance of hydrogen bonding on the formation of the aggregate and gives insight into the aggregate structure. The UV-Visible absorbance and fluorescence spectra for the series of carboxyester terminated OPEs at 20 μM repeat unit concentration with 50 μM SDS in D_2O and H_2O are shown in Figure 2.15.

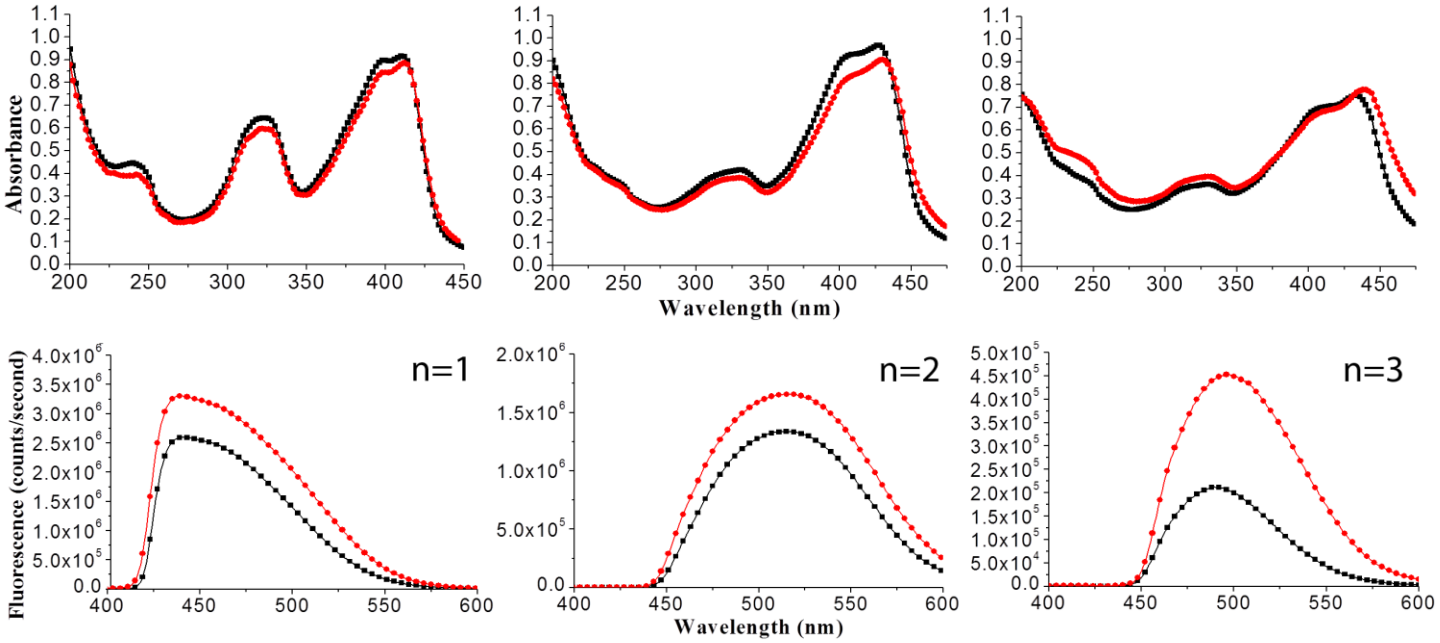

Figure 2.15. Absorbance and Fluorescence of 20 µM of compounds +**1C**, +**2C**, and +**3C** after complexation with 75 µM SDS. Samples in D_2O are in black and H_2O are in red.[66]

The absorbance spectra of the three compounds are mostly the same between D_2O and H_2O. There appears to be some red-shifted tailing absorbance for the n=3 OPE, in addition to an enhanced portion at 240 nm. The fluorescence spectra on the bottom row of Figure 2.15 where detergent has been added show that the samples with water actually have greater fluorescence than those in D2O. The relative fluorescence quantum yields for the complexes in H_2O and D_2O are shown below, in Table 2.3

Table 2.3. Relative fluorescence quantum yields of the complexes between the OPEs and SDS in D_2O and H_2O.[66]

Sample	**Solvent**	**Φ_f**
+**1C**-SDS	H_2O	0.92
+**1C**-SDS	D_2O	0.78
+**2C**-SDS	H_2O	0.46
+**2C**-SDS	D_2O	0.33
+**3C**-SDS	H_2O	0.28
+**3C**-SDS	D_2O	0.12

The isotope effects observed with OPEs in water and D_2O are reversed when comparing the OPEs alone with the OPE-SDS complex, which suggests an influence of extended hydrogen-bonding by interfacial solvent. It can be observed when comparing the bottom-right panels in Figures 1 and 2 that when complexed with SDS, **+3C** shows a clear isotope effect where the complex formed with D_2O actually has less fluorescence than that of the complex formed in water, but also less than the compound in pure D_2O. The complex of **+1C** with SDS in water has a quantum yield of near unity (0.92) and in D_2O it drops to 0.78. The complex formed with **+2C** also shows a strong enhancement to 0.46 in H_2O and 0.33 in D_2O. The larger oligomer with n=3 has an increase from 0.07 to 0.28 in water, but no significant change in quantum yield is observed between the compound alone in D_2O and the complex formed in D_2O.

In the results above, SDS was added to form complexes with the three OPEs and study the changes in photophysical properties. One can see in Figure 2.15 that the fluorescence of **+1C** is the most strongly enhanced, with the fluorescence in water enhanced by 35 times. **+2C** also had strongly enhanced fluorescence of ~20 times that in pure water, but **+3C** had very little fluorescence enhancement. In addition to the complex formed in D_2O having lower fluorescence than that of the uncomplexed oligomer in D_2O (Figure 2.13), the sample in H_2O has a minor enhancement of barely 2 times upon complex formation. The fluorescence quantum yields shown in Table 2.3 reveal strong increases in the quantum yield between pure OPE and the OPE-SDS complex for compounds **+1C** and **+2C**, but only a slight enhancement for compound **+3C** in water and no apparent enhancement in D_2O. The increased fluorescence of the OPE-SDS aggregates in H_2O relative to D2O suggests that the complex that is formed relies on hydrogen-bonding between solvent and the –S=O groups on SDS. The reduced fluorescence of the OPE-SDS complexes in D_2O relative to H_2O suggests that structured water plays a role in the interactions between the OPE and SDS. The change of H to D possibly results in a weaker aggregate between the surfactant and the OPE, leading to lower fluorescence. This result is logical if the H-bonding with structured water is essential to aggregate formation, as the acidity of hydrogen in water is higher than that of a deuterium in D_2O. [82,83]

In addition to the fluorescence enhancement, strong red-shifting was observed in the fluorescence, depending on the size of the backbone. Compound **+1C** had no redshifted fluorescence, the fluorescence maximum actually shifts to the blue (460 -> 440 nm). Compound **+2C** undergoes a strong redshift of 75 nm (450 -> 525 nm), giving it a bright green fluorescence.

The redshift of **+3C** is less than that of **+2C**, with a 50 nm shift (450 nm -> 500 nm). Clearly the size of the molecule plays a role in the ability to undergo a shift in fluorescence wavelength upon complexation, as the smallest oligomer, Compound **+1C**, did not have a red-shifted fluorescence. The results shown herein suggest that the lack of aggregate formation in the **+1H** is caused by a lack of an H-bond accepting group such as a carboxyester. The difference in fluorescence in D_2O compared with H_2O suggests that quenching of the excited state may occur by a mechanism that involves interfacial water acting as an electron acceptor or partial proton donor. It is reasonable to assume that the oxygen through which this mechanism would occur would be the ketone oxygen on the carboxyester group, and that the hydrogen atoms in the structured interfacial water make for ready electron-acceptors that would quench the excited state and thus the fluorescence.

As the size of the backbone is increased, the influence of the carboxyester groups on the overall photophysical properties of the molecule is reduced. First of all, the quenching of the fluorescence by water when compared with D_2O is lowest for **+3C**. The fluorescence enhancement upon surfactant complexation is low (~2 times) for this compound as well, while it is at-least twenty-fold for the other two oligomers. The backbone geometry is likely to play a more influential role in the molecule's photophysical properties as the length increases and the carboxyester groups become further apart and make up a smaller percentage of the molecule. A previous study of these molecules used DFT and semi-empirical methods to explore the effects of backbone planarization on the predicted absorbance spectra of the larger oligomers, in order to explain the red-shift shift observed when complexed with the linear scaffolds CMC and CMA.[1] We expect that the photophysical properties of the larger oligomers and polymers are primarily dictated by the coplanarity of the phenyl rings in the backbone, and that the effect of structured interfacial water on the quenching is far reduced compared with the smaller oligomers **+1H** and **+2H**.

2.4.5.2 *Interfacial Water and H-bonding in Classical MD Simulations*

The hydrogen bonding and its involvement in aggregation with surfactant was examined with classical molecular dynamics simulations using the Amber12 software package.[85] The methods used are described in Chapter 7. Figure 2.16 shows representative snapshots that display the hydrogen bonding environment in the water surrounding the OPE with and without SDS present.

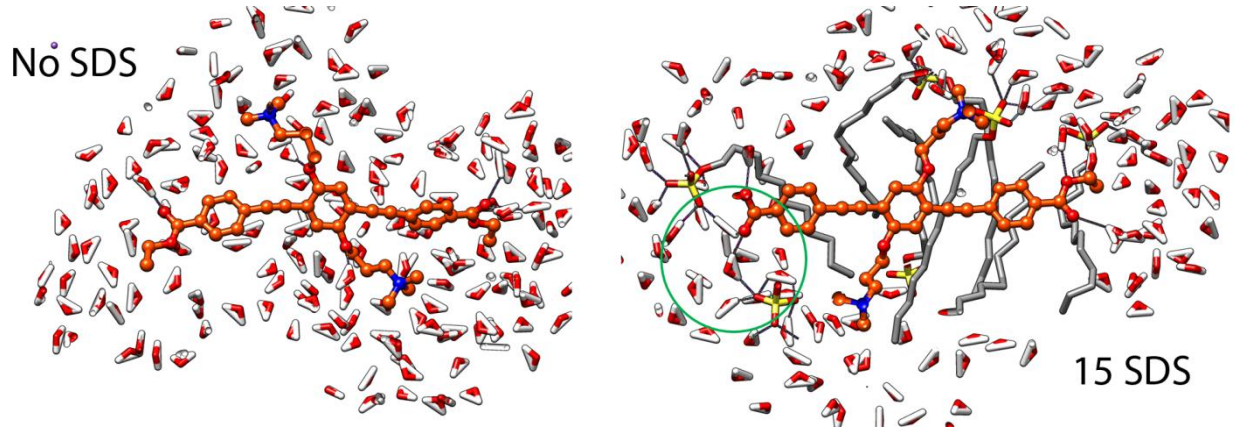

Figure 2.16. Snapshots from simulations trajectories with and without SDS. The OPE is shown in orange, and the SDS has grey hydrocarbon and a yellow sulfur in the center of the head-group. Hydrogen-bonds are depicted as dark lines. The green circle encompasses two water molecules which are each H-bonded to both SDS and the OPE **+1C**.[66]

It can be seen in Figure 2.16 that there is hydrogen-bonding primarily off of the carboxyester oxygens, but also on the ether oxygens on the sidechains. The number of hydrogen bonds of **+1C** was calculated over the course of the 50 nanosecond trajectory and is plotted below in Figure 2.17.

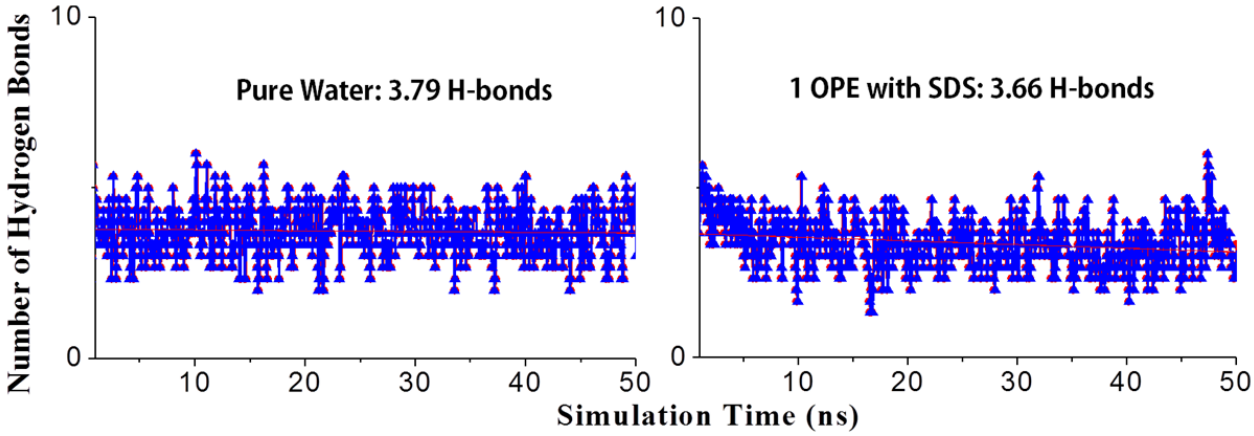

Figure 2.17. Calculated number of hydrogen-bonds between the OPE **+1C** and water over the 50 nanosecond trajectory in pure water or with 15 SDS in solution.[66]

The initial drop observed in the presence of SDS correlates with the displacement of water from the COOEt groups by SDS. The average number of hydrogen bonds is similar whether or not

SDS is present. The simulations revealed that the interactions between SDS and the OPE **+1C** may involve hydrogen-bonding. Waters would be hydrogen-bonding to both SDS and the carboxyester of an OPE at the same time, as can be seen in Figure 2.16. The oxygens of the carboxyester are particularly prone to H-bonding in this manner. As shown in Figure 2.17, there is only a slight decrease in the number of hydrogen bonds between interfacial water and the OPE as the surfactant interacts with the OPE. As these carboxyester groups become a less dominant feature of the molecule with an increase in backbone length, these results suggest that the amount of hydrogen-bonding with solvent would not change. However, a much larger portion of the chromophore would no longer be under the influence of the carboxyester end-groups as the size increases, especially if loss of coplanarity of the backbone occurs. The loss of co-planarity would prevent the quenching effect of the interfacial water from traveling along the backbone, while isolated segment chromophores which are excited in the vicinity of the COOEts would likely still be quenched.

2.5 Conclusions and Outlooks

The OPEs self-assemble upon anionic scaffolds such as CMC and CMA with striking changes in absorbance and fluorescence.[1] Since the complex between the anionic carbohydrate scaffolds and various OPE are likely controlled by Coulombic and electrophile/nucleophile interactions as well as favorable hydrophobic interactions (release of interfacial water), it is reasonable to expect that stronger complexation will occur with the OPE having electrophilic end groups. The increase in fluorescence for the complexed OPE is also reasonable if the quenching of the hydrated monomers occurs in part because of associated interfacial water. The red shift in absorption and fluorescence upon self-assembly of OPEs was previously attributed to either formation of a J-dimer or to planarization during complex formation. As discussed above, for **+1H** the calculated optimized structure is very nearly planar and fully conjugated. Thus for this oligomer it is reasonable that formation of a J-dimer could account for the observed spectral changes.[86,87] However for the n=2 and n=3 OPEs, J-dimerization may compete for or not be a factor for the spectral changes occurring.

To further analyze aggregation effects, ionic oligomers with *p*-phenylene ethynylene backbones complexed with oppositely-charged surfactants were studied, where the variable was the location of the charged moiety on either the terminal ends of the backbone or branching off

opposite sides of the central phenyl ring. This small change in structure led to very different aggregation effects at a OPE to surfactant ratio at and above 1:1.[74] Furthermore, the surfactant used was a simple surfactant with a single alkyl chain, compared with the macromolecular "scaffolds" CMA and CMC which were previously studied. The compounds with terminal ionic groups formed H-aggregates, where end to end interactions are prevented by the location of the charged groups and the oppositely-charged surfactant mitigates the repulsive interactions between the sidechains in this orientation. The OPEs with charged groups coming off the central ring were observed to form red-shifted aggregates with strongly red-shifted absorbance. When surfactant concentration approached the critical micelle concentration, the aggregates formed between OPE and surfactant were dissociated, resulting in a similar absorbance spectrum as in pure water but with enhanced fluorescence afforded by the micellar environment. This work reveals the structural basis for aggregate formation between ionic *p*-phenylene ethynylenes and simple surfactants, and gives an understanding of the structural features of this series of molecules and how they correlate with the formation of different types of molecular aggregates.[74]

The mechanism of fluorescence quenching of a series of cationic *p*-phenylene ethynylene oligomers with carboxyester endgroups in water was explored through a combined experimental and theoretical approach.[66] A deuterium isotope effect in the form of enhanced fluorescence in D_2O versus H_2O suggests interfacial water plays a role in fluorescence quenching. The formation of a complex between the OPE and the anionic surfactant SDS yielded a strong red-shifted absorbance and enhanced fluorescence with a strong red-shift to the green for the oligomers with 2 and 3 repeating units. The fluorescence enhancement observed upon complex formation decreased with increasing number of repeat units. Classical molecular dynamics simulations showed that there is little difference in the number of hydrogen-bonds between the OPE and water when it interacts with the surfactant as SDS tends to locate along the backbone. A network of hydrogen-bonds was present between the SDS and the OPE, suggesting that H-bonding is crucial to the formation of the red-shifted aggregates that are observed. These results support earlier findings and highlight the influence of hydrogen-bonding introduced by the carboxyester group on the photophysical properties of the compound. These results will be useful for developing applications utilizing the p-phenylene ethynylene backbone in sensing, photovoltaics, and organic LEDs.

2.6 References

(1) Tang, Y.; Hill, E. H.; Zhou, Z.; Evans, D. G.; Schanze, K. S.; Whitten, D. G. Synthesis, Self-assembly, and Photophysical Properties of Cationic Oligo(p-phenyleneethynylene)s. *Langmuir* **2011**, *27*, 4945-55.

(2) Pinto, M. R.; Schanze, K. S. Amplified Fluorescence Sensing of Protease Activity with Conjugated Polyelectrolytes. *Proc. Nat. Acad. Sci.* **2004**, *101*, 7505-10.

(3) Liu, Y.; Ogawa, K.; Schanze, K. S. Conjugated polyelectrolytes as fluorescent sensors. *Journal of Photochemistry and Photobiology C: Photochemistry Reviews* **2009,***10*(4), 173-190.

(4) Achyuthan, K. E.; Bergstedt, T. S.; Chen, L.; Jones, R. M.; Kumaraswamy, S.; Kushon, S. A.; Ley, K. D.; Lu, L.; McBranch, D.; Mukundan, H. et al. Fluorescence Superquenching of Conjugated Polyelectrolytes: Applications for Biosensing and Drug Discovery. *J. Mat. Chem.* **2005**, *15*, 2648-2656

(5) Tan, C.; Pinto, M. R.; Schanze. K.S. Photophysics, aggregation and amplified quenching of a water-soluble poly(phenylene ethynylene) *Chem. Commun.* **2002,** 446-447

(6) Law, K. Y. Organic photoconductive materials: recent trends and developments *Chem. Rev.*, **1993**, 93 (1), 449–486

(7) Varghese, S.; Park, S. K.; Casado, S.; Fischer, R. C.; Resel, R.; Milián-Medina, B.; Wannemacher, R.; Park, S. Y.; Gierschner, J. Stimulated Emission Properties of Sterically Modified Distyrylbenzene-Based H-Aggregate Single Crystals *J. Phys. Chem. Lett.*, **2013,** 4 (10), 1597–1602

(8) Kéna-Cohen, S.; Forrest, S. R. Exciton–Polaritons in Organic Semiconductor Optical Microcavities *Springer Series in Solid-State Sciences* **2012,** *172*, 349-375

(9) Holmes, R. J.; Forrest, S. R. Strong exciton–photon coupling in organic materials. *Organic Electronics* **2007**, *8 (*2–3), 77-93

(10) Baldo, M. A.; Holmes, R. J.; Forrest, S. R. Prospects for electrically pumped organic lasers *Phys. Rev. B* **2002,** *66*(3), 035321

(11) Norland, K.; Ames, A.; Taylor, T. Spectral shifts of aggregated sensitizing dyes *Photogr. Sci. Eng.* **1970,** *14,* 295.

(12) Yuzhakov, V. I. Association of dye molecules and its spectroscopic manifestation. *Russ. Chem. Reu.* (Engl. Transl.) **1979,** *48,* 1076.

(13) Herz, A. H. Dye-dye interactions in solution and at AgBr surfaces. *Photogr. Sci. Eng.* **1974**, *18,* 223.

(14) Rabinowitch, E.; Epstein, L. Polymerization of Dyestuffs in Solution. Thionine and Methylene Blue *J. Am. Chem. Soc.* **1941,** *63*, 69

(15) Heesemen J. Studies on monolayers. 1. Surface tension and absorption spectroscopic measurements of monolayers of surface-active azo and stilbene dyes *J. Am. Chem. Soc.* **1980**, *102*, 2167.

(16) Emerson, E.S; M.A., Conlin; Roseno, A.E.; Norland, K.S.; Rodriguez, H.; Chin, D.; Bird, G.R. The geometrical structure and absorption spectrum of a cyanine dye aggregate *J. Phys. Chem.* **1967,** *71*(8):2396-403.

(17) E. Jelley, Molecular, Nematic and Crystal States of I: I-Diethyl--Cyanine Chloride *Nature,* **1937,** *139*, 631

(18) Vaidyanathan, S.; Patterson, L. K.; Mobius, D.; Gruniger, H. R. Molecular architecture in cyanine dye aggregates at the air-water interface. Effect of monolayer composition and organization on fluorescent behavior *J. Phys. Chem.* **1985**, *89*, 491-7

(19) Nakahara, H.; Fukuda, K.; Mobius, D.; Kuhn, H. Two-dimensional arrangement of

chromophores in J aggregates of long-chain merocyanines and its effect on energy transfer in monolayer systems *J. Phys. Chem.***1986**, *90,* 6144-8.
(20) *Reich*, C. Chemisorbed Sensitizing Dye Aggregates with Herringbone Structures *Photogr*. *Sci. Eng*. 1974, *18*, *335*
(21) Davydov, A. S. "Theory of Molecular Excitons", McGraw-Hill, New York, 1962
(22) Kasha, M. Energy Transfer Mechanisms and the Molecular Exciton Model for Molecular Aggregates *Radiat. Res.* **1963,** *20,* 55.
(23) McRae, E. G.; Kasha, M. *The molecular exciton model* In Physical Processes in Radiation Biology; Augenstein, L., Rosenberg, B., Mason, S. F., Eds.; Academic Press: New York, **1963**.
(24) Kasha, M.; Rawls, H. R.; El-Bayoumi, M. A. The exciton model in molecular spectroscopy. *Pure Appl. Chem* **1965,** *11*(3-4), 371-392.
(25) Humphry-Baker, R.; Moroi, Y.; Grätzel, M. Perturbation studies of the photophysics of arenes in functionalized micellar assemblies. Drastic phosphorescence enhancements. *Chemical Physics Letters* **1978,** *58*(2), 207-210.
(26) Vicens, M.C.; Sen, A.; Vanderlaan, A.; Drake, T. J.; Tan, W. Investigation of Molecular Beacon Aptamer-Based Bioassay for Platelet-Derived Growth Factor Detection. *ChemBioChem* **2005,** *6*, 900–907.
(28) Medintz, I.L.; Clapp, A.R.; Brunel, F.M.; Tiefenbrunn, T.; Tetsu, U. H.; Chang, E.L. Proteolytic activity monitored by fluorescence resonance energy transfer through quantum-dot-peptide conjugates. *Nature Materials* **2006,** *5*, 581–589.
(29) Wang, L.; Tan, W. Multicolor FRET Silica Nanoparticles by Single Wavelength Excitation. *Nano Letters* **2005,** *6*, 84–88.
(30) Bugaj, J. E.; Achilefu, S.; Dorshow, R. B.; Rajagopalan, R. Novel fluorescent contrast agents for optical imaging of in vivo tumors based on a receptor-targeted dye-peptide conjugate platform. *Journal of Biomedical Optics* **2001,** *6,* 122–133.
(31) Licha, K.; Riefke, B.; Ntziachristos, V.; Becker, A.; Chance, B.; Semmler, W. Hydrophilic Cyanine Dyes as Contrast Agents for Near-infrared Tumor Imaging: Synthesis, Photophysical Properties and Spectroscopic In vivo Characterization. *Photochemistry and Photobiology* **2000,** *72*, 392–398.
(32) McEvoy, A. K.; McDonagh, C. M.; MacCraith, B. D. Dissolved oxygen sensor based on fluorescence quenching of oxygen-sensitive ruthenium complexes immobilized in sol-gel-derived porous silica coatings. *Analyst* **1996,** *121*, 785–788.
(33) de Cássia Silva Luz, R.; Damos, F. S.; Tanaka, A. A.; Kubota, L. T. Dissolved oxygen sensor based on cobalt tetrasulphonated phthalocyanine immobilized in poly-l-lysine film onto glassy carbon electrode. *Sensors and Actuators B: Chemical* **2006,** *114,* 1019–1027.
(34) Chen, L.; McBranch, D. W.; Wang, H. L.; Helgeson, R.; Wudl, F.; Whitten, D. G. Highly sensitive biological and chemical sensors based on reversible fluorescence quenching in a conjugated polymer. *Proceedings of the National Academy of Sciences* **1999,** *96*(22), 12287-12292.
(35) Bunz, U. H. Poly(aryleneethynylene)s: Syntheses, Properties, Structures, and Applications. *Chem. Rev.* **2000**, *100*, 1605-44.
(36) DiCesare, N.; Pinto, M. R.; Schanze, K. S.; Lakowicz, J. R. Saccharide Detection Based on the Amplified Fluorescence Quenching of a Water-Soluble Poly(phenylene ethynylene) by a Boronic Acid Functionalized Benzyl Viologen Derivative. *Langmuir* **2002,** *18,*7785–7.
(37) Liu, Y.; Schanze, K. S. Conjugated Polyelectrolyte-based Real-time Fluorescence Assay

for Alkaline Phosphatase with Pyrophosphate as Substrate. *Anal. Chem.* **2008**, *80*, 8605-12.
(38) Zhao, X.; Liu, Y.; Schanze, K. S. A Conjugated Polyelectrolyte-based Fluorescence Sensor for Pyrophosphate. *Chem. Comm.* **2007**, 2914-2916.
(39) Thomas, L. H. The calculation of atomic fields. Proc. Cambridge Phil. Soc. **1927,** 23(5), 542–548
(40) Fermi, Enrico Un Metodo Statistico per la Determinazione di alcune Prioprietà dell'Atomo. Rend. Accad. Naz. Lincei **1927,** 6, 602–607.
(41) Hohenberg, P.; Kohn, W.; Inhomogeneous electron gas Physical Review **1964,** 136(3B), B864–B871.
(42) Kohn, W.; Sham, L. J. Self-Consistent Equations Including Exchange and Correlation Effects *Physical Review* **1965,** 140(4A): A1133–A1138.
(43) Ceperley, D. M.; Alder, B. J. Ground State of the Electron Gas by a Stochastic Method Phys. Rev. Lett. **1980,** 45(7), 566–569.
(44) Runge, E.; Gross, E. K. U. Density-Functional Theory for Time-Dependent Systems Physical Review Letters **1984,** 52(12), 997.
(45) Tour, J. M. Conjugated macromolecules of precise length and constitution. Organic synthesis for the construction of nanoarchitectures *Chem. Rev.* **1996**, *96*, 537-553.
(46) Moore, J. S. Shape-persistent molecular architectures of nanoscale dimension *Acc. Chem. Res.* **1997**, *30*, 402-413.
(47) Müllen, K.; Wegner, G. *Electronic Materials: The Oligomer Approach*; Wiley-VCH: Weinheim, 1998.
(48) Ziener, U.; Godt, A. Synthesis and Characterization of Monodisperse Oligo (phenyleneethynylene)s *J. Org. Chem.* **1997**, *62*, 6137-6143.
(49) Pearson, D.L.; Tour, J.M. Rapid syntheses of oligo (2, 5-thiophene ethynylene) s with thioester termini: potential molecular scale wires with alligator clips *J. Org. Chem.* **1997,** *62*(5)*,* 1376-1387.
(50) Stone, M. T.; Heemstra, J. M.; Moore, J. S. The chain-length dependence test *Acc. Chem. Res.* **2006**, *39*, 11-20.
(51) Peyratout, C. S.; Dahne, L. Tailor-made polyelectrolyte microcapsules: from multilayers to smart containers *Angew. Chem., Int. Ed.* **2004**, *43*, 3762-3783.
(52) Haskins-Glusac, K.; Pinto, M. R.; Tan, C. Y.; Schanze, K. S. Luminescence Quenching of a Phosphorescent Conjugated Polyelectrolyte *J. Am. Chem. Soc.* **2004**, *126*(45), 14964-14971.
(53) Sluch, M. I.; Godt, A.; Bunz, U. H. F.; Berg, M. A. Excited-state dynamics of oligo (p-phenyleneethynylene): Quadratic coupling and torsional motions *J. Am. Chem. Soc.* **2001**, *123*, 6447-6448.
(54) Jiang, H.; Taranekar, P.; Reynolds, J. R.; Schanze, K. S. Conjugated polyelectrolytes: synthesis, photophysics, and applications *Angew. Chem.-Int. Edit.* **2009**, *48*, 4300-4316.
(55) Liu, B.; Bazan, G. C. Homogeneous fluorescence-based DNA detection with water-soluble conjugated polymers *Chem. Mat.* **2004**, *16*, 4467-4476.
(56) Zhu, S. S.; Carroll, P. J.; Swager, T. M. Conducting polymetallorotaxanes: a supramolecular approach to transition metal ion sensors *J. Am. Chem. Soc.* **1996**, *118*, 8713-8714.
(57) Thomas, S. W.; Joly, G. D.; Swager, T. M. Chemical sensors based on amplifying fluorescent conjugated polymers *Chem. Rev.* **2007**, *107*, 1339-1386.
(58) Ho, H. A.; Brisset, H.; Elandaloussi, E. H.; Frere, P.; Roncali, Thiophene-based conjugated oligomers and polymers with high electron affinity J. *Adv. Mater.* **1996**, *8*, 990-994.

(59) Roncali, J. Synthetic principles for bandgap control in linear π-conjugated systems *Chem. Rev.* **1997**, *97*, 173-205.
(60) Kukula, H.; Veit, S.; Godt, A. Synthesis of monodisperse oligo (para-phenyleneethynylene) s using orthogonal protecting groups with different polarity for terminal acetylene units *Eur. J. Org. Chem.* **1999**, 277-286.
(61) Kumaraswamy, S.; Bergstedt, T.; Shi, X. B.; Rininsland, F.; Kushon, S.; Xia, W. S.; Ley, K.; Achyuthan, K.; McBranch, D.; Whitten, D. G. Fluorescent-conjugated polymer superquenching facilitates highly sensitive detection of proteases *Proc. Natl. Acad. Sci. U. S. A.* **2004**, *101*, 7511-7515.
(62) Sudeep, P. K.; James, P. V.; Thomas, K. G.; Kamat, P. V. Singlet and triplet excited-state interactions and photochemical reactivity of phenyleneethynylene oligomers *J. Phys. Chem. A* **2006**, *110*, 5642-9.
(63) Tang, Y.; Zhou, Z. J.; Ogawa, K.; Lopez, G. P.; Schanze, K. S.; Whitten, D. G. Photophysics and self-assembly of symmetrical and unsymmetrical cationic oligophenylene ethynylenes *J. Photochem. Photobiol., A* **2009**, *207*, 4-6.
(64) Tang, Y.; Zhou, Z. J.; Ogawa, K.; Lopez, G. P.; Schanze, K. S.; Whitten, D. G. Synthesis, Self-Assembly, and Photophysical Behavior of Oligo Phenylene Ethynylenes: From Molecular to Supramolecular Properties *Langmuir* **2009**, *25*, 21-25.
(65) Zhou, Z.; Corbitt, T. S.; Parthasarathy, A.; Tang, Y.; Ista, L. K.; Schanze, K. S.; Whitten, D. G. "End-Only" Functionalized Oligo(phenylene ethynylene)s: Synthesis, Photophysical and Biocidal Activity. *J. Phys. Chem. Lett.* **2010**, *1*, 3207-3212.
(66) Hill, E. H.; Evans, D. G.; Whitten, D. G. The Influence of Structured Interfacial Water on the Photoluminescence of Carboxyester-terminated Oligo-p-Phenylene Ethynylenes *J. Phys. Org. Chem.* **2014,** DOI:10.1002/poc.3258
(67) Tang, Y.; Achyuthan, K. E.; David G. Whitten. Label-free and real-time sequence specific DNA detection based on supramolecular self-assembly. *Langmuir* **2009,** *26*(9), 6832-6837.
(68) James, P. V.; Sudeep, P. K.; Suresh, C. H.; Thomas, K. G. Photophysical and theoretical investigations of oligo (p-phenyleneethynylene) s: Effect of alkoxy substitution and alkyne-aryl bond rotations *J. Phys. Chem. A* **2006**, *110*, 4329-37.
(69) Li, N.; Jia, K.; Wang, S.; Xia, A. Theoretical study of spectroscopic properties of dimethoxy-p-phenylene-ethynylene oligomers: Planarization of the conjugated backbone *J. Phys. Chem. A* **2007**, *111*, 9393-8.
(70) Miteva, T.; Palmer, L.; Kloppenburg, L.; Neher, D.; Bunz, U.H.F. Interplay of Thermochromicity and Liquid Crystalline Behavior in Poly (p-phenyleneethynylene) s: π-π Interactions or Planarization of the Conjugated Backbone? *Macromolecules*, **2000,** *33* (3), 652–654.
(71) Magyar, R.J.; Tretiak, S.; Gao, Y.; Wang, H-L.; Shreve, A.P. A joint theoretical and experimental study of phenylene–acetylene molecular wires *Chem. Phys. Letters* **2005**, *401*, 149-156.
(72) Frisch, M. J.; Trucks, G. W.; Schlegel, H. B. *et al. Gaussian 03, Revision C.02,*; Gaussian, Inc., Wallingford CT, 2004.
(73) Hill, E. H.; Evans, D. G.; Whitten, D. G. Photochemistry of "End-Only" Oligo-p-phenylene Ethynylenes: Complexation with Sodium Dodecyl Sulfate Reduces Solvent Accessibility *Langmuir* **2013,** *29*(31), 9712-9720
(74) Hill, E. H.; Sanchez, D.; Evans, D. G.; Whitten, D. G. Structural Basis for Aggregation

Mode of oligo-p-Phenylene Ethynylenes with Ionic Surfactants *Langmuir* **2013,** *29* (51), 15732-15737
(75) Lee, J. H.; Paik, U.; Hackley, V. A.; Choi, Y. M. Effect of carboxymethyl cellulose on aqueous processing of natural graphite negative electrodes and their electrochemical performance for lithium batteries *J. Electrochem. Soc.* **2005**, *152*, A1763-A1769.
(76) Dubin, P. L.; Brant, D. A. Charge-Induced Conformational Changes in Carboxymethylamylose *Macromolecules* **1975**, *8*, 831-842.
(77) Kim, O. K.; Je, J.; Jernigan, G.; Buckley, L.; Whitten, D. G. Super-helix formation induced by cyanine J-aggregates onto random-coil carboxymethyl amylose as template *J. Am. Chem. Soc.* **2006**, *128*, 510-516.
(78) Oshima, J.; Yoshihara, T.; Tobita, S.; Water-induced fluorescence quenching of mono- and dicyanoanilines. *Chemical Physics Letters* **2006,** *423,* 306–311.
(79) Tobita, S.; Ida, K.; Shiobara, S. Water-induced fluorescence quenching of aniline and its derivatives in aqueous solution. *Research on Chemical Intermediates* **2001,** *27,* 205–218.
(80) A. T. Laia C, M. B. Costa S. Fluorescence quenching of a squaraine dye by water in AOT reversed micelles. *Journal of the Chemical Society, Faraday Transactions* **1998**, *94*, 2367–73.
(81) Hill, E. H.; Goswami, S.; Evans, D.G.; Schanze, K.S.; Whitten, D.G. Photochemistry of a Model Cationic p-Phenylene Ethynylene in Water *J. Phys. Chem. Letters* **2012,** *3*, 1363-1368.
(82) Mikkelsen, K.; Nielsen, S.O. Acidity Measurements with the Glass Electrode in H2O-D2O Mixtures. *The Journal of Physical Chemistry* **1960,** *64,* 632–637.
(83) Covington, A.K.; Paabo, M.; Robinson, R.A.; Bates, R.G. Use of the glass electrode in deuterium oxide and the relation between the standardized pD (paD) scale and the operational pH in heavy water. *Analytical Chemistry* **1968,** *40*, 700–706.
(84) Rösch, U.; Yao, S.; Wortmann, R.; Würthner, F. Fluorescent H-Aggregates of Merocyanine Dyes *Angew*. *Chem*. *Int*. *Ed*., **2006,** *45*, *7026–7030.*
(85) D.A. Case, T.A. Darden, T.E. Cheatham, III, C.L. Simmerling, J. Wang, R.E. Duke, R. Luo, R.C. Walker, W. Zhang, K.M. Merz, B. Roberts, S. Hayik, A. Roitberg, G. Seabra, J. Swails, A.W. Goetz, I. Kolossváry, K.F. Wong, F. Paesani, J. Vanicek, R.M. Wolf, J. Liu, X. Wu, S.R. Brozell, T. Steinbrecher, H. Gohlke, Q. Cai, X. Ye, J. Wang, M.-J. Hsieh, G. Cui, D.R. Roe, D.H. Mathews, M.G. Seetin, R. Salomon-Ferrer, C. Sagui, V. Babin, T. Luchko, S. Gusarov, A. Kovalenko, and P.A. Kollman (2012), AMBER 12, University of California, San Francisco.
(86) Lu, L.; Helgeson, R.; Jones, R. M.; McBranch, D.; Whitten, D. G. Superquenching in cyanine pendant poly (L-lysine) dyes: dependence on molecular weight, solvent, and aggregation *J. Am. Chem. Soc.* **2002**, *124*, 483-8.
(87) Jones, R. M.; Bergstedt, T. S.; McBranch, D. W.; Whitten, D. G. Tuning of superquenching in layered and mixed fluorescent polyelectrolytes *J. Am. Chem. Soc.* **2001**, *123*, 6726-6727.

Chapter III: PHOTOCHEMISTRY OF WATER-SOLUBLE OLIGO-P-PHENYLENE ETHYNYLENES

3.1 Introduction

3.1.1 Basic Photochemistry Theory

Light, as a predominant form of electromagnetic radiation which has shaped life as we know it, is a source of energy. The Grotthuss-Draper law, formed in 1817 (Grotthuss) and 1848 (Draper), states that only the energy absorbed by a reacting species can bring about a photochemical change in the system.[1] Max Planck in 1900 developed the relation that describes the electromagnetic radiation emitted by a black body at a specific temperature, and provides a stable equilibrium distribution of radiation.[2] Following this between 1908 and 1913, Stark and Einstein independently formulated the photochemical equivalence law, which states that every unit of energy absorbed will cause a primary chemical or physical reaction, therefore marking the first time quantization of light was included in the theory.[3] Mathematically, this can be expressed as E=hv, where E is the energy of the photon, h is Plancks constant, and v is the frequency of the light. When the energy of the photon absorbed exceeds that of the bandgap of the chromophore of a molecule, the molecule reaches an excited state which initiates the photochemical reaction. If the energy of absorbtion is above the activation energy, the excited state of a molecule can induce isomerization or rearrangement on the molecule, or undergo reactions with other molecules or with solvent to form products. In some cases, a reaction is quickly reversible and does not produce a lasting change to a molecule, resulting in the effective quenching of photochemistry. In addition to primary photochemical processes which take place upon the molecule which absorbs the light, secondary photochemical processes can result from the production of species by the molecule involved in the primary process.

3.1.2. Previous Studies of phenylacetylenes and diphenylacetylenes

In some of the earlier work by Porter and coworkers, the photochemistry of substituted benzophenones were explored and phenyl-substituted benzophenones were found to have intermediate reactivity.[4] Initial studies of the photochemistry of phenylacetylenes by Roberts and Woolridge in 1973 and Wan, Culshaw, and Yates in 1982 suggested that the triple-bond can be photo-protonated, leading to the addition of water across the triple bond.[5,6] This mechanism was proposed to involve either an initial photoprotonation step, or nucleophilic attack of structured

interfacial water for electron deficient compounds. Other evidence of photohydration as a dominant mechanism of photolysis for phenylacetylenes was found by Chiang and coworkers, who observed the formation of acetophenone enol upon flash photolysis of phenylacetylene.[7] More recently, Xu *et al* found that diphenylacetylene forms an enol after adding water across the triple-bond, which then tautomerizes into a ketone.[8] Given the presence of multiple functional groups in the polymer it is important to consider whether a given photoreaction can occur multiple times.

3.1.3. *Previous studies of PPV and PPE photochemistry*

As has been discussed previously, the OPEs have significant triplet quantum-yields of 0.2-0.5 depending on the specific OPE. This allows the excited triplet state of the OPE to transfer energy to O_2, which is a ground state triplet. In oxygenated atmosphere this results in the formation of singlet oxygen, which has a very short lifetime in water and reacts with many types of molecules it comes into contact with. Singlet oxygen was initially discovered by Foote, who was able to go back through the 1930's literature and find evidence of singlet-oxygen in dye-sensitized photooxidation reactions.[9] In order to better understand the photochemistry of the OPEs, the processes involving degradation by oxygen must be studied. Several earlier studies highlight the importance of the pathways of photodegradation resulting from oxidation.

Ogilby and coworkers found that OPVs, with double bonds instead of triple bonds linking the phenyls, were susceptible to reaction with singlet oxygen.[10] Separately, Sudeep *et al* found in 2006 that an uncharged OPE had a large proportion (0.4) of triplet states with a long lifetime, and could undergo one-electron oxidation with molecules such as benzoquinone.[11] However, a more recent study by Ogilby and coworkers shows that photoaddition of singlet-oxygen to neutral OPEs is less likely than observed for OPVs.[12] It is important that OPEs with charged sidechains and different geometries are studied in order to shed light on the reaction mechanisms for the different series of OPEs as a whole.

3.1.4. *Basis for this study*

As discussed in previous chapters, recent studies have shown that cationic PPE-based polymers and oligomers exhibit enhanced light-activated anti-microbial activity[13–19]. Hospital-acquired infections are caused by bacteria such as Gram-positive Methicillin-resistant *Staphylococcus*

aureus and Gram-negative *Klebsiella pneumonia* which can easily contaminate surfaces in a hospital environment. Cationic Oligo-p-Phenylene Ethynylenes (OPEs) have been recently studied by the Whitten and Schanze groups for their sensing properties [20-32] and biocidal activity against bacteria.[13-15] They have been shown to be very effective against both Gram-positive and Gram-negative strains of bacteria, particularly when irradiated by UV light. The exposure of bacteria to the OPEs in the light has been recently explored by Ying Wang and coworkers, and dramatic changes to the cell surface and internal organization can be observed. [18] The damage is largely caused by the production of singlet oxygen by the OPEs when irradiated, which does broad-spectrum damage to nucleic acids and proteins in the cell.

One consideration for applications where light exposure is required is the effect of prolonged exposure of these compounds to light in air and moisture. For sensing applications, the chromophore could be destroyed by photobleaching. The conversion of the compound to a product which does not have biocidal properties would also be detrimental to its use as an antimicrobial. Surfactants and micellar solutions have potential as media in which reactions can be modified by the micellar environment. Depending on the type of surfactant and reactant molecule, different effects on polarity, microviscosity, and localization can be observed, strongly affecting thermal and photochemical reactions that may occur. Previous studies have shown strong effects on photoreactions of various molecules, and these effects are often attributed to intercalation with or adsorption onto the micelle.[33-37] In this study, the effects of the surfactant sodium dodecyl sulfate (SDS) at both micellar and premicellar concentrations on the photochemistry of OPEs are studied in order to determine what changes occur, and what the molecular basis for these changes are.

In this study, the compounds studied are designated as in previous sections. The OPEs **+EO** and **+EO$_{C2}$** have their alkylammonium chains located on the two opposite ends of the phenylene ethynylene backbone, as shown below in Scheme 3.1. For this reason, the compounds are referred to as “end-only” OPEs or EO-OPEs. The general structure of a cationic OPE is shown to the left in Scheme 3.1.

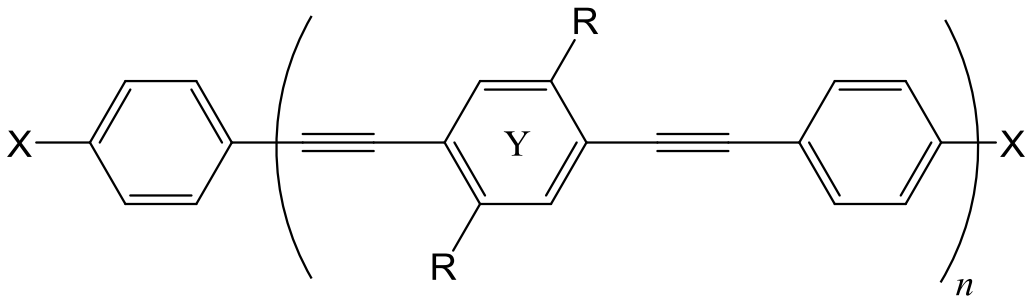

^{+}nC series: X = COOEt, R = $O(CH_2)_3N^+(CH_3)_3$
^{+}nH series: X=H, R = $O(CH_2)_3N^+(CH_3)_3$
^{-}nC series: X = COOEt, R = $O(CH_2)_3SO_3^-$
^{-}nH series: X=H, R = $O(CH_2)_3SO_3^-$
$^{+}$EO: n=1, X = $O(CH_2)_3N^+(CH_3)_3$, R = H
$^{+}EO_{C2}$: n=1, X = $O(CH_2)_2N^+(CH_3)_3$, R = H
$^{-}$EO: n=1, X=$O(CH_2)_3SO_3^-$, R = H
EOT, n=1, X = $O(CH_2)_3N^+(CH_3)_3$, Y =

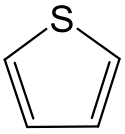

Scheme 3.1. *p*-Phenylene ethynylene oligomers used in this study

As can be seen in the scheme above, the OPEs with charged groups coming off opposite ends have the title EO designating "end-only", while those with charged groups coming off the side are named based on their number of repeat units and end-group functionality. A class of end-only OPEs with a thiophene central ring (EOT) is also briefly discussed.

3.2 Photochemistry of a Model OPE

The progress of the photolysis was followed by UV-Vis fluorescence and absorbance spectroscopy, and characterization was carried out by mass spectrometry, as described in the methods (chapter 7). The UV-visible absorption spectra of **+1H** throughout the photolysis in air-saturated and argon-degassed aqueous solution are shown below, in Figure 3.1.

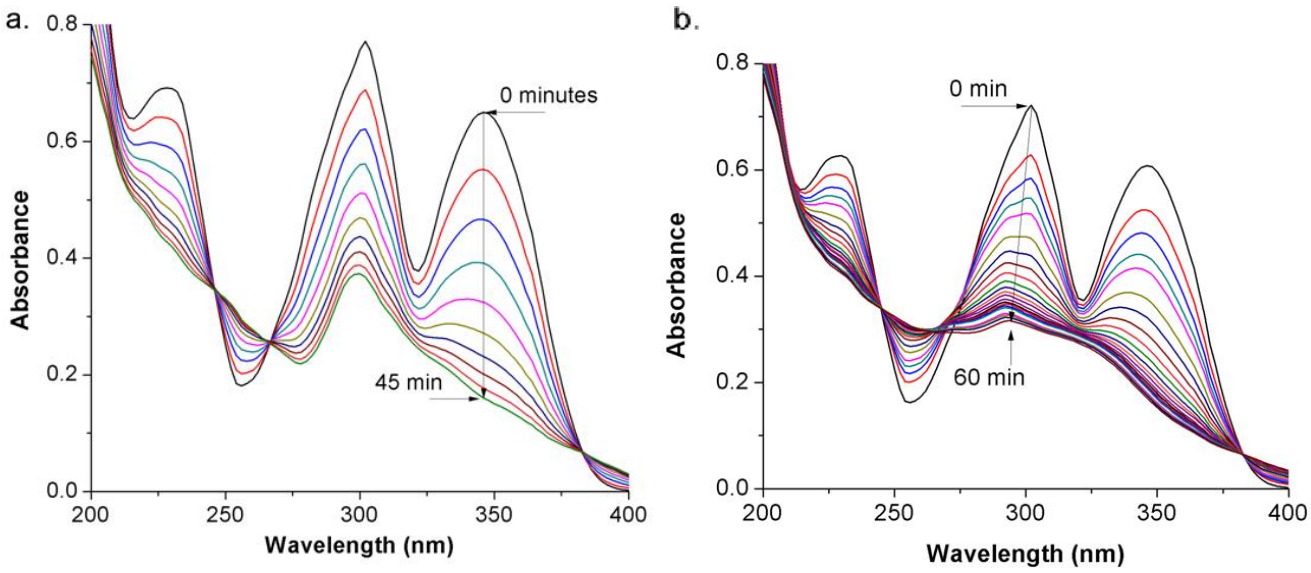

Figure 3.1. UV-visible absorption spectra of 20 μM compound **+1H** in water as a function of photolysis for **A)** air-saturated solution and **B)** argon-degassed solution. Arrows are indicative of change with increasing time. Photolysis effected by using broad-band near-UV light (300-400 nm, 0.98 mW/cm^2).[38]

Changes in the photoproduct distribution occurred when the reactions were carried out in D_2O due to the addition of a deuterium from the solvent. The quantum yields of disappearance were also reduced in D_2O (Table 1).

Table 3.1. Quantum yield of disappearance of **+1H** in water and D_2O.[38]

Solvent	**(Φ_- / 10^{-4}) Argon**	**(Φ_- / 10^{-4}) Air**
H_2O	3.77 +/- 0.02	2.42 +/- 0.08
D_2O	0.75 +/- 0.00	1.12 +/- 0.04

The species observed by high-resolution electrospray ionization mass spectrometry analysis of the photoreaction mixtures are shown below, in Schemes 4.2 and 4.3.

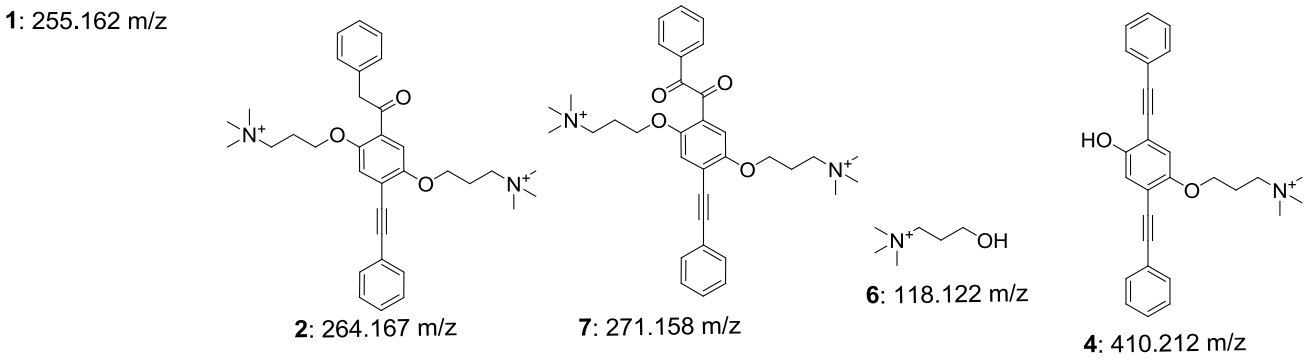

Scheme 3.2. Primary photoproducts of the photolysis of **+1H**.

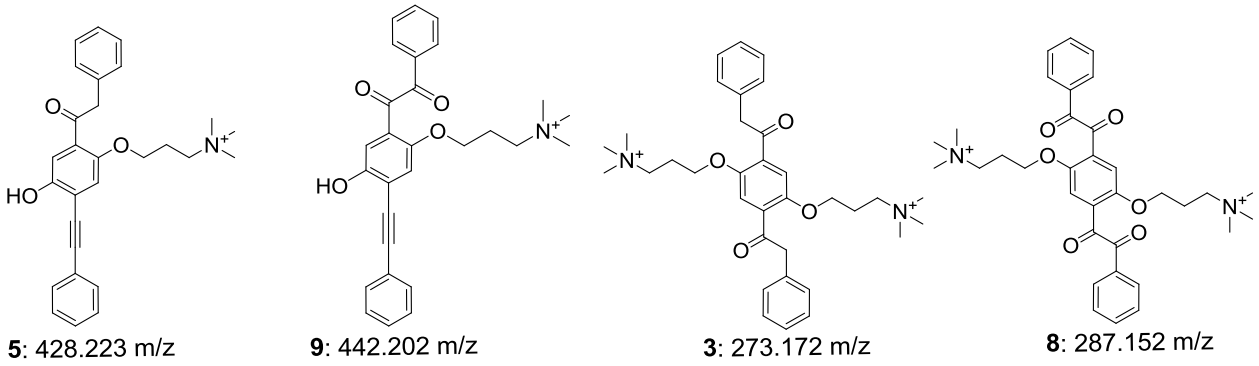

Scheme 3.3. Consecutive and hybrid photoproducts of the photolysis of **+1H**.

When the reaction was carried out in water and air, all of the above products were observed. The products that are most abundant and also the first to appear are compounds **2**, **7**, **4**, and **6** (Scheme 3.2). In addition, products **3**, **5**, **8**, and **9** (Scheme 3.3) indicative of subsequent or hybrid reactions were observed. When the reaction was performed with argon degassing only products **2**, **3**, **4**, **5,** and **6** were observed. When the reaction was performed in D_2O under air, the major products observed to form were **7** and **9**, while **4**, **6**, and **8** were also present. Carrying out the reaction in ^{18}O enriched water did not produce significant changes in the product distribution. The incorporation of deuterium and ^{18}O was observed in many products, and this is described in Table 3.2 below. In addition, the products that exchange ^{18}O passively were determined and denoted with a * in Table 3.2.

Table 3.2. List of products and their change upon incorporation of isotopes. [38]

Compound	m (g/mol)	z	m/z	m/z from D_2O rxn	m/z from ^{18}O rxn
+1H	510.324	2	255.162	N/A	N/A
2	528.334	2	264.167	265.170	265.169
3	546.345	2	273.172	275.179	275.177
***7**	542.313	2	271.157	unchanged	272.159, 273.161
***8**	574.303	2	287.152	unchanged	288.154, 289.156, 290.158
4	410.212	1	410.212	411.218	412.216
5	428.223	1	428.223	429.228	430.226
***9**	442.202	1	442.202	443.208	444.206, 446.210, 448.214
6	118.123	1	118.123	119.129	120.127

* Exchange of ^{16}O by ^{18}O occurs when the compound is dissolved in labeled water for 12 hours.

In Figures 4.1A and 4.1B, a decrease in absorbance and alteration of the absorbance spectrum of the oligomer is clearly observed as the photoreaction takes place. In both samples, distinct isosbestic points are observed, signifying relatively clean reactions which give rise to slightly different spectral profiles. The argon-degassed sample has a relatively stable spectral profile after about 15 minutes of photolysis at 20 μM concentration, whereas the spectral profile of the aerated sample does not stabilize until around 35 or 40 minutes. This is indicative of two different rates for the two pathways. A loss of fluorescence is also observed.

The mechanisms of the reactions were determined from the characterization of products. One mechanism is initiated by photoprotonation of a polarized excited state as shown in Scheme 3.4. The protonated ground state formed in this process can lead to products **2**, **4**, and **6**.

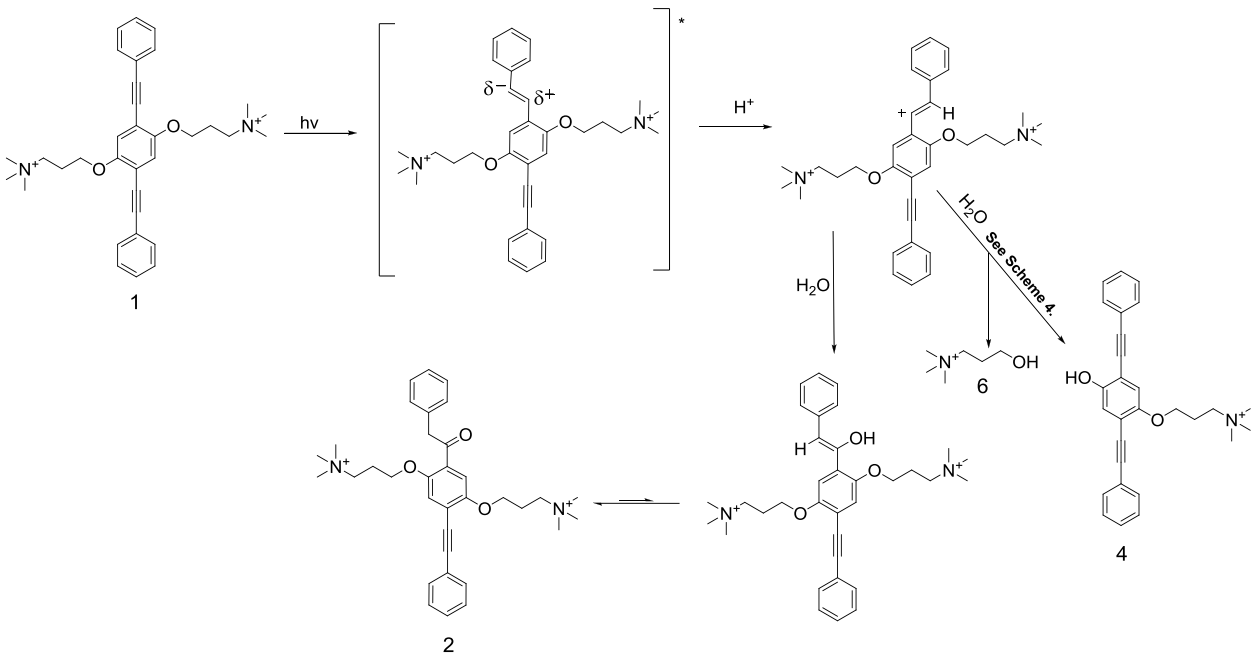

Scheme 3.4. Reaction scheme for pathways involving photoprotonation

A second reaction can generate product **7** by cycloaddition of oxygen to the triple-bond followed by cleavage to yield a 1,2 dione. Since it is clear that in methanol the predominant reaction of O_2 with triplet **+1H** is sensitization of singlet oxygen, the simplest explanation would be cycloaddition of singlet oxygen to the ethynylene in water. This perspective is supported by earlier research which shows that **+1H** exhibits relatively efficient intersystem crossing to form the triplet state, which also is an efficient sensitizer for singlet oxygen[15]. Dam and Ogilby *et al* studied the photooxidation of phenylene-vinylenes and proposed that singlet oxygen added across the double-bond[10]. However, the work of McIlroy and Ogilby et al. suggests that addition of singlet oxygen to neutral phenylene-ethynylenes is inefficient[12]. Since the overall quantum yields for the +*n*H series observed in our work are very small under all conditions (Table 3.1), it is not possible to make firm mechanistic conclusions for this pathway.

The progression of the photolysis of **+1H** in air-saturated or degassed conditions yielded the products **4, 5** or **9** resulting from cleavage of one of the cationic side-groups (**6**), and this cleavage was sufficiently efficient such that **6** built up considerably throughout the duration of the photolysis. In addition, it was observed that the products **4, 5** and **9** begin to precipitate out of solution, likely due to reduced charge in the product leading to low solubility. The photochemistry of aryl alkyl ethers in methanol has previously been shown to yield similar

products[39, 40]. Possible mechanisms for this pathway are shown below, in Scheme 3.5.

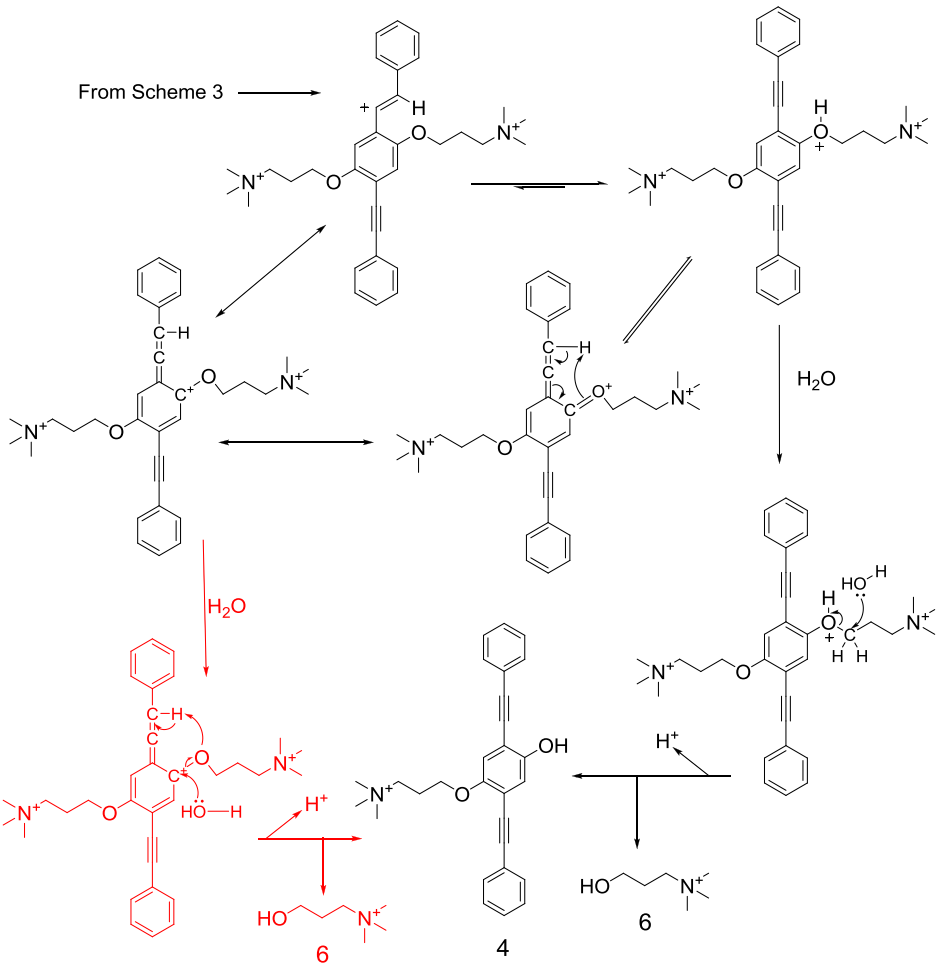

Scheme 3.5. Possible reaction mechanisms for the photolytic cleavage of the alkylammonium sidechain

The pathway highlighted in red has been shown to be unfavorable by reactions carried out in ^{18}O-labeled water, as incorporation of ^{18}O-into photoproduct **6** suggests that the active pathway involves attack of water on the aliphatic carbon. As no exchange of ^{18}O is observed with the unlabeled alcohol oxygen of **6**, we conclude that the pathway highlighted in red in Scheme 3.5 is not favorable.

Quantum yields for disappearance of **+1H** are lower in D_2O than in H_2O under both air and argon, which is attributed to a normal isotope effect on the photo-protonation pathway shown in Scheme 3. As one would expect, in air saturated solution the change of solvent from

H_2O to D_2O has no effect on the oxygen-addition pathway and the attenuation of the overall quantum yield of disappearance of **+1H** is lower. Most notably, in argon degassed D_2O the pathway leading to **2, 4** and **6** is much less efficient based on the product distributions (see supporting information). The reduced efficiency is consistent with a normal isotope effect, and with proton transfer being the rate determining step. We thus suggest that photoaddition of water and side-group cleavage are initiated by protonation of the triple-bond, as shown in Scheme 3.4. This result is supported by the 1982 study by Wan, Culshaw, and Yates, which revealed that either nucleophilic attack of structured water on or protonation of a triple bond could take place depending on the substituent[6]. The rate-limiting step of photoprotonation therein suggests that the addition of water across the triple-bond occurs as a Markovnikov addition. We can also infer from logic and previous research[8] that the initial water adduct is an enol which undergoes tautomerization to yield **2** as shown in Scheme 3.4.

Since the quantum yield of the overall reactions is comparatively low, it is difficult to reach a firm conclusion as to the excited state(s) that are associated with the observed reaction pathways. It was suggested in earlier studies that the quasi-zwitterionic excited state undergoing protonation is a singlet[5,6]. However, it has been shown previously that the fluorescence yield of **+1H** is the same in methanol and water, suggesting that there is no singlet quenching by solvent[15]. This solvent quenching effect was observed for the +nC series of compounds, as discussed in section 3.3 of the previous chapter, and this likely contributed to the lack of photoreactivity of this series of compounds (takes atleast 24 hours to photolyse under the same conditions – see Figure A2 in Appendix).[41] The absorption and fluorescence intensity of **+1H** are identical in H_2O and D_2O, suggesting that there is little or no deuterium isotope effect on the excited singlet state. It was also shown that in methanol with air present all the triplets are quenched to yield $^1O_2$[3]. Studies of neutral OPEs have shown very high triplet yields with long lifetimes[11] in organic solvents such as methanol and cyclohexane. It is thus reasonable to infer that all of the pathways discussed may occur via a triplet pathway.

3.3 Photochemistry of "End-only" OPEs

The photolysis of **+EO** and **+EO$_{C2}$** were followed using UV-visible absorbance and fluorescence spectroscopy. The change in spectra over the duration of photolysis in water can be

seen below, in Figure 3.2. As the progress of photolysis of **+EO** by UV-visible spectroscopy is nearly the same as that of **+EO$_{C2}$**, it has been shown in the Appendix (Figure A3).

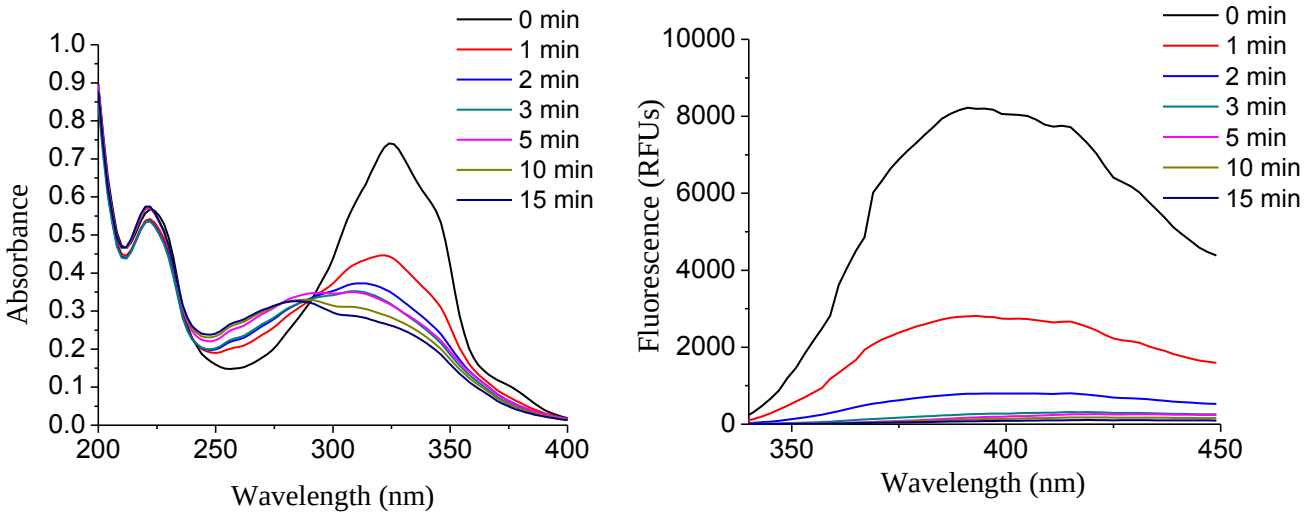

Figure 3.2. Absorbance and fluorescence of **+EO$_{C2}$** throughout photolysis under UVA irradiation with 10 lamps (300-400 nm, 0.98 mW/cm^2).[42]

Compounds **+EO** and **+EO$_{C2}$** were subjected to photolysis in UVA light in water, D_2O, methanol, and 10% ^{18}O water in order to study the major mechanisms of photochemical reactions that take place when these compounds are exposed to light. The most obvious difference in photochemistry from the compound **+1H** studied previously can be seen in the rate of photolysis. It is clear from Figure 3.2 that the amount of time needed to achieve near-complete photobleaching under strong UVA irradiation is only 2 minutes for **+EO$_{C2}$** in water. In the study of compound **+1H**, photobleaching takes an hour in the same exposure conditions (Figure 3.1). The major products of photolysis characterized by high-resolution mass spectrometry are shown below, in Scheme 3.6. Note that there is no cleavage of the alkylammonium end-group.

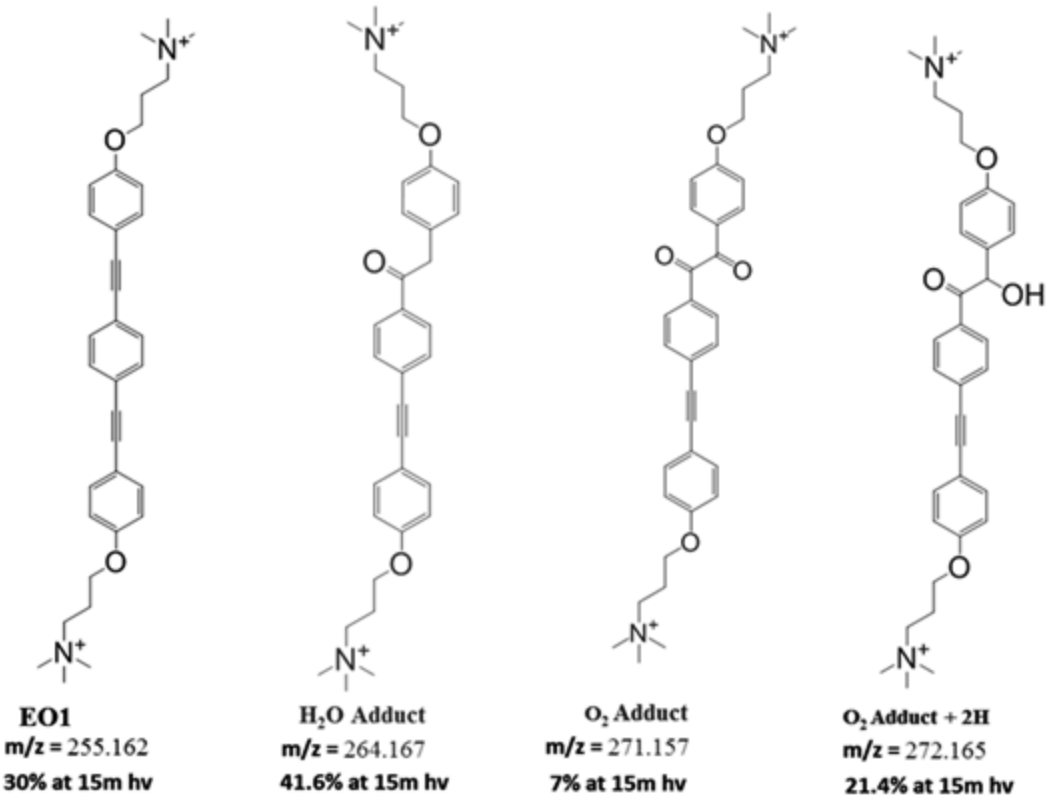

Scheme 3.6. Products of Photolysis of **+EO** with mass to charge (m/z) ratios and percentages observed after 15 minutes.[42]

The characterization results summarized in Scheme 3.6 show similar water and oxygen adducts observed in the photolysis of **+1H**, but important differences in products were noted. Most importantly, the quaternary ammonium end-groups were not cleaved off at the terminal ether oxygen. This was observed to be a very common photoproduct from the exposure of **+1H** to UVA in water, which led to a variety of "hybrid" photoproducts which resulted from multiple different reaction pathways.[16] The lack of this reaction in the photolysis of the end-only OPEs simplified the characterization results. In addition to the water and oxygen adducts, an adduct that correlates with the addition of a peroxide molecule is also observed. This suggests that peroxide is formed in solution as a result of the reactive oxygen species (ROS) resulting from singlet oxygen production by the OPE.[3,11] The peroxide is likely then attacking the triple-bond to produce the observed product. The quantum yields of disappearance are shown below in Table 3.3. The values are nearly 100-fold higher than the previously studied OPE, and there is a decrease in D_2O.

Table 3.3. Quantum Yields of Disappearance for **+EO**, **+EO$_{C2}$**, and **EOT** in Water, Deuterium Oxide, and Methanol

Compound	**+EO**			**+EO$_{C2}$**			**EOT**		
Solvent	H_2O	D_2O	MeOH	H_2O	D_2O	MeOH	H_2O	D_2O	MeOH
φ^- (× 10^{-3})	9.64	2.09	1.04	8.58	5.03	1.36	2.61	2.90	-
$\sigma_{\varphi-}$ (+/- × 10^{-3})	0.76	1.74	0.10	0.75	0.64	0.19	0.33	0.82	-

When comparing the quantum yields of disappearance (in Table 3.3.) of the end-only OPEs with those reported in the study of **+1H** (Table 3.1), the increase in quantum yield for the EO-OPEs is clear. There is a 50-fold difference between the quantum yields of disappearance of **+1H** (2.42×10^{-4}) and **+EO** or **+EO$_{C2}$** which approach 0.01 in water. In addition to the photolysis occurring more quickly and efficiently with the end-only OPEs compared to the OPEs, the end-only compounds also were found to undergo photolysis in methanol under air. The photolysis of **+EO** in Methanol is shown in Figure 3.3. Compound **+1H** does not undergo photolysis in methanol, and neither does EOT, which contains a thiophene middle ring. The mass spectrometry results revealed that the only product formed in methanol was the product of O_2 adding across the triple-bond. This reinforces the result that the addition of oxygen is not reliant on an initial photoprotonation step as is the addition of water. This result also suggests the addition of singlet oxygen or superoxide across the triple-bond is the mechanism for oxygen addition, since there is no possible formation of peroxy-adduct.

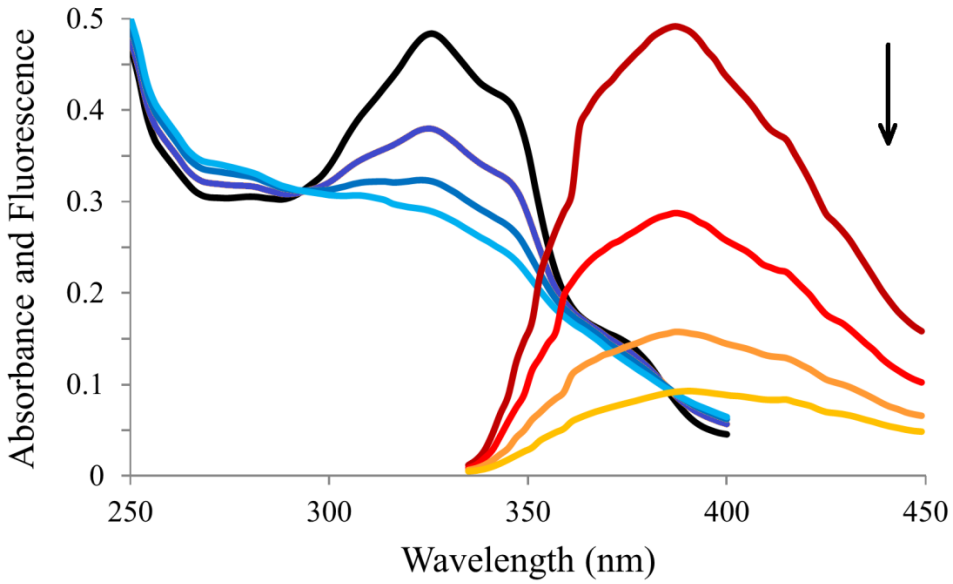

Figure 3.3. Absorbance and normalized fluorescence spectra following photolysis (300-400 nm, 0.98 mW/cm^2) of 10 μM **+EO** in methanol from 0 to 15 minutes, with 5 minute increments between traces. The arrow indicates the direction of change over time.

There are differences between the respective quantum yields of photolysis and the products observed in **+EO** and **+EO$_{C2}$** which suggest solubility plays a role in the photochemistry. A large proportion of the products of water or oxygen addition to **+EO$_{C2}$** are found by mass spectrometry to be subsequently cleaved by water along the former site of the triple bond that has been reacted. Structures of these cleaved products are shown in Scheme 3.7, below. The larger cleavage products may correspond to the broadened 260 nm absorbance band that appears as the photolysis of **+EO$_{C2}$** progresses. As has been reported[13], the solubility of **+EO** in water is much lower than that of **+EO$_{C2}$**. Compound **+EO$_{C2}$** is solubilized completely upon addition of water to the solid, while **+EO** takes up to an hour to completely solvate as measured by absorbance spectroscopy. For this reason, the photolysis studies were carried out using a solution of **+EO** that had been allowed to sit at room temperature for 48 hours. The difference in photoproducts of **+EO** and **+EO$_{C2}$** supports the suggestion in the initial study of phenylacetylenes that structured interfacial water can play a role in the mechanism of photolysis.[6]

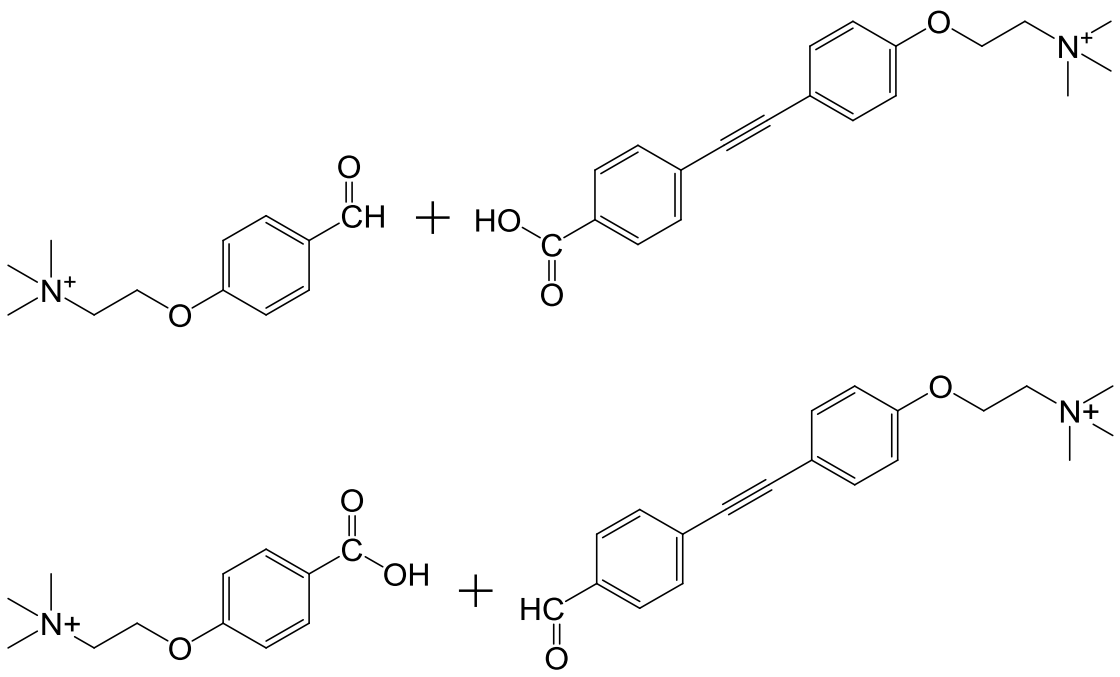

Scheme 3.7. Cleavage Products observed from photolysis of **+EO$_{C2}$**.

The photochemistry of the "end-only" OPEs has similarities to that of the previously studied OPE, **1,** but there are crucial differences that lead to dramatic changes and an overall increase in photolysis efficiency. The most notable difference in the photochemistry of the end-only OPEs and **+1H** is that the alkylammonium chain is not cleaved from the molecule. The photolysis of **+EO** and **+EO$_{C2}$** in methanol is unique considering that in the series of cationic OPEs that has been studied so far no other OPEs is able to undergo photolysis in Methanol. Finally, the increased rate of photolysis in a freshly-made solution and the backbone cleavage that results in the products of the more water-soluble compound **+EO$_{C2}$** suggests a relationship between interaction with solvent and photochemistry.

The singlet oxygen quantum yields of the OPEs are fairly high (20-70%), but the damage to microbes is likely further enhanced by the close proximity of the OPE to the cell due to the interaction of the cationic OPEs with negatively-charged lipids in the bacterial membrane or anionic residues in proteins. Recent experiments showed strong interactions between bacterial membranes and OPEs that can result in phase changes,[14,18] and a classical Molecular Dynamics (MD) study has shown the strong interaction of a large OPE with model bacterial membranes resulting in bilayer damage.[43] The strong interactions observed with both real and model membranes suggested that the OPEs would strongly interact with other amphiphilic molecules,

such as detergents. This gave rise to the idea that OPEs may be encapsulated and partially protected from photolysis by detergent micelles. To explore this phenomenon, photochemistry experiments and molecular simulations involving **+EO** with the anionic surfactant sodium dodecyl sulfate were carried out as described in section 4.5, and the interactions with surfactant molecules such as SDS were found to be strong effectors of the photochemistry of the "end-only" OPEs.[42]

3.4 Photochemistry of Larger OPEs and PPEs

The mechanistic determinations of the photolysis for the model compound **+1H** allows us to extend the study to the larger oligomers and polymers without expecting a significant change in the mechanisms of photochemical breakdown. In order to determine whether the reaction rate is affected by the size of the backbone, the photochemistry of the larger oligomers, including the series +*n*C and +*n*H, were studied in water under air and Ar atmospheres. It is crucial to explore the effects of backbone length on the overall kinetics of the photolysis so that possible advantages and disadvantages to using the polymers or oligomers for applications involving prolonged light-exposure are known.

The changes in absorbance spectra for **+2H** and **+3H** are shown below, in Figure 3.4.

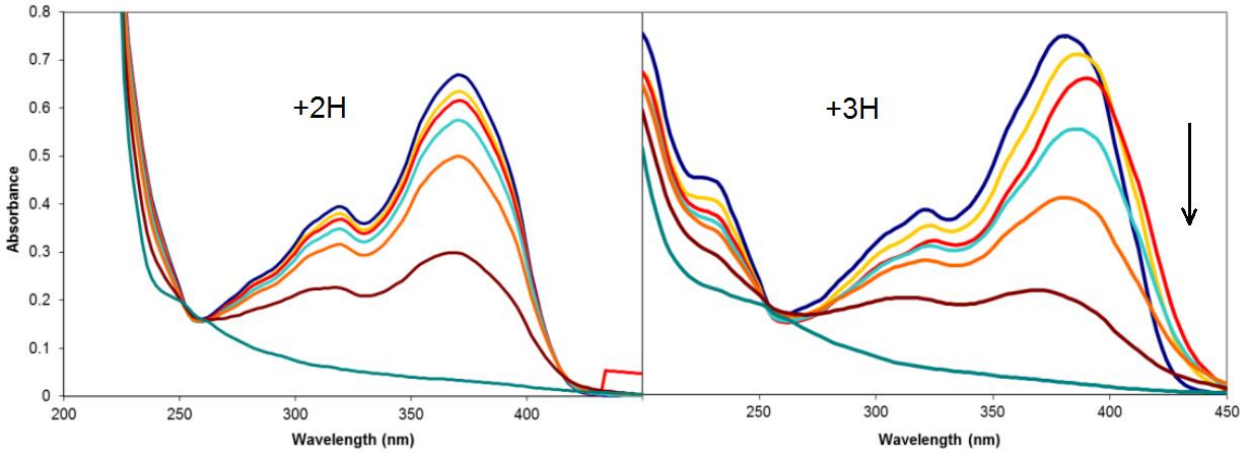

Figure 3.4. Absorbance of 10 µM **+2H** and **+3H** following photolysis under UVA irradiation (300-400 nm, 0.98 mW/cm^2) after 0, 0.5, 1.5, 3, 6, 12, and 24 hours of irradiation. The arrow indicates the direction of change

As can be seen in Figure 3.4, the photolysis of the n=2 and n=3 oligmers takes many hours

longer than that of **+1H**. The quantum yields of disappearance for **+2H** and **+3H** were calculated as described in the methods section (Chapter 7), and are given below in Table 3.4

Table 3.4 Quantum yields of disappearance for **+2H** and **+3H**.

Compound	**+2H**	**+3H**
φ^- (× 10^{-4})	4.51 +/- 2.04	7.84 +/- 2.72

The results above clearly show that the +nH OPEs have comparable quantum yields of photodegradation, despite the clear decrease in rate of degradation shown for **+2H** and **+3H** (24 hours) relative to **+1H** (45 mins). This suggests that slight changes in repeat unit number do not have a significant effect on the kinetics of the photochemistry. As a further study of the effect of increased repeat unit number, two anionic PPEs were irradiated under a visible light source, and their absorbance spectra were measured over the course of the photolysis. These are shown below, in Figure 3.5

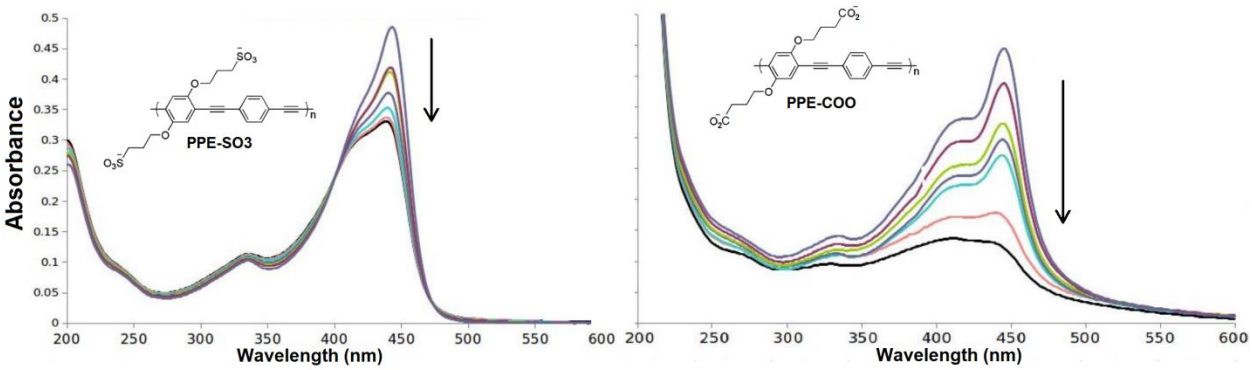

Figure 3.5 Absorbance spectra of 7 μM PPE-$SO3^-$ and 3 μM PPE-COO^- after 0, 5, 10, 15, 30, 60, and 120 minutes of irradiation under a high-pressure mercury lamp with an intensity of ~1 W/cm^2. The arrows indicate the direction of spectral change with increasing irradiation time.

The anionic polymer PPE-SO3[44] shows great attenuation in photodegradation following **+1H** hour of exposure to a strong visible light source, as can be seen in Figure 3.5. Another anionic polymer, PPE-COO, exhibits no such effect. This result suggests that some of the PPEs may show the same attenuation of photodegradation over time, which may be due to the formation of trap sites along the backbone which quench the photochemistry. As was shown in section 4.2, the dominant products formed in the photochemistry of the model contain a ketone moiety, which is

likely to quench the excited state upon transient protonation by water.

While the polymers did show an attenuation of photolysis, there still remains the desire to have an OPE which can perform sensing or biocidal functions despite long-term irradiations by the excitation source. This is particularly important in applications such as biocidal applications in clothing or on surfaces, as prolonged exposure to sunlight could photodegrade the OPE as shown in the sections above, compromising the proposed application. To this aim, strategies for the "photoprotection" of the OPEs by use of surfactants were explored.

3.5 Reduction of Photolysis with Surfactant Complexes

3.5.1 Experimental Studies of Photolysis

In previous studies, it has been suggested that the water addition pathway may be partially attributed to the high reactivity of interfacial water with the excited state. The idea to attempt a strategy to protect the OPEs from photodegradation arose from an experiment where the OPEs **+1H** and **-1H** were complexed with lipid vesicles of different lipid composition, and then irradiated under UVA. Surprisingly, attenuation of photodegradation along with formation of a highly-structured aggregate is observed in the changes in absorbance and fluorescence observed throughout the photolysis. These spectra are shown below, in Figure 3.6.

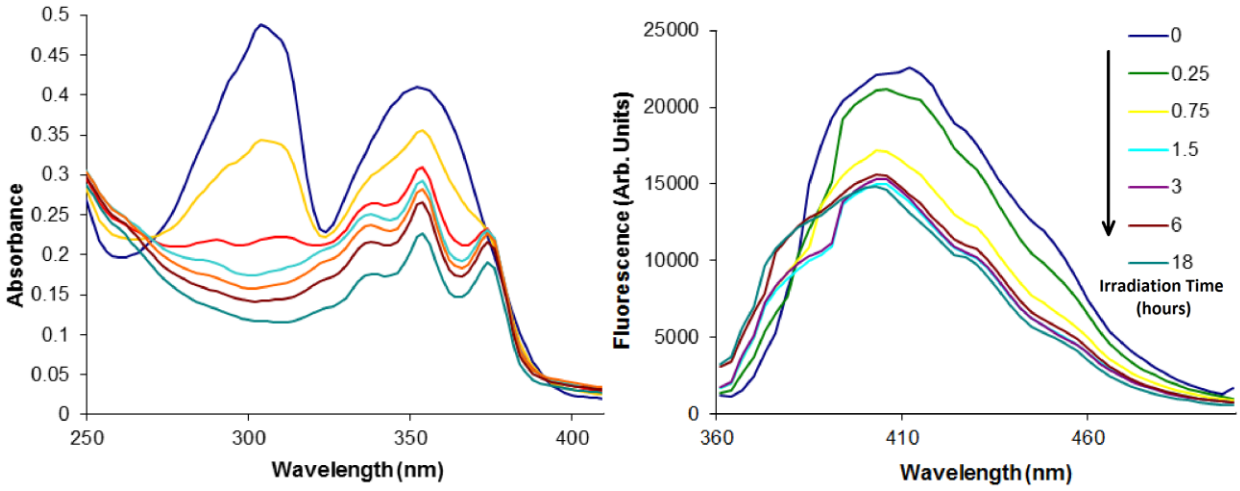

Figure 3.6. The absorbance and fluorescence (exc. 350 nm) of 10 µM **-1H** with DPPG lipid vesicles after photodegradation in UVA (300-400 nm, 0.98 mW/cm^2) from 15 minutes to 18 hours.

We hypothesized based on this result that the interactions of the OPEs with micelles and premicellar aggregates of amphiphiles will influence their photoreactivity, and have carried out simulations and experiments to investigate. The effects on photolysis can be observed in the UV-Visible absorbance and fluorescence spectra. Compound **+1H** is not photo-protected by SDS, as there is no significant difference between the rate of absorbance decrease in this spectrum and **+1H** alone in water. The absorbance spectrum over an hour of photolysis is shown in the Appendix (Figure A4). In order to determine possible effects of premicellar aggregates on photochemistry, the changes in absorbance and fluorescence over the duration of photolysis of **+EO_{C2}** with SDS at 0.33 mM (1:20 OPE:SDS ratio) in water are shown below, in **Figure 3.7**.

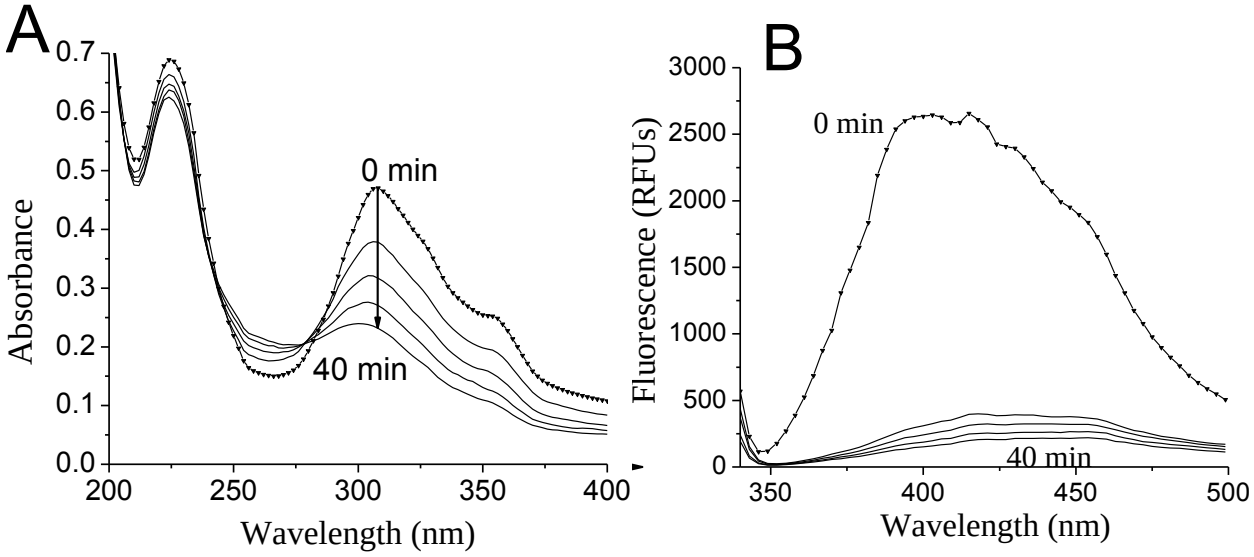

Figure 3.7. A. Absorbance and **B.** Fluorescence of **+EO_{C2}** throughout the duration of UVA photolysis (300-400 nm, 0.98 mW/cm^2) in 0.33 mM SDS in water

The changes in absorbance and fluorescence over the duration of photolysis of **+EO_{C2}** with SDS at 11 mM (critical micelle concentration of SDS is 8.3 mM [45]) in water are shown below, in Figure 3.8.

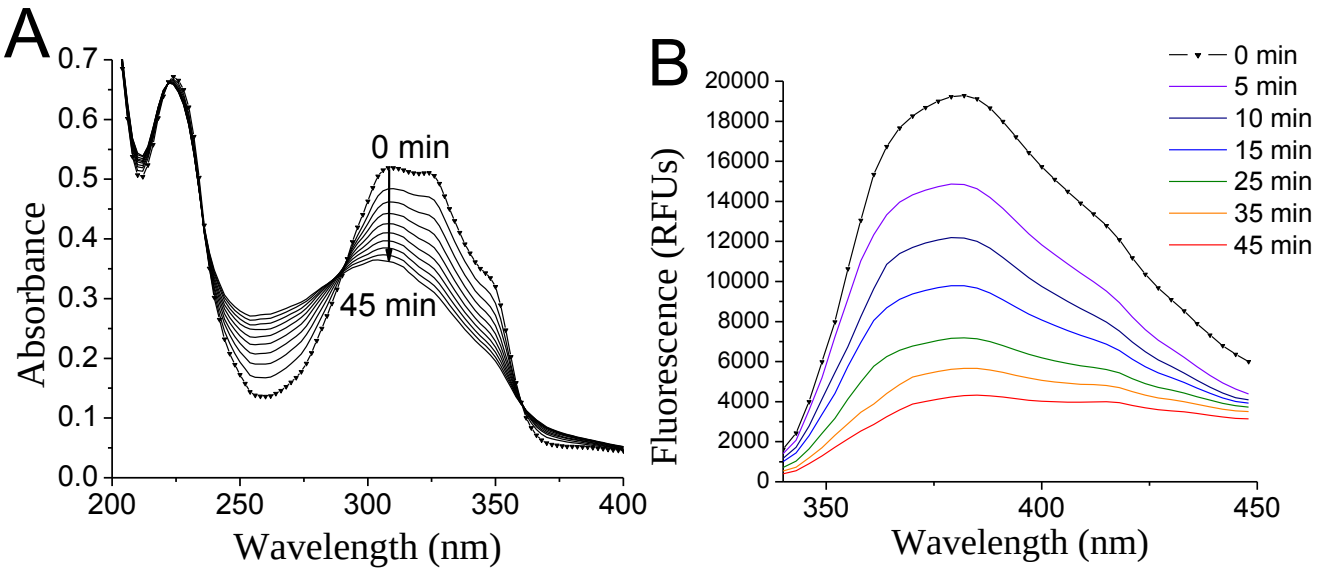

Figure 3.8. A. Absorbance and **B.** Fluorescence of **EO-2** throughout the duration of UVA photolysis (300-400 nm, 0.98 mW/cm^2) in 11 mM SDS (above the critical micelle concentration) in water

The changes in UV-Vis absorbance upon addition of SDS to +**EO$_{C2}$** in water are shown below, in Figure 3.9A**.** The enhanced fluorescence of both +**EO** and +**EO$_{C2}$** upon complexation with SDS micelles is observed, as shown below with +**EO$_{C2}$** in Figure 3.9B.

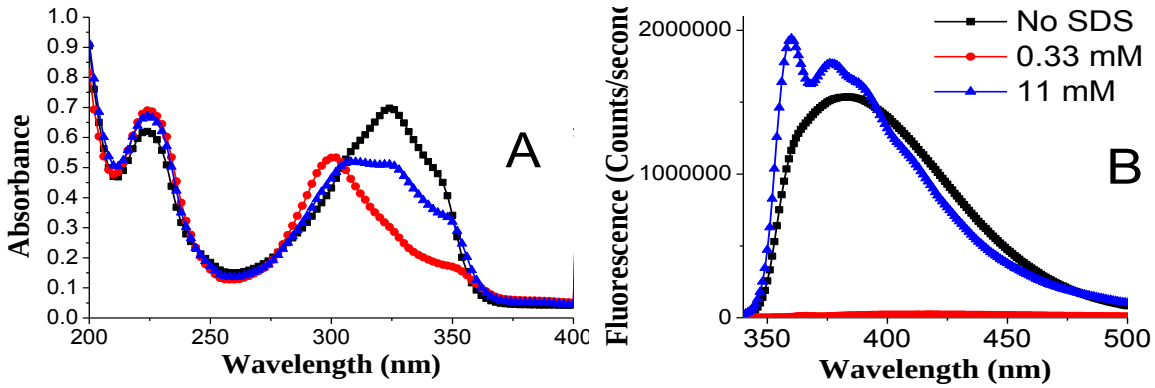

Figure 3.9. Change of **A.** Absorbance and **B.** Fluorescence of 16 µM +**EO$_{C2}$** with SDS added

There is a clear blue-shift in the absorbance and quenching of fluorescence of the sample with 0.33 mM SDS and +**EO$_{C2}$**, but as more SDS is added, the absorbance shifts back to the red while the fluorescence is enhanced. The fluorescence enhancement seen in the presence of the micelle is indicative of complexation.

The photolysis of **+EO$_{C2}$** and **+1H** in an aqueous solution of SDS at 10.4 mM revealed startling differences in their ability to be protected from photolysis. Comparing Figure 3.2 and Figure 3.8, one can clearly see that the compound **+EO$_{C2}$** completely photolyzes in 3 minutes without SDS, but with SDS at the CMC the absorbance and fluorescence spectra are still mostly unchanged after 45 minutes. In addition, the quantum yield of disappearance for **+EO$_{C2}$** was calculated to be 3.31 x 10^{-3}, 38.5% of the quantum yield without SDS (Table 3.3). The photolysis of **+1H**, on the other hand, does not appear to be altered by interactions with SDS micelles. In fact, there is little to no change in the absorbance spectrum of **+1H** when in the presence of SDS at any concentration near the CMC. As can be seen in the appendix (Figure A4), the photolysis of **+1H** seems to progress at the same rate with SDS at the CMC as without SDS. These results suggest that structural differences between OPEs can dictate their ability to become photo-protected by SDS micelles. [38]

One can observe rather pronounced changes in Figure 3.9A where absorption blueshifts initially, and then red-shifts near to the same wavelength of maximum absorbance as in solution without SDS. Similarly, looking at the change in fluorescence in Figure 3.9B**,** one can see a near-complete loss of fluorescence at the 0.33 mM SDS concentration. Once the concentration of SDS is brought near the CMC, however, the fluorescence is enhanced to become greater than the compound in water with no SDS added. This blue-shift in the main band and decreased oscillator strength when SDS is at the 0.33 mM concentration is consistent with the formation of an H-aggregate.[46] This complex formation is similar to that discussed in section 3.4.1.

3.5.2 *Molecular Dynamics Simulations*

In order to explain the experimental results, classical MD simulations were performed with sodium dodecyl sulfate and the OPEs shown in Scheme 3.1. The simulations were performed using Amber12[47-49] for simulation and AmberTools12 for system and parameter preparation, as described in the methods section. A summary of the different simulations performed and their size, number of atoms, and length of simulation is given in section 7.2.7.7 of the methods section (Chapter 7). Since simulation results from **+EO** were very similar to **+EO$_{C2}$**, the **+EO** results can be found in the appendix (Figures A5 and A6).

Pre-micellar aggregates between SDS and **+EO$_{C2}$** can be observed to form at and above a 1:1 molar ratio through the changes in absorbance and fluorescence seen in Figure 3.9. In

addition, we see in Figure 3.7 that the rate of photolysis for **+EO$_{C2}$** is reduced in a solution of pre-micellar SDS. Snapshots taken along the simulation trajectory reveal the formation of the complex between the **+EO** and the SDS using classical molecular dynamics are shown below, in Figure 3.10

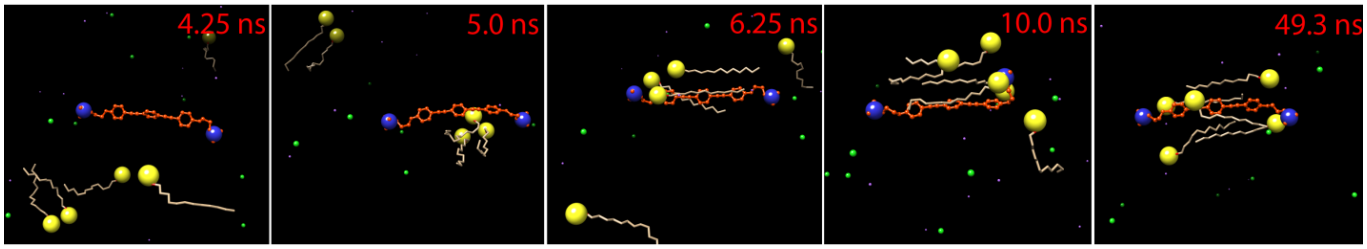

Figure 3.10. Timeline of the aggregation of 5 SDS molecules around an **+EO** in water

An image of the complex formed from the simulation of an **+EO$_{C2}$** with 6 SDS molecules is shown below, in Figure 3.11A**.** The number of waters within 3.4 Angstroms of the backbone of the OPE (all phenyl rings and triple bonds) are shown along the simulation trajectory in Figure 3.11B. Results from a similar simulation with 12 SDS molecules are given in Figure 3.12.

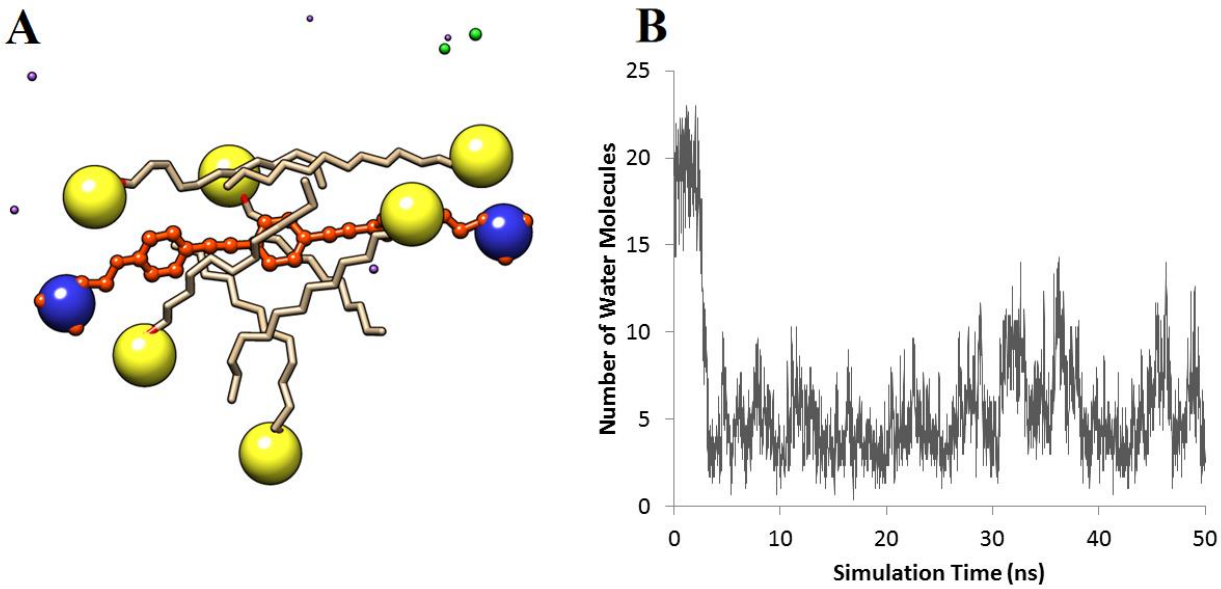

Figure 3.11. A. Image of complex resulting from 6 SDS molecules simulated with **+1H +EO$_{C2}$** molecule; Nitrogen atoms are shown in blue, Sulfur atoms in yellow, Chloride ions in green, and Sodium ions in purple. The OPE backbone is shown in orange. **B.** Number of water molecules within 3.4 Angstroms of the backbone of the OPE. [42]

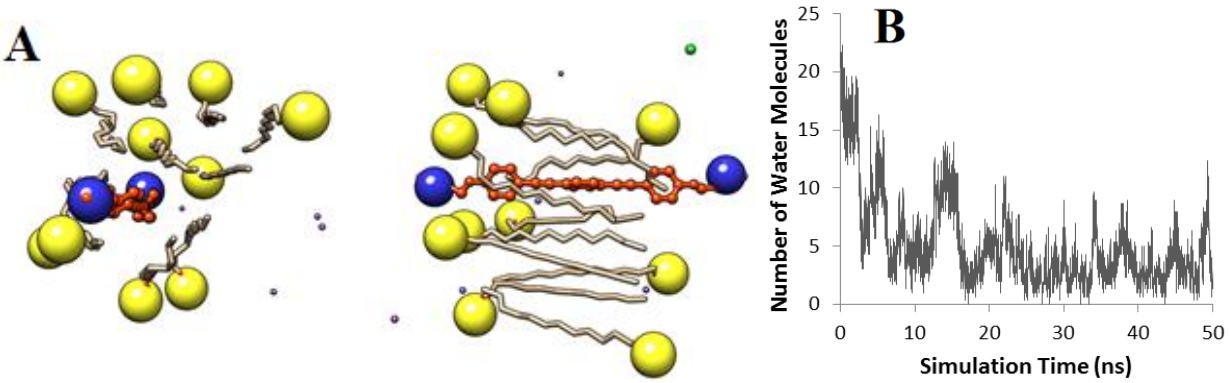

Figure 3.12. A. Image of complex resulting from 12 SDS molecules simulated with 1 **+EO$_{C2}$** molecule **B.** Number of water molecules within 3.4 Angstroms of the backbone of the OPE.

In Figures 4.10, 4.11 and 4.12, the formation of pre-micellar aggregates of **+EO$_{C2}$** and SDS molecules in water is shown. The interaction between **+EO$_{C2}$** and SDS is initiated by the attraction of the quaternary ammonium end-group on the OPE and the sulfate head-group of the SDS molecules. This is followed by a strong interaction between the backbone of the OPE and the tail of the SDS molecule which leads to the displacement of water. In Figure 3.11B, the number of water molecules in the first solvation shell (waters within 3.4 Angstroms) of the backbone of the OPE is shown along the simulation trajectory. It is clear from this figure that as the SDS molecules aggregate around **+EO$_{C2}$**, water is displaced, reducing the number of water molecules from 20 to an average of 5. The result is similar to that shown in Figure 3.12, where 6 additional SDS molecules are added to the simulation. This initial complex where the backbone is "solvated" by the SDS tails foreshadows the further displacement of water when complexed with an entire SDS micelle. Simulations with 2 **+EO$_{C2}$** molecules and 12 SDS molecules reveal dominant face-face interactions between the OPEs, as can be observed in Figure 3.9. This result from the classical MD simulations agrees with the conclusion that an H-aggregate is forming when the SDS:OPE ratio is relatively low (6:1). Since the photodegradation was decreased in micellar solution relative to pre-micellar solution, it was important to simulate the micellar system as well.

The structure of SDS micelles, while originally proposed to be a spherical bubble-shape[50], was shown to be a less-ordered structure of SDS molecules.[51] The average aggregation number for SDS above the critical micelle concentration has been shown to be 63.[52] More recently, the process of micelle formation has also been studied through the use of classical MD

simulations.[53] In addition to the formation of micelles from a randomized system of SDS and water, other studies have used classical MD to explore the interactions of peptides with SDS micelles.[54,55] In order to achieve coordinates for an SDS micelle, the study by Sammalkorpi et al.[53] was repeated using the methods described in chapter 7.[42] As was reported in the study, a 200 ns simulation at a 1M concentration yielded micelles of the appropriate aggregation number. A micelle consisting of 63 SDS molecules selected from the simulation trajectory is shown from two different angles in Figure 7.13 in the methods section. The coordinates of the SDS micelle were used for simulating the interactions of the OPEs.

Results of the simulation of **+EO$_{C2}$** with an SDS micelle are shown in Figure 3.13.

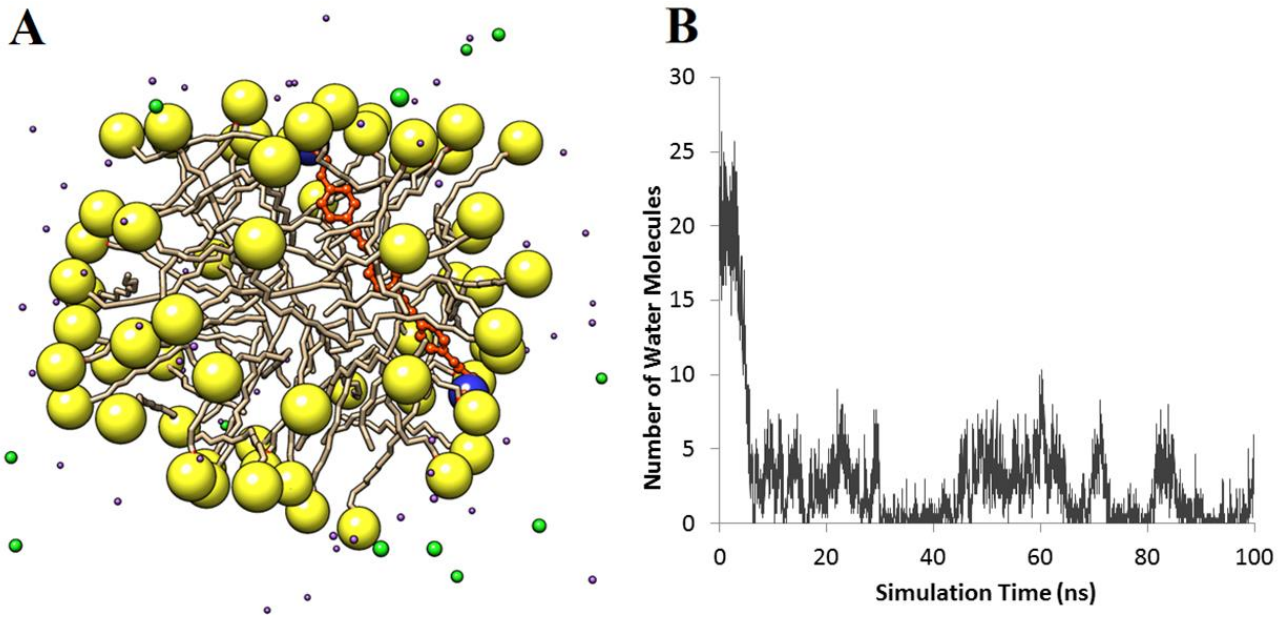

Figure 3.13. A. Snapshot of **+EO$_{C2}$** at 100 ns with an SDS micelle simulated at 303K in water. **B.** Number of water molecules within 3.4 Å of the backbone of **+EO$_{C2}$** throughout the simulation trajectory.

In Figure 3.13, **+EO$_{C2}$** first makes contact with the micelle through the ion-pair interactions between the quaternary ammonium end-group and the anionic head of a SDS molecule. Once the molecule is drawn close to the micelle through this ionic interaction, the backbone of **+EO$_{C2}$** is seen to "sink" into the interior of the micelle. By the end of a 100 ns simulation it is apparent that **+EO$_{C2}$** can bridge the width of a micelle by association of the cationic end-groups with the SDS head-groups, while the backbone of the molecule is solvated by the hydrocarbon in the interior of the micelle. It is clear from Figure 3.13A that the backbone of **+EO$_{C2}$** loses water upon insertion.

As shown in Figure 3.13B, there are initially ~20 water molecules within 3.4 Å of the backbone. Following intercalation of **+EO$_{C2}$** with the micelle, the number of waters can be seen to approach 0 for a significant portion of the simulation trajectory. These results show that as the phenylene ethynylene chromophore in **+EO$_{C2}$** is deeply buried in the micelle, there is little to no contact between it and water.

Results of the simulation of compound **+1H** with an SDS micelle are shown in Figure 3.14.

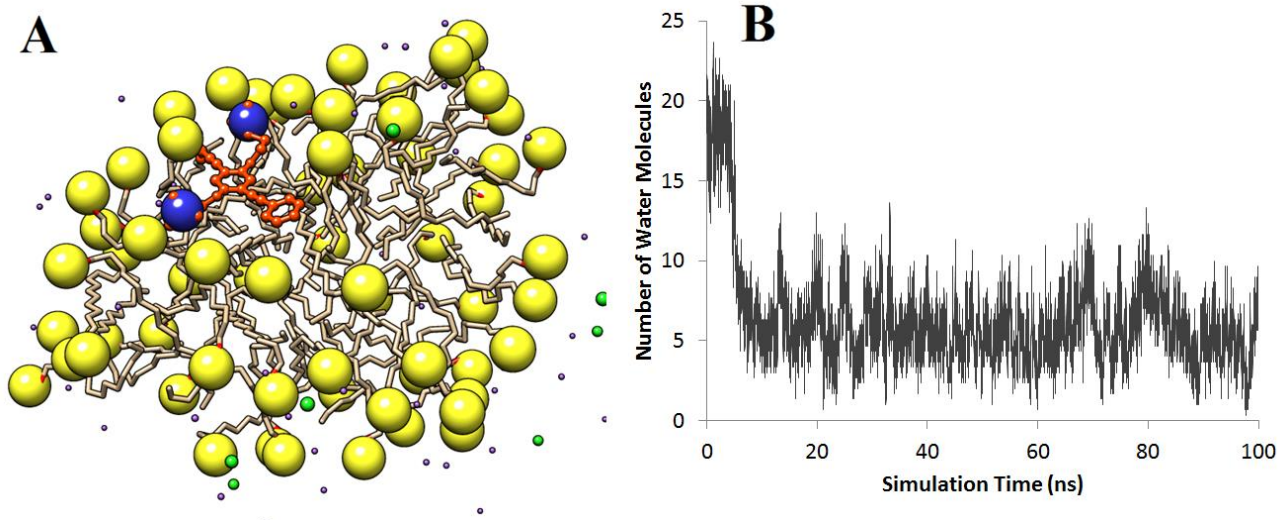

Figure 3.14. A. Snapshot of compound **+1H** simulated with an SDS micelle **B.** Number of water molecules within 3.4 Å of the backbone of **+1H** throughout the simulation trajectory. The average number of water molecules within 3.4 Å of the OPE Nitrogen atoms is 8.9.

The interactions of **+EO$_{C2}$** with the SDS micelle are very different than what is observed with **1**. As can be seen in Figure 3.14A, the OPE does interact with the SDS micelle. However, the interaction is largely restricted due to the OPE residing at the surface of the micelle and the interface between water and the micelle. While **+1H** occasionally dips part of the way into the micelle, the backbone of the molecule is never buried within the hydrocarbon to the same extent that **+EO$_{C2}$** is. As a result of this intercalation, **+EO$_{C2}$** and **+EO** have much less contact with water than **+1H.** This suggests that the removal of water from the vicinity of the OPE backbone may be the mechanism by which photolysis is prevented. As shown in Figure 3.14B, some water of solvation is lost when **+1H** begins to interact with the micelle, however many molecules of water remain within the first solvation shell. This suggests that the water that remains may be involved in the photolysis observed with compound **+1H** in the presence of SDS micelles.

The results from these simulations revealed that the end-only OPEs **+EO** and **+EO$_{C2}$**

interact quite differently with SDS than does compound **+1H**. The classical Molecular Dynamics simulations showed that as the SDS molecules clustered around the oppositely-charged OPE, the accessibility of the phenylene-ethynylene backbone to water is reduced due to steric hindrance from the hydrocarbon chains of the surfactant. The results of the classical MD simulations showed that the end-only OPEs are able to deeply penetrate and extend across the SDS micelles, whereas the non-end-only OPEs mostly associate with the micelle at the interface of the headgroups and water. Since the end-only OPEs are photoprotected by SDS micelles while **+1H** is not, it stands to reason that their intercalation in the micelle protects them from the photolysis. The simplest explanation for the protection is that the displacement of water from the neighborhood of the triple-bond will prevent the initial photoprotonation step for water or peroxide addition.

3.6 Conclusions and Outlook

In this study, the photochemistry of a model cationic oligomer was explored by studying changes in the UV-visible absorbance and fluorescence, determining quantum yields of disappearance, and characterizing products by high-resolution mass spectrometry in order to understand the effects of light exposure on these compounds in the presence of air and water. The main pathways of degradation were the photoprotonation of the triple bond followed by addition of water, addition of singlet oxygen across the triple-bond, and cleavage of the quaternary ammonium side-chains. The isotope effect of D_2O on the photoaddition of water revealed that the rate-limiting step of this pathway is protonation of the triple-bond. The changes in absorbance and fluorescence were significant, and a loss of solubility was observed upon the loss of the charged side-chains. Interestingly, the finding of consecutive and hybrid products shows that the primary products are also photoreactive and that PPE polymers may undergo similar reactions at several sites under prolonged irradiation in aqueous, aerated solution. While the efficiency of the photoreactions is low, their occurrence can be detrimental to the long-term use of OPEs in sensors and biocides. The results show that this is not likely to be a significant problem with some of the phenylene ethynylene polymers, as photodegradation is attenuated after an initial period.

The photochemistry of the end-only OPEs was also explored The major products observed followed the general trend that was established in the previous study of molecule **+1H**,

but with some important differences such as no cleavage of the alkylammonium chains and the prevalent formation of a peroxide adduct. In addition, the end only compounds were able to undergo photolysis in methanol to yield only the product of oxygen addition across the triple bond. The propensity for the end-only OPEs and the previously studied OPE to be protected from photolysis by SDS micelles was explored through classical molecular dynamics simulations. The results of the simulations revealed that the end-only OPEs deeply intercalated into the SDS micelles so that their backbones were "solvated" by the hydrocarbon of SDS tails, while the OPE **+1H** resided at the interface of the SDS head groups with the water in solution. This is experimentally verified in the finding that the end-only OPEs are "protected" from photodegradation compared to pure aqueous solution while compound **+1H** is not. The results of this study will be useful for the design of sensors, organic light-emitting diodes, and light-activated biocides.

3.7 References

(1) "Radiation". *Encyclopædia Britannica Online*. Retrieved 2009-11-09.
(2) Planck, M. Über eine Verbesserung der Wienschen Spektralgleichung. *Verhandlungen der Deutschen Physikalischen Gesellschaft* **1900,** *2*, 202–204.
(3) "Photochemical equivalence law". *Encyclopædia Britannica Online*. Retrieved 2009-11-07.
(4) Porter, G.; P. Suppan Primary photochemical processes in aromatic molecules. Part 12.—Excited states of benzophenone derivatives." *Transactions of the Faraday Society* **1965,** *61*, 1664-1673.
(5) Wooldridge, T.; Roberts, T. D. Vinyl Cations as Intermediates in Photohydration of Acetylenes. *Tetrahedron Lett.* **1973**, *14*, 4007-4008.
(6) Wan, P.; Culshaw, S.; Yates, K. Photohydration of Aromatic Alkenes and Alkynes. *J. Am. Chem. Soc.* **1982**, *104*(9), 2509-2515.
(7) Chiang, Y.; Kresge, A. J.; Capponi, M.; Wirz, J. Direct Observation of Acetophenone Enol Formed by Photohydration of Phenylacetylene. *Helv. Chim. Acta* **1986**, *69*, 1331-1332.
(8) Xu, M.; Chen, C. Z.; Wan, P. Intramolecular charge transfer in photoexcited hydroxyterphenyls: Evidence for formation of terphenyl quinone methides in aqueous solution. *J. Photochem. Photobiol. A* **2008**, *198*, 26-33.
(9) Foote, C.S. Photosensitized oxygenations and the role of singlet oxygen *Acc. Chem. Res.* **1968** *1* (4), 104-110
(10) Dam, N.; Scurlock, R. D.; Wang, B.; Ma, L.; Sundahl, M.; Ogilby, P. R.; Science, A. Singlet Oxygen as a Reactive Intermediate in the Photodegradation of Phenylenevinylene Oligomers. *Chem. Mat.* **1999**, 5344-5347.
(11) Sudeep, P. K.; James, P. V.; Thomas, K. G.; Kamat, P. V. Singlet and triplet excited-state interactions and photochemical reactivity of phenyleneethynylene oligomers. *J. Phys. Chem. A* **2006**, *110*, 5642-9.

(12) McIlroy, S. P.; Cló, E.; Nikolajsen, L.; Frederiksen, P. K., Nielsen, C. B.; Mikkelsen, K. V.; Gothelf, K. V.; Ogilby, P. R. Two-Photon Photosensitized Production of Singlet Oxygen: Sensitizers with Phenylene−Ethynylene-Based Chromophores *J. Org. Chem.* **2005,** *70* (4), 1134-1146
(13) Zhou, Z.; Corbitt, T. S.; Parthasarathy, A.; Tang, Y.; Ista, L. K.; Schanze, K. S.; Whitten, D. G. "End-Only" Functionalized Oligo(phenylene ethynylene)s: Synthesis, Photophysical and Biocidal Activity. *J. Phys. Chem. Lett.* **2010**, *1*, 3207-3212.
(14) Wang, Y.; Corbitt, T. S.; Jett, S. D.; Tang, Y.; Schanze, K. S.; Chi, E. Y.; Whitten, D. G. Direct Visualization of Bactericidal Action of Cationic Conjugated Polyelectrolytes and Oligomers *Langmuir* **2011**, *28*, 65-70.
(15) Tang, Y.; Corbitt, T. S.; Parthasarathy, A.; Zhou, Z.; Schanze, K. S.; Whitten, D. G. Light-induced antibacterial activity of symmetrical and asymmetrical oligophenylene ethynylenes *Langmuir* **2011**, *27*, 4956-62.
(16) Ji, E.; Parthasarathy, A.; Corbitt, T. S.; Schanze, K. S.; Whitten, D. G. Antibacterial activity of conjugated polyelectrolytes with variable chain lengths *Langmuir* **2011**, *27*, 10763-9.
(17) Ji, E.; Corbitt, T. S.; Parthasarathy, A.; Schanze, K. S.; Whitten, D. G. Light and dark-activated biocidal activity of conjugated polyelectrolytes. *ACS Appl. Mat. Int.* **2011**, *3*, 2820-9.
(18) Wang, Y.; Jett, S. D.; Crum, J.; Schanze, K. S.; Chi, E. Y.; Whitten, D. G. Understanding the dark and light-enhanced bactericidal action of cationic conjugated polyelectrolytes and oligomers. *Langmuir* **2013,** *29*(2), 781–92.
(19) Wang, Y.; Canady, T. D.; Zhou, Z.; Tang, Y.; Price, D. N.; Bear, D. G.; Chi, E. Y.; Schanze, K. S.; Whitten, D. G. Cationic phenylene ethynylene polymers and oligomers exhibit efficient antiviral activity. *ACS Appl. Mater. Interfaces* **2011**, *3*, 2209-14.
(20) Zhu, S. S.; Carroll, P. J.; Swager, T. M. Conducting Polymetallorotaxanes: A Supramolecular Approach to Transition Metal Ion Sensors. *J. Am. Chem. Soc.* **1996**, *118*, 8713-8714.
(21) Zhao, X.; Liu, Y.; Schanze, K. S. A conjugated polyelectrolyte-based fluorescence sensor for pyrophosphate. *Chem. Comm.* **2007**, 2914-2916.
(22) Thomas, S. W.; Joly, G. D.; Swager, T. M. Chemical Sensors Based on Amplifying Fluorescent Conjugated Polymers. *Chem. Rev.* **2007**, *107*, 1339-1386.
(23) Tang, Y.; Hill, E. H.; Zhou, Z.; Evans, D. G.; Schanze, K. S.; Whitten, D. G. Synthesis, self-assembly, and photophysical properties of cationic oligo(p-phenyleneethynylene)s. *Langmuir* **2011**, *27*, 4945-55.
(24) Tang, Y.; Achyuthan, K. E.; Whitten, D. G. Label-free and real-time sequence specific DNA detection based on supramolecular self-assembly. *Langmuir* **2010**, *26*, 6832-7.
(25) Pinto, M. R.; Schanze, K. S. Amplified fluorescence sensing of protease activity with conjugated polyelectrolytes. *Proc. Nat. Acad. Sci.* **2004**, *101*, 7505-10.
(26) Liu, Y.; Schanze, K. S. Conjugated Polyelectrolyte Based Real-Time Fluorescence Assay for Adenylate Kinase. *Anal. Chem.* **2009**, *81*, 231-239.
(27) Liu, Y.; Schanze, K. S. Conjugated polyelectrolyte-based real-time fluorescence assay for alkaline phosphatase with pyrophosphate as substrate. *Anal. Chem.* **2008**, *80*, 8605-12.
(28) Liu, Y.; Ogawa, K.; Schanze, K. S. Conjugated polyelectrolytes as fluorescent sensors. *J. Photochem. Photobiol. C* **2009**, *10*, 173-190.
(29) Kumaraswamy, S.; Bergstedt, T.; Shi, X.; Rininsland, F.; Kushon, S.; Xia, W.; Ley, K.; Achyuthan, K.; McBranch, D.; Whitten, D. Fluorescent-conjugated polymer superquenching facilitates highly sensitive detection of proteases. *Proc. Nat. Acad. Sci.* **2004**, *101*, 7511-5.

(30) Jiang, H.; Taranekar, P.; Reynolds, J. R.; Schanze, K. S. Conjugated polyelectrolytes: synthesis, photophysics, and applications. *Angew. Chem. Int. Ed.* **2009**, *48*, 4300-16.
(31) Achyuthan, K. E.; Bergstedt, T. S.; Chen, L.; Jones, R. M.; Kumaraswamy, S.; Kushon, S. A.; Ley, K. D.; Lu, L.; McBranch, D.; Mukundan, H.; Rininsland, F.; Shi, X.; Xia, W.; Whitten, D. G. Fluorescence superquenching of conjugated polyelectrolytes: applications for biosensing and drug discovery. *J. Mat. Chem.* **2005**, *15*, 2648-2656.
(32) Bunz, U. H. Poly(aryleneethynylene)s: Syntheses, Properties, Structures, and Applications. *Chem. Rev.* **2000**, *100*, 1605-44.
(33) Turro, N.J.; Cox, G.S.; Paczkowski, M.A. Photochemistry in micelles *Topics in Current Chemistry* **1985,** *129,* 57-97
(34) Braun, A.M.; Krieg, M.; Turro, N.J.; Aikawa, M.; Gould, I.R.; Graf, G.A.; Lee, P. C. C. Photochemical processes of benzophenone in microheterogeneous systems *J. Am. Chem. Soc.* **1981,** *103*(24)*,* 7312-7316
(35) Rao, B.N.; Turro, N.J.; Ramamurthy, V. Modification of chemical reactivity via inclusion complex formation: photochemistry of dibenzyl ketones and benzyl phenylacetates *J. Org. Chem.* **1986,** *51*(4)*,* 460-464
(36) Ramnath, N.; Ramesh, V.; Ramamurthy, V. Micellar structure and micellar control of photochemical reactions *J. Photochem.* **1985,** *31*(1)*,* 75-94
(37) Junqueira, H.C.; Severino, D.; Dias, L.G.; Gugliottia, M.S.; Baptista, M.S. Modulation of methylene blue photochemical properties based on adsorption at aqueous micelle interfaces *Phys. Chem. Chem. Phys.* **2002,** *4,* 2320-2328
(38) Hill, E. H.; Goswami, S.; Evans, D.G.; Schanze, K.S.; Whitten, D.G. Photochemistry of a Model Cationic p-Phenylene Ethynylene in Water *J. Phys. Chem. Letters* **2012,** *3*, 1363-1368.
(39) DeCosta, D. P.; Bennett, A.; Pincock, A. L.; Pincock, J. A.; Stefanova, R. Photochemistry of Aryl tert-Butyl Ethers in Methanol: The Effect of Substituents on an Excited State Cleavage Reaction. *J. Org. Chem.* **2000**, *65*, 4162-4168.
(40) Pincock, A. L.; Pincock, J. A. The structure, photochemical reactivity, and photophysical properties of adamantyl X-substituted aryl ethers and a comparison with the alkyl groups, methyl, tert-butyl, and allyl. *Canadian Journal of Chemistry* **2005**, *83*, 1237-1252.
(41) Hill, E. H.; Evans, D. G.; Whitten, D. G. The Influence of Structured Interfacial Water on the Photoluminescence of Carboxyester-terminated Oligo-p-Phenylene Ethynylenes J. Phys. Org. Chem. **2014,** DOI:10.1002/poc.3258
(42) Hill, E. H.; Evans, D. G.; Whitten, D. G. Photochemistry of "End-Only" Oligo-p-phenylene Ethynylenes: Complexation with Sodium Dodecyl Sulfate Reduces Solvent Accessibility *Langmuir* **2013** *29* (31), 9712-9720
(43) Hill, E. H.; Stratton, K.; Whitten, D. G.; Evans, D. G. Molecular Dynamics Simulation Study of the Interaction of Cationic Biocides with Lipid Bilayers: Aggregation Effects and Bilayer Damage. *Langmuir* **2012**, *28,* 14849−14854.
(44) C. Tan, M. R. Pinto and K. S. Schanze. Photophysics, aggregation and amplified quenching of a water-soluble poly(phenylene ethynylene) *Chem. Commun.* **2002,** 446-447
(45) Mukerjee, P.; Mysels, K. J.; Critical Micelle Concentration of Aqueous Surfactant Systems, *NSRDS-NBS 36*, US. Government Printing Office, Washington, D.C., *197*1.
(46) Rabinowitch, E.; Epstein, L. Polymerization of Dyestuffs in Solution *J. Am. Chem. Soc.* **1941,** 63, 69
(47) D.A. Case, T.A. Darden, T.E. Cheatham, III, C.L. Simmerling, J. Wang, R.E. Duke, R. Luo, R.C. Walker, W. Zhang, K.M. Merz, et al. AMBER 12 **2012,** University of California, San

Francisco.
(48) Goetz, A.W.; Williamson, M.J.; Xu, D.; Poole, D.; Le Grand, S.; Walker, R.C. Routine microsecond molecular dynamics simulations with AMBER - Part I: Generalized Born *J. Chem. Theory Comput.* **2012,** *8* (5), 1542-1555
(49) Salomon-Ferrer, R.; Goetz, A.W.; Poole, D.; Le Grand, S.; Walker, R.C. Routine microsecond molecular dynamics simulations with AMBER on GPUs. 2. Explicit Solvent Particle Mesh Ewald *J. Chem. Theory Comput.* **2013,** DOI: 10.1021/ct400314y
(50) Menger, F. M. On the Structure of Micelles *Acc*. *Chem*. *Res*. **1979,** *12*, *111*–117
(51) Russell, J. C.; Whitten, D. G.; Braun, A. M. Hydrophobic-hydrophilic interactions in sodium dodecyl sulfate micelles. Stilbene-viologen complex formation as a probe of the micelle interior *J. Am. Chem. Soc.* **1981,** *103*, 3219-3220
(52) Turro, N.J.; Yekta, A. Luminescent Probes for Detergent Solutions. A Simple Procedure for Determination of the Mean Aggregation Number of Micelles *J. Am. Chem. Soc.* **1978,** *100*, 5951
(53) Sammalkorpi, M., Karttunen, M., & Haataja, M. Structural properties of ionic detergent aggregates: a large-scale molecular dynamics study of sodium dodecyl sulfate *J. Phys. Chem. B* **2007,** *111*(40), 11722–33.
(54) Khandelia, H., Langham, A. a, & Kaznessis, Y. N. Driving engineering of novel antimicrobial peptides from simulations of peptide-micelle interactions. *Biochimica et Biophysica Acta* **2006,** *1758*(9), 1224–34.
(55) Khandelia, H., & Kaznessis, Y. N. Molecular dynamics simulations of helical antimicrobial peptides in SDS micelles : What do point mutations achieve? *Peptides* **2005,** *26*, 2037–2049.

Chapter IV: INTERACTIONS WITH BACTERIAL CELLS I: MODIFYING THE BIOCIDAL PROPERTIES OF OPES THROUGH SURFACTANT COMPLEXATION

4.1 Introduction

4.1.1 Mechanisms and Previous Biocidal Work with OPEs

Recently, the Whitten and Schanze groups have developed a class of compounds based on the *p*-Phenylene Ethynylene backbone, with end-chain and side-chain functionalization for the purpose of solubility or covalent modification for grafting onto surfaces and fibers.[1] These compounds were originally developed as sensors[2], but several types of cationic oligo-*p*-phenylene ethynylenes (OPEs) were found to be effective light-activated biocides against both Gram-positive and Gram-negative strains of bacteria.[3-5] In the dark, OPEs have been shown to induce dye leakage and liposome disruption in bacterial membrane mimics, and a computational study suggests that the larger oligomers induce pore formation in the membrane.[5-7] OPEs efficiently sensitize the generation of singlet oxygen upon the absorption of light, leading to the formation of reactive oxygen species (ROS). In a recent study, major changes to the bacterial structure were observed upon exposure to the OPEs, resulting from ROS- induced damage to proteins and nucleic acids in the light, as well as the release of cellular contents from membrane damage.[5] Both of these mechanisms of biocidal action are broad-spectrum, and kill bacteria with similar effectiveness regardless of antibiotic resistance. In addition, it is unlikely that bacteria would evolve a resistance to these compounds due to the non-specific nature of the killing mechanisms. A broader overview of the biocidal mechanisms at play and the processes involved in antimicrobial resistance is given in the introduction, Chapter 1.

4.1.2 Light-activation: a double-edged sword

Recent studies have shown that the OPEs are susceptible to photodegradation in water and air, which foreshadows the possible problem of loss of biocidal activity in long-term usage.[8,9] Zhijun Zhou and coworkers synthesized a class of "end-only" OPEs, which are functionalized on the ends of the phenylene-ethynylene backbone, and show remarkable biocidal activity.[10] The "end-only" OPEs are also particularly susceptible to photodegradation, with quantum yields of disappearance approaching 1% in water.[9] As discussed in the previous chapter (4.3), the mechanism of photoreactivity is the addition of water or oxygen across one of the ethynyl groups. While the biocidal activity of these compounds is strong, the quick photodegradation

observed without bacteria under the same light source (section 4.3) calls into question the biocidal processes that are taking place over the course of an experiment, and whether or not the OPE would be able to perform over a prolonged period of time.

The need to irradiate these photosensitive compounds is, in effect, a double-edged sword if the same light that induces biocidal activity also destroys the biocide. To this end, the effect of surfactant complexation on photostability of the OPE was assessed, and is discussed in section 3.5. The results showed that a photostable complex was formed between the OPE and surfactant, but the resulting effects on biocidal activity were not initially known. It was not clear from the outset whether the cationic OPE would bind to the net-anionic bacterial membrane as well when complexed with the anionic detergent SDS. In this section the effects of photodegradation and surfactant-induced aggregation on the biocidal effectiveness of the OPEs is discussed. To avoid repetition, the structures of OPEs are given in the previous chapters of this thesis.

4.2 Effects of Prolonged Irradiation on Biocidal Activity of OPE

The cationic end-only OPE **+EO$_{C2}$** was irradiated with UVA (~365 nm) at a power of 0.975 μw/cm^2 as described in the methods section (Chapter 7), for times of 30, 60, and 120 minutes. The solution was then added to a bacterial culture of either *S. aureus* or *E. coli* to result in a final OPE concentration of 10 μM and a final bacterial concentration of 1*10^7 cells/mL, and the samples were then irradiated again for 30 minutes for *E. coli* and 15 minutes for *S. aureus* prior to live/dead staining and analysis by confocal fluorescence microscopy and flow cytometry. The results of the live/dead assay as a function of pre-irradiation time are given in Figure 4.1. Confocal fluorescence microscopy images of E. coli exposed to the **+EO**$_{c2}$-SDS complex after 2 hours UVA of irradiation prior to biocidal testing are given in Figure A7 of the Appendix.

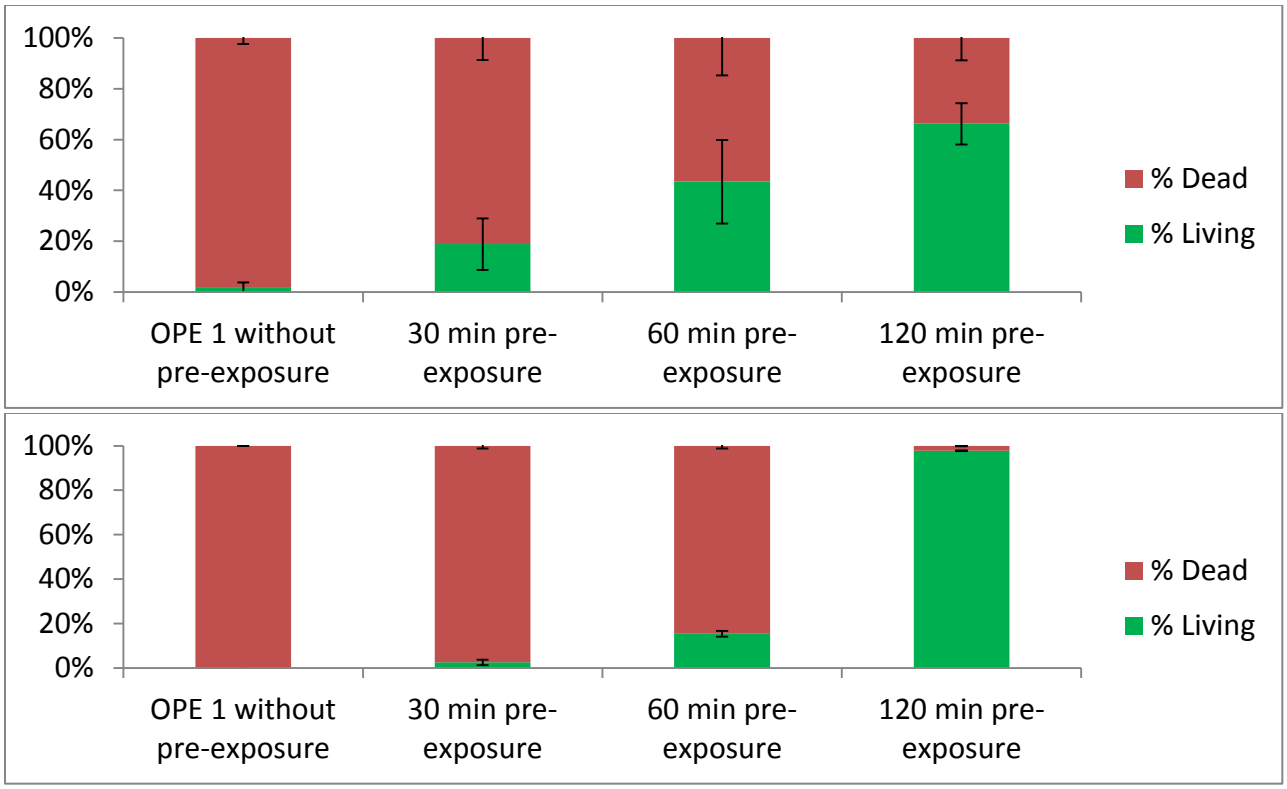

Figure 4.1. Biocidal activity of +$\mathbf{EO_{C2}}$ vs. (Top) E.coli, and (Bottom) *S. aureus* with samples irradiated for 0, 30, 60, or 120 minutes prior to bacterial exposure under UVA.

The results of the live/dead assay carried out using flow cytometry reveal a significant drop in biocidal activity of +$\mathbf{EO_{C2}}$, even after only 30 minutes of UVA irradiation prior to bacterial exposure. While this drop in biocidal activity is significant, there is a much quicker decrease in absorbance and fluorescence upon irradiation. It was shown (Figure 3.2) that within 2 minutes of photolysis under the same conditions, the absorbance of the compound was observed to diminish and the fluorescence was completely quenched.[9] However, as shown in Figure 4.1 there was still some biocidal activity at 30 minutes and beyond. This suggests that the initial photoproducts may still be biocidal, and may continue to function for a time, albeit less efficiently. However, by 2 hours of pre-exposure the biocidal activity is nearly lost for *E. coli*, and entirely lost for *S. aureus*. This result confirms that these compounds can be rendered harmless against bacteria with prolonged exposure to UVA light.

Since +$\mathbf{EO_{C2}}$ is very photolabile as discussed in section 4.1.2, it is reasonable to test the effects of photodegradation on the biocidal effectiveness of an OPE which has a much longer time before photodegradation is apparent. The photochemistry of the n=2 OPE +**2H** is discussed in section 4.5, and the time needed for complete degradation as measured by UV-Vis absorbance

spectra is in excess of 24 hours. The biocidal activity of this OPE was assessed against the bacteria *P. aeruginosa*, which is also a known candidate for antibiotic-resistant hospital-acquired infections. The samples of **+2H** were irradiated as described above for 0, 2, 6, and 12 hours and then mixed with *P. aeruginosa* and irradiated again for 30, 60, or 120 minutes. The results of live/dead analysis by flow cytometry using Syto21 and propidium iodide are shown in the Appendix, in Figure A11.

As was observed with the smaller "end-only" OPE, **+EO**, in Figure 3.1, a loss of biocidal activity is observed as the length of the photolysis time increases. In the case of **+2H**, the biocidal activity drops off roughly proportional to the change in absorbance spectrum seen in Figure 3.4. The results given in this section clearly show that the prolonged irradiation of OPEs results in a compromised ability to kill bacteria upon UVA exposure. It is likely that the resulting products do not have a significant absorption cross-section to produce singlet oxygen as they tend to absorb in the UV rather than the 325-370 region occupied by the OPEs, or that the products do not otherwise have a significant proportion of excited triplet states to generate singlet oxygen. In an effort to stave off the lost biocidal activity resulting from the photodegradation of the OPEs, the complexes of OPE and surfactant which were previously shown to be stable under long irradiations due to removal of interfacial water (sections 2.4 and 3.5) are tested for their biocidal properties against *S. aureus* and *E. coli*.

4.3 Photostable OPE-SDS Complexes Induce Killing throughout Long Irradiations

The previous chapter focused on the photo-protective effect observed upon complexation of the OPEs with sodium dodecyl sulfate (SDS), an anionic surfactant.[9] The complex was formed with SDS either at the critical micelle concentration (8.3 mM) or below it at 0.33 mM, and in both cases a profound decrease in photoreactivity was observed. With assistance of classical Molecular Dynamics, this decrease in photoreactivity was attributed to the desolvation of the OPE backbone. The mixing of+$\mathbf{EO_{C2}}$ with SDS led to a highly photostable complex, but the biocidal activity of this complex was not known, nor was it clear what effects the surfactant would have on the biocidal activity of the OPE. In this section we explore the biocidal activity of the complex formed with+$\mathbf{EO_{C2}}$ and SDS against both Gram-negative and Gram-positive bacteria using flow cytometry and confocal fluorescence microscopy, focusing on the changes in

biocidal activity incurred with prolonged irradiation. The results of this study revealed whether these complexes can adequately protect the OPE from prolonged exposure to UVA light, while still maintaining a high light-activated biocidal activity against *Escherichia coli* and *Staphylococcus aureus*. The methods used can be found in Chapter 7.The bacterial killing of *E. coli* and *S. aureus* by +**EO**-SDS as a function of pre-irradiation time is shown below in Figure 4.3**.**

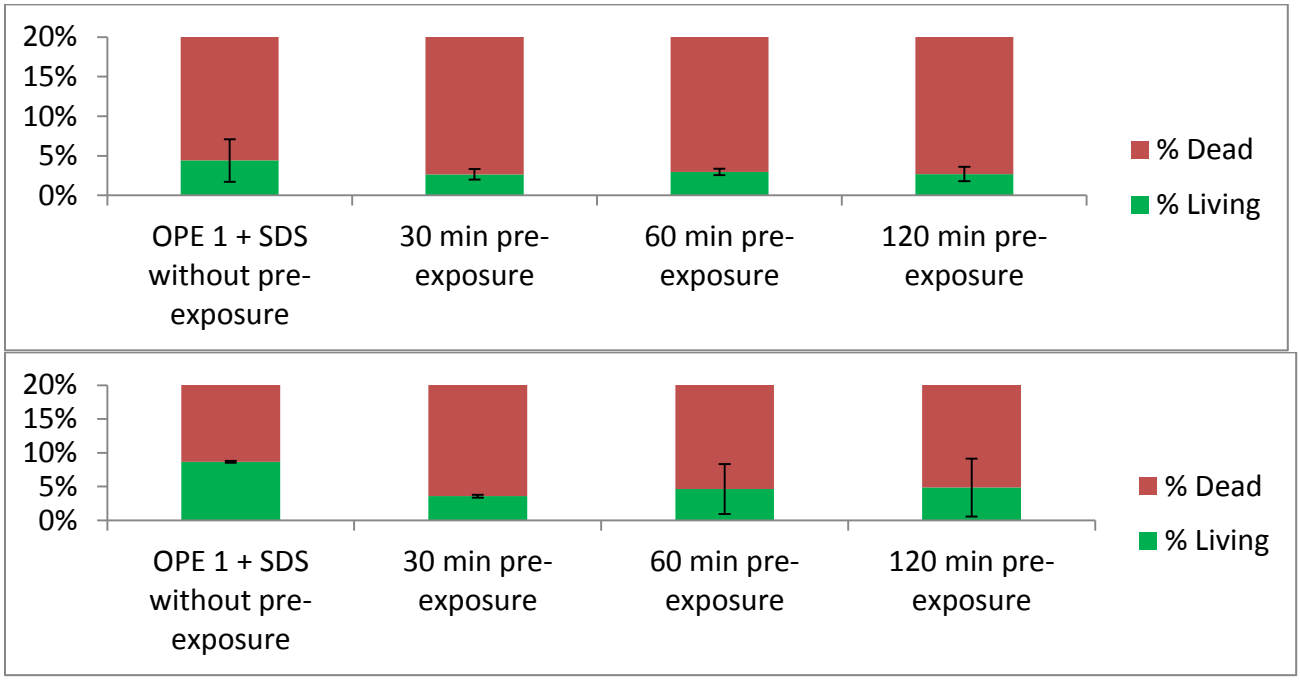

Figure 4.3. Biocidal activity of **+EO$_{C2}$ -SDS** vs. (Top) *E. coli*, and (Bottom) *S. aureus* with samples irradiated (300-400 nm, 0.98 mW/cm^2) for 0, 30, 60, or 120 minutes prior to bacterial exposure. The exposure times were 30 minutes for *E. coli* and 15 for *S. aureus*. Note that the y-axis maximum is set to 20% live bacteria.

The results shown in Figure 4.3 reveal that the **+EO$_{C2}$** -SDS complex is able to effectively kill both *S. aureus* and *E. coli* despite prolonged UVA irradiation prior to bacterial exposure. The killing effectiveness of both *E. coli* and *S. aureus* was maintained at more than 95% , even after two hours of irradiation. This result is significant, as it supports the use of molecular self-assembly of surfactants onto OPEs to confer resistance to photodegradation. The structure of the aggregate is likely an H-aggregate with interfacial water removed by the interaction with the hydrocarbon tails of SDS. SDS does not absorb light in the UVA region, nor should it react with singlet oxygen that is produced. Thus, complexation with SDS allows the OPEs to maintain their biocidal activity while being protected from photolysis.

It should be noted that while SDS itself is bactericidal to both *E. coli* and *S. aureus* at the critical micelle concentration (~8.3 mM [11]), a low level of killing is observed at the 40 μM concentrations used for complex formation. In addition, it was observed in the control experiments that the two bacteria exhibit different levels of resistance to SDS. As shown in Figure A8 in the Appendix, *S. aureus* was observed to be viable in the presence of 0.33 mM SDS, yet this concentration was sufficient to achieve significant killing of *E. coli*. 40 μM SDS killed ~40% of the *E. coli* cells (Figure A9). In order to avoid this loss of viability in future studies, it may be useful to assess the performance of a surfactant with less innate biocidal activity, such as a phospholipid. The complexes between OPE and phospholipids has already been shown to be viable, but effects on biocidal activity have not yet been examined. This may be worth looking at in future studies of biocides. When comparing *S. aureus* and *E. coli*, it is clear that *S. aureus* is much more resistant of the effects of SDS. In light of this fact and the close relation of Rosenbach *S. aureus* to methicillin-resistant *S. aureus* (MRSA), *S. aureus* serves as a useful model organism for this study as it reveals the biocidal activity of the **+EO$_{C2}$** -SDS complex without any bias from killing by SDS.

Overall, both strains of bacteria undergo ~5-10% less killing with the **+EO$_{C2}$** -SDS complex compared with**+EO$_{C2}$** alone. In the case of *E. coli*,**+EO$_{C2}$** has 99% killing, while the **+EO$_{C2}$**-SDS complex exhibits just 95% killing. Against *S. aureus* the results are similar, with >99% killing for **+EO$_{C2}$** and 95% for the **+EO$_{C2}$**-SDS complex. With longer irradiations, the total killing will increase, as the *E. coli* and *S. aureus* were only irradiated with the samples for 30 and 15 minutes, respectively. However, it is difficult to determine whether this reduction in killing is simply due to a remainder of healthy bacteria or whether different phases of cell growth that are induced by stress contribute to this total. The ~5% reduction in killing of the complex may also result from electrostatic repulsion between the SDS molecules in the complex and the anionic lipids in the bacterial membrane. In order to further explore the possible modification of the attraction of an OPE-surfactant complex to the membrane surface, a biocidal study involving an anionic OPE and a cationic surfactant was carried out.

4.4 Enhancement of the Biocidal Activity of a Non-Biocidal Anionic OPE

The prior section used the surfactant sodium dodecyl sulfate to form a complex with a cationic oligo-*p*-phenylene ethynylene (OPE), protecting it from photodegradation over long irradiations

and allowing the retention of antimicrobial activity despite high doses of UVA prior to bacterial exposure.[12] Additionally, it was previously observed that anionic and cationic OPEs from this series form similar complexes with oppositely charged surfactants through spectroscopic measurements.[13] The anionic OPEs have been previously shown to be very weakly biocidal, with –EO giving 10-30% killing of *E. coli* and *S. aureus*.[10] In light of these results, the biocidal activity of an anionic OPE was compared with that of an OPE-surfactant complex.

The biocidal activity of the anionic OPE **-EO**, TTAB, and a 1:4 complex between **-EO** and TTAB were compared for both Gram-positive *S. aureus* and Gram-negative *E. coli* by flow cytometry, standard plating techniques, and confocal fluorescence microscopy. This study describes the influence that complexation with an oppositely-charged surfactant has on the biocidal activity of an anionic OPE. The OPE and TTAB both have a low level of biocidal activity on their own at the micromolar range of concentrations used. It was unexpected that the addition of the two reagents to form a complex would result in a significant shift in bactericidal properties. In order to provide additional support for the confocal fluorescence microscopy and flow cytometry analysis of live/dead bacteria, standard plating techniques were used to assess killing. The full details of the methods used can be found in section 7.1.3. The results of biocidal testing for *S. aureus* and *E. coli* using standard plating techniques is shown in Figure 4.4, below.

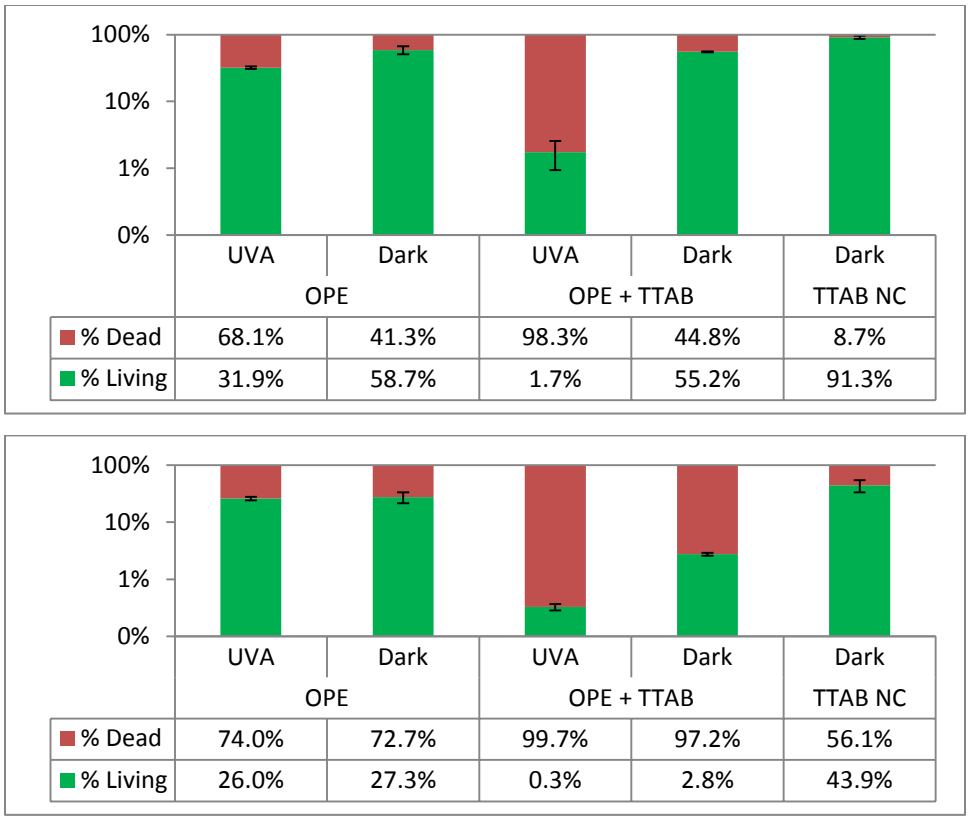

Figure 4.4. Viability of (Top) *S. aureus* and (Bottom) *E. coli* in logarithmic scale after one hour of exposure to **-EO**, TTAB, or the **-EO**-TTAB complex. Viability is calculated relative to that of a negative control exposed to UVA light for 1 hour (300-400 nm, 0.98 mW/cm^2).

The –EO to TTAB ratio was kept at a 1:4 ratio so that complex formation is assured and the concentration of TTAB (40µM) is mostly non-biocidal. This concentration is far below the reported values (5 mM) for the minimum inhibitory concentration of TTAB against both *S. aureus* and *E. coli*.[14] In Figure 4.4 it is shown that only 8.7% of Gram-positive *S. aureus* was killed by TTAB alone. Higher killing is observed with *E. coli* (Figure 2, 56.1%) than with *S. aureus*. This differences between killing of Gram-positive and Gram-negative bacteria by surfactant has also been observed previously with SDS.[12] As the concentration of TTAB used (40 µM) is far below the critical micelle concentration (4.3 mM)[15], the biocidal activity is relatively low and allows study of the effect of complexation of OPEs without a significant bias due to killing by TTAB.

The anionic OPE alone did exhibit modest biocidal activity against both strains of bacteria in both light and dark. As shown in Figure 4.4, 10 µM **-EO** killed 68.1% of *S. aureus* in

the light and 41.3% in the dark. It is worth noting that immediate killing observed by Flow cytometry showed lower killing than standard plating techniques, with 34.1% killed under UVA irradiation and 23.2% in the dark. Interestingly, the biocidal activity of **-EO** alone was higher against *E. coli*, with 74% killed under UVA and 72.7% killed in the dark. It is reasonable that the biocidal activity of this compound is low, as this has been previously shown for anionic OPEs.[10] It has been also shown with *in vitro* studies of model membranes that the anionic biocides do not affect the integrity of the membrane.[6] This is likely the result of unfavorable electrostatic interactions between the **-EO** and the net-anionic bacterial membrane, which would result in the repulsion of the **-EO** sulfonates from the negatively-charged lipids.

The complex between the **-EO** and TTAB showed significant enhancement of biocidal activity under UVA irradiation compared to either **-EO** or TTAB alone. As shown in Figure 4.4, 98.3% of *S. aureus* were killed by the –EO -TTAB complex in the light. The killing in the dark was significantly lower (44.8%), with little change from the dark killing observed with the OPE alone. Against Gram-negative *E. coli*, the complexation with TTAB resulted in significant enhancement of both light and dark killing, as shown in Figure 4.4. Under UVA irradiation, the **-EO** -TTAB complex resulted in a 3 log reduction of bacteria, with 99.7% dead. Even in the dark, significant enhancement was observed, with 97.2% of *E. coli* killed by the **-EO** -TTAB complex. The concentration of 10 μM **-EO** is reduced by a factor of 10 to 100 compared to the concentrations that have been reported for 4-6 log killing for this class of compounds, and these levels could easily be reached with an increase of the OPE concentration.

In addition to the live/dead analysis by flow cytometry and standard plating techniques, confocal fluorescence microscopy was used as described in the methods section to visualize and verify the biocidal measurements. Images of *S. aureus* which highlight the differences between the OPE alone and the OPE-TTAB complex are shown below, in Figure 4.4. Images with *E. coli* are given in the Appendix (Figures A10 and A11).

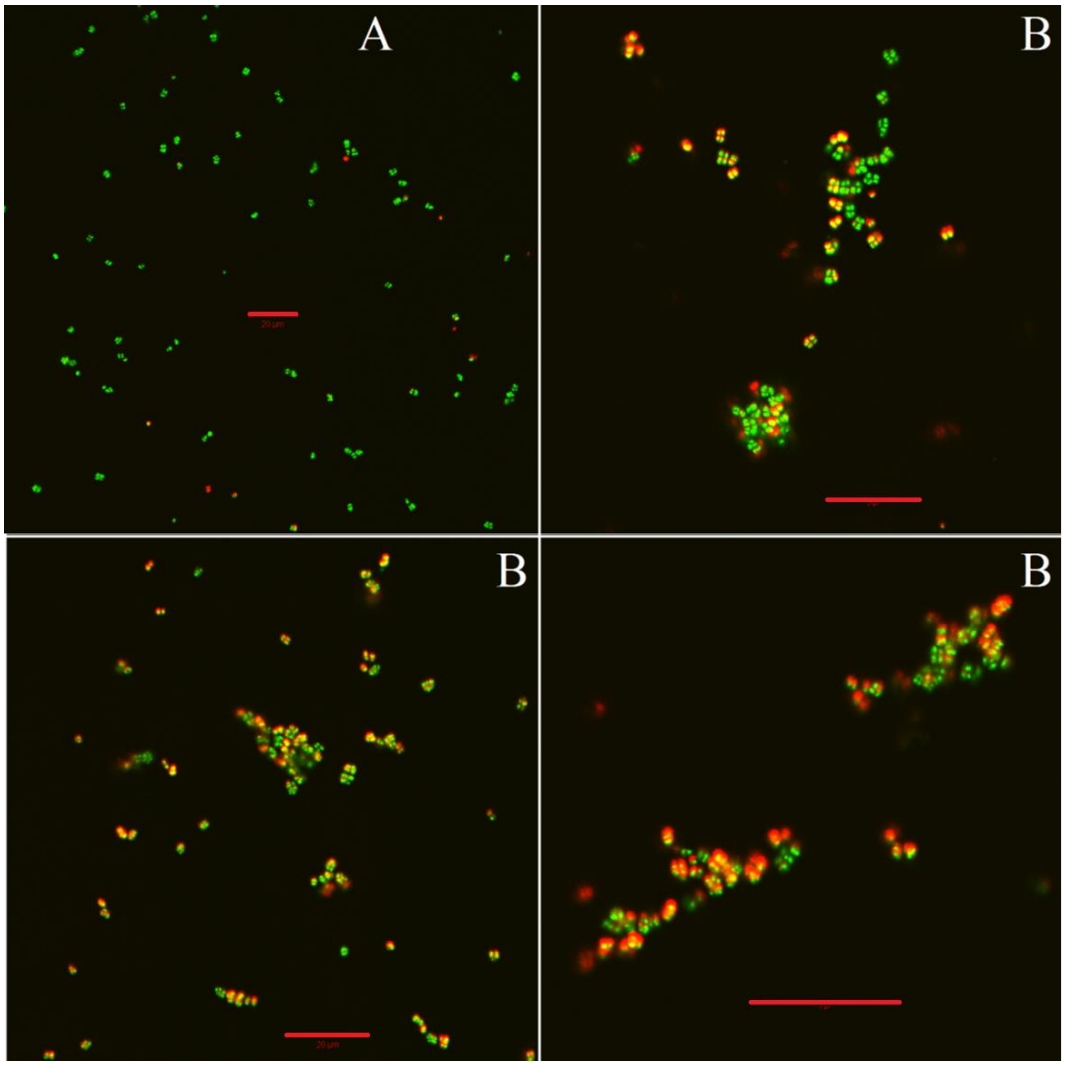

Figure 4.5 Confocal Fluorescence Microscope Image of *S. aureus* after 1 hour of UVA irradiation (300-400 nm, 0.98 mW/cm^2) with (A) –EO; (B) with –EO - TTAB complex. The green color indicates live stain SYTO 21, and the red color indicates dead stain propidium iodide. The red scale bar in each image is 20 µM.

The images in Figure 4.5 give a visual representation of what the results in Figure 4.4 show quantitatively. Figure 4.5 shows a clear increase in clumping and presence of the red color indicating the dead stain propidium iodide has intercalated with nucleic acids in a compromised cell. In addition, the dead cells shown in the B panels have a diffuse aura which suggests the cells no longer have a defined structure due to membrane deformation and/or leakage of contents. These results suggest that the surfactant enhances the ability of the anionic OPE to associate with the cell membrane, particularly in the case of Gram-negative *E. coli*. Since the

primary mechanism of light-induced biocidal activity is singlet-oxygen generation leading to reactive oxygen species (ROS), and singlet-oxygen has a very short lifetime in water, close proximity to the cell is essential.[16] Bacterial cell membranes are net-anionic, and it is likely that the reason the anionic compound is not an effective biocide is that it cannot get close enough to affect the cell membrane with ROS.[17-19] Based on the results of this study one can predict that a layer of cationic surfactant surrounding the OPE provides the electrostatic attraction needed to bring the complex into close proximity of the membrane. The increased killing of *E. coli* (56%) by the TTAB alone compared to *S. aureus* (9%) suggests that the interactions between TTAB and the Gram-negative bacterial membranes are greater. In addition, the dark biocidal activity of the **-EO**-TTAB complex was enhanced with *E. coli* but not with *S. aureus*. This is reasonable, as the structure of the Gram-positive cell wall is more complex, and the thick peptidoglycan outer layer may serve as a greater barrier to entry to the plasma membrane.[20] The outer membrane of the Gram-negative cell wall is known to contain negatively-charged lipids such as glycerophospholipids, and these would readily associate with the quaternary ammonium headgroup of TTAB. In addition, it is likely that the TTAB is involved in a cation exchange process with the lipids in the Gram-negative bacterial membrane. This suggests that the enhancement of biocidal activity observed is the result of increased interactions between the OPE and the membrane due to the cationic TTAB layer.

While close proximity is enough to significantly enhance biocidal activity in the light, there may be additional mechanisms for the biocidal enhancement in both light and dark. In-vitro studies of bacterial membrane mimics also show that the anionic OPEs do not induce membrane damage. It has been suggested in an earlier section that the structure of the **-EO**-TTAB complex consists of the aliphatic backbone of several TTAB molecules solvating the backbone of the OPE, while the quaternary ammoniums of the TTAB are associated with the sulfonate groups of the OPE. With this structure, it is likely that TTAB molecules are able to associate on the periphery of the complex without electrostatic association with the OPE sulfonates, due to favorable hydrophobic interactions between the hydrocarbon tails of the TTAB. This net-cationic complex would strongly interact with the net-negative bacterial membrane.

If incorporation of the **-EO** -TTAB complex into the membrane occurs, it would be likely that the TTAB would "dissolve" into the fluid environment of lipids in the membrane. Once disassociated from its "shield" of TTAB, the OPEs would repel the negative lipids in the

membrane. There are two mechanisms by which this could enhance biocidal activity. First, the repulsion of lipids in the membrane may cause instabilities that lead to membrane disruption or leakage, ultimately causing cell death. As the **-EO** is repelled, it may be ejected from the membrane into the cytoplasm or periplasm, where it would then be able to easily damage cytoplasmic contents with ROS when irradiated. This proposed mechanism of enhanced biocidal activity is shown in the schematic in Figure 4.6.

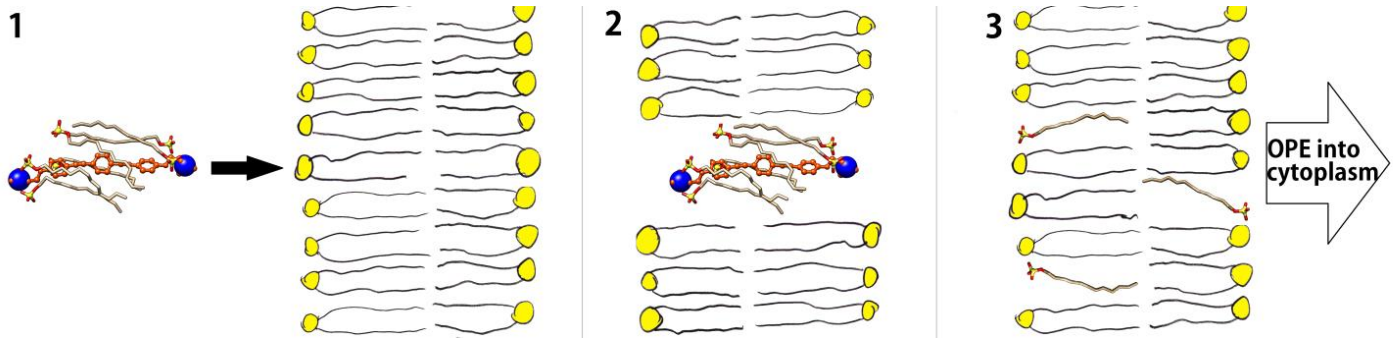

Figure 4.6. Schematic of the proposed mechanism behind enhancement of light-activated biocidal enhancement. 1: The **-EO** -TTAB complex is formed and added to the solution with the bilayer (lipids shown with yellow headgroups). 2: The **-EO** -TTAB complex, with net-positive charge, intercalates with the anionic lipid bilayer. 3: The TTAB from the complex dissociates into the bilayer and associates with anionic lipids; this results in repulsive electrostatic force between the OPE and the bilayer, ejecting it from the membrane into either the periplasmic space (for Gram-negative bacterial outer membranes) or the cytoplasm.

The enhanced ability of the **-EO** -TTAB complex to kill both Gram-negative and Gram-positive bacteria over either **-EO** or TTAB alone suggests that the TTAB plays a role in transporting the OPE to a site where it can induce damage. The development of colloidal particles or vesicles to transport compounds has been well-studied for the purpose of enhanced drug-loading for drug delivery.[21,22] Many delivery strategies are developed to generally enhance uptake of drugs through different routes, such as oral or topical.[23-25] The use of surfactants to enable transport across biological membranes has been recently studied for delivery of cargo to specific regions, such as the brain.[26] These studies highlight the importance of colloidal effects for modifying the interactions between small molecules of interest and biological barriers such as membranes. This study shows through the enhancement of biocidal activity of a singlet-oxygen sensitizer

with a simple bacterial model that ionic surfactants and the resulting colloidal particles formed could be used for transmembrane delivery of ionic compounds.

4.5 Damage-induced Stress Responses of Bacteria to OPEs

In the course of conducting biocidal experiments and examining the results through confocal fluorescence microscopy, several interesting features were observed when the OPEs were exposed to the bacteria. These features were found particularly in the light and in conditions where bacterial killing is high, but did not occur when cell lysis was induced using ethanol or Triton X-100. In this section, these features are discussed and possible explanations for their occurrence are given.

4.5.1 Increased Filamentous E. coli Cells

Confocal fluorescence microscopy revealed that *E. coli* cells exposed to **+EO$_{C2}$** or **+EO$_{C2}$**-SDS were more likely to undergo filamentous growth than untreated cells, as is shown in Figure 4.7.

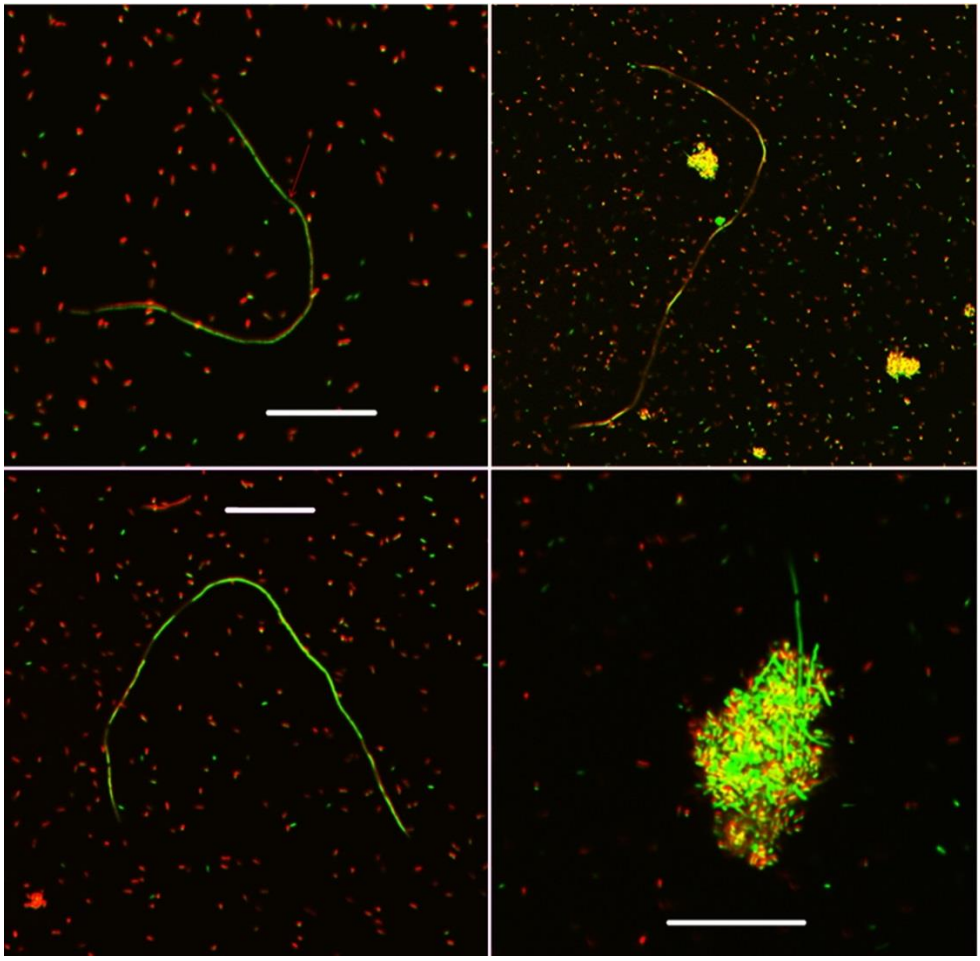

Figure 4.7. Filamentous *E. coli* observed upon exposure to **+EO$_{C2}$** or **+EO$_{C2}$**-SDS; the white line is 20 μm. Green is Syto-9 and Red is propidium iodide.

Cell elongation (or filamentation) is a known stress response that *E. coli* is prone to exhibit upon exposure to high heat[27], antibiotics[28], and UV irradiation[29]. Due to the lack of frequent occurrence of these filaments in a UVA-treated *E. coli* control†, such behavior is attributable to the presence of **+EO$_{C2}$** or **+EO$_{C2}$**-SDS. While the mechanism by which these biocides elicit such behavior is not well understood, it is reasonable that the damage caused by the OPE causes a significant level of oxidative stress and degradation of DNA and proteins, since this has been demonstrated in previous work.[5] Filament growth does not appear to be mitigated by the complexation of **+EO$_{C2}$** with SDS. There are several likely possibilities for the cause of filamentation upon exposure to the biocides, concerning DNA and protein damage caused by reactive oxygen species (ROS).[30,31] Oxidative stress is known to occur in *E. coli* when the ROS exposure exceeds the capacity of the cell to repair membrane and DNA damage, while still producing proteins to counteract ROS. [32]

Inspection of Figure 4.7 reveals several features that may indicate specific cellular structures formed by stress responses. The reduced amount of red fluorescence emitting from the filaments suggests that the filaments have taken up less Propidium iodide (dead stain) than the surrounding dead cells. It is important to note that the darker regions of the filament in the top-right image occur as a result of the filaments twisting conformation, causing it to leave the confocal plane. Evidence suggests that the short, dim sections of the filament, such as that indicated by the red arrow in the top-left image, arise from the "Z-ring" formed by FtsZ: an essential division protein that mediates septation.[33-39] FtsZ generally occupies regions of septation, where cell division is to occur. Due to its importance in bacterial cell division, FstZ serves as a target for broad-spectrum antimicrobials, largely due to a lack of homology with human proteins.[33] Oxidative stress incurred by the presence of **+EO$_{C2}$** may be sufficient to elicit a depletion of guanosine-5'-triphosphate (GTP), which in turn would reduce the amount of active FtsZ. A lack of FtsZ has been attributed to the formation of filamentous cells.[32] An interesting feature that has been observed in several filaments is the occurrence of helical-shaped patterns within the filament that are brightly-stained with SYTO-21. Two images of these structures are shown below, in Figure 4.8.

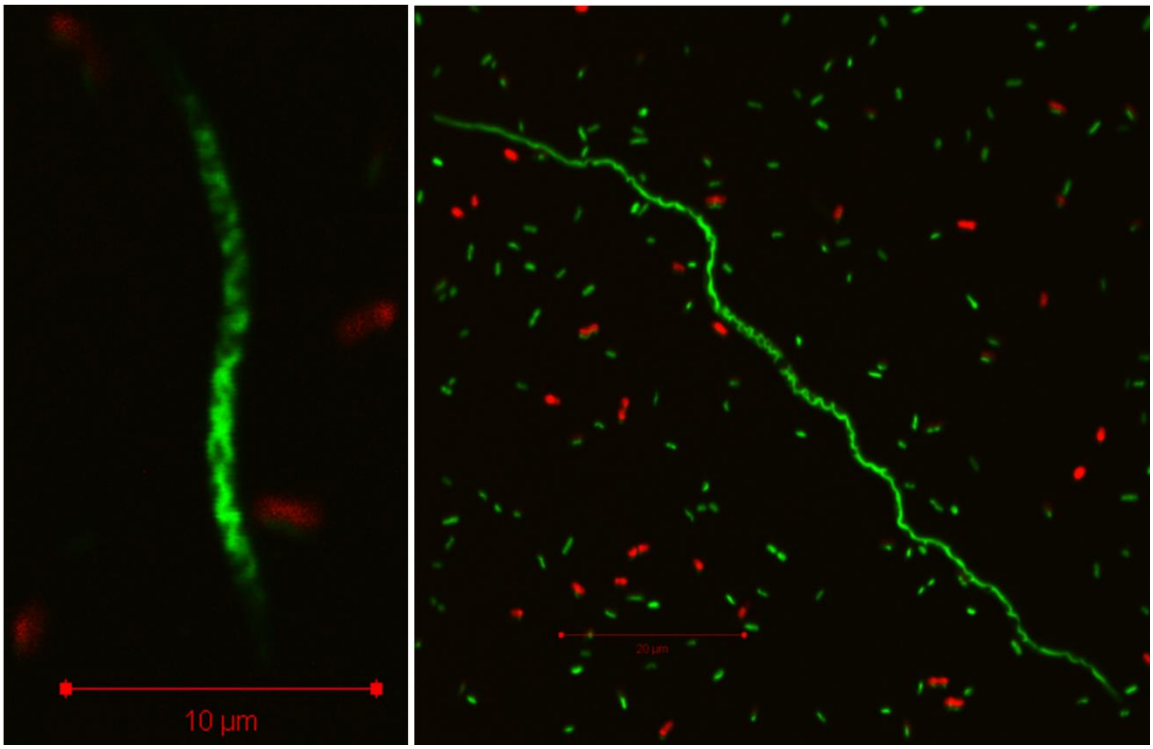

Figure 4.8. Helical structures within filamentous *E. coli*

Though both SYTO-21 and Propidium iodide are nucleic acid stains, the helical structures shown above, in Figure 4.8, resemble several previously observed structures of different cell-division proteins. In one study, helical GFP-tagged FstZ structures were observed when FstZ levels were greatly elevated.[40] MreB (an actin homolog) also maintains a helical structure similar to that seen in the left panel of Figure 4.8, and damage of this protein has been shown to induce filamentation. [41]

In recent work, it has been shown that specific genetic mutations can give rise to elongated cells.[42] Filament formation may also be induced by oxidative DNA damage resulting in the SOS response, in which the protein SulA prevents cell division and further chromosome damage.[38] Boeneman *et al*. observed similar helical structures to those in the left panel of Figure 4.8 in *E. coli* by tracking GFP-labeled DnaA protein, which is responsible for initiating chromosomal replication during a filamentous phase of growth.[43] Another protein that may induce DNA into a helical structure, RecA, is responsible for DNA repair during the SOS response and has a strong tendency to bind with ssDNA in a filament formation. As it has been shown in previous in-vitro experiments[5,6], broad-spectrum damage caused by **+EO$_{C2}$** damages DNA and many of the mentioned proteins whose dysfunction may be responsible for filament

formation. As the complex with SDS does significant killing and induces the same signs of stress as the OPE alone, it must only benefit from the photo-protection offered by the SDS.

4.5.2 *Clumping of S. aureus into Large Plaques*

The damage caused by irradiation of *S. aureus* in the presence of **+EO$_{C2}$** leads to clusters of large numbers of cells. While S. aureus typically forms small clusters of less than 20 cells, the clusters observed upon irradiation in the presence of OPE or OPE-SDS complexes are found to be quite large. Confocal microscopy images of *S. aureus* under different conditions are shown in Figure 4.9.

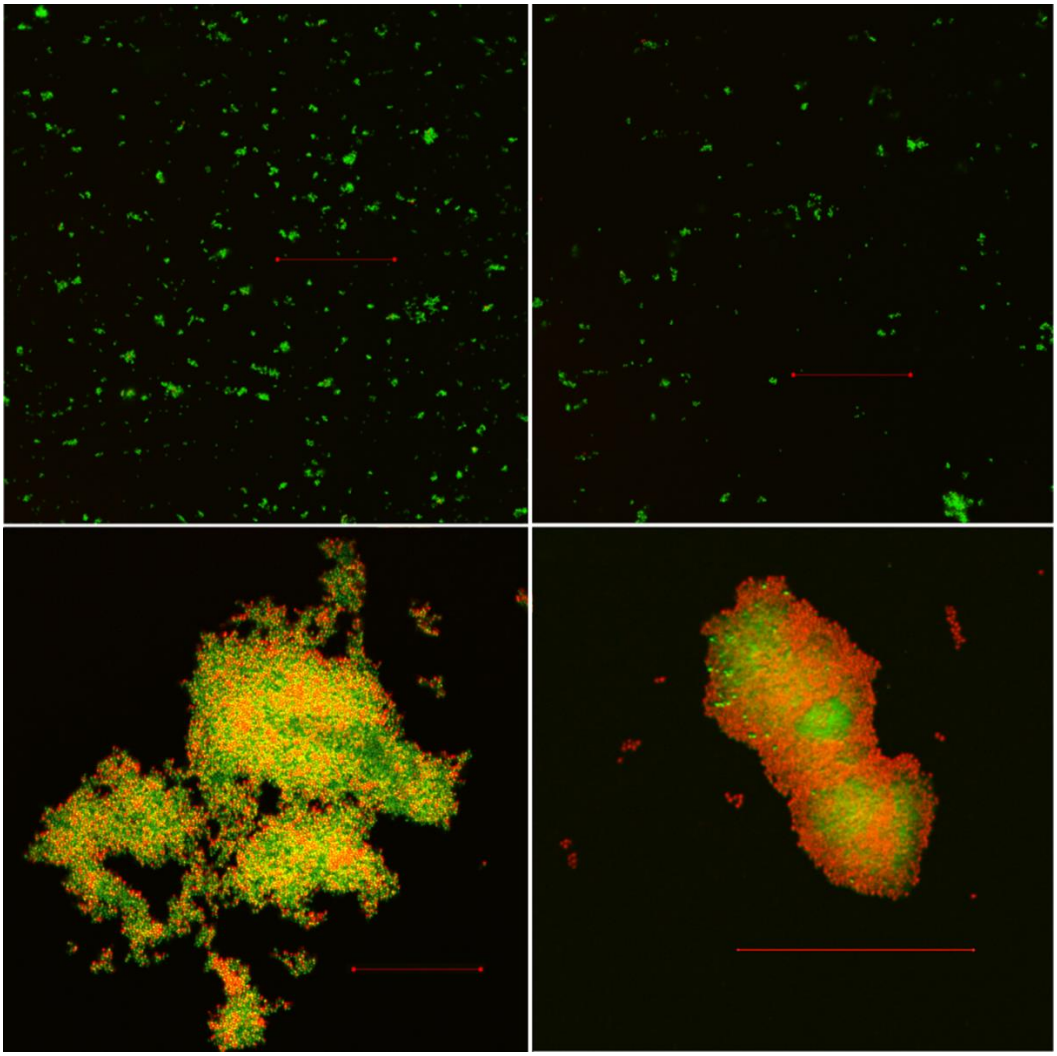

Figure 4.9. Confocal Microscopy images of *S. aureus*, where red and yellow indicate dead bacteria and green indicates live bacteria. The red line indicates 50 µM. Top-left: Negative control; Top-right: SDS control; Bottom-left: **+EO$_{C2}$** w/ UVA; Bottom-right: **+EO$_{C2}$**-SDS

w/UVA

In Figure 4.9, we can clearly see in the top row of images that *S. aureus* that was irradiated without **+EO$_{C2}$** formed clusters of ~10 bacteria. In the bottom panel we observe that large numbers of dead bacteria have agglomerated to form massive clusters, some larger than 100 μM in diameter. These clusters may be indicative of the initial stages of biofilm formation. Biofilm formation in *S. aureus* is a response to environmental stress and has been shown to be caused by UV exposure, metal toxicity[44], acid exposure[45], dehydration and salinity[46], phagocytosis[47], and several antibiotics and antimicrobial agents.[48-50] Previous studies reveal images of *S. aureus* biofilms that are remarkably similar to what we observe in the bottom row of Figure 4.9.[47,51-54]

Biofilm formation is both a stress-response and a result of released cell contents inducing adhesion between cells. The formation of *S. aureus* biofilms has been shown to be dependent on cell-lysis, so it stands to reason that the light-activated damage caused by **+EO$_{C2}$** could induce such a response.[53-55] It has also been suggested that DNA, proteins, and other cell contents play an important role in the initial aggregation of the cells.[56] It has been previously shown by Ying Wang and coworkers that the cells can be emptied as a result of the damage inflicted on the cell membrane.[5,6] It is likely that the DNA and proteins emptied from the cells induce the initial aggregation between cells that leads to these large clusters. We also observe in the bottom-right panel and the top of the bottom-left panel of Figure 4.9 that some of the clusters observed have an abundance of dead bacteria on the periphery of the cluster, while fewer dead bacteria are found in the center of the cluster. This is consistent with results observed in previous studies of *S. aureus* biofilms.[53]

4.6 Conclusions and Outlooks

Several different studies were carried out which explored the effects of photodegradation and complex formation on biocidal activity. The cationic "end-only" OPE **+EO$_{C2}$** was shown to lose biocidal activity with prolonged exposure to UVA light, leading to an ineffective composition of non-biocidal photoproducts. The evidence of biocidal activity of **+EO$_{C2}$** after 30 minutes irradiation, despite the complete loss of fluorescence and absorbance of the OPE, suggests that the early photoproducts are biocidal. The mixing of "end-only" cationic oligo-p-phenylene ethynylenes with the anionic surfactant sodium dodecyl sulfate forms a complex which has drastically reduced photoreactivity, but retains high light-activated biocidal activity against both

Gram-negative and Gram-positive bacteria. This work will increase the capability for applications where protection of broad-spectrum biocides from sunlight for long periods of time is necessary. In addition to enhancing the lifetime of biocides, the same approach could possibly be applied to enhance the lifetime of sensors, dyes, and organic LEDs.

The biocidal activity of an anionic OPE was studied, and the effects of complexation with TTAB were studied by flow cytometry and confocal microscopy. The OPE and TTAB separately had a marginal amount of biocidal activity in both the light and the dark for *S. aureus*, but *E. coli* was killed 50% by TTAB and 75% by **+EO$_{C2}$**. The complex formed between **+EO$_{C2}$** and TTAB at a 1:4 OPE:TTAB ratio exhibited high light-activated biocidal activity, with 3 logs killing against Gram-negative *E. coli* and 2 logs killing against Gram-positive *S. aureus*. Biocidal activity was also enhanced in the dark for *E. coli*, but not *S. aureus*, indicating increased outer membrane penetration for the **+EO$_{C2}$**-TTAB complex relative to either compound alone. This study reveals an effective and inexpensive method for activating the biocidal activity of a non-biocidal singlet-oxygen sensitizing compound. The results of this study suggest that this method of surfactant complexation could be applied to many useful anionic singlet-oxygen sensitizers and different surfactants including lipids. Besides the implications for biocidal applications, this approach may be useful for developing applications for transport across cell membranes and in-vitro studies such as delivering cargo into vesicles.

Confocal fluorescence microscopy using SYTO9 and propidium iodide as stains revealed evidence of filamentous *E. coli* formation, which was attributed to oxidative stress or protein damage caused by the OPE. A different type of stress response was seen in *S. aureus*, where large clusters of bacteria resembling the initial formation of a biofilm occurred with UVA exposure in the presence of **+EO$_{C2}$**. These features were largely observed in cases where OPEs were present under UVA irradiation, resulting in a high level of killing. This further suggests the development of these morphological features as a consequence of release of cell contents upon membrane rupture inducing adhesion between cells in the case of clumped *S. aureus*, and as a stress response in the case of filamentous *E. coli*. The material covered in this chapter gave an overview on the different cases studied in which biocidal properties can be influenced by inducing aggregation of the OPEs. In the following chapter, the aggregation of the OPEs with

bacterial cell membranes is further explored through rigorous computational simulations based on classical mechanics.

4.7 References

(1) Ista, L. K.; Dascier, D.; Ji, E.; Parthasarathy, A.; Corbitt, T. S.; Schanze, K. S.; Whitten, D. G. Conjugated-Polyelectrolyte-Grafted Cotton Fibers Act as "Micro Flypaper" for the Removal and Destruction of Bacteria. *ACS Applied Materials & Interfaces* **2011,** *3*(8), 2932-2937.

(2) Pinto, M. R.; Schanze, K. S. Amplified Fluorescence Sensing of Protease Activity with Conjugated Polyelectrolytes. *Proc. Nat. Acad. Sci.* **2004**, *101*, 7505-10.

(3) Parthasarathy, A.; Goswami, S.; Corbitt, T. S.; Ji, E.; Dascier, D.; Whitten, D. G.; Schanze, K. S. Photophysics and light-activated biocidal activity of visible-light-absorbing conjugated oligomers. *ACS applied materials & interfaces* **2013,** *5*(11), 4516-4520.

(4) Tang, Y.; Corbitt, T. S.; Parthasarathy, A.; Zhou, Z.; Schanze, K. S.; Whitten, D. G. Light-induced antibacterial activity of symmetrical and asymmetrical oligophenylene ethynylenes. *Langmuir* **2011,** *27*(8), 4956-4962.

(5) Wang, Y.; Jett, S. D.; Crum, J.; Schanze, K. S.; Chi, E. Y.; Whitten, D. G. Understanding the dark and light-enhanced bactericidal action of cationic conjugated polyelectrolytes and oligomers. *Langmuir* **2013,** *29*(2), 781–92.

(6) Wang Y.; Tang Y.; Zhou Z.; Ji E.; Lopez G. P.; Chi E. Y.; Schanze K. S.; Whitten D. G. Membrane Perturbation Activity of Cationic Phenylene Ethynylene Oligomers and Polymers: Selectivity against Model Bacterial and Mammalian Membranes. *Langmuir* **2010,** *26,* 12509-12514

(7) Hill, E. H.; Stratton, K.; Whitten, D. G.; Evans, D. G. Molecular Dynamics Simulation Study of the Interaction of Cationic Biocides with Lipid Bilayers: Aggregation Effects and Bilayer Damage. *Langmuir* **2012**, *28,* 14849−14854.

(8) Hill, E. H.; Goswami, S.; Evans, D.G.; Schanze, K.S.; Whitten, D.G. Photochemistry of a Model Cationic p-Phenylene Ethynylene in Water *J. Phys. Chem. Letters* **2012,** *3*, 1363-1368.

(9) Hill, E. H.; Evans, D. G.; Whitten, D. G. Photochemistry of "End-Only" Oligo-p-phenylene Ethynylenes: Complexation with Sodium Dodecyl Sulfate Reduces Solvent Accessibility *Langmuir* **2013,** *29*(31), 9712-9720

(10) Zhou, Z.; Corbitt, T. S.; Parthasarathy, A.; Tang, Y.; Ista, L. K.; Schanze, K. S.; Whitten, D. G. "End-only" functionalized oligo (phenylene ethynylene) s: Synthesis, photophysical and biocidal activity. *The Journal of Physical Chemistry Letters* **2010,** *1*(21), 3207-3212.

(11) Turro, N.J.; Yekta, A. Luminescent Probes for Detergent Solutions. A Simple Procedure for Determination of the Mean Aggregation Number of Micelles *J. Am. Chem. Soc.* **1978,** *100*, 5951

(12) Hill, E. H.; Pappas, H. C.; Evans, D. G.; Whitten, D. G. Cationic oligo-*p*-phenylene ethynylenes form complexes with surfactants for long-term light-activated biocidal applications *Photochem. Photobiol. Sci.* **2014,** *13*, 247-253

(13) Hill, E. H.; Sanchez, D.; Evans, D. G.; Whitten, D. G. Structural Basis for Aggregation Mode of oligo-p-Phenylene Ethynylenes with Ionic Surfactants *Langmuir* **2013,** *29* (51), 15732-15737

(14) Buffet-Bataillon, S.; Tattevin, P.; Bonnaure-Mallet, M.; Jolivet-Gougeon, A. Emergence of resistance to antibacterial agents: the role of quaternary ammonium compounds—a critical

review, *International Journal of Antimicrobial Agents* **2012,** *39*(5), 381-389
(15) Evans, D.F.; Allen, M.; Ninham, B. W.; Fouda, A. Critical Micelle Concentrations for Alkyltrimethylammonium Bromides in Water from 25 to 160 C. *J. Solution Chem.***1984,** *13*, 87
(16) Lindig, B. A.; Rodgers, M. A.; Schaap, A. P. Determination of the lifetime of singlet oxygen in water-d2 using 9, 10-anthracenedipropionic acid, a water-soluble probe. *Journal of the American Chemical Society* **1980,** *102*(17), 5590-5593.
(17) Neuhaus, F. C.; Baddiley, J. A continuum of anionic charge: structures and functions of D-alanyl-teichoic acids in gram-positive bacteria. *Microbiology and Molecular Biology Reviews* **2003,** *67*(4), 686-723.
(18) Nikaido H. Outer membrane. In: Neidhardt F C, Curtiss III R, Ingraham J L, Lin E C C, Low K B Jr, Magasanik B, Reznikoff W S, Riley M, Schaechter M, µMbarger H E, editors. *Escherichia coli* and *Salmonella*: cellular and molecular biology. 2nd ed. Washington, D.C: American Society for Microbiology; **1996**. pp. 29–47.
(19) Träuble, H.; Overath P. The structure of Escherichia coli membranes studied by fluorescence measurements of lipid phase transition. *Biochim. Biophys. Acta* **1973**, *307,* 491–512
(20) Vollmer, W.; Blanot, D.; De Pedro, M. A. Peptidoglycan structure and architecture. *FEMS Microbiol. Rev.* **2008,** *32*(2), 149-167.
(21) Lawrence, M. J.; Rees, G. D. Microemulsion-based media as novel drug delivery systems. *Adv. Drug Deliv. Rev.* **2000,** *45*(1), 89-121.
(22) Rabinow, B. E. Nanosuspensions in drug delivery. *Nature Reviews Drug Discovery* **2004,** *3*(9), 785-796.
(23) Gursoy, R. N.; Benita, S. Self-emulsifying drug delivery systems (SEDDS) for improved oral delivery of lipophilic drugs. *Biomedicine & Pharmacotherapy* **2004,** *58*(3), 173-182.
(24) Müllertz, A.; Ogbonna, A.; Ren, S.; Rades, T. New perspectives on lipid and surfactant based drug delivery systems for oral delivery of poorly soluble drugs. *Journal of Pharmacy and Pharmacology* **2010,** *62*(11), 1622-1636.
(25) Williams, A. C.; Barry, B. W. Penetration enhancers. *Advanced Drug Delivery Reviews* **2012,** *64*, 128-137.
(26) Gelperina, S.; Maksimenko, O.; Khalansky, A.; Vanchugova, L.; Shipulo, E.; Abbasova, K.; Kreuter, J. Drug delivery to the brain using surfactant-coated poly (lactide-co-glycolide) nanoparticles: influence of the formulation parameters. *Eur. J. Pharm. Biopharm.* **2010,** *74*(2), 157-163
(27) Ron, E. Z.; Davis, B. D. Growth rate of Escherichia coli at elevated temperatures: limitation by methionine *Journal of Bacteriology*, 1971, **107**(1), 391-396.
(28) Rolinson, G. N. Forty years of beta-lactam research. *Journal of Antimicrobial Chemotherapy,* 1998, **41**: 589-603.
(29) Burton, P.; Holland, I. B. Rifampicin-induced replication of the plasmid pBR322 in Escherichia coli strains carrying dnaA mutations. *Mol Gen Genet.* **1983,** *190*(1), 128-32.
(30) Storz, G.; Imlay, J. A. Oxidative stress *Current Opinion in Microbiology* **1999,** *2*, 188-194.
(31) Cabiscol, E.; Tamarit, J.; Ros, J. Oxidative stress in bacteria and protein damage by reactive oxygen species *International Microbiology* **2000,** *3*, 3-8.
(32) Jones, T. H.; H.-c. Wong, Editor. *Stress Response of Foodborne Microorganisms* **2012,** Nova Science Publishers, 293-330.
(33) Lock, R. L.; Harry, E. J. Cell-division inhibitors: new insights for future antibiotics *Nature Reviews Drug Discovery*, **2008,** *7,* 324-338.

(34) Addinall, S. G.; Cao, C.; Lutkenhaus, J. Temperature shift experiments with an ftsZ84(Ts) strain reveal rapid dynamics of FtsZ localization and indicate that the Z ring is required throughout septation and cannot reoccupy division sites once constriction has initiated. *Journal of Bacteriology,* **1997,** *179*(13), 4277-4284.
(35) Stricker, J.; Maddox, P.; Salmon, E. D.; Erickson, H. P. Rapid assembly dynamics of the Escherichia coli FtsZ-ring demonstrated by fluorescence recovery after photobleaching *Proc. Nat. Acad. Sci.*, **2002,** *99*(5), 3171-3175.
(36) Romberg, L.; Levin, P.A. Assembly dynamics of the bacterial cell division protein FtsZ: poised at the edge of stability *Annual Review of Microbiology*, **2003,** *57*, 125-154.
(37) Anderson, D. E.; Gueiros-Filho, F. J.; Erickson, H. P. Assembly dynamics of FtsZ rings in Bacillus subtilis and Escherichia coli and effects of FtsZ-regulating proteins *Journal of Bacteriology*, **2004,** *186*(17), 5775-5781.
(38) Goehring, N. W.; Beckwith, J. Diverse paths to midcell: assembly of the bacterial cell division machinery *Current Biology*, **2005,** *15*, R514-R526.
(39) Rico, A. I.; Garcia-Ovalle, M.; Palacios, P.; Casanova, M.; Vicente, M. Role of Escherichia coli FtsN protein in the assembly and stability of the cell division ring *Molecular Microbiology,* **2010,** *76*(3), 760-771.
(40) Ma, X.; Ehrhardt, D. W.; Margolin, W. Colocalization of cell division proteins FtsZ and FtsA to cytoskeletal structures in living Escherichia coli cells by using green fluorescent protein *Proc. Nat. Acad. Sci.,* **1996,** *93*(23), 12998-3003.
(41) Kruse, T.; Møller-Jensen, J.; Løbner-Olesen, A.; Gerdes, K. Dysfunctional MreB inhibits chromosome segregation in Escherichia coli *EMBO J.,* **2003,** *22*(19), 5283–5292.
(42) Maciąg-Dorszyńska, M.; Ignatowska, M.; Jannière, L.; Węgrzyn, G.; Szalewska-Pałasz, A. Mutations in central carbon metabolism genes suppress defects in nucleoid position and cell division of replication mutants in *Escherichia coli Gene* **2012,** *503*, 31-35.
(43) Boeneman, K.; Fossum, S.; Yang, Y.; Fingland, N.; Skarstad, K.; Crooke, E. Escherichia coli DnaA forms helical structures along the longitudinal cell axis distinct from MreB filaments *Molecular Microbiology,* **2009,** *72*, 645–657.
(44) Teitzel, G. M.; Parsek, M. R. Heavy metal resistance of biofilm and planktonic Pseudomonas aeruginosa *Applied and Environmental Microbiology*, **2003,** *69*(4), 2313-2320.
(45) McNeill, K.; Hamilton, I. R. Acid tolerance response of biofilm cells of Streptococcus mutans *FEMS Microbiology Letters*, **2003,** *221*, 25-30.
(46) Le Magrex-Debar, E.; Lemoine, J.; Gelle´, M.-P.; Jacquelin, L.-F.; Choisy, C. Evaluation of biohazards in dehydrated biofilms on foodstuff packaging *Food Microbiology,* **2000,** *55*, 239-243.
(47) Leid, J. G.; Shirtliff, M. E.; Costerton, J. W.; Stoodley, P. Human leukocytes adhere to, penetrate, and respond to Staphylococcus aureus biofilms *Infection and Immunity*, **2002,** *70*(11), 6339-6345.
(48) Stewart, P. S.; Costerton, J. W. Antibiotic Resistance of Bacteria in Biofilms. *Lancet,* **2001,** *358*(9276), 135-138.
(49) Gilbert, P.; Allison, D. G.; McBain, A. J. Biofilms in vitro and in vivo: do singular mechanisms imply cross-resistance? *J Appl Microbiol.,* **2002,** *92* Suppl, 98S-110S
(50) Mah, T. F.; O'Toole, G. A. Mechanisms of biofilm resistance to antimicrobial agents. *Trends in Microbiology,* **2001,** *9*(1), 34-39.
(51) Hall-Stoodley, L.; Costerton, J. W.; Stoodley, P. Bacterial biofilms: from the natural environment to infectious diseases *Nature Reviews: Microbiology* **2004,** *2*, 95-108.

(52) Shanks, R.M.Q.; Donegan, N.P.; Graber, M. L.; Buckingham, S. E.; Zegans, M. E.; Cheung, A. L.; O'Toole, G. A. Heparin stimulates Staphylococcus aureus biofilm formation *Infection and Immunity,* **2005,** *73*(8), 4596-4606.
(53) Mann, E. E.; Rice, K. C.; Boles, B. R.; Endres, J. L.; Ranjit, D.; Chandramohan, L.; Tsang, L. H.; Smeltzer, M. S.; Horswill, A. R.; Bayles, K. W. Modulation of eDNA release and degradation affects Staphylococcus aureus biofilm maturation *PLOS One,* **2009,** *4*(6), e5822.
(54) Rice, K. C.; Mann, E.E.; Endres, J. L.; Weiss, E.; Cassat, J. E.; Smeltzer, M. S.; Bayles, K. W. The cidA murein hydrolase regulator contributes to DNA release and biofilm development in Staphylococcus aureus *Proc. Nat. Acad. Sci.,* **2007,** *104*(19), 8113-8118.
(55) Cramton, S. E.; Gerke, C.; Schnell, N. F.; Nichols, W. W.; Götz, F. The intercellular adhesion (ica) locus is present in Staphylococcus aureus and is required for biofilm formation. *Infect Immun.,* **1999,** *67*(10), 5427-33.
(56) Flemming, H. C.; Wingender, J. Extracellular enzymes affect biofilm formation of mucoid Pseudomonas aeruginosa. *Nat Rev Microbiol.,* **2010,** *8*(9), 623-33.

Chapter V: INTERACTIONS WITH BACTERIAL CELLS II: MOLECULAR SIMULATIONS OF WATER-SOLUBLE OLIGO-P-PHENYLENE ETHYNYLENES WITH MODEL BACTERIAL MEMBRANES

5.1 Introduction

5.1.1 Outline of OPEs and "dark" biocidal mechanisms

As discussed in Chapter 1, OPEs were developed as broad-spectrum biocides, to combat antibiotic resistant strains of bacteria which are currently a significant problem in hospitals.[1] As antibiotics generally kill beneficial human flora while antibiotic-resistant bacteria thrive, the development of broad-spectrum antibiotics is necessary for treatment of hospital-acquired infections.[2-6] The cationic OPEs and PPEs are soluble in aqueous solution, and cationic groups enhance their interactions with net-anionic bacterial membranes.[7-10] This close association likely improves the broad-spectrum light-activated biocidal activity enabled by the singlet-oxygen sensitization properties of the phenylene-ethynylene backbone.[11] Both classes of molecules discussed in this dissertation, those with charged endgroups and those with charged sidechains, have antimicrobial activity against Gram-positive and Gram-negative bacteria under UVA light and in the dark.[12,13] Further studies of the dark biocidal activity of the OPEs with model bacterial membranes revealed evidence of membrane disruption through dye-leakage studies.[14] In addition, several *in vivo* and *in vitro* experiments were performed which revealed significant changes to the membranes of both Gram-negative and positive bacteria after exposure to the OPEs in the dark, and also revealed differences between the action of the different types of OPEs.[15] The characterization of bacterial membrane mimics after exposure to both +*n*H and **+EO** by ^{31}P NMR spectra and small angle x-ray scattering (SAXS) revealed different profiles for the +*n*Hs and **+EO**. [15] The difference in resulting lipid bilayer phases indicated different mechanisms of membrane disruption. While these results revealed the resulting lipid phases after membrane disruption in both live and model systems, the initial molecular mechanisms of how these structures arise has not heretofore been determined. The MD simulations focus on the same DOPE:DOPG composition used in experimental studies of dye-leakage from large unilamellar vesicles, where OPEs are shown to be very effective at causing leakage.[14]

5.1.2 Interactions of peptides and small molecules with membranes

In order to better understand the biocidal mechanisms in OPEs, Wang and coworkers used the

cationic peptide melittin in studies of model bacterial membranes.[14-17] Cationic polymers and peptides including melittin have been shown to be effective biocidal agents against both Gram-negative and Gram-positive strains of bacteria.[17-32] As bacterial cell membranes have a net-negative charge, cationic groups induce strong interactions with the membrane. Aggregates of antimicrobial peptides have previously been observed to induce instabilities or pores which disrupt the membrane structure and integrity.[24-41] The main mechanisms of membrane disruption for antimicrobial peptides are generalized into the "carpet" model, and the toroidal pore or barrel-stave pore models which describe water pore formation. The carpet mechanism involves biocidal agents adsorbing onto the membrane surface and inducing dissociation in a detergent-like manner. This occurs after sufficient coverage is reached, and its success is dependent on a high peptide to lipid ratio.[25,26] Peptides such as alamethicin insert into the membrane perpendicular to the membrane surface and then induce an ordered pore, known as barrel-stave pore.[27,28] Most other antimicrobial peptides, including magainins, melittin, and protegrins, form water pores which contact both lipid headgroups and peptides, and have a more toroidal shape.[29-32] Cationic peptides, particularly the melittin and 2-magainin, have been extensively studied both experimentally and through molecular dynamics (MD) simulations as toroidal pore-forming peptides.[22-45]

5.1.3 *Simulating Biophysical Phenomena*

The theory of molecular dynamics was pioneered by the works of Alder and Wainwright in the late 1950s.[46,47] In their work they modeled hard spheres using square potential wells in order to determine physical observables to compare with those experimentally obtained, and this led to much insight concerning the behavior of liquids. In the 1960s, Rahman and coworkers were able to extend this theory to simulate liquid argon and then liquid water.[48,49] The first simulation of a biomolecule was accomplished in 1977 by McCammon and coworkers, with the simulation of bovine pancreatic trypsin inhibitor.[50] Modern molecular dynamics simulations cover phenomena including the binding of inhibitors and substrates to enzymes, membrane structure and dynamics, protein folding and structure, and chemical reactions. Many different observables can be derived from molecular simulations and compared to experiment, such as free-energy of binding, X-ray and NMR structure, and SAXS scattering profiles. In addition, a molecular-level view of the system of interest is given, allowing one to make qualitative judgements in addition to the values

obtained by analysis of the simulation.

An area of particular interest for discussion in this thesis is that of the properties of membranes that can be predicted by molecular dynamic simulations. In addition to allowing one to observe the structure of the membrane, binding characteristics, membrane density, thickness, lipid headgroup area, and lipid lateral diffusion rate can be calculated. One consideration that needs to be made for MD is the timescale of the phenomenon that is being studied. If the process that is being studied takes place over a period of time that exceeds what is reasonably capable to simulate within a normal timeframe, then the initial configuration must sample more conformational space. MD simulations of an agent binding to a membrane tend to reach a conclusion in 5 ns to a microsecond of simulation time. Complex membrane phenomena such as remodeling of structure, lipid flip-flop, and insertion of peptides, may take a significant amount of time, sometimes exceeding milliseconds experimentally, and sampling of conformational space is needed to help develop a clearer picture of such interactions. In this section, a systematic molecular dynamics study of both types of OPEs which have been discussed in this thesis is performed on timescales from 0.1-1 us at the all-atom level and beyond 1 us using GPU acceleration or a coarse-grained model.

5.2 Interactions of OPEs with Cationic Side-chains with Lipid Bilayers

In an effort to determine the molecular mechanisms behind the ability of OPEs to disrupt membranes without exposure to light, MD was used to study the interactions between the OPEs and model bacterial membranes mimicking the previous *in vitro* experimental study. A key effort to achieve this goal was the analysis of the +*n*H series of OPEs with n=1,2, and 3, which is described in this section.

5.2.1 *Aggregation of +nH OPEs on the Bilayer Surface*

Experimental results show that the OPEs readily form complexes with scaffolds such as carboxymethylcellulose, DNA, or surfactant molecules as discussed in the previous sections. Interactions of ligands at the surface of a membrane on the sub-microsecond timescale generally indicate their propensity to interact or intercalate with the membrane at longer timescales exceeding a millisecond. Although it is unlikely that full insertion of several OPEs from solution into the lipid bilayer can be observed on the sub-microsecond timescale, sampling with OPEs

initially in solution above the lipid bilayer, and then OPEs half-inserted into the bilayer gives insight into the stages, or steps, that can ultimately lead to bilayer disruption. Simulations to study the interaction of +*n*H OPEs with the lipid bilayer were started with the OPEs outside of the lipid bilayer, as depicted in Figure 5.1.

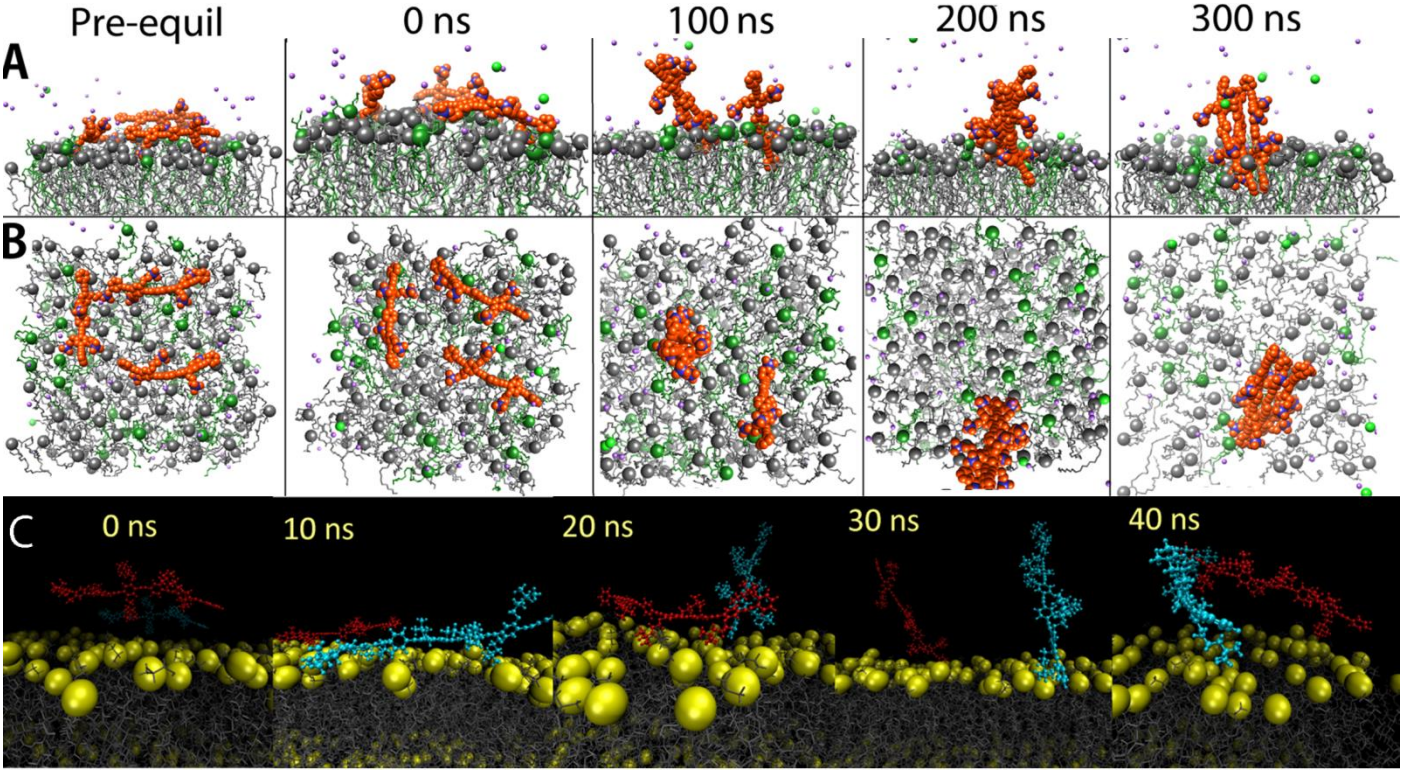

Figure 5.1. Timeline of the simulation of 3 **+2H**s initially placed at the bilayer surface, with (A) side views and (B) top-down views shown. OPEs are shown in orange, DOPG are green, DOPE are grey, Na^+ is purple, and Cl^- is bright green. Phosphorous atoms are represented as spheres and are colored according to their parent lipid. Waters are omitted for clarity. (C) The interaction of two **+3H** OPEs (one red, the other cyan) with the upper leaflet of the lipid bilayer. Lipids are shown in grey, and the phosphate head groups of the phospholipids are shown in yellow. Water and ions are not shown for clarity.[51,52]

In these simulations, an interesting phenomenon was observed: the OPEs readily aggregate to form complexes of two or three in solution. The OPEs were found to associate with the lipid bilayer within 10 ns In this simulation, and in several similar simulations, some of the cationic OPE side groups become embedded in the upper leaflet in less than 50 ns, as the cationic quaternary ammonium groups associate with the phosphate head groups of the DOPG and DOPE. The simulations of **+3H** at the bilayer-water interface were carried out to just 50 ns due to the amount of simulation time needed for the large number of water molecules needed to

properly separate the OPEs in the water box from the opposite leaflet of the membrane within the periodic boundary conditions.[53] In a more extensive study, the surface interactions between **+2H** with the bilayer are sampled on much longer timescales. The interactions of the OPEs with the surface of the lipid bilayer were then studied through examining their self-assembly, relative affinity for DOPG and DOPE, and effects on bilayer thickness.

Initially, the three OPEs are parallel to the bilayer surface, but as the simulation proceeds they begin to aggregate. It is clear from both the images in Figure 5.1 and radial distribution plots in Figure 5.3C and D that two of the OPEs are aggregated by 100 ns, and these two aggregate with the third OPE by 200 ns. Following the snapshots along the trajectory in Figure 5.1, it is shown that the aggregated OPEs become perpendicular to the plane of the bilayer and insert their terminal phenyl rings into the membrane. The third OPE remains parallel with the bilayer until it aggregates with the dimer, at which point it also takes on a perpendicular conformation. Aggregation effects are also seen in the simulation of 3 **+2H**s, which has an initial state with three **+2H**s inserted halfway into the bilayer, as shown in Figure 5.2.

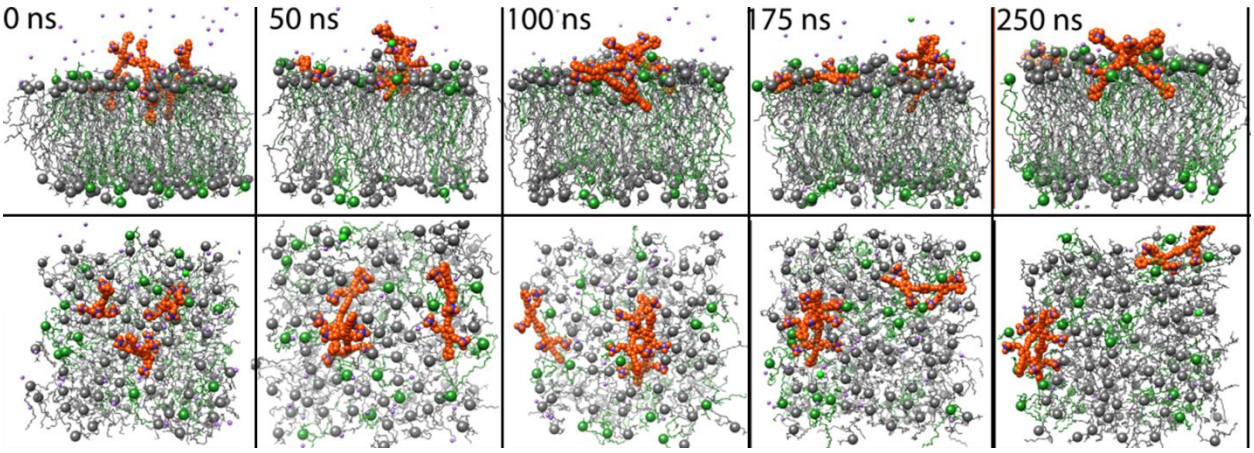

Figure 5.2. Timelines of the simulation trajectory of 3 **+2H**s initially half-inserted into the bilayer, showing the side view (top panel) and the top view (bottom panel). OPEs are shown in orange, DOPG are green, DOPE are grey, Na^+ is purple, and Cl^- is bright green. Phosphorous atoms in the lipid headgroups are represented as spheres and are colored according to their parent lipid. Waters are omitted for clarity.[52]

The three OPEs in Figure 5.2 start with their ends buried at a similar depth to those of the aggregates observed towards the end of the simulation trajectory in Figure 5.1A. This is equivalent to about 2 phenyl rings or an insertion distance of 1 nm into the bilayer. As the

simulation proceeds, two of the OPEs aggregate with one another and align near-perpendicular to the bilayer surface. The single OPE continues to interact strongly with the bilayer in a parallel orientation, as seen with the OPEs in the simulation trajectory in Figure 5.1A. These simulation trajectories show that the self-aggregation of OPEs at the membrane surface plays an important role in how the OPEs interact with the lipid bilayer. It is likely that the perpendicular orientation of the OPE aggregates may enhance their ability to penetrate across the membrane, as those in a parallel orientation are more likely to insert laterally or not at all.

In addition to the self-assembly and resulting changes in geometry and interactions with the bilayer, a strong affinity for the OPEs to bind to DOPG was observed. DOPG is one of the lipid components by which a bacterial membrane obtains its net-negative charge. As the OPEs are positively-charged, it is likely that the OPEs and lipids would attract each other strongly through Coulombic interactions. The radial distribution functions of the center of mass (COM) of the quaternary ammonium groups of the OPEs relative to the COM of the phosphate headgroups of DOPE and DOPG for are shown below, in Figure 5.3.

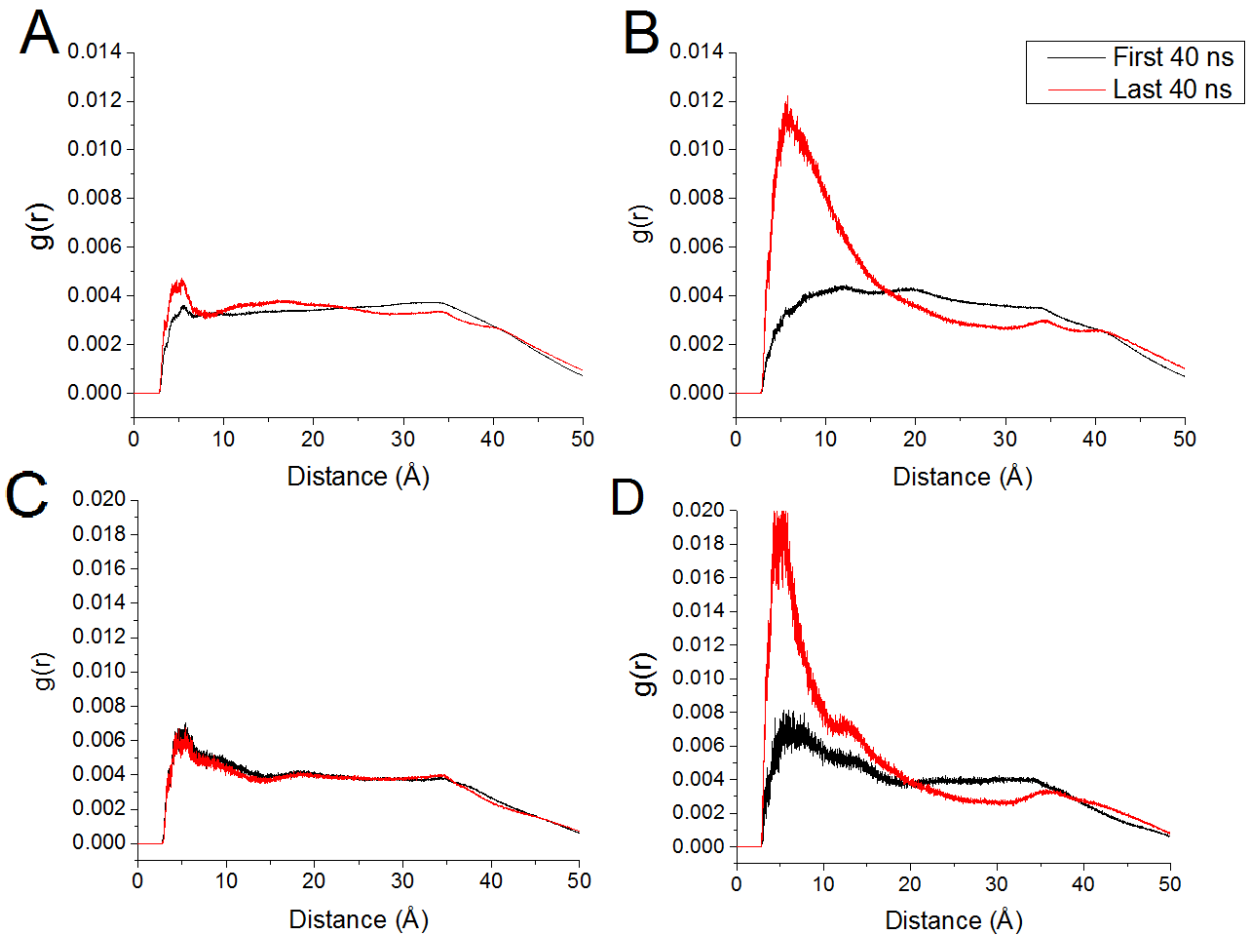

Figure 5.3. Radial distribution functions from simulation of 3 +**2H** initially in the water box at the bilayer interface (shown in Figure 5.1) of the COM of quaternary ammonium nitrogen of OPEs relative to the COM of phosphate groups of A)DOPE and B) DOPG Panel B clearly indicates a closer association of OPEs to DOPG than DOPE over the course of the simulation trajectory. Also given in the bottom row are Radial distribution functions of the quaternary ammonium nitrogen of OPEs relative to the phosphorous atoms of (C) DOPE and (D) DOPG for 3 +**2H**s initially half-inserted in the bilayer (shown in Figure 5.2). [52]

In both systems the distribution of DOPE phosphate (PO_4^-) groups relative to the OPE quaternary ammonium groups, $N^+(CH_3)_{3,}$ is unchanged throughout the course of the simulation. The distribution of DOPG phosphate groups in relation to OPE $N^+(CH_3)_3$ groups in the simulation of 3 +**2H**s at the bilayer interface (Figure 5.1A) clearly increases over the course of the trajectory as shown in Figure 5.3D. In both simulations shown in Figs 5.1A and 5.2, a higher number of phosphates associated with OPE $N^+(CH_3)_3$ groups belonged to a DOPG than a DOPE. It is important to note that there are four times as many DOPE molecules as DOPG in the system, which means that the DOPG-OPE association is strong and leads to a very specific interaction of

the OPEs with the lipid bilayers. Indeed, this association may account for a possible cause of membrane disruption by DOPG sequestration. As DOPG is not a good membrane-forming lipid due to unfavorable electrostatic interactions, OPEs may form DOPG-rich regions in the bilayer which become unstable and lead to membrane disruption.

5.2.2 *Interactions of +nH OPEs in the Bilayer and Water Pore Formation*

Given the limitations of running full atomistic molecular dynamics simulations beyond 100 ns, and anticipating that the insertion process into the lipid bilayer from solution is expected to take much longer with numerous modes of insertion likely (based on our results at the interface in section 5.2.1) it is reasonable to consider initial OPE configurations where one or more OPEs are initially placed fully-inserted into the bilayer. Using the initial configurations of one, two, or three **+3H**s fully inserted into the lipid bilayer, molecular dynamics simulation trajectories were monitored for up to 100 ns.[51] Starting from these configurations, significant thinning of the lipid bilayer was observed by 20 ns, even when only one OPE is inserted, as shown in Figure 5.4, below.

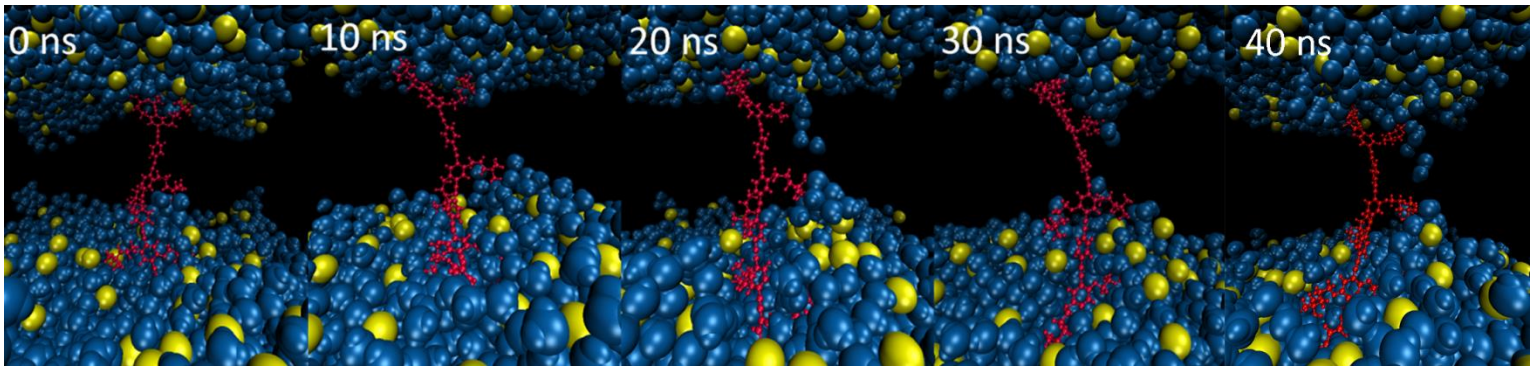

Figure 5.4. A timeline of one fully-inserted OPE, shown in red. Waters are in blue, the phosphate head groups are in yellow, and the lipid tails of DOPG/DOPE have been omitted for clarity.[51]

In the case where multiple OPEs are placed into the bilayer, significant changes to the bilayer structure are observed. During the course of a simulation of three **+3H** in the bilayer, two **+3H** were observed to closely associate with each other. This can be seen clearly in Figure 5.5, where 2 OPEs are clearly aggregated with one another, at 40 ns for example. The third OPE was somewhat removed from the other two laterally. The lipid bilayer thickness was also monitored as the system evolved from the initial configuration of three OPEs. The average bilayer thickness

was calculated over the course of the simulation trajectory. Snapshots of the average lipid bilayer thickness, as determined from Gridmat-MD[53], are shown in Figure 5.5C.

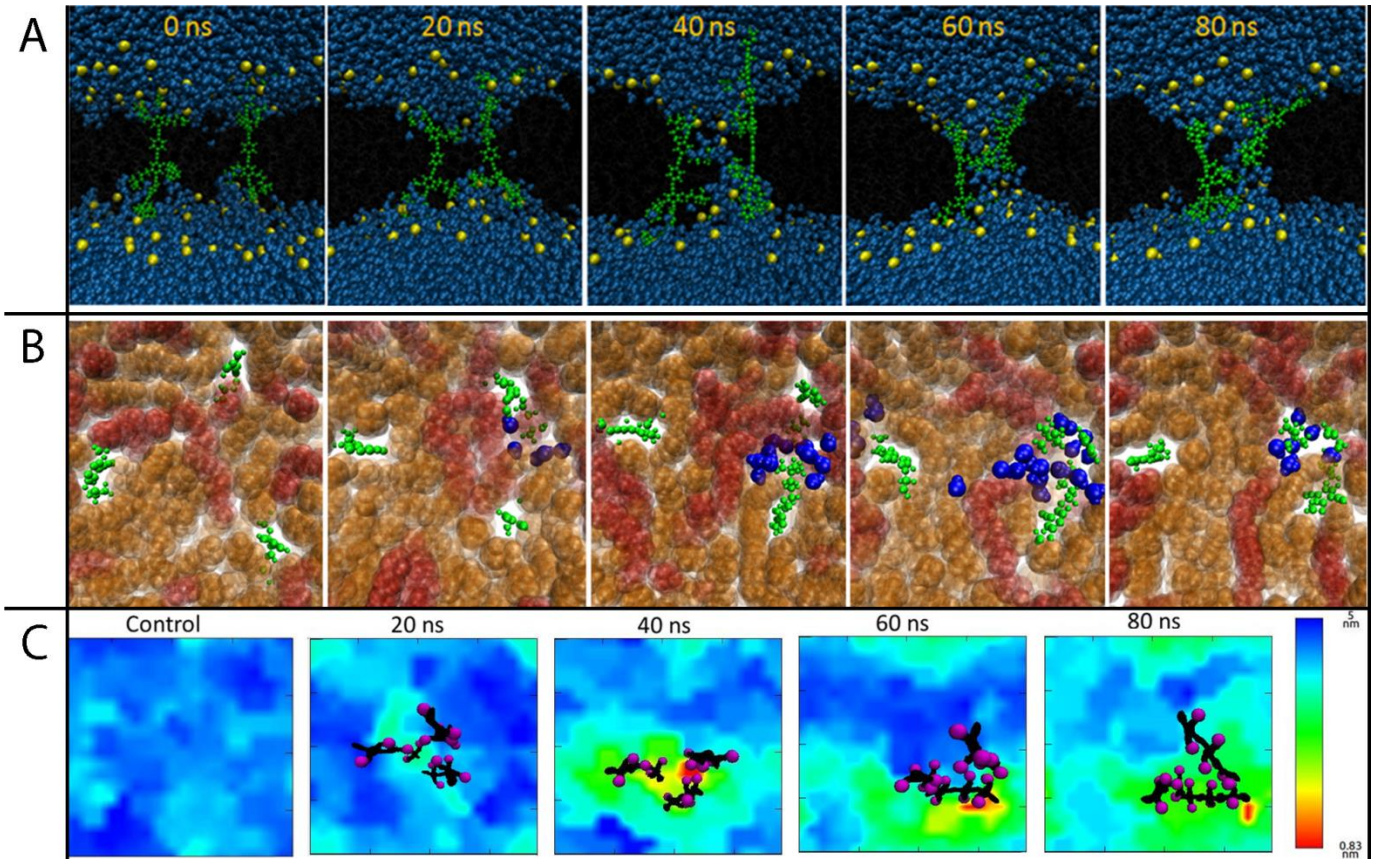

Figure 5.5. Snapshots along the simulation trajectory show the timeline of the formation of a water channel and pore in the lipid bilayer. **A)** A transverse view of the lipid bilayer, showing only the OPEs in green, the P in the lipid head groups in yellow, and the water molecules in blue. Other atoms are omitted for clarity **B)** A cross-sectional view of the membrane showing a view of the upper leaflet. The DOPE are shown in orange, the DOPG in red, the OPEs in green, and the water molecules in blue. **C)** Average lateral bilayer thickness along the simulation trajectory for the simulation shown in Fig 5.5A. The OPE positions are shown in black, and the total area shown in each box is 75Åx75Å. The cationic side groups are shown in magenta.[51]

The two **+3H** that were closer to one another had their cationic groups facing towards one another, and aligned at the same approximate depth in the lipid bilayer. Beyond 30 ns a much more drastic reduction in the thickness of the bilayer is observed, starting from an initial average thickness of 37 Å, to around 10-20 Å in the immediate vicinity of the OPEs in the later stages of the simulation. Changes in the morphology of the lipid bilayer can also be seen clearly from the area occupied per lipid, which increases noticeably for lipids in the vicinity of the OPES. The cationic groups of the aligned and aggregated OPEs in the lipids ultimately result in extensive

damage to the integrity of the bilayer. The presence of the cationic groups on the aggregated OPEs provides a polar channel across the lipid bilayer, in a region where the thickness of the bilayer has significantly decreased. As a result of the cationic groups in this damaged region, infiltration of water into the lipid bilayer is observed after a fairly short time (20-40 ns) along the simulation trajectory, followed by the creation of a water channel or "pore" as the simulation evolves. Formation of the water channel is observed around 30 ns in Figure 5.5.

In Figure 5.5B, a cross-sectional view of the lipid bilayer from the upper leaflet clearly shows how changes to the bilayer are brought about due to the aggregation of two of the OPEs. The water molecules, shown in blue in Figure 5.5B, are shown to be closely associated with this pair of **+3H**s. This view also shows clearly how the water associates along the channel created by the OPEs, and shows that the lipid bilayer is significantly damaged after about 60 ns. At 70 ns, one of the two OPEs involved in the formation of the pore slipped out of the pore and associated entirely with the upper leaflet of the lipid bilayer. The passage of specific water molecules was followed through this channel. Water molecules that crossed the bilayer were detected by defining planes parallel to the bilayer leaflets. Water molecules that cross these planes from either direction (+, or – z) were identified and tracked individually. Between 30 and 120 ns along the simulation trajectory, 346 water molecules were detected passing through the pore, 153 in the +z direction and 195 in the –z direction. The lipid morphology in the bilayer is observed to change drastically along the simulation trajectory (see Figure 5.11).

In the study of **+3H**s, aggregation between OPEs was found to be critical for the initial formation of a water pore, due to the resulting polar environment which is introduced into the bilayer.[51] Aggregation of more than one **+3H** was a critical factor for pore formation due to introduction of polarity into the membrane, which is discussed in detail in section 5.2.3, below. This effect was also observed with **+2H** and **+1H**. The shorter chain-length *n*=2 and *n*=1 OPEs are studied to determine whether these smaller molecules have a similar ability to disrupt the lipid bilayer structure and form water pores like the **+3H**s. In Figure 5.6 the timeline for three **+2H**s fully inserted into the bilayer is shown.

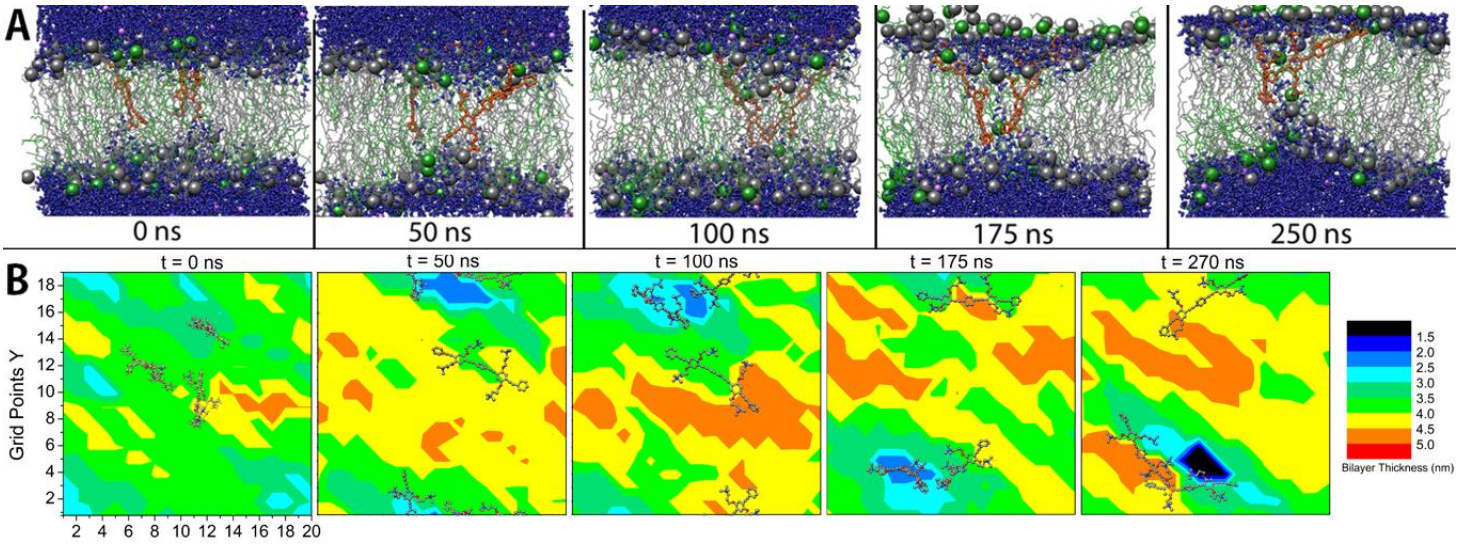

Figure 5.6. (A)Timeline of the simulation of 3 **+2H** fully inserted in the lipid bilayer. **+2H**s are shown in orange, DOPG are green, DOPE are grey, water is blue, Na^+ is purple, and Cl^- is bright green. Phosphorous atoms are represented as spheres and are colored according to their parent lipid. (B) Plot of bilayer thickness over the course of the simulation trajectory shown in Fig. 5.6A.The OPEs are overlaid in black in their respective positions at the time of the snapshot, and each frame has linear dimensions of x = y = 7 nm. [52]

In the figure above, clear evidence of the water pore forming by 175 ns can be observed, and by 250 ns the pore is fully formed. It is clear from Figure 5.6 that two **+2H** are not yet aggregated at 50 ns, but have become aggregated within the membrane by 100 ns. This result with the **+2H**s confirms the importance of self-aggregation in membrane disruption. In the GRIDMAT thickness plot in Figure 5.6B, an average increase in bilayer thickness is observed when comparing the positions of the lipid headgroups at 0 ns and 270 ns. In addition, a dramatic local reduction of thickness in the vicinity of the OPEs can be clearly seen, and by 270 ns the pore is clearly visible in black, denoting a thickness of less than 1.5 nm.

The MD simulations of three **+2H**s inserted into the lipid bilayer resulted in pore formation upon OPE self-aggregation in the bilayer.[52] The mechanism of bilayer damage is very similar to that observed previously for aggregates of **+3H**s. At 2 nm, the length of **+1H** is far shorter than **+2H** or **+3H** and consequently it is not able to span the average length (3.5 to 4 nm) of the membrane. It is therefore a reasonable conjecture that this difference may significantly reduce the ability of **+1H** to form a transmembrane water pore. To test this hypothesis, four **+1H**s were placed in the interior of the membrane. After 5 ns of equilibration, one of the OPEs had risen to the interface. The timeline of the simulation trajectory is shown in Figure 5.7. Apparent thinning of the bilayer can be observed at 60 ns, and the passage of water across a pore begins

around 100 ns. The thinning of the bilayer can be observed in Figure 5.7B, in which the contour plot of average bilayer thickness calculated using GRIDMAT-MD is shown. The bottom panel in Figure 5.7 shows that by 50 ns there is a region of the bilayer which has become 1-1.5 nm thinner than the average thickness of ~3.5-4 nm for a normal equilibrated membrane. This region progressively thins for the duration of the simulation and by 145 ns a fully-formed pore is evident as the black region of Figure 5.7B.

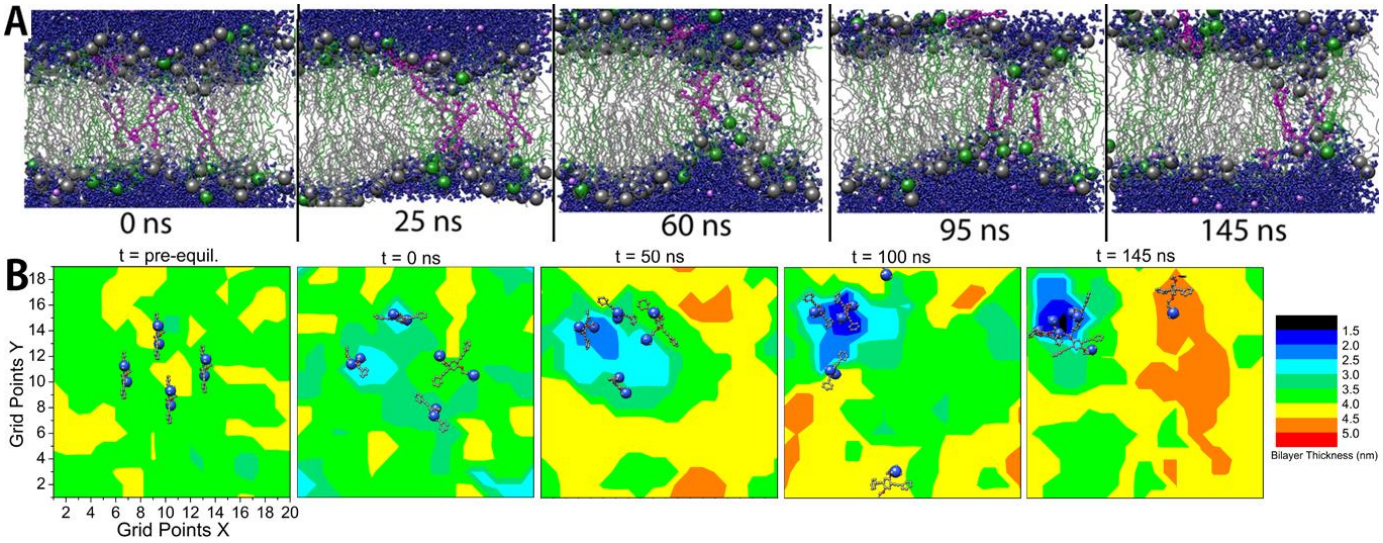

Figure 5.7. (A)Timeline of the simulation of 4 **+1H**s inserted in the lipid bilayer. **+1H**s are shown in magenta, DOPG are green, DOPE are grey, water is blue, Na^+ is purple, and Cl^- is bright green. Phosphorous atoms are represented as spheres and are colored according to their parent lipid. (B) Plot of bilayer thickness over the course of the simulation trajectory shown in Fig 5.7A.The OPEs are overlaid in black in their respective positions at the time of the snapshot, and each frame has linear dimensions of x = y = 7 nm. [52]

The formation of a water pore observed in the simulations of **+1H** and **+2H** was quantified by calculating electron densities along the Z-axis using cpptraj in AmberTools13.[54] These plots examine the positions of the lipid headgroups and water molecules from the start to the end of the simulation. The electron density plots along the bilayer Z-axis are shown in Figure 5.8, below.

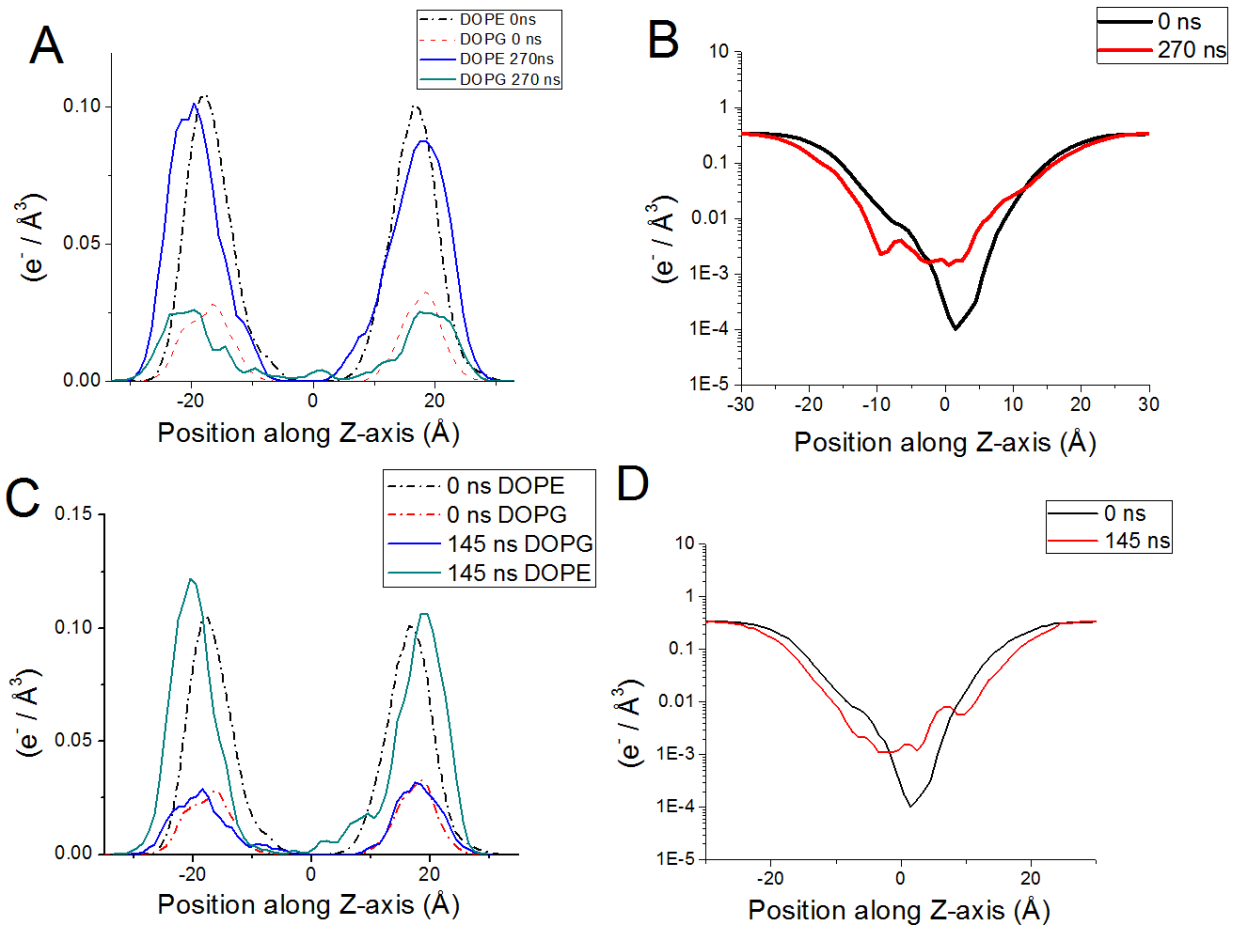

Figure 5.8. Electron densities in simulation of 3 **+2H** of (A) Lipid headgroups and (B)Water at beginning and end of simulation trajectory and (C) Lipid headgroups and (D) Water in simulation of 4 **+1H** inserted in the bilayer Note: Electron density of water is scaled logarithmically for clarity. [52]

It is clear from Figure 5.8 that the lipids which show the greater perturbation due to the OPE insertion are predominantly DOPGs, where their headgroups are drawn into the interior of the bilayer structure. The electron density data confirms the observation of DOPG aggregation in snapshots along the simulation trajectories of **+2H** aggregating at the bilayer interface (Figs 5.3A and 5.7). The electron density of water in both simulations (Figs. 5.8 B and D) clearly shows the presence of water in the interior of the membrane by the end of the simulation, in comparison to 0 ns where there is almost no water penetration into the center of the lipid bilayer structure.

The perturbation of both DOPE and DOPG by the formation of the pore is evident in Figures 5.8A and C. A large number of DOPE P atoms, as well as some from DOPG, are found in the internal region) of the bilayer (within 1 nm of the origin in + or – z directions). Despite its short length, **+1H** aggregates in the lipid bilayer and after 100 ns, a water pore is seen and

accompanied by significant membrane damage. In addition to the changes to membrane thickness and water pore formation, the lateral area per lipid (APL) in both simulations are observed to decrease to 57-58 $Å^2$. The simulations of OPEs outside of the membrane result in APLs closer in agreement to the equilibrated values, suggesting that the formation of a pore forces the lipid headgroups to become more closely packed and significantly changes the lipid packing in the bilayer structure

Classical molecular dynamics simulations of +*n*H (with *n*=1,2 and 3) inserted into a model bacterial membrane show that the mechanism of membrane disruption for these structures is quite similar. Formation of transmembrane water pores on timescale of hundreds of nanoseconds is observed for all of the +*n*Hs when pre-inserted into a membrane. In all cases, self-aggregation of the OPEs with one another was found to be a necessary prerequisite for the formation of a water pore. The initial passage of water from one leaflet of the bilayer to the other requires the polar environment provided by multiple charged groups at different depths within the membrane, and this is not provided when only a single OPE is present, especially with *n*=1 OPEs. While the length of the OPE does influence the structure of the aggregates, the determining factor for pore formation in this case appears to be the orientation of the charged sidechains and the self-aggregation of OPEs. As the distance between the charged groups of the two sidechains of an +*n*H is only an average of 14 Å, an aggregate of OPEs will have the ability to attract phosphate headgroups of the lipids in the bilayer which are 35-40 Å apart. As the phosphate groups are attracted to the cationic ammonium groups on the +*n*Hs, this leads to the thinning and destabilization of the membrane. The simulation results also shown that the length of time needed for pore formation in these systems was dependent on the degree of self-aggregation, and not on the backbone length of the individual OPEs.

The MD simulation results show that the resulting bilayer distortion and pore formation observed with +*n*Hs inserted into the bilayer is similar to the membrane disruption mechanism of toroidal pore formation observed for the antimicrobial peptides 2-magainin and melittin.[31-41] Aggregation of +*n*Hs pre-inserted into a lipid bilayer induces pore formation by the processes of local membrane thinning and penetration of water molecules into the bilayer interior aided by the cationic OPE sidegroups. This mechanism is clearly operable in both light and dark conditions, and these simulations provide support for the strong biocidal activity of OPEs against bacteria even in the dark.[15] The MD simulations also show that partial insertion of +*n*Hs into the

bilayer structure is possible, even on the timescale of hundreds of nanoseconds.

5.2.3 The Role of Self-Assembly in Water Pore Formation

The creation of a polar channel across the lipid bilayer by OPEs is shown above to result in significant leakage of water through the lipid bilayer in the vicinity of the OPEs. The passage of water molecules through the channel occurs as a result of the presence of the cationic groups along the channel and the proximity of the upper and lower leaflets in this damaged zone. After the formation of the water channel at 30 ns, the initial progress of water molecules through the pore was observed to occur via a simple mechanism: the water molecules individually move down a "ladder" created by the multiple cationic sidechains of the OPEs to end up on the opposite leaflet. The progress of individual water molecules crossing through this pore was followed to illustrate this mechanism clearly. In Figure 5.9, the proximity of specific water molecules to the nitrogen atom in the cationic quaternary ammonium groups is tracked in time along the simulation trajectory.

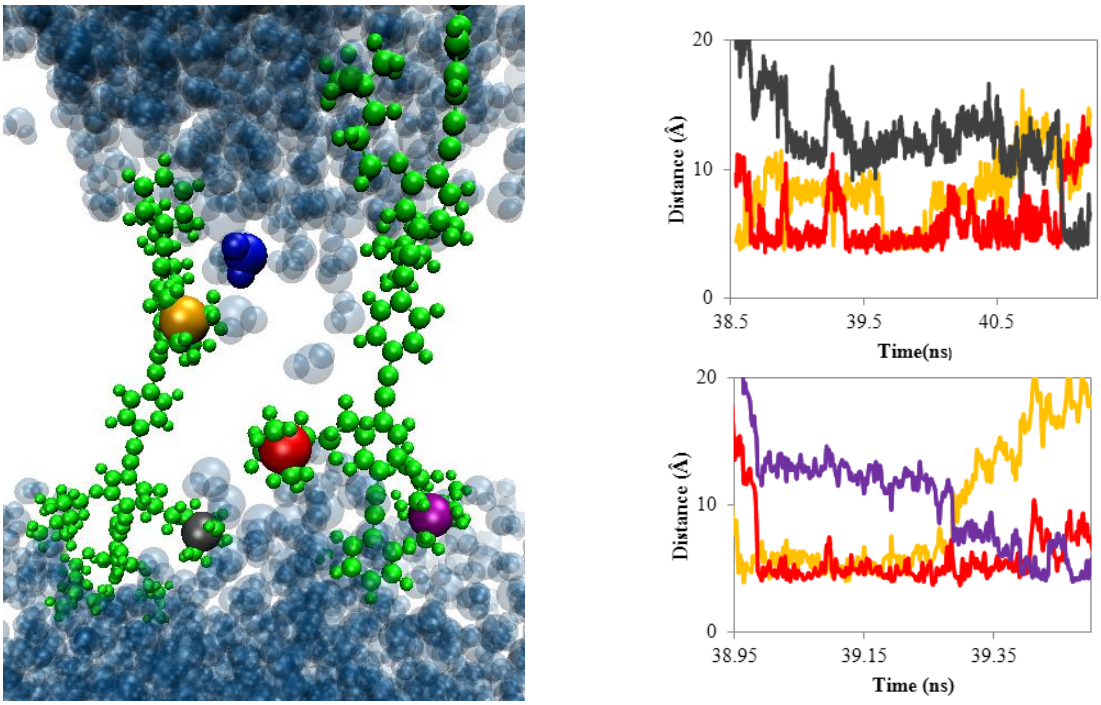

a) **b)**

Figure 5.9. a) Nitrogen atoms in 4 cationic quaternary ammoniumgroups are illustrated in grey, red, yellow and purple. The backbones of the OPEs creating the pore are shown in green. Waters are shown as diffuse blue spheres, and a specific water molecule is shown in dark blue. **b)** Two specific water molecules that pass through the pore are monitored as they pass through the channel: the distance between each water molecule and the colored nitrogen atoms is shown in that color (red, yellow, purple or grey) as the simulation proceeds.[51]

For the water molecule shown in the top panel of Figure 5.9b, it is clear that the water molecule "jumps" from close proximity to the nitrogen atom shown in purple, to the yellow and red nitrogen atoms at 39.29 ns. Similar "jumps" are observed for other water molecules seen traversing the pore at other snapshots early in the simulation. Essentially, the water molecules associate strongly with the cationic groups in the lipid layer, and jump from one cationic group to the next along a polar "ladder" created by the OPE side chains. Once the larger pore forms at around 60 ns, the water molecules flow along the polar channel created in the lipid bilayer.

The characteristics of formation of a pore vary slightly when simulations are repeated. In a repeat simulation of that of three **+3H** fully inserted in the bilayer, a pore suddenly forms at 100 ns, and once formed, it seems to have more rapid growth and larger size than in the simulation discussed in Figure 5.1A. In this repeat simulation, the three OPEs all span the membrane and play a part in the pore formation, whereas in the simulation trajectory in Figure 5.1A, only two OPEs seem to be involved in pore formation. It is interesting to note that the insertion of one OPE into the bilayer results in thinning of the bilayer and water moving along a limited cationic "ladder". However no formation of a large pore for a sustained amount of time is observed.

5.2.4 Lipid Flip-Flop and its Role in Pore Formation

While full insertion from solution into the bilayer most likely occurs on much longer timescales than is possible for all-atom simulations such as these, recent experimental studies point to other mechanisms that may enhance incorporation into a membrane. A fluorescence labeling experiment showed that the presence of 2-magainin increased the rate of lipid flip-flop from half-lives on the order of hours or days to minutes.[32] In separate studies by Wu *et al* [55] and Matsuzaki *et al*[56] on cationic antimicrobial peptides, flipping of lipids bound to peptides induces them to form irregular aggregates within the membrane, which implicitly results in formation of aqueous pores.' These experimental studies suggest that binding of OPEs to the membrane surface could increase the lipid flip-flop rate and result in their incorporation into the lipid bilayer structure via another mechanism. In simulations where a complex between two **+3H** results in pore formation, lipids are observed to move from one leaflet to the other leaflet in the area that surrounds the OPEs. In Figure 5.10, snapshots taken along this simulation trajectory show a lipid transitioning between the leaflets.

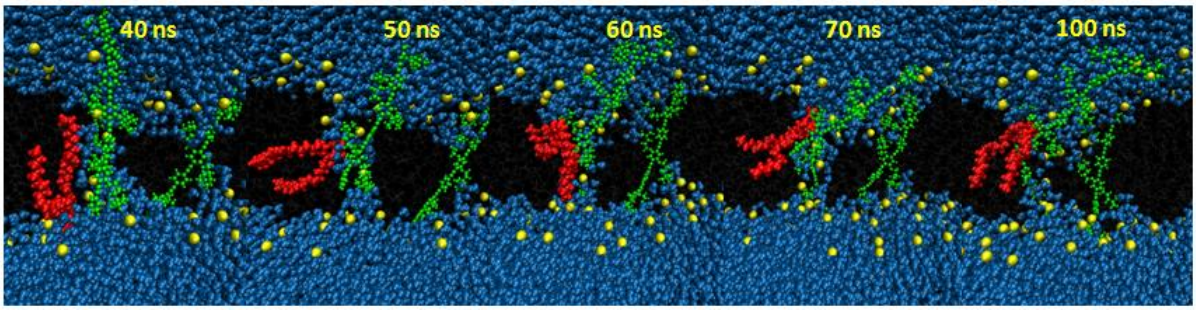

Figure 5.10. A DOPG in the region of the pore (shown in red) between 40 and 60 ns on the lower leaflet flipping and becoming stable on the upper leaflet after 100 ns.[51]

This mechanism is aided by the significant OPE-induced distortions of the phosphate headgroup positions in the bilayer. This lipid movement begins to occur after 45 ns in the simulation trajectory, and is fully completed by 100 ns. Similar lipid flip-flop events have also been observed in simulations of pore-forming antimicrobial peptides such as magainin with lipid bilayers[57-61]. While flip-flop occurs, lipids in the region of the pore also become highly disordered.

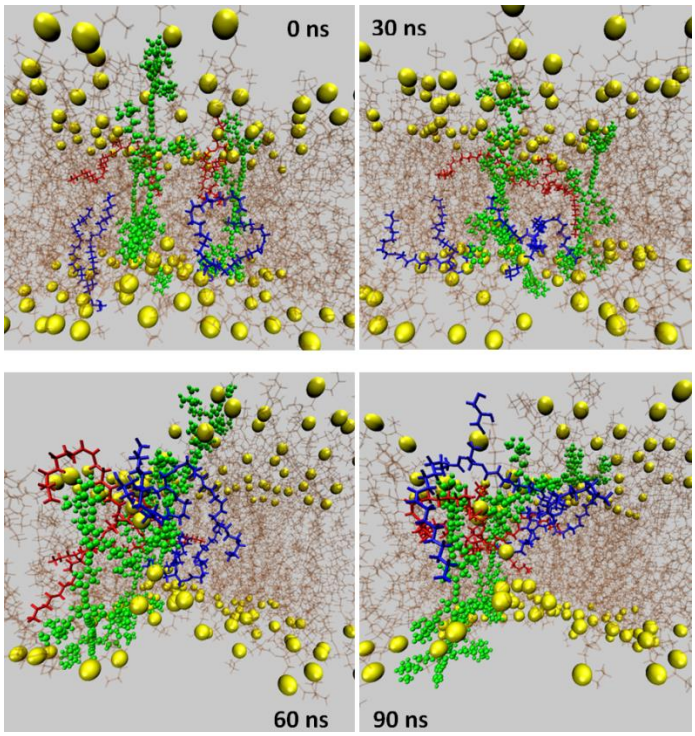

Figure 5.11. Changes in the lipid morphology along the simulation trajectory starting from the configuration in Fig. 5.1A. Lipids in the vicinity of the pore created by the **+3H** (shown in green) show larger scale motion in the membrane, and some lipids flip between upper and lower leaflets, as a result of the strong interactions with the **+3H**s.

In Figure 5.11 the flip of two lipids (shown in blue) from one leaflet to the opposite leaflet occurs over 90 ns, while two lipids on the opposite leaflet (shown in red) become highly disordered. The replication of lipid flip-flop that is observed with cationic, pore-forming antimicrobial peptides is good support for the attribution of pore-forming to the initial mechanism of biocidal activity in the dark for bacteria.

5.3 Interactions of "end-only" OPEs with Model Bacterial Membranes

In addition to the study of the length-dependence of OPEs on their interactions with each other and a model bacterial membrane, studies of an "end-only" OPE were carried out as described in the methods section (Chapter 7). The goal was to determine what effects the terminal cationic groups on **+EO** would have in terms of their interactions with each other and with a bacterial membrane mimic. The timelines over the simulation trajectory of 8 **+EO**s, either in the water box at the bilayer interface or fully inserted perpendicular to the bilayer, are shown in Figure 5.12

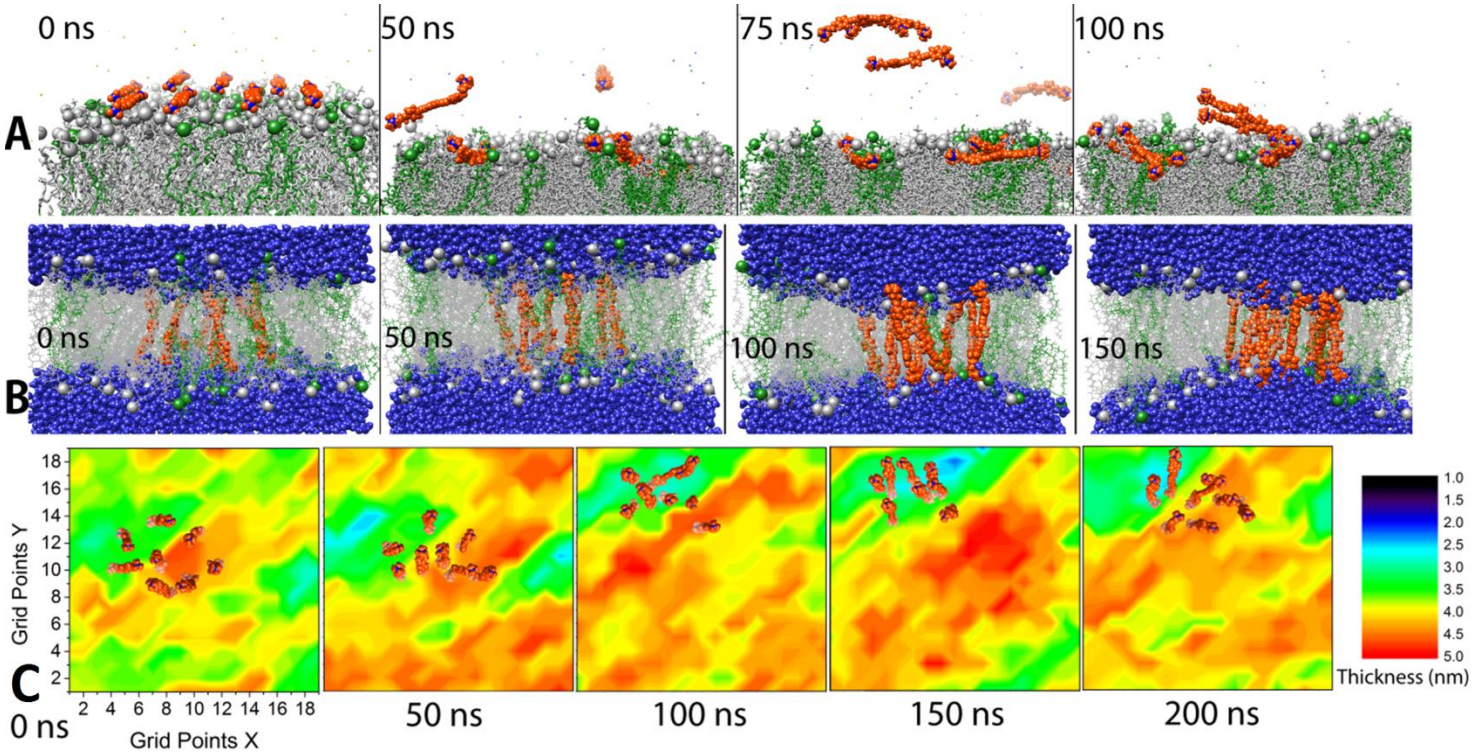

Figure 5.12 Timelines along simulation trajectories of 8 **+EO**s (A) Initially outside the bilayer and (B) Initially fully inserted in the bilayer, both viewed from the side. **+EO**s are shown in orange, DOPG are green, DOPE are grey, water is blue, Na^+ is purple, and Cl^- is bright green.

Phosphorous atoms are represented as spheres and are colored according to their parent lipid. (C) Bilayer thickness over the course of the simulation trajectory shown in Fig. 5.12B. The OPEs are shown in orange overlaid in their respective positions, and each frame is 10.3 nm on a side. In (A) waters are omitted for clarity. [52]

In Figure 5.12A, the **+EO**s are initially placed in aqueous solution parallel to the membrane. No spontaneous trans-membrane insertion is observed within 100 ns. However, as shown in Figure 5.13, the **+EO**s are observed to lie down with their backbones buried inside the hydrocarbon of the lipid and the charged groups remaining at the surface, as if they were buoys floating on top of the membrane. This structure is observed to be the predominant outcome for many simulation trajectories where the **+EO** are initially placed in the water solution outside of the bilayer, and it is generally achieved within the first 10 ns of simulation.

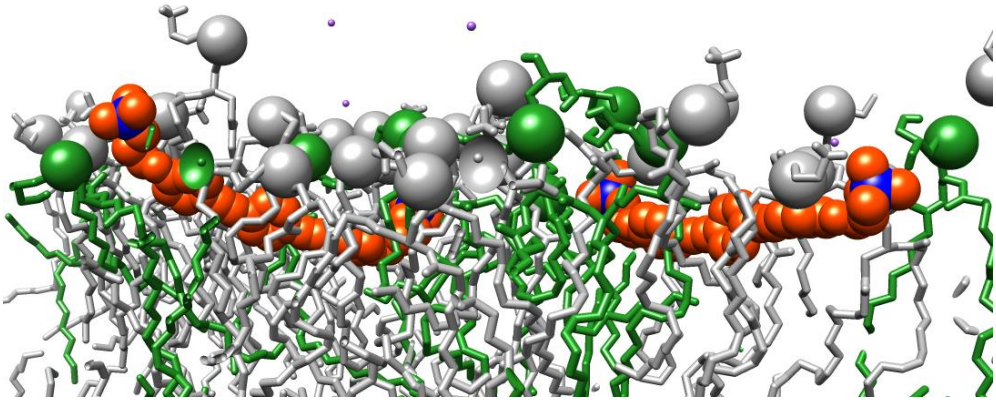

Figure 5.13. Snapshot of simulation of 8 **+EO**s at the bilayer interface showing the OPE backbone buried in the bilayer with the charged ammonium groups (shown in blue) associated with the phosphate headgroups. Waters are omitted for clarity.[52]

It is conceivable that **+EO**s can become inserted into the membrane on much longer timescales than accessible through classical MD, perhaps due to minor fluctuations and damage caused by aggregations of other **+EO**s on the membrane surface. Consequently, it is also of interest to simulate **+EO**s pre-inserted to span across the bilayer structure, with each terminal cationic ammonium group associated with phosphates on opposite leaflets as a starting configuration. To address what the effect of embedded **+EO**s might be on the membrane structure, 8 **+EO**s were initially placed within the bilayer, aligned with the principal axis as shown in Figure 5.12B. Observation of the membrane thickness over the course of the trajectory in Figure 5.12B shows an obvious decrease in bilayer thickness in the region of the **+EO**s. This is shown more clearly in the membrane thickness plot in Figure 5.12C, where the membrane thins to less than 2.5 nm from leaflet to leaflet by 50 ns.

The thickness in this region fluctuates, and does not seem to decrease significantly beyond this amount throughout the course of the simulation trajectory. In addition, the portions of the bilayer that are not in the vicinity of the OPEs seem to greatly increase in thickness, approaching 5 nm thick. While disruption of the bilayer could result from this change in thickness of the bilayer, no explicit water pore formation was observed in the simulation of **+EO**s in the membrane. The change in average thickness and lack of water permeation is also confirmed by the electron density plots shown in Figure 5.14.

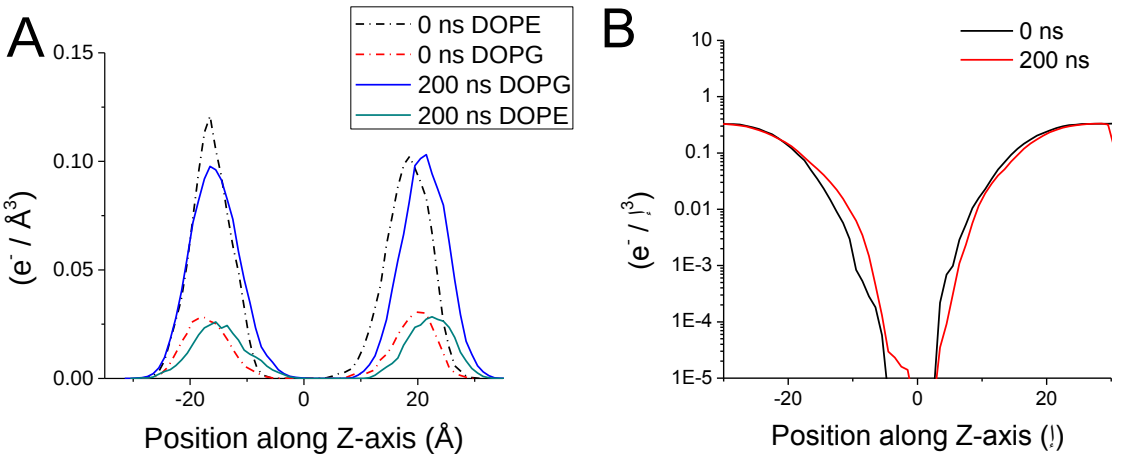

Figure 5.14. Electron densities of (A) Lipid headgroups and (B) Water at the beginning and end of the simulation trajectory of 8 **+EO**s fully inserted in the bilayer. The electron density of water is scaled logarithmically for clarity.

One explanation for this reduced thickness without pore formation is the distance between the two charged groups of the two different types of OPE: +*n*H and **+EO**. The average distance between cationic ammonium groups is 27-30 Å for **+EO**, whereas for the +*n*H series the distance is 14-16 Å. This makes the +*n*H interaction with both leaflets more significant and the strong interaction between the OPE cationic groups and the phosphate headgroups of the lipids leads to extensive thinning in the region of the OPEs, as they draw the upper and lower phosphate groups on the leaflets together. The cationic groups on **+EO** are further apart and are only 5 to 10 Å shorter than the thickness of the bilayer. Therefore, the change in thickness and the local thinning observed in the vicinity of the OPE clusters upon insertion is much reduced for **+EO** compared with +*n*H. In addition, cationic groups in **+EO** do not penetrate into the bilayer structure. For **+3H** and **+2H**, the cationic groups are embedded into the bilayer, and their presence is a crucial first step to water penetration as they provide a ladder for the initial influx of water molecules

into the hydrophobic region into the bilayer, and ultimately, water pore formation. In addition to effects from the oligomer itself, membrane instabilities caused by enrichment of DOPG into regions are also considered using radial distribution functions in Figure 5.15 below.

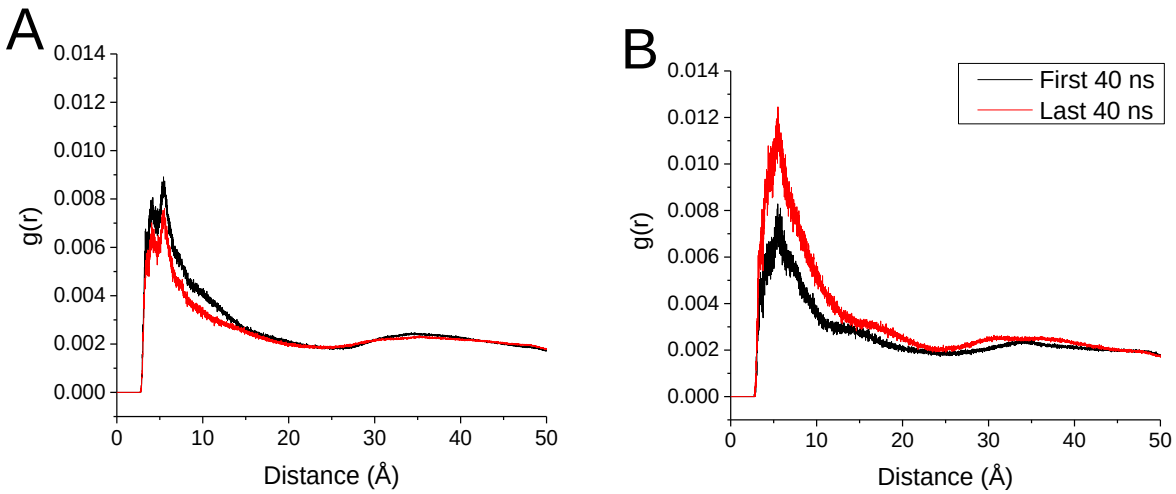

Figure 5.15. Radial distribution functions of the quaternary ammonium nitrogen of OPEs and the phosphorous atoms of A) DOPG and B) DOPE for 8 +**EO**s fully inserted at the beginning and end of the simulation trajectory.

As shown in Figure 5.15, the radial distribution function of the quaternary ammoniums of the OPEs relative to the phosphates of the DOPG or DOPE reveals significantly greater interaction with DOPG over the simulation trajectory. Like the case of the +*n*Hs, interaction with DOPE, however, remains at a similar level of association with only a slight decrease at 210-250 ns compared with 0-40 ns. E. *coli* cell membranes, on which the model bacterial membranes in this study are based, are a good model to test lipid clustering as they have been shown to cluster readily with antimicrobial peptides.[62-65] It is therefore possible that the interaction of +**EO**s leads to instabilities of the membrane due to the aggregation of DOPG in the region of the +**EO**s.

The MD simulations show that end-only OPEs, +**EO**s, with their charged moieties on the terminal ends did not induce water pore formation, but did induce changes in local thickness of the membrane and induce DOPG aggregation. The difference in lengths between charged moieties on different OPEs was a deciding factor in whether an OPE could form a water pore. The +*n*H series has only a 14 Å separation at most between mobile cationic sidegroups, and is consequently more likely to bridge lipids from opposite leaflets to induced local membrane thinning and initiate pore formation. In +**EO**, the terminal cationic groups are 28 Å apart and consequently the cationic groups of +**EO** can insert into upper and lower leaflets with less

disruption to the bilayer structure and reduced membrane thinning in the local region surrounding the +**EO**s.

While +**EO**s do not result in water pore formation, it is possible that the end-only class of OPEs induces membrane damage through other mechanisms. This could be either through bilayer phase changes induced through the effects of +**EO** on local membrane curvature, or through +**EO** induced aggregation of DOPG lipids into DOPG-rich regions which would be unstable. The simulations show the aggregation of DOPG in the vicinity of +**EO**s, and the incorporation of +**EO**s from solution to lie horizontally just below the surface of the lipid bilayer, with the cationic terminal groups strongly interacting with the phosphate lipid headgroups and the +**EO** backbone embedded in the hydrophobic region. The altered chain packing induced by the aggregation of anionic lipids may allow increased internalization of +**EO**, as has been observed for antimicrobial peptides.[64] The results show that this internalization of +**EO**s across the membrane leads to changes in the local thickness of the membrane, which could lead to pitting on a larger scale. In fact, experimental studies of model bacterial membranes after disruption by +**EO** or the surfactant Triton X-100 point to a "carpet-like" mechanism for both. The bacterial membranes revealed the characteristics of an inverse hexagonal phase after treatment with Triton X-100, a typical surfactant which disrupts the bilayer by the "carpet" model mechanism.[14,15] An inverse hexagonal phase has also been observed to form from a bacterial membrane mimic after treatment with +**EO**, which suggests a similar mechanism of disruption by Triton X-100 and it. [15]

5.4 Gaining Access to Longer Timescales

In a continued effort to sample longer timescales in our simulations, several strategies have been attempted and a few have been successful to varying degrees. Initially a coarse-grained model was made for both end-only and a n=3 OPE following the Martini model by Marrink and coworkers. While this model was useful, the interactions for the larger OPEs were not described accurately enough for continued usage. More recently, the Lipid14 parameters for Amber forcefields were published and this allowed the adaptation of simulations described above to this model.[66] One of the benefits of Amber is that it can run entirely on a Graphics Processing Unit (GPU) in a computer.[67] This allows for extremely fast simulation speeds relative to what is

normally achieved on a CPU, which in turn makes calculations of 1-5 microseconds feasible in a reasonable timeframe. In this section, the results from these two approaches are discussed, and possible future directions are given.

5.4.1 *Amber Lipid14 Parameters for GPU Acceleration*

A recently developed forcefield, the Lipid14 (formerly Lipid12 and Lipid11) set of parameters for lipids is a modular forcefield which allows accurate simulations of lipids without forcing a constant surface tension into the interface. As the previous simulations were performed using CHARMM36, a top contender among lipid forcefields, it was necessary for the GPU-accelerated simulations to have a quality near that of the previous all-atom simulations using CHARMM forcefields and NAMD.[68,69] In the validation of the Lipid14 forcefield, it was found to reproduce values such as NMR order parameters and scattering data in good agreement with experiment. It is worth noting that the POPE lipids were found to be artificially "too ordered" and that little work with the PG lipids was reported in the initial study.[66] All of the simulations discussed in this section were simulated on GPUs to allow access to longer timescales, as the CPU and GPU results were found in the initial validation study to be comparable.[66] The methods used for system preparation and analysis, as well as additional system information, are detailed in the methods section (Chapter 7). Four simulations were repeated from the above two studies of the OPEs, with particular focus on the end-only OPEs as no clear mechanism was observed in the original all-atom studies.

The simulation of 3 **+2H** initially in the water box with backbones aligned with the membrane surface was repeated on the microsecond timescale. A snapshot at 325 ns from this simulation trajectory is given below, in Figure 5.15.

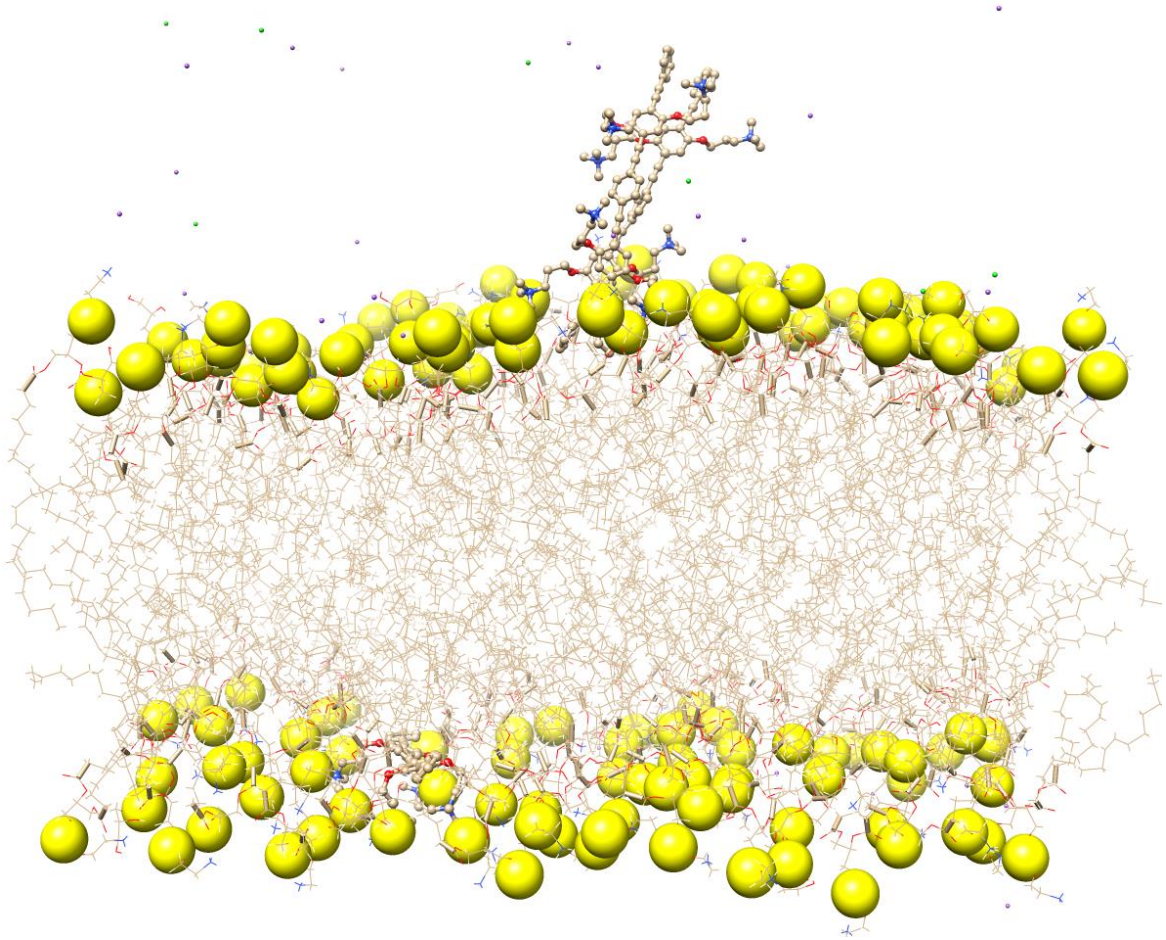

Figure 5.15. Snapshot at 325ns of aggregate of **+2H** oriented perpendicular to bilayer surface

In Figure 5.16 we can observed that the same self-assembly between OPEs seen in section 5.2.1 also occurs on a similar timescale (~100 ns). As was also observed, the complex of two OPEs tends to stand up perpendicular to the membrane where the single OPE lies down on the surface of the membrane.

The end-only OPEs were studied by 3 or 8 **+EO** fully inserted into the bilayer or 8 **+EO** initially in the water box above the bilayer surface oriented along the membrane surface. The simulations of **+EO** initially embedded across the bilayer yield a similar result of slight membrane thinning that is discussed in sections 5.3.1 and 5.4.2, and are not shown. The simulation of 8 **+EO** initially in the water box on the microsecond timescale allowed observation of interesting aggregation and bilayer damage effects which have been previously discussed but not yet observed in simulation. Timelines along the course of this simulation is given below, in Figure 5.17.

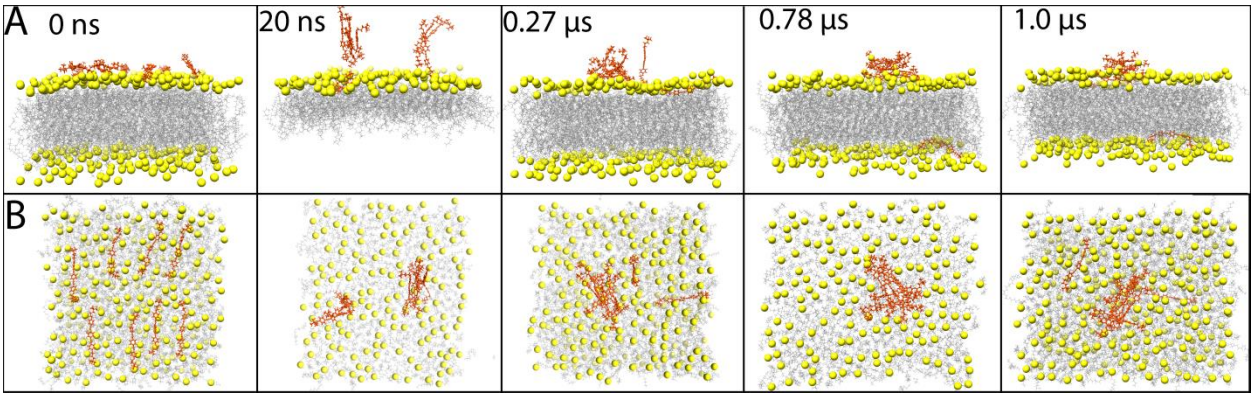

Figure 5.17. Timeline of 8 **+EO**s interacting with a 4:1 DOPE:DOPG bilayer with 300 lipids in explicit water using the Amber Lipid14 force field with GPU acceleration over 1 microsecond of simulation.

In Figure 5.17 above, we can clearly see that the **+EO** molecules aggregate with one another in the water box over the course of the first 800 ns to form a large complex with many of the OPEs. Once this complex is formed and stuck to the membrane surface, lipids at the edge of the complex are observed to start "crawling" up the sides of the OPE complex. This is the result of electrostatic attraction between the phosphates of the lipids and the cationic quaternary ammonium headgroups of the OPEs. Recent experimental studies of cationic phenylene vinylene oligomers (OPV) with structural similarities to **+EO** has shown that membrane pitting occurs to model bacterial membranes and bacteria.[70] Clearly the results given in this microsecond-timescale study support the pitting of the membrane as a precursor of or component of the membrane disruption activity of these molecules. While these results are of good quality, the system size (number of lipids and OPEs) is too low to observe slight effects on membrane curvature or the effects of large numbers of OPEs in the system. It would be difficult to apply these constraints to an all-atom system, as the computational time would increase dramatically despite the speed offered by GPUs. Therefore a coarse-grained representation was used for the OPEs in accordance with the Martini model, as discussed in the following section.

5.4.2 *Coarse-Grained Simulations with the Martini Model*

One of the most used and adapted coarse-grained models for biomolecular simulations, particularly those involving lipids, is the Martini coarse-grained model by S. Marrink and

coworkers.[71] This model generally applies a 4-to-1 strategy for reduction of 4 heavy atoms to "beads", particles which represent 4 atoms, except for in the case of aromatic or cyclic systems which may be better represented using 3 heavy atoms per bead. The adaptation of the OPEs to the Martini model and the associated bead types are described in the methods section (Chapter 7). Two OPEs, the n=3 OPE **+3H** and the end-only OPE **+EO**, were represented and parametrized for use in simulation. Several previous simulations were adapted to the Martini CG model and repeated, such as that with 3 **+2H** fully inserted. In addition, test systems with a large excess of OPEs and larger bilayers were prepared using the Martini model with Polarizable water[72], and compared with a recently developed "dry" model which uses implicit solvent.[73] All relevant coarse-grained simulations performed are listed in section 7.2.3.3 of the methods section.

The end-only OPEs were examined using coarse-grained simulations, as the carpet model of aggregation is suspected to occur upon longer timescales than can be observed on the sub-microsecond timescale. Several different coarse-grained simulations with **+EO** were performed, as described in the methods section (Chapter 7). The original all-atom simulations discussed in section 5.3 were converted into the martini CG model using bead definitions as described in the methods section, in order to make a direct comparison between the two models. The trajectories of two simulations with 8 **+EO**s inside and outside of the membrane are shown below, in Figure 5.18

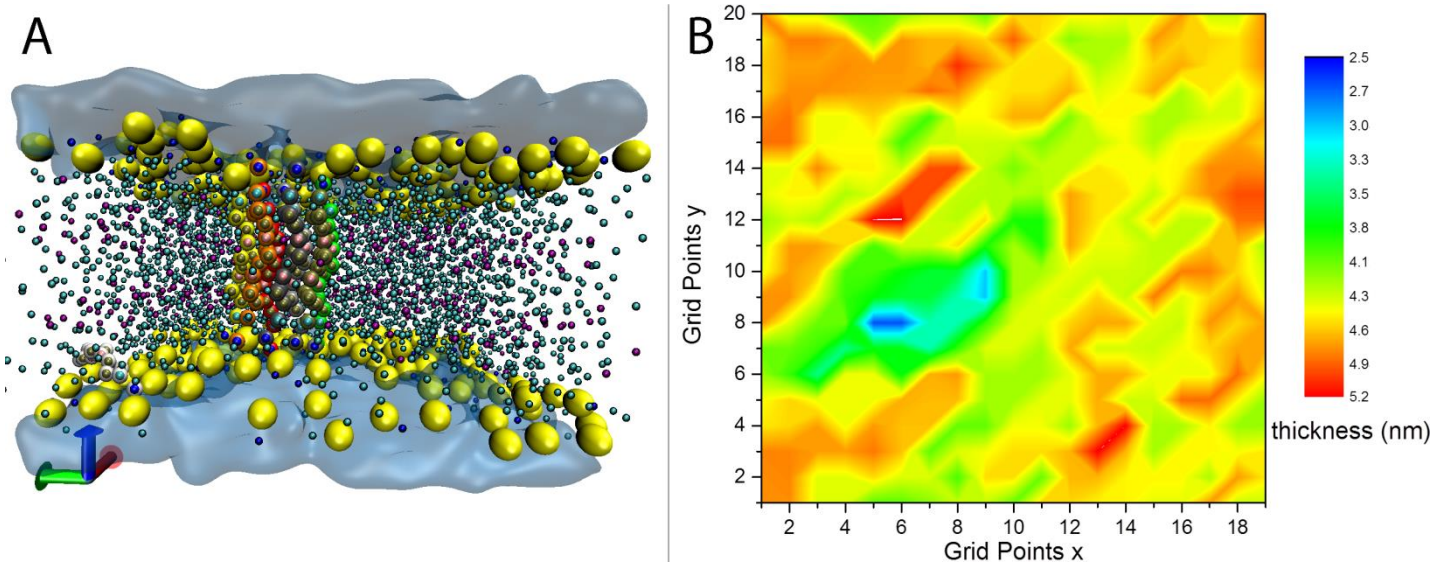

Figure 5.18 (A) Snapshot after 6 us of simulation of 8 **+EO**s with a 300 lipid bilayer in polarizable water, and (B) Membrane thickness at the same time, where x and y axes have

dimensions of 10 nm. The lipid headgroups are yellow spheres and the water is transparent blue. It is clear when comparing the snapshots in Figure 5.18 with the results of the all-atom study of the same system in section 5.3 that the results of the CG model for **+EO** closely resemble those observed at the all-atom level of description. In the case of the fully inserted **+EO**s, there was a similar slight reduction in local membrane thickness. In addition, the OPEs seemed to pack closely into a defined region, more closely packed and with a more defined structure than observed at the all-atom level. In the water box, the OPEs appeared to form aggregates at the membrane surface and affect the local curvature. This same result was observed at microsecond timescales at the all-atom level using Amber-GPU, as described in the previous section. The change in membrane structure is not significant over the course of a 6 microsecond simulation, which casts doubt on the hypothesis that this inserted mode leads to membrane disruption. It does, however, support the use of these types of molecules as membrane stains in low concentrations, as has been performed in recent studies with a similar compound. [71] In order to better understand the effects of OPE aggregation on larger membranes, a membrane with four times as many lipids was formed and several situations involving **+EO** at the surface were explored. Two timelines of 50 and 100 OPEs on this surface are given below, in Figure 5.19.

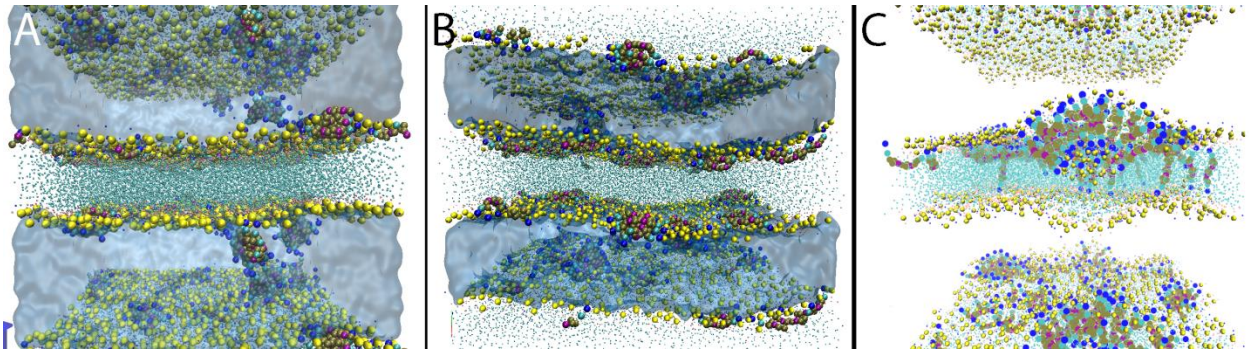

Figure 5.19. Snapshots from the simulations of (A)50 **+EO** with polarizable water after 400 ns, (B) 100 **+EO** with polarizable water after 6 us, and (C) 100 **+EO** after 1.2 us with the "dry" Martini implicit solvent model

In Figure 5.19 we can observe many aggregates on the surface forming at only 50 **+EO** in the water box. The result of 100 **+EO** in the water box was clearly catastrophic to the membrane, as one can clearly see the formation of a blister of lipids on the surface of the membrane which results from the membrane enveloping a large aggregate of OPEs. This may in fact be the carpet

mechanism of end-only OPEs at work. Despite this observation, this blister formation did not occur in all iterations of this simulation. Both the simulations with nonpolarizable water and the simulations with polarizable water yielding only complex formation at the interface resulting in changes to membrane curvature as seen in the all-atom results. Following a similar workflow, the "dry" Martini CG forcefield, which uses an implicit solvent model for water, was used to assess the effects of large numbers of OPEs at the interface.[73]

The analysis of the interactions at the membrane-water interface that leads to OPE insertion is crucial for understanding the mechanisms leading to pore formation, but is difficult through simulation studies as they occur on a long timescale. The coarse-grained simulations of the OPEs with sidechains somewhat reproduced the phenomena observed at the all-atom level, but there were some notable discrepancies. The simulation of 3 **+3H** molecules fully inserted into the bilayer followed a similar path as observed in the all-atom simulations, but the formation of a water pore occurred much more quickly (20 ns). In addition, the width of the pore was found to be transient and there were not always water molecules passing between leaflets as in the all-atom simulations. In addition to the differences in pore severity and structure, there were differences in the orientation of the aggregates of OPEs on the surface of the membrane. This can be observed in Figure 5.20, below.

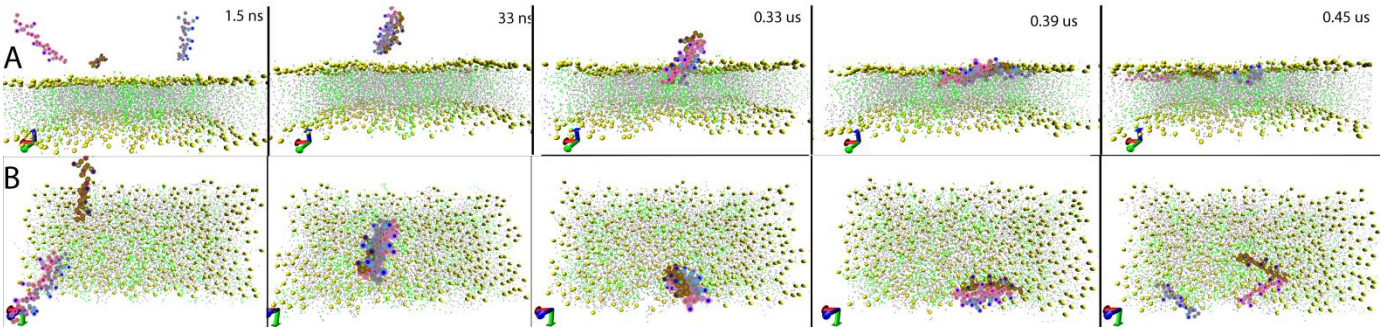

Figure 5.20. Timeline of the coarse-grained simulation trajectory of 3 **+3H** molecules interacting with a bilayer of 150 lipids in polarizable water shown from the (A) side, and (B) top. Water is not shown for clarity.

Similar structures of aggregates of **+3H** within and outside of the membrane were observed using the Martini CG model as in the previous all-atom studies, however in the coarse-graining model there were discrepancies which can be attributable to the lack of rigidity of the backbone compared to the all-atom representation. In the previous sections in this chapter the classical

molecular dynamics of **+3H** and **+2H** in the water box outside of the membrane revealed the formation of aggregates which stood perpendicular to the membrane surface. In the case of the coarse-grained model, this aggregate of **+3H** only briefly (335 ns-390 ns) stands up from the membrane, and then upon coming into lateral contact with the bilayer the complex dissociates and the different OPEs lie in the lipid phase at the interface with water.

The difficulty of enforcing a truly rigid backbone in a coarse-grained system for a large rigid molecule such as **+3H** is not trivial. As the timestep is 20 to 30fs, this can affect the stability of any bonds which have a frequency of motion which is faster than the timestep. This adds to the differences in physical properties that result from the use of pseudoatoms rather than representing each individual atom as is the case in classical MD. Some of the problems with keeping the backbone of **+3H** properly rigid while accurately flexible are mitigated through rigorous parametrization and use of different restraints as detailed in the methods section. Despite this, the complexity of the larger OPEs adds to the difficulty of properly parametrizing a CG model to agree correctly with the all-atom model. **+EO** was straightforward to parametrize and reproduces all-atom characteristics well as it is much smaller and more of a rigid rod than the **+3H**.

5.5 Conclusions and Outlook

The mechanism for disruption of model bacterial membranes by cationic oligo-*p*-phenylene ethynylenes has been explored using all-atom molecular dynamics, by which it was possible to determine how the structure of the OPEs and the degree of self-aggregation affect the stability of a lipid bilayer on the microsecond timescale. The effects of self-aggregation on OPE-bilayer interactions were found to be significant, both when the OPEs are placed in and out of the bilayer. The +*n*Hs (with *n*=1,2,3) aggregate outside of the membrane to form complexes that align with the principal axis of the membrane and partially insert over fractions of a microsecond timescale, which is a likely precursor to full insertion into the bilayer. The OPEs were also found to preferentially aggregate with DOPGs rather than DOPEs, suggesting that large aggregates could induce the formation of DOPG-rich domains which are easily destabilized due to high repulsion between the anionic headgroups. The end-only OPE (**+EO**) with cationic groups on the ends showed a different type of interaction with the membrane as a result of its different structural characteristics and position of charged groups. The “end-only” **+EO**s self-aggregate on

the surface of the bilayer and unlike the +*n*Hs, they do not partially insert along their long axes into the hydrophobic center of the membrane. In addition, when pre-inserted to span across the membrane axis, aggregates of **+EO** induced only a small degree (1-1.5 nm) of local thinning, almost no water penetration into the bilayer structure, and no clear formation of a water pore.

MD simulations of +*n*H OPEs interacting with a model bacterial membrane mimic show that these OPEs strongly associate with and disrupt the lipid bilayer. While one or two OPEs can insert into and partially distort the membrane, the aggregation of three OPEs in the lipid bilayer results in extensive damage and the formation of a water channel and a pore through which significant water leakage occurs. Multiple cationic OPEs provide a favorable polar environment inside the lipid bilayer for the incursion and passage of water molecules. The cationic side groups of **+3H** initially create a "ladder" for water molecules to leak through a pore in the lipid bilayer on the nanosecond timescale. This corroborates recent experimental observations of rapid vesicle leakage caused by **+3H**.[15] The simulation results show that the mechanism of membrane interaction for **+EO** and the +*n*Hs is quite different, and largely a consequence of the difference in the separation of the cationic ammonium groups.

This study provides insight into bacterial membrane disruption by these novel biocides, and gives two possible mechanisms to account for the difference between the +*n*Hs and **+EO**s in their morphological changes to bacteria. The simulation data shows that the two classes of OPEs interact differently with a bacterial membrane mimic, when placed in solution above the membrane, and when inserted into the membrane structure. The placement and mobility of the charged cationic groups on the OPEs plays a vital role in their interactions with each other, and the lipid bilayer. The simulations demonstrate that the two classes of OPEs: +*n*H and **+EO** result in significantly different outcomes with bilayer structures on the microsecond timescale. +*n*Hs result in the formation of water pores, while the only effects of **+EO** on similar timescales are to produce some membrane thinning and aggregation of DOPG around the oligomers.

The classical MD results are in agreement with recent experimental findings.[14,15] ^{31}P NMR and SAXS profiles of model bacterial membranes after disruption by either **+EO** or the surfactant Triton X-100, both revealed the characteristics of an inverse hexagonal phase.[15] The +*n*H series revealed a different membrane phase, quite distinct in appearance from an inverse hexagonal phase. Interestingly, the simulation results show that all the +*n*Hs result in significant membrane disruption through membrane thinning and water pore-formation, whereas **+EO**

shows no water pore formation and only modest membrane thinning in the vicinity of the **+EO**s. The MD results are consistent with the experimental data that shows that the "end-only" oligomers and the +*n*H family interact and disrupt the membrane structure in fundamentally different ways. This new knowledge of the mechanism will be used in future synergistic experimental and computational studies to design antimicrobial agents based on the phenylene-ethynylene motif with higher efficacy and specificity.

5.6 References

(1) Klevens, R. M.; Edwards, J. R.; Richards, C. L. *et al.* Estimating health care-associated infections and deaths in U.S. hospitals, 2002. *Public Health Rep.* **2007,** *122* (2), 160–166.

(2) Tacconelli, E.; De Angelis, G.; Cataldo, M. A.; Pozzi, E.; Cauda, R. Does antibiotic exposure increase the risk of methicillin-resistant Staphylococcus aureus (MRSA) isolation? A systematic review and meta-analysis. *J. Antimicrob. Chemother.* **2008,** *61* (1), 26–38.

(3) Cooper, B. S.; Medley, G. F.; Stone, S. P. *et al.* Methicillin-resistant Staphylococcus aureus in hospitals and the community: stealth dynamics and control catastrophes". *Proc. Nat. Acad. Sci.* **2004,** *101*(27), 10223–8.

(4) Chamchod, F.; Ruan, S.; Modeling methicillin-resistant *Staphylococcus aureus* in hospitals: Transmission dynamics, antibiotic usage and its history *Theor. Biol. Med. Model.* **2012,** *9*(25)

(5) Nickerson, E. K.; West, T. E.; Day, N. P.; Peacock, S. J. Staphylococcus aureus Disease and Drug Resistance in Resource-Limited Countries in South and East Asia. *Lancet Infect. Dis.* **2009,** *9*, 130–135.

(6) Gorwitz, R.; Fridkin, S. K.; Workowski, K. A. More Challenges in the Prevention and Management of Community-Associated, Methicillin-Resistant Staphylococcus aureus Skin Disease. *Ann. Intern. Med.* **2008,** *148,* 310–312.

(7) Bunz, U. H. Poly(aryleneethynylene)s: Syntheses, Properties, Structures, and Applications. *Chem. Rev.* **2000**, *100*, 1605-44.

(8) Jiang, H.; Taranekar, P.; Reynolds, J. R.; Schanze, K. S. Conjugated Polyelectrolytes: Synthesis, Photophysics, and Applications. *Angew. Chem. Int. ed.* **2009**, *48*, 4300-16.

(9) Achyuthan, K. E.; Bergstedt, T. S.; Chen, L.; Jones, R. M.; Kumaraswamy, S.; Kushon, S. A.; Ley, K. D.; Lu, L.; McBranch, D.; Mukundan, H. et al. Fluorescence Superquenching of Conjugated Polyelectrolytes: Applications for Biosensing and Drug Discovery. *J. Mat. Chem.* **2005**, *15*, 2648-2656.

(10) Lu, L.; Rininsland, F. H.; Wittenburg, S. K.; Achyuthan, K. E.; McBranch, D. W.; Whitten, D. G. Biocidal activity of a light-absorbing fluorescent conjugated polyelectrolyte. *Langmuir* **2005,** *21*(22), 10154-10159.

(11) Corbitt, T. S.; Ding, L.; Ji, E.; Ista, L. K.; Ogawa, K.; Lopez, G. P.; Schanze, K. S.; Whitten, D. G. Light and dark biocidal activity of cationic poly(arylene ethynylene) conjugated polyelectrolytes*Photochem. Photobiol. Sci.* **2009**, *8*, 998-1005.

(12) Zhou, Z.; Corbitt, T. S.; Parthasarathy, A.; Tang, Y.; Ista, L. K.; Schanze, K. S.; Whitten, D. G. "End-Only" Functionalized Oligo(phenylene ethynylene)s: Synthesis, Photophysical and Biocidal Activity. *J. Phys. Chem. Lett.* **2010**, *1*, 3207-3212.

(13) Tang, Y.; Corbitt, T. S.; Parthasarathy, A.; Zhou, Z.; Schanze, K. S.; Whitten, D. G. Light-induced Antibacterial Activity of Symmetrical and Asymmetrical Oligophenylene Ethynylenes. *Langmuir* **2011**, *27*, 4956-62.
(14) Wang Y.; Tang Y.; Zhou Z.; Ji E.; Lopez G. P.; Chi E. Y.; Schanze K. S.; Whitten D. G. Membrane Perturbation Activity of Cationic Phenylene Ethynylene Oligomers and Polymers: Selectivity against Model Bacterial and Mammalian Membranes. *Langmuir* **2010,** *26,* 12509-12514
(15) Wang, Y.; Jett, S. D.; Crum, J.; Schanze, K. S.; Chi, E. Y.; Whitten, D. G. Understanding the dark and light-enhanced bactericidal action of cationic conjugated polyelectrolytes and oligomers. *Langmuir* **2013,** *29*(2), 781–92.
(16) Wang, Y.; Corbitt, T. S.; Jett, S. D.; Tang, Y.; Schanze, K. S.; Chi, E. Y.; Whitten, D. G. Direct Visualization of Bactericidal Action of Cationic Conjugated Polyelectrolytes and Oligomers. *Langmuir* **2011,** *28*, 65–70.
(17) Wang Y.; Chi E. Y.; Schanze K. S.; Whitten D. G. Membrane Activity of Antimicrobial Phenylene Ethynylene based Polymers and Oligomers. *Soft Matter* **2012,** *8,* 8547-8558
(18) Hancock, R. E. W.; Lehrer, R. Cationic peptides: a new source of antibiotics *Trends in Biotechnology* **1998,** *16*(2), 82-88
(19) Hancock, R. E.W.; Rozek, A. Role of membranes in the activities of antimicrobial cationic peptides. *FEMS Microbiology Letters* **2002,** *206*, 143–149.
(20) Kanazawa, A.; Ikeda, T.; Endo, T. Polymeric phosphonium salts as a novel class of cationic biocides. II. Effects of counter anion and molecular weight on antibacterial activity of polymeric phosphonium salts. *J. Polym. Sci. A Polym. Chem.* **1993,** *31*, 1441–1447.
(21) Kawabata, N.; Nishiguchi, M. Antibacterial activity of soluble pyridinium-type polymers. *Appl. Environ. Microbiol.* **1988,** *54*(10), 2532-2535
(22) Kenawy, E.-R.; Worley, S. D.; Broughton, R. The Chemistry and Applications of Antimicrobial Polymers: A State-of-the-Art Review *Biomacromolecules*, **2007**, *8*(5), 1359–1384
(23) Arnt, L.; Nüsslein, K; Tew, G. N. Nonhemolytic abiogenic polymers as antimicrobial peptide mimics. *J. Polym. Sci. A Polym.* Chem. **2004,** *42*, 3860–3864.
(24) Tew, G. N.; Scott, R. W.; Klein, M. L.; Degrado, W. F. De novo Design of Antimicrobial Polymers, Foldamers, and Small Molecules: from Discovery to Practical Applications. *Accts. Chem. Res.* **2010**, *43*, 30–9.
(25) Shai, Y. Molecular recognition between membrane-spanning polypeptides *Trends Biochem. Sci.* **1995,** *20*, 460−464.
(26) Melo, M. N.; Ferre, R.; Castanho, M. Antimicrobial peptides: linking partition, activity and high membrane-bound concentrations *Nature Reviews Microbiology* **2009,** *7*, 245-250
(27) Baumann, G.; Mueller, P. A molecular model of membrane excitability. *J. Supramol. Struct.* **1974,** *2*, 538-557.
(28) Boheim, G. Statistical analysis of alamethicin channels in black lipid membranes. *J. Membr. Bio.* **1974,** *19*, 277-303.
(29) Mollay, C.; Krell, G.; Fluorometric measurements on the interactton of melittin with lecithin *Biochimica et Biophysica Acta (BBA) - Lipids and Lipid Metabolism* **1973,** *316*(2), 196–203
(30) Verma, S. P.; Wallach, D. F. H.; Smith, I. C. P. The action of melittin on phosphatide multibilayers as studied by infrared dichroism and spin labeling. A model approach to lipid-protein interactions *Biochimica et Biophysica Acta (BBA) – Biomembranes* **1974,** *345*(1),129-140

(31) Zasloff, M. Magainins, a class of antimicrobial peptides from Xenopus skin: isolation, characterization of two active forms, and partial cDNA sequence of a precursor. *Proc. Nat. Acad. Sci.* **1987,** *84*, 5449
(32) Matsuzaki, K.; Sugishita, K.; Harada, M.; Fujii, N.; Miyajima, K. Interactions of an antimicrobial peptide, magainin 2, with outer and inner membranes of Gram-negative bacteria *Biochimica et Biophysica Acta (BBA) – Biomembranes* **1997,** 1327(1), 119–130
(33) Yang**, L.;** Harroun**, A. T.;** Weiss**, T. M.;** Ding, L.; Huang, H. W. Barrel-Stave Model or Toroidal Model? A Case Study on Melittin Pores *Biophysical Journal* **2001,** *81*(3), 1475-1485
(34) Woo, H.-J.; Wallqvist, A. Spontaneous buckling of lipid bilayer and vesicle budding induced by antimicrobial peptide magainin 2: a coarse-grained simulation study. *J. Phys. Chem. B* **2011,** *115*, 8122–9.
(35) Lin, J.-H.; Baumgaertner, A. Molecular Dynamics Simulations of Hydrophobic and Amphiphatic Proteins Interacting with a Lipid Bilayer Membrane. *Comp. and Theor. Polymer Sci.* **2000**, *10*, 97–102.
(36) Santo, K. P.; Berkowitz, M. L. Difference between Magainin-2 and Melittin Assemblies in Phosphatidylcholine Bilayers: Results from Coarse-grained Simulations. *J. Phys. Chem. B* **2012**, *116*, 3021–30.
(37) Soliman, W.; Bhattacharjee, S.; Kaur, K. Interaction of an Antimicrobial Peptide with a Model Lipid Bilayer using Molecular Dynamics Simulation. *Langmuir* **2009**, *25*, 6591–5.
(38) Irudayam, S. J.; Berkowitz, M. L. Influence of the Arrangement and Secondary Structure of Melittin Peptides on the Formation and Stability of Toroidal Pores. *Biochimica et Biophysica Acta* **2011**, *1808*, 2258–66.
(39) Sengupta, D.; Leontiadou, H.; Mark, A. E.; Marrink, S. Toroidal Pores Formed by Antimicrobial Peptides Show Significant Disorder. *Biochimica et Biophysica Acta* **2008,** *1778*(10), 2308-2317
(40) Irudayam, S. J.; Berkowitz, M. L. Binding and Reorientation of Melittin in a POPC Bilayer: Computer Simulations. *Biochimica et Biophysica Acta* **2012**, *1818*, 2975–2981.
(41) Manna, M.; Mukhopadhyay, C. Cause and Effect of Melittin-induced Pore Formation: a Computational Approach. *Langmuir* **2009**, *25*, 12235–42.
(42) Shepherd, C. M.; Vogel, H. J.; Tieleman, D. P. Dermaseptin S3 with Lipid Bilayers : Molecular-dynamics Simulations. *Biochem. J.* **2003**, *370*, 233-243.
(43) Ivanov, I.; Vemparala, S.; Pophristic V.; Kuroda, K.; DeGrado , W. F.; McCammon, J. A.; Klein, M. L. Characterization of Nonbiological Antimicrobial Polymers in Aqueous Solution and at Water−Lipid Interfaces from All-Atom Molecular Dynamics *Journal of the American Chemical Society* **2006,** *128* (6), 1778-1779
(44) Leontiadou, H.; Mark, A. E.; Marrink, S. J. Antimicrobial Peptides in Action *Journal of the American Chemical Society* **2006,** *128* (37), 12156-12161
(45) Dittmer, J.; Thøgersen, L.; Underhaug, J.; Bertelsen, K.; Vosegaard, T.; Pedersen, J. M.; Schiøtt, B.; Tajkhorshid, E.; Skrydstrup, T.; Nielsen, N. C. Incorporation of Antimicrobial Peptides into Membranes: a Combined Liquid-state NMR and Molecular Dynamics Study of Alamethicin in DMPC/DHPC Bicelles. *J. Phys. Chem. B* **2009**, *113*, 6928–37.
(46) Alder, B. J. and Wainwright, T. E. Phase transition for a hard sphere system *J. Chem. Phys.* **1957,** *27*, 1208
(47) Alder, B. J. and Wainwright, T. E. Studies in molecular dynamics. I. General method *J. Chem. Phys.* **1959,** *31*, 459
(48) Rahman, A. Correlations in the motion of atoms in liquid argon. *Phys. Rev.* **1964,** *A136*,

405
(49) Stillinger, F. H.; Rahman, A. Molecular dynamics study of liquid water under high compression *J. Chem. Phys.* **1974,** *60*, 1545
(50) McCammon, J. A.; Gelin, B. R.; Karplus, M. Dynamics of folded proteins. *Nature (Lond.)* **1977,** *267*, 585-590
(51) Hill, E. H.; Stratton, K.; Whitten, D. G.; Evans, D. G. Molecular Dynamics Simulation Study of the Interaction of Cationic Biocides with Lipid Bilayers: Aggregation Effects and Bilayer Damage. *Langmuir* **2012**, *28,* 14849−14854.
(52) Hill, E. H.; Whitten, D. G.; Evans, D. G. Computational Study of Bacterial Membrane Disruption by Cationic Biocides: Structural Basis for Water Pore Formation *J. Phys. Chem. B,* Article ASAP **DOI:** 10.1021/jp504297s
(53) Allen, W. J.; Lemkul, J. A.; Bevan, D. R. GridMAT-MD: A Grid-based Membrane Analysis Tool for Use With Molecular Dynamics. *J. Comput. Chem.* **2009,** *30* (12): 1952-1958
(54) Roe, D.R.; Cheatham, T.E., III; PTRAJ and CPPTRAJ: Software for Processing and Analysis of Molecular Dynamics Trajectory Data *J. Chem. Theor. Comp.* **2013,** 9 (7), 3084–3095
(55) Wu, M.; Maier, E.; Benz, R.; Hancock, R. E. W. Mechanism of Interaction of Different Classes of Cationic Antimicrobial Peptides with Planar Bilayers and with the Cytoplasmic Membrane of Escherichia coli *Biochemistry* **1999** *38* (22), 7235-7242
(56) Matsuzaki, K.; Mitani, Y.; Akada, K. Y.; Murase, O.; Yoneyama, S.; Zasloff, M.; Miyajima, K. Mechanism of synergism between antimicrobial peptides magainin 2 and PGLa *Biochemistry* **1998,** *37*, 15144−15153.
(57) Fattal, E; Nir, S.; Parente, R. A.; Szoka, F.C. Jr. Pore-Forming Peptides Induce Rapid Phospholipid Flip-Flop in Membranes. *Biochemistry* **1994,** *33,* 6721-6731
(58) Matsuzaki, K.; Murase, O.; Fujii, N.; Miyajima, K. An Antimicrobial Peptide, Magainin 2, Induced Rapid Flip-Flop of Phospholipids Coupled with Pore Formation and Peptide Translocation. *Biochemistry* **1996,** *35,* 11361-11368
(59) Tieleman, D.P.; Marrink, S. Lipids Out of Equilibrium: Energetics of Desorption and Pore Mediated Flip-Flop. *J. Am. Chem. Soc.* **2006,** *128,* 12462-12467
(60) Gurtovenko, A. A.; Vattulainen, I. Molecular Mechanism for Lipid Flip-Flops. *J. Phys. Chem. B* **2007,** *111,* 13554-13559
(61) Hwang, H.; Schatz, G. C.; Ratner, M. A. Coarse-Grained Molecular Dynamics Study of Cyclic Peptide Nanotube Insertion into a Lipid Bilayer. *J. Phys. Chem. A* **2009,** *113*(16), 4780-4787
(62) Epand, R. M.; Epand, R. F.; Shai, Y. Lipid clustering by three homologous arginine-rich antimicrobial peptides is insensitive to amino acid arrangement and induced secondary structure. *Biochim. Biophys. Acta.* **2010,** *1798*, 1272–1280.
(63) Wadhwani, P.; Epand , R. F.; Heidenreich, N.; Bürck, J.; Ulrich, a. S.; Epand, R. M. Membrane-active peptides and the clustering of anionic lipids. *Biophys. J* **2012,***103,* 265–74.
(64) Jobin, M.-L.; Bonnafous, P.; Temsamani, H.; Dole, F.; Grélard, A.; Dufourc, E. J. et al. The enhanced membrane interaction and perturbation of a cell penetrating peptide in the presence of anionic lipids: toward an understanding of its selectivity for cancer cells. *Biochim. Biophys. Acta.* **2013,** *1828,* 1457–70.
(65) Walrant, A.; Correia, I.; Jiao, C.-Y.; Lequin, O.; Bent, E. H.; Goasdoué, N.; Lacombe, C.; Chassaing, G.; Sagan, S.; Alves, I. D. Different membrane behaviour and cellular uptake of three basic arginine-rich peptides, *Biochim. et Biophys. Acta – Biomembranes* **2011,** *1808*(1)*,* 382-393

(66) Dickson, C. J.; Madej, B. D.; Skjevik, A. A.; Betz, R. M.; Teigen, K.; Gould, I. R.; Walker, R. C. Lipid14: The Amber Lipid Force Field. *Journal of Chemical Theory and Computation* **2014,** *10*(2), 865–879
(67) Salomon-Ferrer, R.; Goetz, A.W.; Poole, D.; Le Grand, S.; Walker, R.C. Routine microsecond molecular dynamics simulations with AMBER on GPUs. 2. Explicit Solvent Particle Mesh Ewald *J. Chem. Theory Comput.* **2013,** DOI: 10.1021/ct400314y
(68) Lee, S.; Tran, A.; Allsopp, M.; Lim, J. B.; Henin, J.; Klauda, J. B. CHARMM36 United-Atom Chain Model for Lipids and Surfactants. *The Journal of Physical Chemistry B* **2014,** *118* (2), 547–556
(69) Phillips, J. C.; Braun, R.; Wang, W.; Gumbart, J.; Tajkhorshid, E.; Villa, E.; Chipot, C.; Skeel, R. D.; Kale, L.; Schulten, K. Scalable molecular dynamics with NAMD. *Journal of Computational Chemistry* **2005,** *26,* 1781-1802, http://www.ks.uiuc.edu/Research/namd/
(70) Hinks, J., et al. Modeling Cell Membrane Perturbation by Molecules Designed for Transmembrane Electron Transfer. *Langmuir* **2014,** *30*(9), 2429-2440.
(71) Marrink, S. J.; Risselada, H. J.; Yefimov, S.; Tieleman, D. P.; de Vries, A. H. The MARTINI force field: coarse grained model for biomolecular simulations. *The Journal of Physical Chemistry B* **2007,** *111*(27),7812-7824.
(72) de Jong, D. H.; Singh, G.; Bennett, W. F. D.; Arnarez, C.; Wassenaar, T. A.; Schaefer, L. V.; Periole, X.; Tieleman, D. P.; Marrink, S. J. Improved parameters for the martini coarse-grained protein force field. *Journal of Chemical Theory and Computation* **2012,** *9*(1), 687-697.
(73) Arnarez, C.; Uusitalo, J. J.; Masman, M. F.; Ingólfsson, H. I.; de Jong, D. H.; Melo, M. N.; Periole, X.; de Vries, A. H.; Marrink, S. J. Dry Martini, a coarse grained implicit water force field for (bio)molecular simulations, In preparation.

Chapter VI: Summary and Future Directions

6.1 Summary

This work discusses several different themes involving the photophysical and photochemical properties of the OPEs which are of note. It was previously thought that the red-shifted absorbance band seen upon aggregation of OPEs on cellulose scaffolds was due to J-aggregation. The photophysical properties of the OPEs were studied through DFT calculations of ground-state optimized geometries and excited-state energies, which suggested that the coplanarity of phenyl rings along the backbone strongly contribute to a reduced excitation energy. This provided a rationale for the redshifted absorbance seen for larger OPEs rather than an n=1 OPE, and the lack of a continued red-shift as the number of repeat units goes beyond 3. The aggregation-induced photophysical changes were further studied by the formation of complexes between the two types of OPEs, end-only and with side-chains, with oppositely-charged surfactants. There was a strong structural effect, where the placement of ionic chains dictated whether an aggregate would result in a strongly red-shifted or blue-shifted absorbance spectrum. It was found that the end-only OPEs would form H-aggregates, but the OPEs with charged sidechains formed red-shifted aggregates with ionic surfactants. Interestingly, a strong dependence on H-bonding was observed in the formation of the red-shifted aggregates, with no aggregation observed for weakly or non H-bonding surfactants (e.g. **-1H** and TTAB). The effects of H-bonding on the photophysical properties of the OPEs were further explored for the series of OPEs with carboxyester endgroups, which have very weak fluorescence in water. A strong isotope effect on the fluorescence was observed, with both the fluorescence intensity and quantum yield increasing in deuterium oxide relative to water. The involvement of an extended H-bonding network between solvent, surfactant, and OPE was observed as an increase in fluorescence enhancement upon complexation in H_2O relative to D_2O, despite the opposite trend for OPE without surfactant. Once again molecular simulations were able to provide a clear picture of this extended H-bonding network between OPE, interfacial water, and surfactant.

The photodegradation efficiency, major photoproducts, and the effects of photodegradation on biocidal activity were studied to improve the current level of understanding of the use of OPEs as biocides and deciding which chemical structures are more useful for long-term stability. The products were found to be the result of water or oxygen adding across the triple-bond, and in the case of OPEs with sidechains, also the ether linkage of the sidechains.

Inspiration was taken from a study of photophysical changes upon complexation with lipids and simple surfactants, and it was found that the use of surfactants can significantly prolong the photochemical stability of the OPEs in solution. Through the use of experiment and molecular simulations, it was clear that the enhanced photostability of an OPE-surfactant complex was the result of removal of interfacial water. This strategy of surfactant complexation to modify the photochemistry was also attempted to modify the affinity of the OPE for bacterial cells. Anionic compounds do not bind strongly with bacterial membranes, as the membranes are net-anionic as well. The same goes for the OPEs, where the anionic OPEs such as **-1H** or –EO exhibit very poor killing of bacteria in the dark and under UVA irradiation. However, complexation with a low concentration of the cationic surfactant TTAB allowed the –EO to induce significant killing of both Gram-positive and Gram-negative bacteria. It is thought that the complex between the OPE and TTAB consists of a loosely-bound shell of TTAB molecules. Once the complex is able to associate with the membrane, the TTABs likely "dissolve" in the lipid bilayer, freeing the OPE to possibly enter the cell, where the damage from reactive oxygen species would be significant.

Interactions with the membrane were further studied through molecular simulations of model bacterial membranes and their interactions with different OPEs. The model membrane and bacterial experiments performed by Ying Wang and coworkers gave an excellent experimental benchmark that was used as the inspiration for the preparation of the molecular simulations. In his experiments, the OPEs with cationic end-groups gave rise to different resulting patterns of damage and lipid phases, as discussed in Chapter 1. All-atom molecular dynamics using CHARMM forcefields revealed detailed information about the interactions between the OPEs and the membrane when the OPEs were initially placed inside the bilayer, or in water at the bilayer interface. The OPEs with cationic sidegroups were able to aggregate in the membrane and form transmembrane water pores, with longer OPEs producing more significant pore formation and damage on a shorter (<0.1 μs) timescale. The end-only OPEs exhibited no tendency to form pores and only slightly reduced local membrane thickness when fully inserted into the bilayer, but many end-only OPEs can aggregate on the surface of the bilayer. These large aggregates were shown to induce pitting and surface irregularities which cause global membrane deformation using GPU-accelerated AMBER MD simulations and the martini coarse-grained model to achieve simulation times up to 10 μs. Molecular simulations were able to show that the damage induced by the end-only OPEs is similar to the "carpet model" of disruption which is

typical of detergents, where the OPEs with sidechains have the propensity to form toroidal water pores and induce similar damage as helical antimicrobial peptides. This molecular-level view of the interactions of OPEs with membranes serves as an excellent complement to the results of the experimental studies by Ying Wang *et al*, and provides a starting point for further computational studies.

6.2 Future Directions

Quantitative Simulations of OPEs with Model Bacterial Membranes

The timescale needed to observe the process of membrane disruption from an initial position of a molecule bound to the exterior of the membrane is significantly longer than current MD methods can reach. Future studies will need to access much longer timescales, and may focus on the study of spontaneous insertion of OPEs into the membrane using recently-developed methods which greatly enhance the capability to study insertions into a membrane. One method employs a membrane mimetic which is highly mobile and increases the rate of insertion by a factor of 3, while still replicating the same intermediate states.[1] The other uses surface-tension replica-exchange MD which gives a broad range of conformational sampling and increases lateral diffusion of lipids, and could be useful for detailed study of the aggregation both on and in the membrane.[2] These simulations will provide insight into membrane insertions events and enable further study of the interactions of cationic biocides with membrane mimics and the effects on local membrane curvature, membrane phase composition and structural integrity on longer timescales. The coarse-grained simulations have proved to be very useful thus far, and this will continue to be explored. These simulations will provide insight into membrane insertions events and enable further study of the interactions of cationic biocides with membrane mimics and the effects on local membrane curvature, membrane phase composition and structural integrity on longer timescales.

OPEs as Enzyme and Inhibitor Detectors

Recent work has followed the aggregation of OPEs with enzyme substrates such as phospholipids and acetylcholine analogs for sensing purposes. The OPEs have been shown to form strongly red-shifted aggregates with enhanced fluorescence upon binding to the analyte, which can then be degraded by an enzyme. This has been previously achieved with anionic PPEs

by the Schanze group at the University of Florida.[3,4] Examples of this for phospholipids with phospholipases and lauroylcholine with acetylcholinesterase are given in Figure 6.1 below.

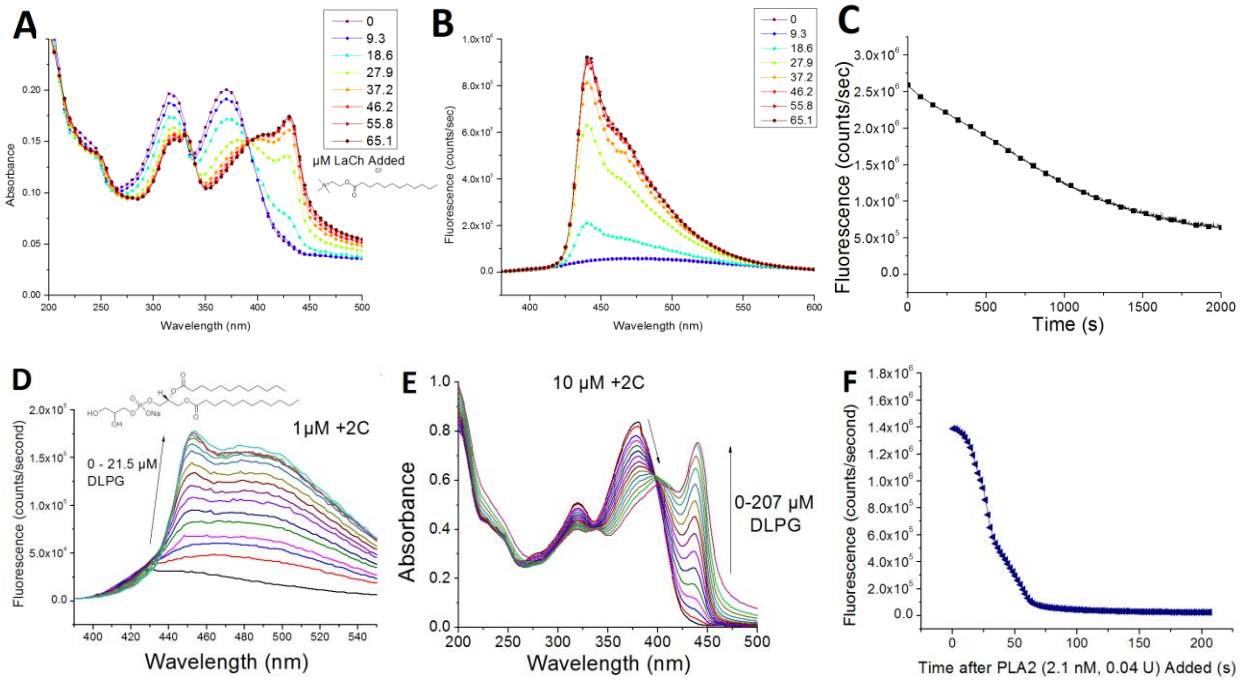

Figure 6.1. Change in (A) Absorbance and (B) Fluorescence of **+1C** under excitation at 360 nm as lauroyl choline chloride is added to the solution. (C) 0.5 Units of induced loss of fluorescence, signifying breakdown of the aggregate. (D) Change in absorbance and (E) Fluorescence of **+2C** upon addition of the phospholipid 1,2-dilauroyl-sn-glycero-3-phospho-(1'-rac-glycerol) (DLPG). (F) The breakdown of a complex of 20 nM DLPG and 1.2 µM **+2C** by Phospholipase A2 is visible by the loss of fluorescence.

As seen in Figure 6.1, the fluorescence is strongly quenched by the degradation of the OPE-surfactant complex by an enzyme. This may be useful to develop for detection of enzyme inhibition. Since the OPEs have such strong fluorescence quenching and unquenching properties and are water-soluble, they could have great use as sensors of health hazards such as neurotoxins and other enzyme inhibitors in the water supply, and possibly in the air. This work is currently under way with undergraduate Yue Zhang.

OPE-laponite Assemblies as a Biocidal Platform

The synthetic clay Laponite forms a thixotropic gel with a smectic phase, and has a strong

loading capacity for cationic molecules on the exposed faces or in the interlayer spaces. Thixotropy is a shear-thinning property where the return to a gel state after stress is usually quick. We have been recently looking into the loading of OPEs onto laponite in solution, and also processing into surface layers for biocidal applications. Previous work has shown that cyanine dyes can be loaded onto exfoliated laponite particles, and recently we have found that this can also be done with OPEs.[5-7] However, the concentration of laponite used to form a complex with OPE must be carefully monitored, as anything above the max loading threshold causes the complex to precipitate from aqueous solution. This can be seen in Figure 6.2, below.

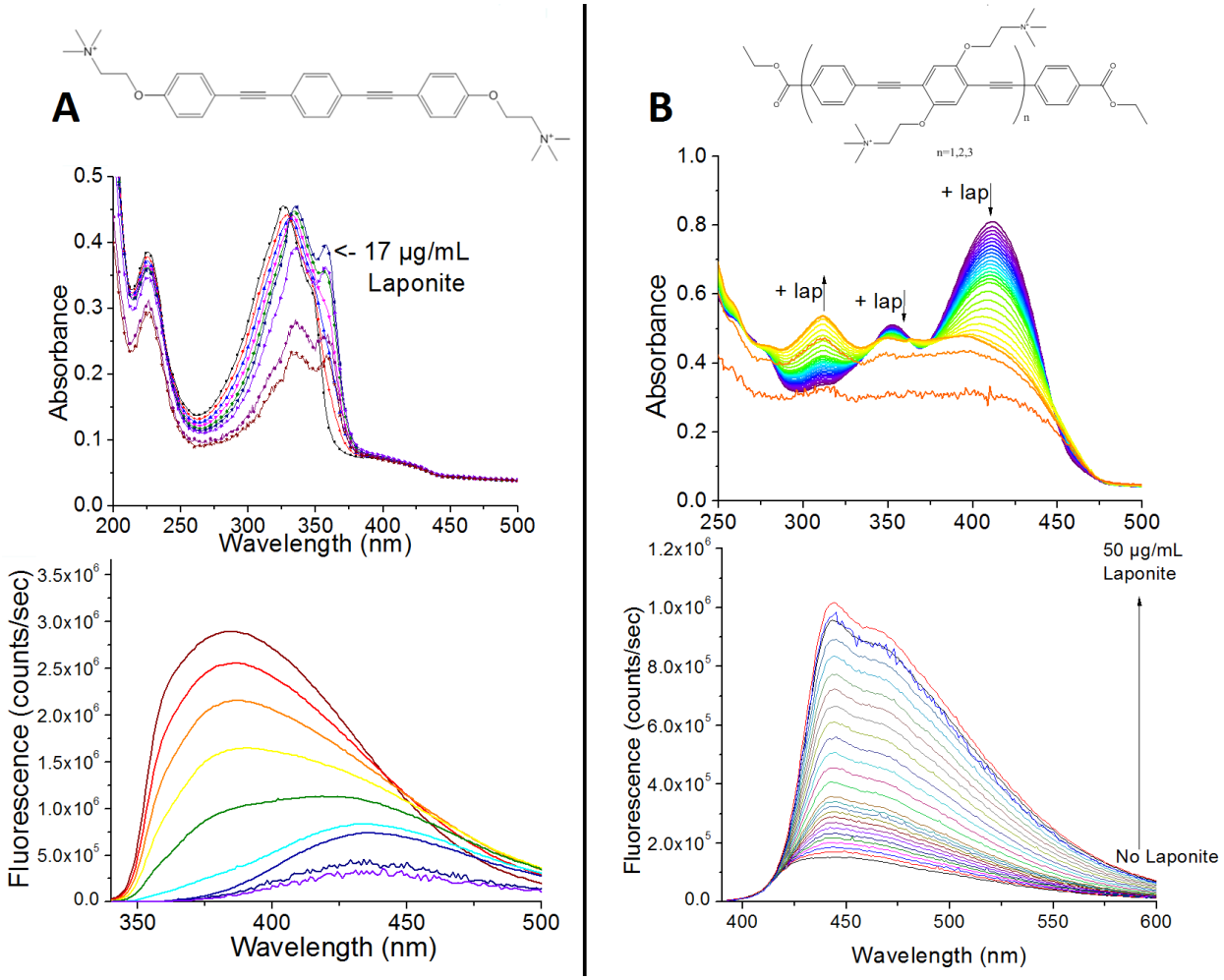

Figure 6.2. Changes in UV-Vis absorbance and fluorescence of (A) 10 µM +**EO$_{c2}$** and (B) 10 µM +**2C** in aqueous solution with varying concentrations of laponite; Note the formation of insoluble aggregates as the formation of laponite passes 20 ug/mL or 50 ug/mL for +**EO$_{c2}$** or +**2C**, respectively.

One interesting facet of the changes observed in Figure 6.2, is that when compared to those for simple surfactants such as lipids, the changes are opposite of what is observed. In the case of the end-only OPE in Figure 7.2A, the absorbance and fluorescence are both red-shifted, but the fluorescence is broadened and diminished. With the n=2 OPE +**2C**, a broadened absorbance spectrum with a sharp peak at 305 nm is observed rather than forming a red-shifted aggregate as observed with simple surfactants, though the fluorescence enhancement is still observed. There have been interesting studies recently which discuss the formation of LbL films using laponite which exhibit enhanced structural properties.[8-12] A strong degree of intercalation of OPEs into the laponite interlayer spaces may enable the creation of biocidal solid films based on this technology. The biocidal and materials testing of these films are currently underway with the help of undergraduate student Yue Zhang at UNM.

Enhancement of Biocidal Activity of Anionic OPEs with Surfactants

A set of membrane simulations which explores the biocidal enhancement of the anionic OPEs through complexation with cationic surfactants will be explored. Initial configurations will consist of OPE-surfactant (likely CTAB or TTAB) complexes placed in the water box with a separation of atleast 2 nm from the bilayer surface. AMBER with the lipid14 forcefield and GPU acceleration will be utilized for these large systems. In addition, Harry Pappas at UNM plans to further study the interactions of these complexes with model systems such as Langmuir monolayers to attempt to assess the mechanism of enhanced membrane activity.

6.3 References

(1) Vermaas, J. V.; Tajkhorshid, E. A Microscopic View of Phospholipid Insertion into Biological Membranes *J. Phys. Chem. B,* **2014**, *118* (7), 1754–1764

(2) Mori, T.; Jung, J.; Sugita, Y. Surface-Tension Replica-Exchange Molecular Dynamics Method for Enhanced Sampling of Biological Membrane Systems *J. Chem. Theory Comput.* **2013,** *9*(12), 5629–5640

(3) Pinto, M. R.; Schanze, K. S. Amplified Fluorescence Sensing of Protease Activity with Conjugated Polyelectrolytes. *Proc. Nat. Acad. Sci.* **2004**, *101*, 7505-10.

(4) Liu, Y.; Ogawa, K.; Schanze, K. S. Conjugated Polyelectrolytes as Fluorescent Sensors. *J. Photochem. Photobiol. C* **2009**, *10*, 173-190.

(5) Miyamoto, N.; Kawai, R.; Kuroda, K.; Ogawa, M. Adsorption and aggregation of a cationic cyanine dye on layered clay minerals. *Applied Clay Science* **2000,** *16*(3), 161-170.

(6) Jones, R. M.; Bergstedt, T. S.; Buscher, C. T.; McBranch, D.; Whitten, D. G. Superquenching and its applications in J-aggregated cyanine polymers. *Langmuir* **2001,** *17*(9),

2568-2571.
(7) Lu, L.; Jones, R. M.; McBranch, D.; Whitten, D. G. Surface-enhanced superquenching of cyanine dyes as J-aggregates on Laponite clay nanoparticles. *Langmuir* **2002,** *18*(20), 7706-7713.
(8) Schoonheydt, R. A. Functional hybrid clay mineral films. *Applied Clay Science* **2014,** *96*, 9-21
(9) Gu, R.; Yuan, X.; Wu, R.; Li, H.; Xu, S.; Wang, J. Layer-by-layer assembled hydrogel nanocomposite film with a high loading capacity. *Journal of Applied Polymer Science* **2014,** *131*(2).
(10) Gaharwar, A. K.; Schexnailder, P. J.; Kline, B. P.; Schmidt, G. Assessment of using Laponite® cross-linked poly (ethylene oxide) for controlled cell adhesion and mineralization. *Acta Biomaterialia* **2011,** *7*(2), 568-577.
(11) Wang, J.; Cheng, Q.; Tang, Z. Layered nanocomposites inspired by the structure and mechanical properties of nacre. *Chemical Society Reviews* **2012,** *41*(3), 1111-1129.
(12) Le Luyer, C.; Lou, L.; Bovier, C.; Plenet, J. C.; Dumas, J. G.; Mugnier, J. A thick sol–gel inorganic layer for optical planar waveguide applications. *Optical Materials* **2001,** *18*(2), 211-217.

Chapter VII – Methods

As a point of reference: The general structure which describes the different OPEs studied in this dissertation is given below, in Scheme 7.1.

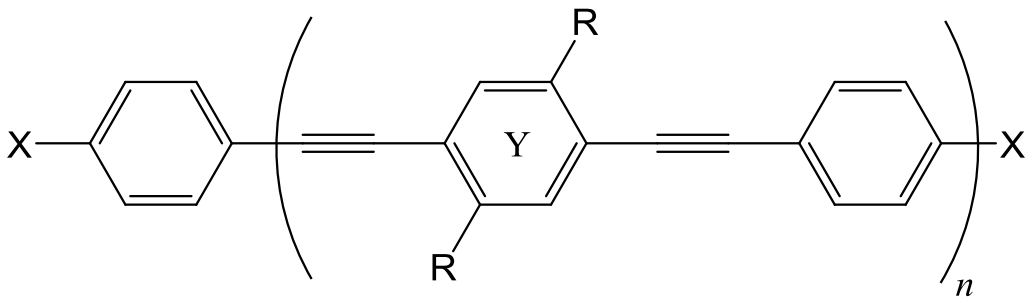

^{+}nC series: X = COOEt, R = $O(CH_2)_3N^{+}(CH_3)_3$
^{+}nH series: X=H, R = $O(CH_2)_3N^{+}(CH_3)_3$
^{-}nC series: X = COOEt, R = $O(CH_2)_3SO_3^{-}$
^{-}nH series: X=H, R = $O(CH_2)_3SO_3^{-}$
$^{+}$EO: n=1, X = $O(CH_2)_3N^{+}(CH_3)_3$, R = H
$^{-}$EO: n=1, X=$O(CH_2)_3SO_3^{-}$, R = H

p-Phenylene ethynylene oligomers used in this study

7.1 Experimental Methods

7.1.1 *General Methods and Calculations*

7.1.1.1 Sample Preparation

The solid OPEs**,** as iodide or chloride salts, were dissolved in either 3 mL filtered water with a resistivity of 18 MΩ*cm or 99.9% D_2O to a final concentration of 10-20 μM OPE repeat unit concentration in a 1 cm quartz cuvette.

Preparation of OPE-surfactant complexes proceeds as follows:

The solid compounds **+1H and +EO** as iodide salts, and **-1H** and **-EO** as sodium salts, were dissolved in 3 mL filtered water with a resistivity of 18 MΩ*cm to a final concentration of 15 μM in a 1 cm quartz cuvette. Solutions of pure OPE had surfactant added 1 μL at a time, so that

the OPE:surfactant ratio at which a complex was formed could be determined. The surfactant solutions were made at 15 mM for additions to 3 mL solutions of 15 μM OPE or, in the case of compound **-1H**, 20 mM for additions to 2 mL solutions of 20 μM OPE (This scheme allowed for the larger concentration needed to achieve complexation of **-1H**). This information could then be used to attempt to make assumptions about the structure of the aggregate. Following this determination, solutions of **-EO** and **-1H** with an OPE concentration of 15 μM were made with surfactant concentrations above and below the critical micelle concentration to study the effects on complexation with OPEs. The surfactant concentrations used for this study were 1, 2, 3, 4, 6, and 8 mM of surfactant. This is a range starting far below and ending far above the CMC of 3.79 mM[1] for TTAB and ending near the CMC of 8.3 mM for SDS. Solutions were allowed to sit at room temperature (25ºC) for 24 hours in order to allow for any latent spectral changes. Following measurements taken in pure solvent, SDS was added to a final concentration of 75 μM and the absorbance and fluorescence spectra were recorded.

7.1.1.2 Fluorescence Quantum Yields

Fluorescence quantum yields were calculated using the comparative method[2] and are reported relative to known values.[3-5] The optical density at the excitation wavelength was ≤ 0.1 for quantum yield measurements. For determination of fluorescence quantum yields, a Photon Technology International (PTI) fluorescence spectrometer equipped with a 75 W xenon arc lamp in an elliptical reflector housing monochromated to the wavelength of maximum absorbance of the OPE was used and this absorbance was kept below 0.15.

7.1.1.3 Photodegradation

The solid compound, as dichloride or diiodide salt, was dissolved in filtered water with a resistivity of 18.2 MΩ*cm to a final concentration of 20 μM. The solution was then exposed to UV radiation via a Luzchem LZC-ORG photoreactor (Luzchem Research, Ontario, Canada) in a quartz tube or cuvette. This particular photoreactor configuration consists of 10 UVA lamps (>5.3 mW-cm^{-2} over 316-400 nm) with a fan-powered exhaust to keep a stable temperature and a carousel for homogeneous irradiation of samples. Power was measured using Thorlabs PM-100 power meter to have flux of 0.975 mW/cm^2 at the site of the sample holder. For samples that were reacted in the absence of oxygen, argon degassing was carried out for 30 minutes with

stirring of the solution prior to irradiation. The photoreactions were also studied in D_2O to investigate a possible solvent isotope effect. In order to assist with mechanistic determinations water with 10% ^{18}O was used as the solvent for the photolysis, and was also mixed with the lyophilized product to determine which products undergo oxygen exchange with solvent. Power statistics for the UVA lamps are given below.

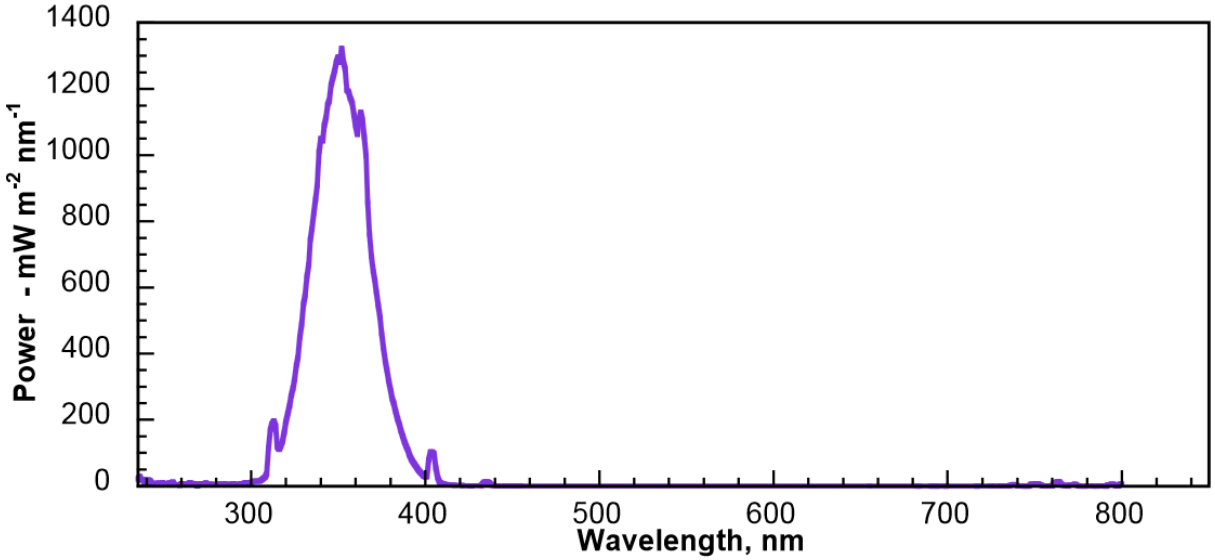

Region	Range, nm	Dose mWm^{-2}	% energy
UVA	316-400	52670	95.51
UVB	281-315	1209	2.19
UVC	235-280	367.5	0.67
Visible	401-700	711.0	1.29
NIR	701-850	187.0	0.34

Figure 7.1 Lamp exposure standards, as obtained from Luzchem.com.

7.1.1.4 Quantum Yields of Disappearance

UV-visible absorption spectra for the measurements on the quantum yield of disappearance were obtained with samples contained in a 1 cm quartz cuvette on a Varian Cary 50 spectrometer. Samples were irradiated on a Photon Technology International (PTI) fluorescence spectrometer equipped with a 75 W xenon arc lamp in an elliptical reflector housing. An aqueous solution of **1** (13.2 μM) was irradiated with a monochromatic light-source (355 nm, 3.26 mW, measured with

a calibrated energy meter, S350, UDT Instruments) and the quantum yield of disappearance was obtained by measuring the decrease in absorbance at 355 nm as a function of time. The calculation of quantum yield of disappearance was carried out as shown in the equation below.

(1)

$$\phi^{-} = \frac{\left(\frac{\Delta\left(\frac{A}{\varepsilon \times 1\ \mathrm{cm}}\right) \times N_a \times 10 - 3\mathrm{L}}{t \times 60 \frac{\mathrm{seconds}}{\mathrm{minute}}}\right)}{\left(\frac{\mathrm{P} \times \lambda}{h \times \mathrm{c}}\right) \times (1 - T)}$$

Where:

P = Lamp power (Watts);

λ = Wavelength used for excitation (m);

h = Planck's constant, 6.626×10^{-34} J·s;

c = The speed of light in vacuum, 3×10^{8} m/s;

T = Transmittance of light at wavelength λ through the sample;

A = Absorbance of light at wavelength λ by the sample;

ε = Extinction Coefficient of the molecule studied, at wavelength λ (L mol^{-1} cm^{-1}) ;

N_a = Avogadro's number, 6.022×10^{23} mol^{-1};

t = Amount of time sample is exposed (minutes)

7.1.2 Photoproduct Characterization

7.1.2.1 Mass Spectrometry

The Progress of the photolysis was monitored by mass spectrometry using a Micromass/Waters (Waters Corporation, Milford, MA) LCT Premier electrospray ionization time-of-flight (TOF) mass spectrometer in positive ion mode, with the TOF configuration in W mode. The elemental compositions of the observed product peaks were either calculated using the LCT Premier built in software, or the Elemental Composition Calculator v1.0 of the medical school of the University of Utah[6] to within 5 ppm difference. Representative mass-spectrometry results which indicate formation of products from photolysis are shown in the figures below.

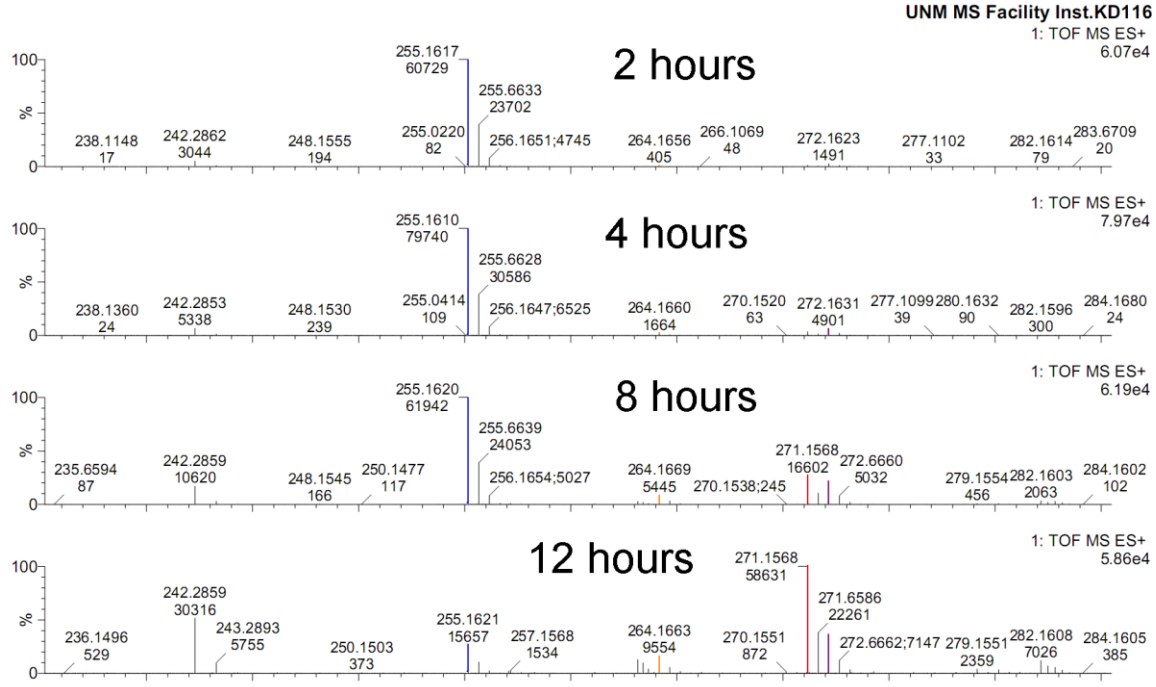

Figure 7.7. Exact-mass analysis of photoproducts of **+1H** in H_2O by Mass Spectrometry

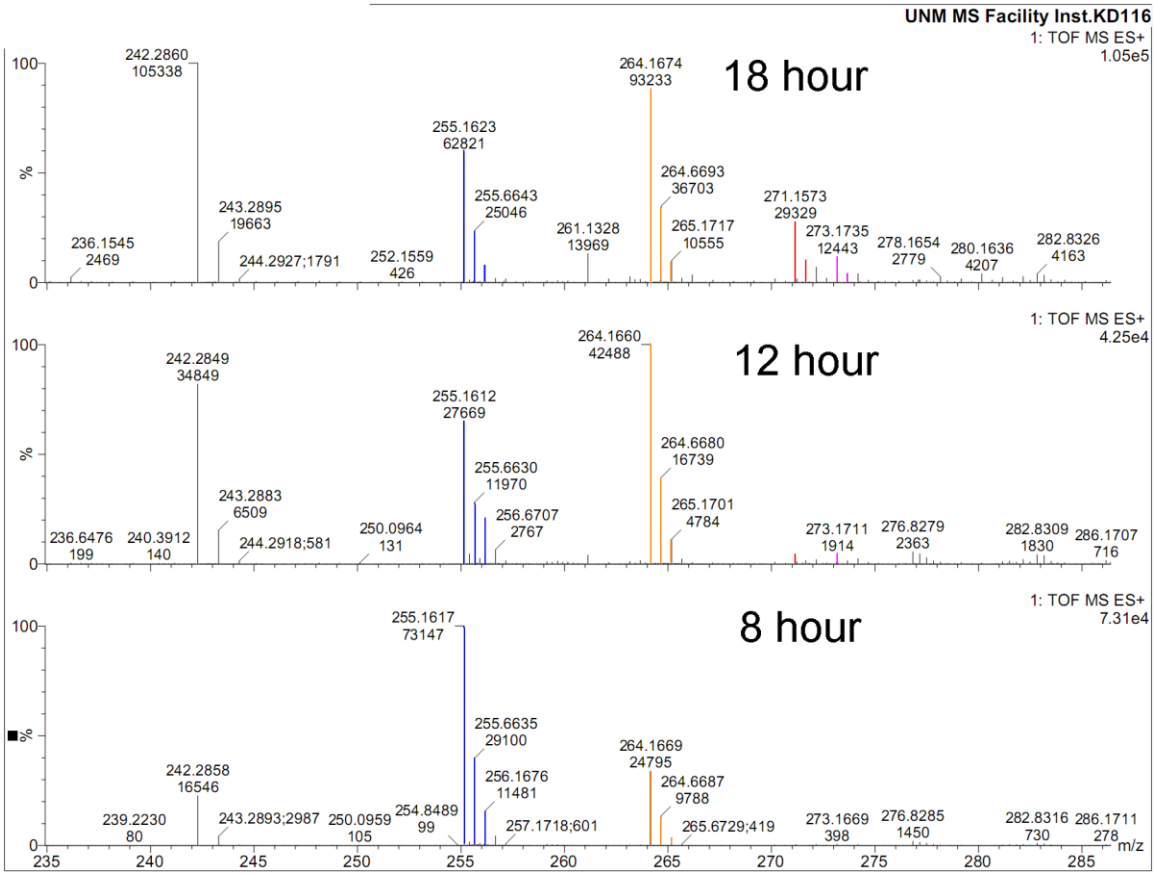

Figure 7.3. Exact-mass analysis of photoproducts of **+1H** in H_2O under Ar by Mass Spectrometry

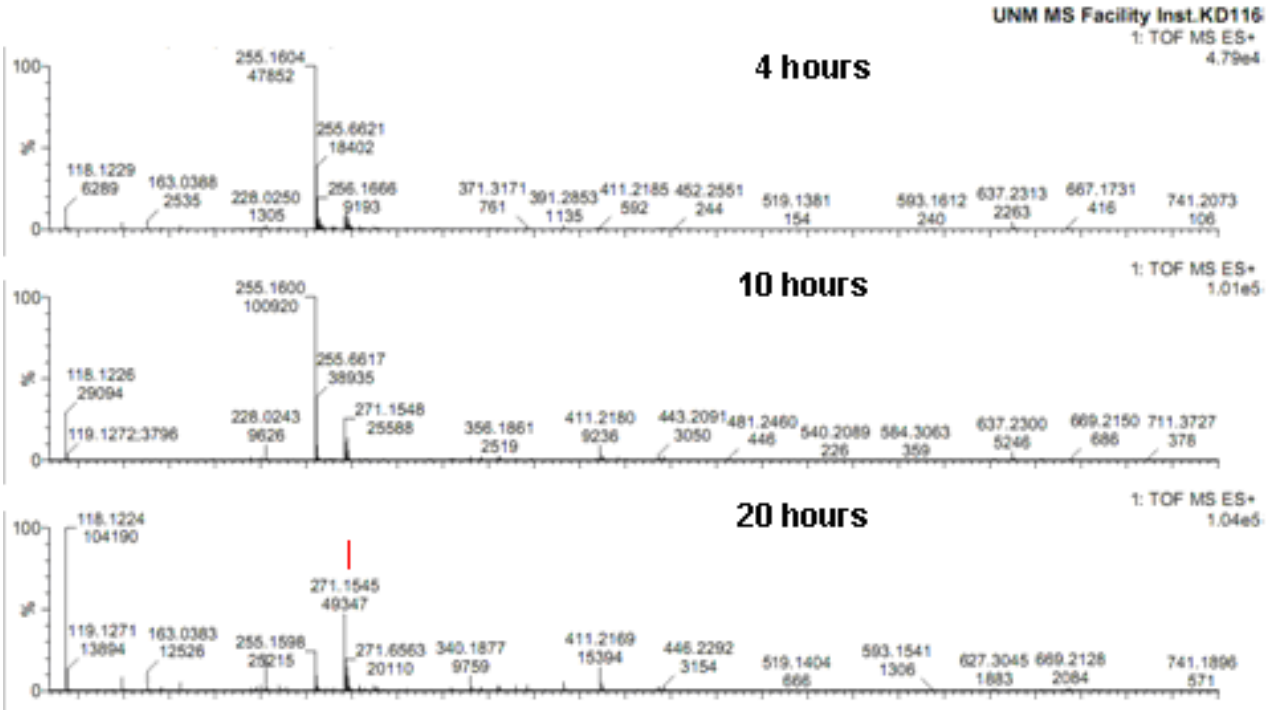

Figure 7.4. Exact-mass analysis of photoproducts of **+1H** in D_2O under air by Mass Spectrometry

The relative abundance of the different products and starting material were determined by dividing the intensity of one ion over the intensity of all the ions detected by ESI+ Mass Spectrometry. These results are summarized in the plots shown below, where the relative ion abundance is plotted against photolysis time.

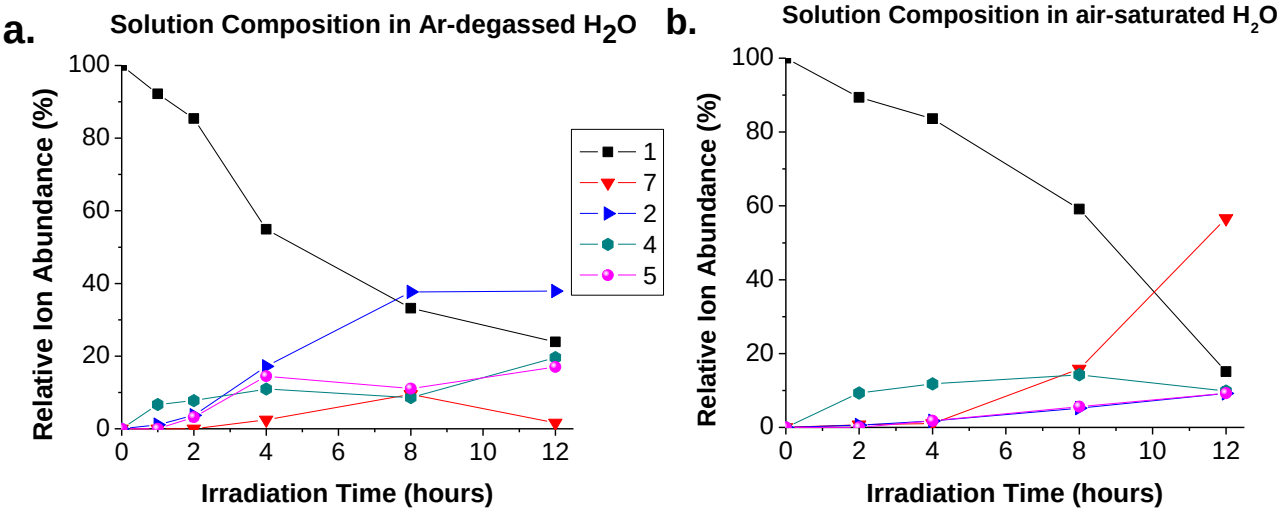

Figure 7.5. Comparison of sample composition under **a)** argon and **b**) air after irradiation.

7.1.2.2 UV-Vis Spectroscopy

The wavelength of excitation for fluorescence measurements of all compounds was assigned using the wavelength of maximum absorption. UV-visible absorption and fluorescence spectroscopy was performed with a Molecular Devices Spectramax M5 spectrophotometer (Molecular Devices, Sunnyvale, CA). Fluorescence spectra were obtained using a Photon Technology International (PTI) fluorescence spectrometer equipped with a 75 W xenon arc lamp housed in an elliptical reflector. UV-visible absorption spectroscopy was performed with a Lambda-35 UV-VIS Spectrometer (Perkin Elmer, Waltham, MA). Fluorescence spectra were obtained using either a Spectramax M5 spectrometer (Molecular Devices, Sunnyvale, CA), or a Quantamaster 30 fluorescence spectrometer equipped with a 75 W xenon arc lamp in an elliptical reflector (Photon Technology International, Birmingham,NJ).

7.1.2.3 Liquid Chromatography

The high-resolution ESI mass spectrometry results were confirmed in an ABSciex API 3200 triple-quad LC-MS (ABSciex, Foster City, CA). A 10 mm I.D., 150 mm Luna™ Pentafluoropropyl (PFP) column (Phenomenex Inc., Torrance, CA) was used in an isocratic 53%MeOH/47%H_2O HPLC run at 5 mL/min, where both solvents contained 0.1% formic acid. The size of the sample loop was 20 uL, and the concentration (reflecting the starting material concentration prior to reaction) upon injection was 1 mM. A 51:1 split flow was used for sample introduction into the mass spectrometer, resulting in a flow rate of 100 uL/min. The figures below show a typical experiment, where the separated products are measured by both the mass spectrometer and a UV-Vis detector.

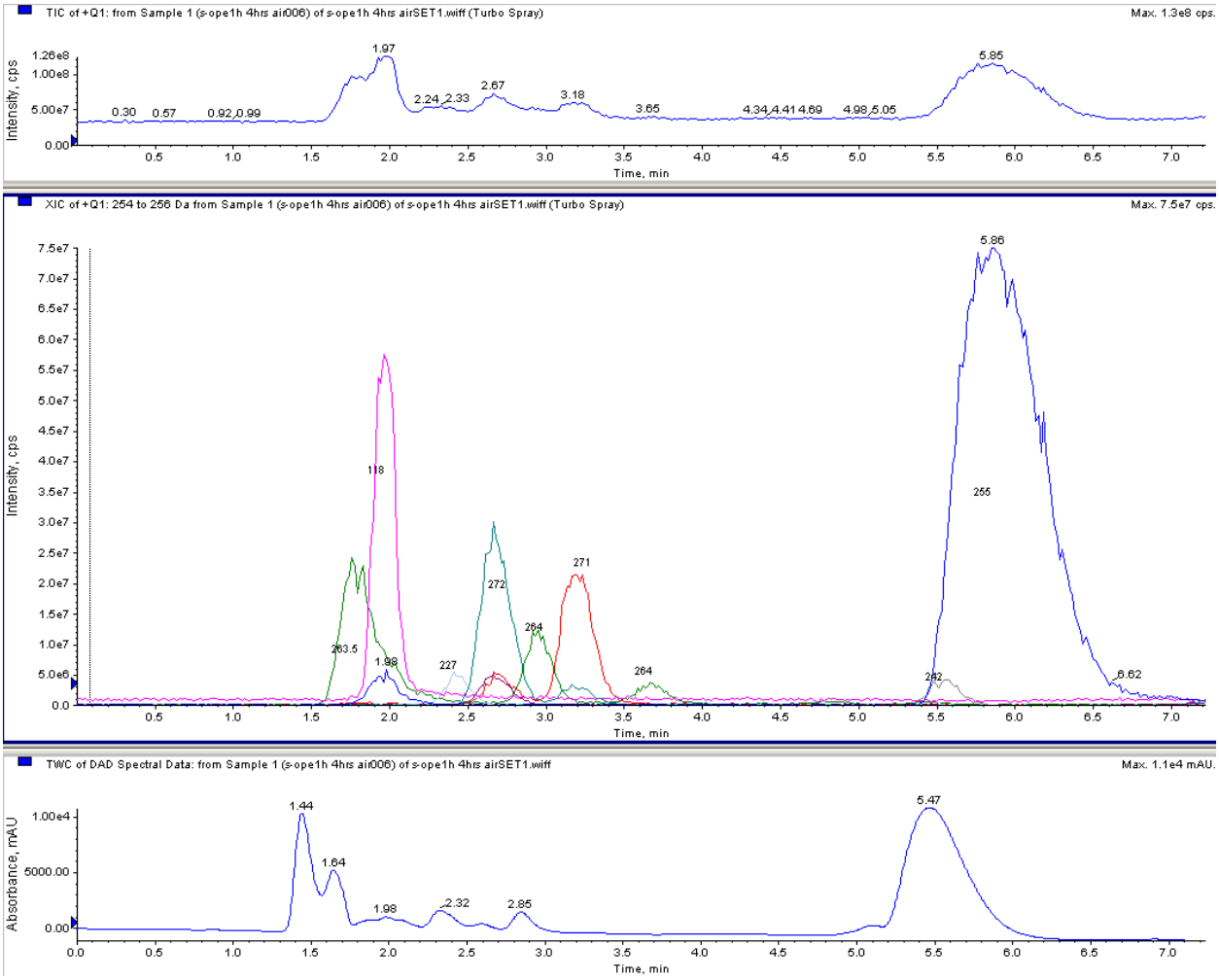

Figure 7.6 Example of HPLC-MS using Pentafluorophenyl column with EtOH/water gradient to separate photoproducts from a solution of 10 µM **+1H** after 4 hours of UVA irradiation in water and under air.

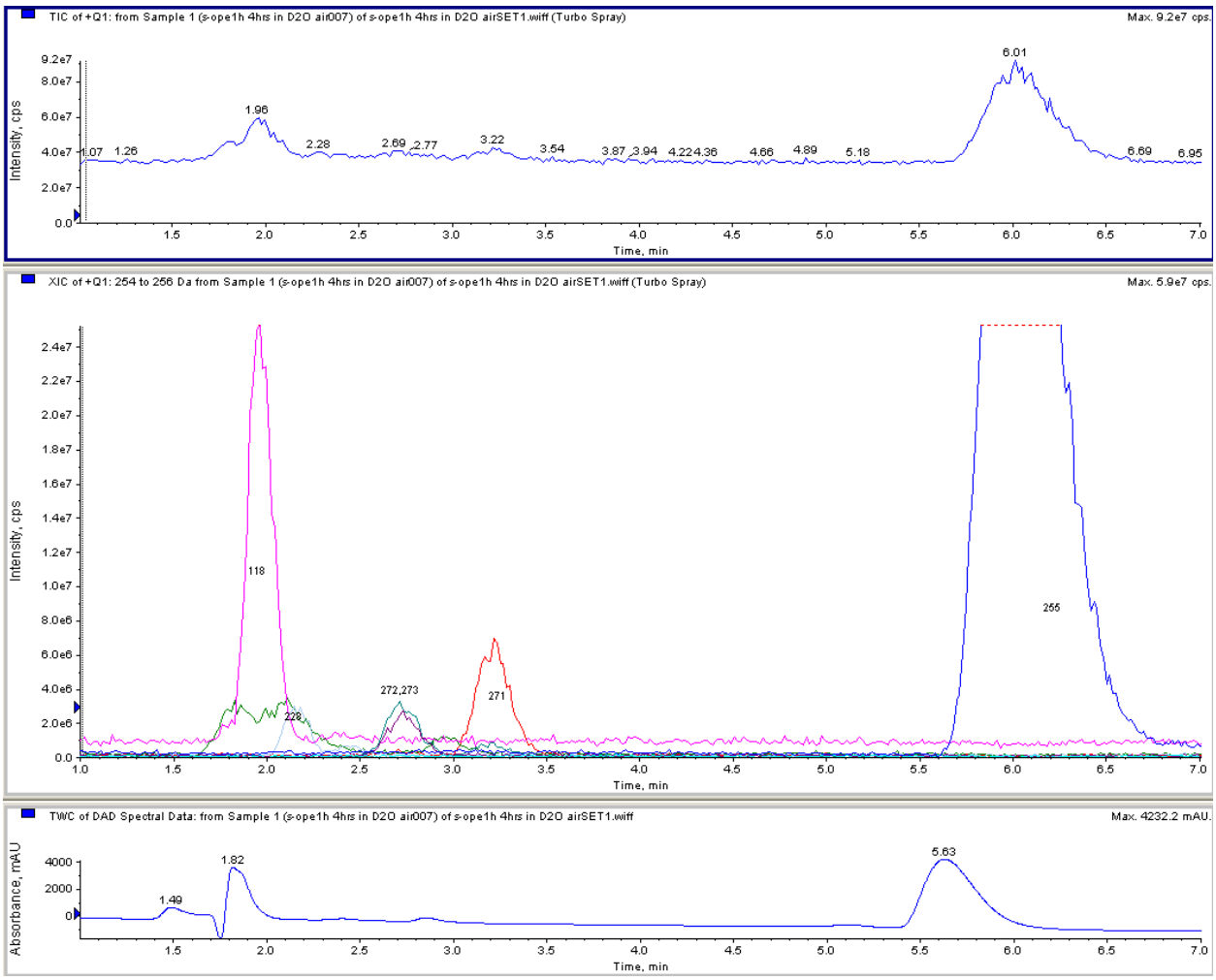

Figure 7.7 Example of HPLC-MS using Pentafluorophenyl column with EtOH/water gradient to separate photoproducts from a solution of 10 µM **+1H** after 4 hours of UVA irradiation in deuterium oxide and under air.

7.1.2.4 Infrared Spectroscopy

The product formation was confirmed by Fourier-transform infrared (FT-IR) spectroscopy using a Nicolet 6700 FT-IR with an ATR attachment (Thermo Fisher Scientific, Waltham, MA). The solution of **+1H** at 0.2 mM in H_2O was photolyzed and the solution was frozen at -80ºC for lyophilization (freeze drying). The solid sample was placed directly on the surface of the ATR crystal for FT-IR analysis. The spectrum below shows an IR spectrum of photolyzed **+1H** which was lyophilized after irradiation in H_2O under air.

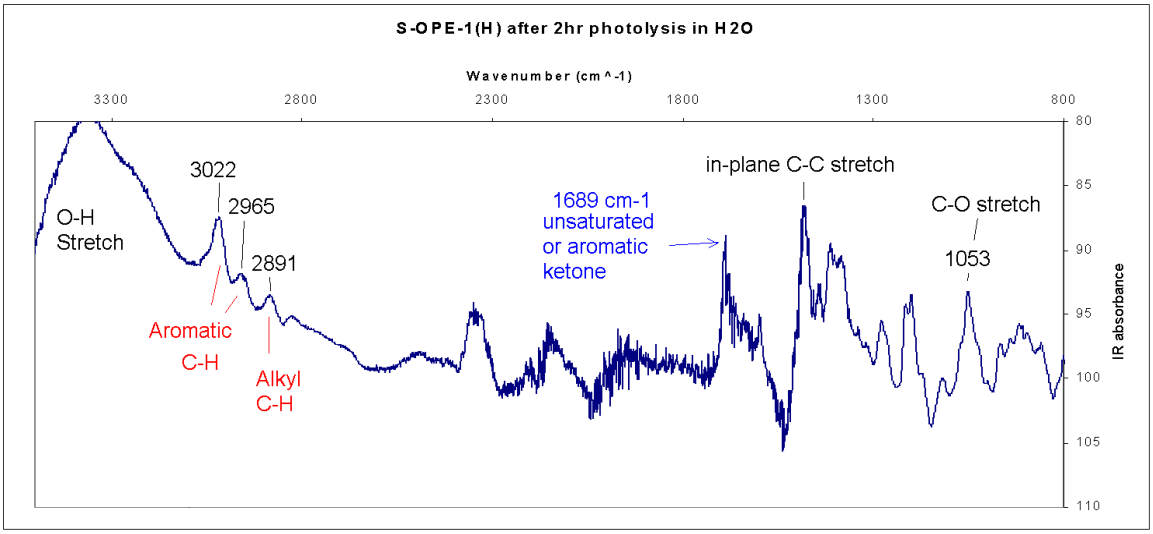

Figure 7.8. FT-IR spectrum of **+1H** photoproducts

7.1.3 Microbiology Procedures

7.1.3.1 Cell Preparation

All media and buffers were prepared using deionized water with a resistivity exceeding 18 MΩ*cm. Nutrient Broth 234000 (Difco) was prepared according to manufacturer's instructions, and Nutrient Agar was prepared upon the addition of 8 g/L Bacto agar (Difco). Both *Staphylococcus aureus* (ATCC 25923) and *Escherichia coli* (ATCC 29425) were grown from glycerol-preserved stock. The frozen stock aliquots were generated from first-generation cultures of the original ATCC lyophilate, which were grown in Nutrient Broth containing 20% glycerol, and subsequently stored at -70°C. The cells were grown by inoculating the glycerol stock on Difco Nutrient Agar for 24 hours at 37° Celsius. For biocidal testing, *S. aureus* and *E. coli* cells were scraped off the agar plate with a flame-sterilized wire and transferred to nutrient broth. Cells were incubated in an Orbital Incubator Shaker (American Instruments, Lafayette, CA) at 37° Celsius in nutrient broth with rapid shaking (250 rpm) for 18 hours. Following the 18-hour incubation period, cells were separated from the nutrient broth by two 15-minute centrifugations at 4,400 rpm, each of which was followed by removal of the supernatant and re-suspension in 30 mL 0.85% NaCl.

7.1.3.2 Sample Preparation and Exposure

***OPE and OPE-SDS complex*:** The solid compound **+EO_{c2},** as a dichloride salt, was dissolved in filtered water with a resistivity of 18 MΩ*cm to a final concentration of 10 µM. For the OPE-

SDS complexes, 10 μM **+EO$_{c2}$** was mixed with 40 μM SDS, 0.24% of the critical micelle concentration (CMC). *S. aureus* samples were exposed to a **+EO$_{c2}$**-SDS complex where the concentration of SDS was 0.33 mM, as they were much more resilient to killing caused by SDS. Samples were irradiated for 0, 30, 60, and 120 minutes prior to exposure to bacteria. Once exposed to **+EO$_{c2}$** or **+EO$_{c2}$**-SDS complex, *E.coli* and *S. aureus* samples were irradiated with UVA in the photoreactor for 30 minutes and 15 minutes, respectively.

***OPE and OPE-TTAB complex*:** The bacterial stock solution was either diluted or concentrated to 2×10^7 cells/mL. Samples were diluted by the addition of 0.85% NaCl, while concentrating the sample entailed centrifugation to pellet the cells, followed by removal of the necessary amount of supernatant and subsequent resuspension of the pellet by vortexing. 500 μL of bacterial solution was added to glass vials with 500 μL of sample solution to reach a final volume of 1 mL prior to analysis. Samples tested contained 10 μM **-EO**, 40 μM TTAB, or both 10 μM –EO and 40 μM TTAB. Biocidal activity under UVA irradiation was determined using a Luzchem LZC-ORG photoreactor (Luzchem Research, Ontario, Canada). This photoreactor was configured with 10 UVA lamps (0.975 mW/cm^2 over 316-400 nm) with a fan-powered exhaust to keep a stable temperature of 28ºC and a rotating carousel for homogeneous irradiation of samples. Samples exposed in the dark were kept at room temperature, 25ºC. 70% Ethanol was used as a positive control, and a 60 minute UVA-irradiated sample of bacteria was used as a negative control.

7.1.3.3 Biocidal Testing by Live/Dead Staining Assay

***Flow Cytometry Analysis*.** Flow cytometry was implemented to determine the cell concentration of the 0.85% NaCl-suspended bacterial stock solutions. An Accuri C6 flow cytometer (Becton Dickinson, Franklin Lakes, New Jersey) equipped with a blue laser that excites at 488 nm was utilized. Two filters were used: a green fluorescence filter (FL-1: 530 nm) and a red fluorescence filter (FL-3: 670 nm long pass). Two thresholds were used, a primary threshold and a secondary threshold. The primary threshold ensured that only events exhibiting 40,000 FSC-A scatter units or greater were included in the data. The secondary threshold was utilized to remove events exhibiting less than 250 FL-1 fluorescence units (live stain fluorescence channel) from the data. Flow cytometer core size in all experiments was 10 μm, with a flow rate of 14 μL/minute. Using these settings, 20 μL of un-stained stock solution was sufficient for identifying the stock

concentration of cells. 100,000 events were recorded in each sample. Cells were stained with 5 mM SYTO 21 (live stain; Life Technologies, Grand Island, NY) and 1.5 mM propidium iodide (dead stain; Life Technologies, Grand Island, NY) for 15 min prior to flow cytometry analysis. Flow cytometry gating schemes are shown for *S. aureus* and *E. coli* in Figures S2 and S3 of the supporting information, respectively.

An example of the flow cytometry gating scheme for *E. coli* is shown below, in **Figure 1.** The UVA-irradiated negative control is shown on the left side of the figure, and the Ethanol positive control is shown on the right.

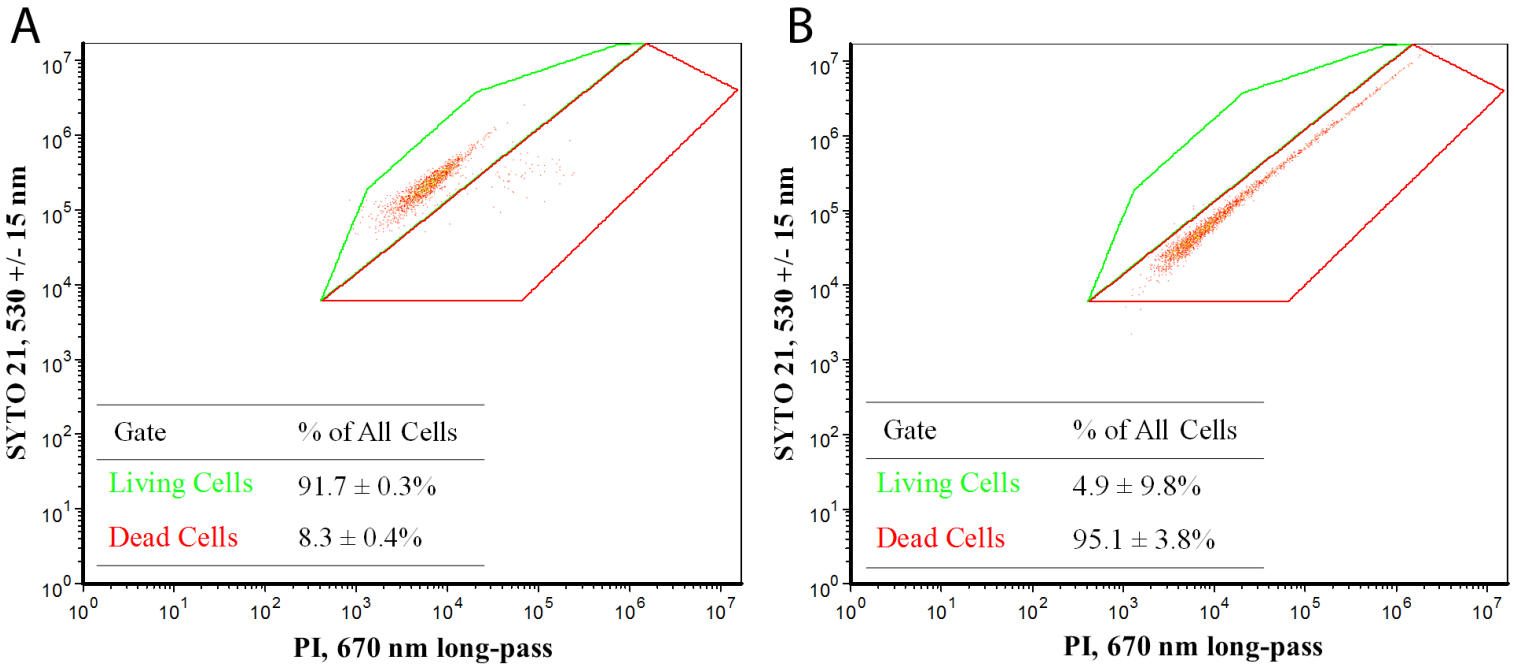

Figure 7.9. Flow cytometry gating for *E.coli;* A. UVA – irradiated negative control; B. 70% Ethanol positive control

An example of the flow cytometry gating scheme for *S. Aureus* is shown below, in Figure 7. The UVA-irradiated negative control is shown on the left side of the figure, and the Ethanol positive control is shown on the right.

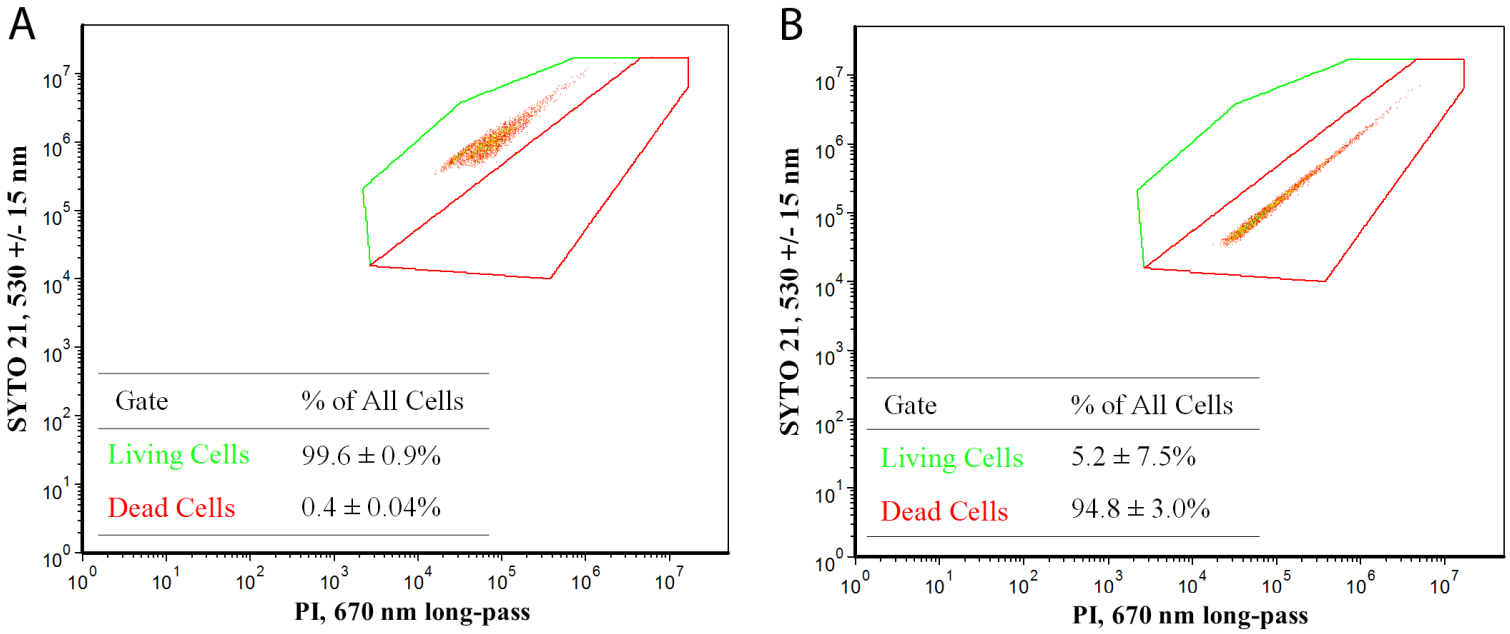

Figure 7.10 Flow cytometry gating for *S. Aureus*; A. UVA – irradiated negative control; B. 70% Ethanol positive control

7.1.3.4 Biocidal Testing by Standard Plating Techniques

Standard plating techniques were utilized to validate flow cytometry data. This entailed pipetting and spreading 50 µL aliquots of diluted, unstained sample, onto nutrient agar plates. The plates were incubated at 37 °C for 18 hours, colonies were counted, and viabilities were calculated relative to the UVA negative control. All exposure times for OPE with bacteria in light or dark were 60 minutes in duration.

7.2 Computational Methods

7.2.1 Density Functional Theory Calculations

7.2.1.1 Energy minimized geometries

The oligomers were modeled theoretically using electronic structure methods at the density functional theory (DFT) level. Starting with several conformations, DFT calculations were used to generate optimized ground state geometries and molecular orbital information. The initial geometries were first optimized at the semiempirical AM1 level. Further optimizations of the ground state were done at the DFT level of theory. All density functional calculations were performed using the hybrid B3LYP (Becke, three-parameter, Lee-Yang-Parr) exchange-

correlation energy functional.[7] The exchange term of B3LYP consists of hybrid Hartree-Fock and local spin density (LSD) exchange functions with Becke's gradient correlation to LSD exchange. This level of theory provides an efficient method of accounting for electron correlation in larger molecules and oligomers with reasonable computational cost and resources. Successive geometry optimizations with DFT were completed using the 3-21g and the 6-31g basis sets, ultimately arriving at the 6-31g** basis set. In order to ensure that a global minimum was reached for the optimized structures, the frequencies of the molecular vibrations were also calculated. The frontier molecular orbitals (the Highest Occupied Molecular Orbital (HOMO) and the Lowest Unoccupied Molecular Orbital (LUMO)) were also analyzed at the B3LYP/6-31g** level. In addition, the HOMO and LUMO of a forced-planarized S-OPE-2(H) were calculated to compare conjugation with the unconstrained ground state. For all calculations, the Gaussian 03 or 09 and Gaussview 4 software packages by Gaussian Inc. were used.[8,9]

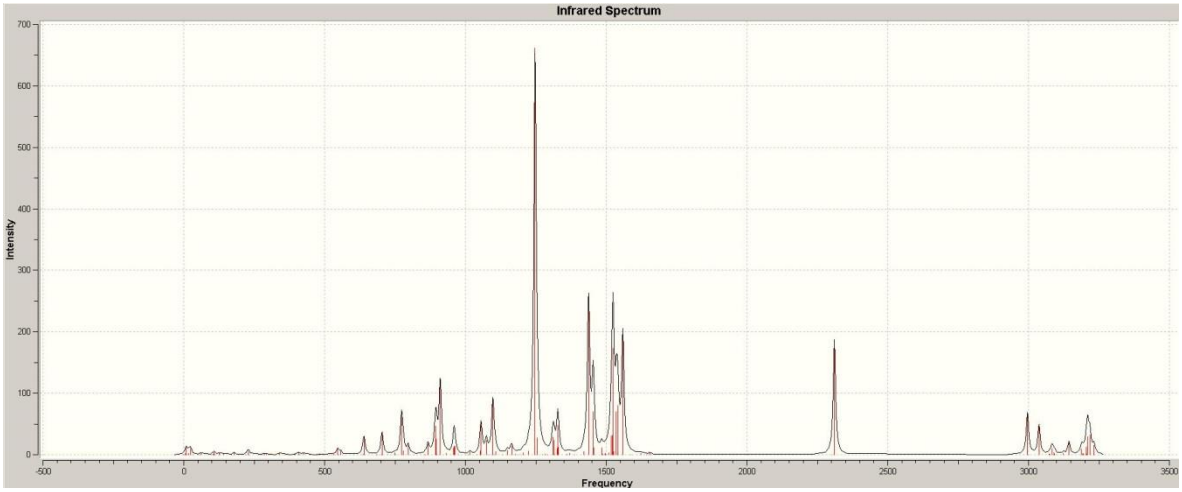

Figure 7.11 Calculated Frequencies of Vibrations of Optimized Geometry of +1H

7.2.1.2 Energy Scans

In order to determine the energy landscape of the conformational states of the OPE, "scans" were performed using the B3LYP/6-31g** level of theory. In this programmed set of calculations, the dihedral angle of the triple-bond which dictates the co-planarity of adjacent rings is rotated by 10º every step, and the total energy of the system is recorded. By plotting the dihedral angles of two triple-bonds on separate axes, a heightmap which describes the energy barriers of this

geometrical transition can be obtained. This is shown in section 3.7.

7.2.1.3 TD-DFT and Semiempirical methods of calculating electronic energies

Calculation of excitation energies of the OPEs was performed using semi-empirical and density functional theory methods. The method known as Time-dependant DFT (TD-DFT) was used with the B3LYP/6-31g** level of theory to obtain the excitation energies of the OPEs in vacuum.[10] The results were compared with experiment and also with those obtained by a semi-empirical method known as Zerner's method of intermediate neglect of differential overlap for singlets, or ZINDO/S for short.[11] The results are shown in section 3.7.

7.2.2 *Molecular Dynamics Simulations*

7.2.2.1 Parametrization of OPE to Generalized Amber Force Field

OPEs were parametrized to the generalized Amber forcefield (GAFF) framework using the antechamber program in AmberTools17.[12] The Gaussian09 software package was used for all quantum-level calculations for residue parametrization.[9] The ground-state geometries were determined using Hartree-Fock and a 6-31g basis set with diffuse and polarizability functions. GAFF atomtypes were used to assign Van der Waals parameters and bonding force constants.[13] The assigned partial charges of the OPE were calculated using the RESP charge fitting method on the QM output. [14,15] The TIP3 water model was used.[16]

Table 7.1. Generalized Amber Force-field Atomtype Assignments

Moiety	Structure	GAFF atomtype
Ether group		os
Sulfate Oxygen	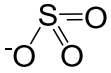	o
Methyl Carbon	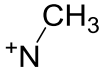	c3
Methylene Carbon	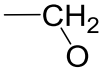	c3
Phenyl Carbon	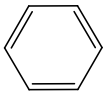	ca
Triple-bonded Carbons		ch, cg
Methylene Hydrogen 1	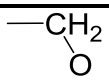	h1
Methylene Hydrogen 2	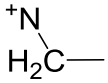	hx
Methylene Hydrogen 3	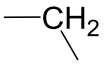	hc
Aromatic Hydrogen		ha
Methyl Hydrogen	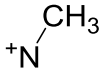	hx
Quaternary Nitrogen	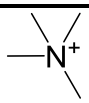	n4
Sulfate	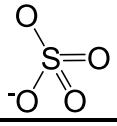	s6

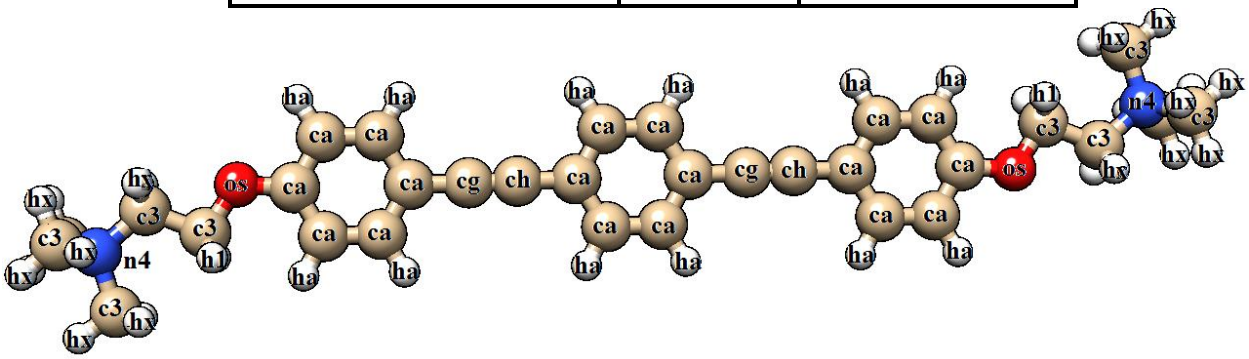

Figure 7.17. Illustrated GAFF atomtype assignments on **+EO$_{c2}$**

7.2.2.2 Preparing and Simulating a Model Membrane system using NAMD

All simulations use a bacterial cell membrane mimic with 1,2-Dioleoyl-sn-Glycero-3-Phosphoethanolamine (DOPE) and 1,2-Dioleoyl-sn-glycero-3-phospho-rac-(1-glycerol) (DOPG) phospholipids in a 4:1 ratio and OPEs (shown in scheme 1) starting from various positions inserted into the membrane or in the water box surrounding the membrane. The lipid composition was chosen to mimic experimental conditions from reference 40. A 4:1 DOPE:DOPG lipid bilayer with either 150 or 300 lipids was built and equilibrated with TIP3 water and 0.15M NaCl using CHARMM-GUI[17]. The system was minimized and then equilibrated on CHARMM-GUI.org for 1 ns. Prior to addition of OPEs to the system, water and ions from the CHARMM-GUI membrane were stripped, and the system was resolvated and ionized after addition of the OPEs. After addition of OPEs to the simulation, the system was minimized in NAMD[18] using the steepest descent method for 20 ps, followed by 1 ns of NVT equilibration with the timestep reduced to 1 fs for the first 50 ps and 4 ns of NPT equilibration. The simulations of **+EO** were performed with twice as many lipids in order to better sample effects on bilayer curvature, and consequently the number of OPEs in the initial configurations was increased to 8 to make the starting concentrations of OPE per lipid commensurate and comparable. The TIP3 water model[16] was used with the CHARMM36 lipid forcefield[19,20], and all simulations were performed using the NAMD software package[18]. All simulations were carried out in the NPT ensemble using cubic periodic boundary conditions.[21] Full system electrostatics were calculated using the particle mesh Ewald (PME) method.[22] The Langevin temperature thermostat was used without coupling to hydrogens and with a damping coefficient of 1/ps, and set at physiological conditions, 310.15 K.[23] The Langevin barostat with an oscillation period of 50 fs and a decay of 25 fs was used to maintain the pressure at 1 atm.[23] The OPE force fields were obtained from swiss-param.ch[24], and the bond lengths and angles were optimized by electronic structure calculations performed using Gaussian09.[9] In Tables 7.3 and 7.4, the details for each configuration simulated are given. This includes information of the structure, number and initial placements of the OPEs relative to the lipid bilayer as well as the number of lipid molecules and water molecules and total trajectory length. For clarity, the "0 ns" time-point is the set of coordinates immediately after the 5 ns equilibration step. Following equilibration, all simulations had a lateral area per lipid of 62-65 $Å^2$ (See Table 7.2).

Table 7.2. Lateral area per lipid calculated with GridMAT-MD

	Equilibrated		**End of Simulation**	
Configuration	APL ($Å^2$)	δ (±$Å^2$)	APL ($Å^2$)	δ (±$Å^2$)
1	63.6	0.3	61.9	1.3
2	64.6	3.3	65.1	0.3
3	64.1	0.3	57.5	0.5
4	65.6	0.7	58.4	1.1
5	64.4	0.4	65.6	1.3
6	67.4	0.1	61.3	0.9

7.2.2.3 Surfactant Simulation Preparation

The initial system configurations were prepared using Packmol, from Unicamp, BR[25]. Systems were solvated with water and neutralized with sodium and chloride ions. Simulations used full PME electrostatics[22] and cubic periodic boundary conditions. The system was first minimized using the steepest descent method for 2500 steps, followed by a 250 step gradient minimization. Heating was carried out from 0 K to 100 K in 500 ps, and then from 100 K to 298 K in 500 ps using the NVT ensemble. Simulations were performed for 50 ns using the NPT ensemble with the Langevin barostat and thermostat with a time constant of 1/ps.[21,23] The Amber12-GPU software package was used with SPFP precision.[26-28]

7.2.2.4 Generating micelles for use in simulations

In order to generate micelles of SDS for simulations, PACKMOL was used to generate a configuration of randomized water and 200 SDS molecules in a water box with 6000 waters. The system was simulated using AMBER, and micelles with no more than 62-63 SDS molecules are revealed. The coordinates of the micelle are saved and can then be used to create the initial systems where the OPEs and micelles are placed near one another in the water box and simulated. An image of one of the SDS micelles formed from one of these simulations is shown below.

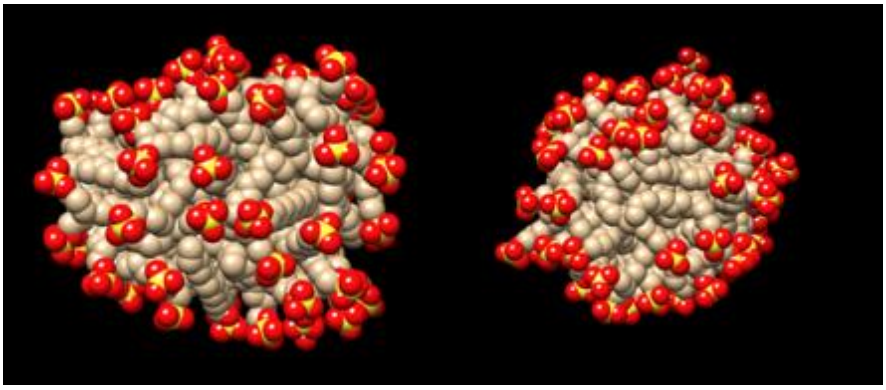

Figure 7.13 SDS micelle from two different angles

7.2.2.5 GPU-accelerated MD Simulations of Lipid Bilayers

Recently, the Lipid14 parameters for Amber forcefields were published and this allowed the adaptation of OPE-bilayer simulations described above to this model.[29] In order to adapt a system to amber, the ambertools script charmmlipid2amber.x is modified to see the OPE as a lipid, so that it is correctly added into the system.[12] This script converts the CHARMM atomtypes used in the above studies of the model membranes to an AMBER format which can be loaded into the ambertools program tleap. These simulations are performed using the same pressure and temperature coupling methods, water model, and other simulation details were also kept the same as in the above studies using NAMD. The primary difference between the two studies is the use of the GAFF atomtypes and RESP-derived forcefields for the OPEs instead of CHARMM, and the use of AMBER as the MD engine, allowing GPU-acceleration. These simulations were able to achieve times of ~50 ns/day for a system of 30000 atoms.

7.2.2.6 Analysis of results

Lipid bilayer properties before and after OPE insertion were characterized by mapping the bilayer thickness and calculating the atomic density profiles across the lipid bilayer. The program GridMAT-MD was used to calculate lateral area per lipid, and bilayer thickness was measured using the phosphorous atoms on the upper and lower leaflets.[30] Electron density plots were obtained using the VMD Density Profile Tool.[31] The software VMD was used for system preparation, analysis, and calculation of radial distribution functions. [32] Radial distribution functions were measured over 40 ns of the simulation trajectory using the center of masses of the groups correlated in the beginning and end of the trajectory using the cpptraj program in

AmberTools.[33] The permeation rate of water through the lipid bilayer was estimated by counting the number of water molecules that crossed the interfacial planes during a simulation trajectory. The identification of particular water molecules and all visualizations and graphical images were obtained using VMD. UCSF Chimera version 1.8 was used for rendering snapshots of the trajectories and hydrogen-bonding analyses.[34]

7.2.7.7 Simulation Details

Table 7.3. OPE-Bilayer Simulation Information 1

Type of OPE	**+2H**	**+2H**	**+2H**	**+1H**	**+EO**	**+EO**
Number of OPEs	3	3	3	4	8	8
Orientation (w.r.t. membrane)	Parallel	90º	90º	45º	Parallel	90º
Degree of Insertion	Not inserted	Half inserted	Fully inserted	Fully inserted	Not inserted	Fully inserted
Number of Atoms	39431	36697	37906	54679	82574	69741
Number of Lipids	150	150	150	150	300	300
Number of Waters	6503	5595	5996	11509	14354	10055
Length of Simulation (ns)	490	325	270	145	100	256

Table 7.4. OPE-Bilayer Simulation Information 2

Number of +3H	**Orientation (w.r.t. normal)**	**Degree of Insertion**	**Initial System Size (Angstroms)**	**# Atoms**	**# Lipids**	**# Waters**
3	Parallel	Fully inserted	75x76x68	33420	144	4697
2	Perpendicular	Not inserted	77x77x100	51038	150	10368
2	Parallel	Half inserted	75x76x92	47415	150	9163
3	Parallel	Half inserted	79x80x97	54679	150	11509
1	Parallel	Fully inserted	77x78x64	32966	150	4428
2	Parallel	Fully inserted	80x82x69	40395	150	6829
3	Parallel	Fully inserted	77x78x71	38074	144	5986

Table 7.5. Simulation Information 3

Subject (# *simulations*)	**# OPEs**	**# SDS**	**# Na**	**# Cl**	**# Waters**	**# atoms**	**Periodic box length (Å)**	**Simulation Length (ns)**	**Ionic Strength (M)**
Micelle-forming (*1*)	0	200	220	20	7902	32346	62	200	0.40
+EO (*1*)	1	5	15	12	7902	24023	62	50	0.20
+EO (*3*)	1	63	73	12	15804	50213	80	100	0.10
+EO_{c2} (*1*)	1	8	37	31	15804	47892	80	50	0.29
+EO_{c2} (*1*)	4	12	41	37	15804	48292	80	50	0.29
+EO_{c2} (*3*)	1	6	17	13	15804	47768	80	50	0.11
+EO_{c2} (*3*)	1	12	22	12	15804	48024	80	50	0.10
+EO_{c2} (*3*)	1	63	83	22	15804	50201	80	100	0.20
+EO_{c2} (*3*)	2	12	22	14	15804	48102	80	100	0.10
+1H (*3*)	1	63	78	17	15804	50227	80	100	0.15

7.2.3 Coarse-grained MD of OPEs with model membranes

7.2.3.1 Bead Definition of Coarse-grained model of OPEs

In order to fit the OPEs to the martini coarse-grained model, the atoms were mapped according to established mappings.[35,36] The figure below gives bead assignments for the OPEs, and gives **+EO** as an example. The molecules were reduced from 80 atoms to 15 beads for **+EO**, and from 216 atoms to 39 beads for **+3H**. In early iterations, the SC4 bead type was used for phenyl beads, but in recent studies was changed to SC5.

Bead Type	Q0	N0	SC5	C4
Chemical Moiety in EO-OPE-C3 model	$N(C_3)$	C_3O	C=C-C	$C_2 \equiv C_2$
Atom Mapping	4 to 1	4 to 1	3 to 1	4 to 1

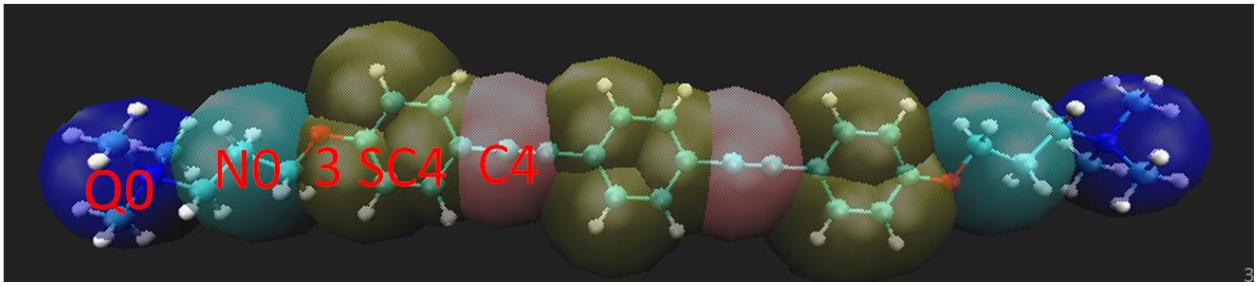

Figure 7.14 Martini-CG bead assignment for general atom types and **+EO** shown

7.2.3.2 Parametrization and Mapping of All-atom Values onto CG System

Part of the standard protocol for assessing the fidelity of the CG bilayer is the comparison with the all-atom bilayer. In the figure below, the "atomic" density of the system is compared for the all-atom and coarse-grained 4:1 DOPE:DOPG bilayers.

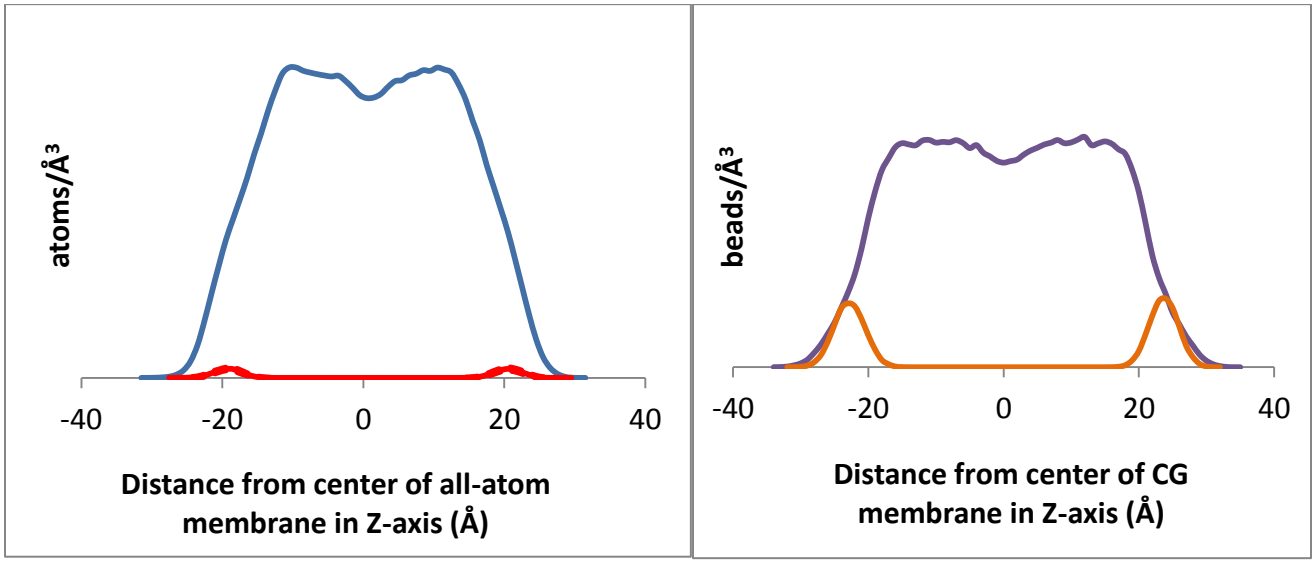

Figure 7.15 Atomic density plots of 4:1 DOPE:DOPG bilayers represented at all-atom level and with the martini coarse-grained model, respectively.

While the rigid end-only OPE **+EO** was adequately parametrized for the Martini model with respect to molecular geometry, the larger OPE with 3 repeat units was fairly difficult to adapt. The large timesteps of 20-30 fs used in the martini forcefield led to instabilities along the backbone of the larger OPEs, often leading to early termination of the simulation. In order to address this, an "elastic" network of extended bonds was established, using the method developed by Periole and coworkers.[37] In addition, distance restraints were also added in the **+3H** forcefield used for the coarse-grained simulations. This resulted in a reasonably accurate structure, an example of which is given in the figure below.

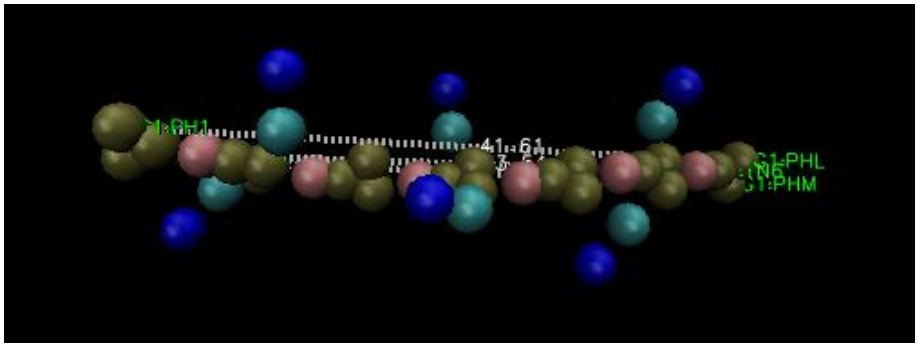

Figure 7.16. Snapshot of a coarse-grained **+3H** in a water box (water not shown)

7.2.3.3 Simulation Setup

The CG systems were prepared from the all-atom coordinates using the CG builder in the program Visual Molecular Dynamics.[32] The simulations were performed using Gromacs 4.6.[38,39] The timestep was 30 fs for **+EO** and 20 fs for **+3H**, and NPT with isotropic pressure coupling using the berendsen method was used. Temperature was maintained at 310.15 K using berendsen temperature coupling. The CG simulations were performed using several different solvent models in order to try and improve the accuracy of the results. In addition to the standard martini 4-water CG beads, the polarizable water model (PW) by Yesylevskyy and coworkers was used.[40] PME electrostatics were utilized for the polarizable water simulations. Also, an implicit solvent model was tested for several large-scale systems with 1200 lipids and 50 or 100 **+EO**s, which is known as the "Dry-martini" model.[41] The details of simulations between OPEs and lipid bilayers that were carried out with the Martini-CG model are given below in Table 7.6.

Table 7.6. Coarse-grained OPE-Bilayer Simulation Details

OPE	Position	# OPEs	# Lipids	# Particles	Simulation Length (ns)	Water type
+3H	Water	2	150	4862	6 μs	W
+3H	In Membrane	2	150	6456	6 μs	W
+3H	In Membrane	2	150	6456	6 μs	W
+3H	Water	3	150	9962	10 μs	W
+3H	Water	3	150	20916	6 μs	PW
+3H	Water	3	150	20916	6 μs	PW
+EO	Water	8	300	7827	10 μs	W
+EO	Water	8	300	14593	6 μs	PW
+EO	In Membrane	8	300	6168	6 μs	W
+EO	Water	50	1200	91530	10 μs	PW
+EO	Water	100	1200	62472	10 μs	PW

+EO	Water	100	1200	62472	10 µs	PW
+EO	Water	50	1200	17872	6 µs	Dry
+EO	Water	100	1200	18522	6 µs	Dry
+EO	Water	60	4800 vesicle	69362	3µs	Dry

7.3 References

(1) Turro, N.J.; Yekta, A. Luminescent Probes for Detergent Solutions. A Simple Procedure for Determination of the Mean Aggregation Number of Micelles *J. Am. Chem. Soc.* **1978,** *100*, 5951

(2) Williams, A.T.R.; Winfield, S. A.; Miller, J. N. Relative fluorescence quantum yields using a computer-controlled luminescence spectrometer *Analyst* **1983,** *108,* 1067-1071

(3) Tang, Y.; Hill, E. H.; Zhou, Z.; Evans, D. G.; Schanze, K. S.; Whitten, D. G. Synthesis, Self-assembly, and Photophysical Properties of Cationic Oligo(p-phenyleneethynylene)s. *Langmuir* **2011**, *27*, 4945-55.

(4) Zhou, Z.; Corbitt, T. S.; Parthasarathy, A.; Tang, Y.; Ista, L. K.; Schanze, K. S.; Whitten, D. G. "End-Only" Functionalized Oligo(phenylene ethynylene)s: Synthesis, Photophysical and Biocidal Activity. *J. Phys. Chem. Lett.* **2010**, *1*, 3207-3217.

(5) Tan, C.; Pinto, M. R.; Schanze, K. S. Photophysics, aggregation and amplified quenching of a water-soluble poly(phenylene ethynylene) *Chem. Commun.* **2002,** 446-447

(6) URL: http://library.med.utah.edu/masspec/elcomp.htm, last accessed 9-2012

(7) Becke, A. D. A new mixing of Hartree-Fock and local density-functional theories *J. Chem. Phys.* **1993,** *98*(2), 1372–1377.

(8) M. J. Frisch, G. W. T., H. B. Schlegel et. al. *Gaussian 03, Revision C.02,*; Gaussian, Inc., Wallingford CT, 2004.

(9) Gaussian 09, Revision C.1, Frisch, M. J.; Trucks, G. W.; Schlegel, H. B.; Scuseria, G. E.; Robb, M. A.; Cheeseman, J. R.; Scalmani, G.; Barone, V.; Mennucci, B.; Petersson, G. A.; Nakatsuji, H.; Caricato, M.; Li, X.; Hratchian, H. P.; Izmaylov, A. F.; Bloino, J.; Zheng, G.; Sonnenberg, J. L.; Hada, M.; Ehara, M.; Toyota, K.; Fukuda, R.; Hasegawa, J.; Ishida, M.; Nakajima, T.; Honda, Y.; Kitao, O.; Nakai, H.; Vreven, T.; Montgomery, Jr., J. A.; Peralta, J. E.; Ogliaro, F.; Bearpark, M.; Heyd, J. J.; Brothers, E.; Kudin, K. N.; Staroverov, V. N.; Kobayashi, R.; Normand, J.; Raghavachari, K.; Rendell, A.; Burant, J. C.; Iyengar, S. S.; Tomasi, J.; Cossi, M.; Rega, N.; Millam, J. M.; Klene, M.; Knox, J. E.; Cross, J. B.; Bakken, V.; Adamo, C.; Jaramillo, J.; Gomperts, R.; Stratmann, R. E.; Yazyev, O.; Austin, A. J.; Cammi, R.; Pomelli, C.; Ochterski, J. W.; Martin, R. L.; Morokuma, K.; Zakrzewski, V. G.; Voth, G. A.; Salvador, P.; Dannenberg, J. J.; Dapprich, S.; Daniels, A. D.; Farkas, Ö.; Foresman, J. B.; Ortiz, J. V.; Cioslowski, J.; Fox, D. J. Gaussian, Inc., Wallingford CT, **2009**.

(10) Runge, Erich; Gross, E. K. U. Density-Functional Theory for Time-Dependent Systems. *Phys. Rev. Lett.* **1984,** *52*(12), 997–1000.

(11) Ridley, J. ; Zerner, M. Intermediate neglect of differential overlap technique for spectroscopy—pyrrole and azines. *Theor. Chim. Acta* **1973,** *32,* 111 – 134.

(12) D.A. Case, V. Babin, J.T. Berryman, R.M. Betz, Q. Cai, D.S. Cerutti, T.E. Cheatham, III, T.A. Darden, R.E. Duke, H. Gohlke, A.W. Goetz, S. Gusarov, N. Homeyer, P. Janowski, J. Kaus, I. Kolossváry, A. Kovalenko, T.S. Lee, S. LeGrand, T. Luchko, R. Luo, B. Madej, K.M. Merz, F. Paesani, D.R. Roe, A. Roitberg, C. Sagui, R. Salomon-Ferrer, G. Seabra, C.L. Simmerling, W. Smith, J. Swails, R.C. Walker, J. Wang, R.M. Wolf, X. Wu and P.A. Kollman (2014), AMBER

14, University of California, San Francisco.
(13) Wang, J., Wolf, R. M.; Caldwell, J. W.;Kollman, P. A.; Case, D. A. "Development and testing of a general AMBER force field". *Journal of Computational Chemistry* **2004,** *25*, 1157-1174.
(14) Bayly, C. I., Cieplak, P., Cornell, W., & Kollman, P. A. A well-behaved electrostatic potential based method using charge restraints for deriving atomic charges: the RESP model. *The Journal of Physical Chemistry* **1993**, *97*(40), 10269-10280.
(15) Cieplak, P., Cornell, W. D., Bayly, C., & Kollman, P. A. Application of the multimolecule and multiconformational RESP methodology to biopolymers: Charge derivation for DNA, RNA, and proteins. *J. Comp. Chem.* **1995,** *16*(11), 1357-1377.
(16) Jorgensen, W.L.; Chandrasekhar, J.; Madura, J.D.; Impey, R.W.; Klein, M.L. Comparison of simple potential functions for simulating liquid water *J. Chem. Phys.* **1983,** *79,* 926
(17) Jo, S.; Kim, T.; Iyer, V.G.; Im, W. CHARMM-GUI: a Web-based Graphical User Interface for CHARMM. *J. Comput. Chem.* **2008,** *29,* 1859–1865.
(18) Phillips, J. C.; Braun, R.; Wang, W.; Gumbart, J.; Tajkhorshid, E.; Villa, E.; Chipot, C.; Skeel, R. D.; Kale, L.; Schulten, K. Scalable Molecular Dynamics with NAMD. *Journal of Computational Chemistry* **2005,** *26,* 1781-1802, http://www.ks.uiuc.edu/Research/namd/
(19) Schlenkrich, M.; Brickmann, J.; MacKerell, Jr., A.D.; Karplus, M. An Empirical Potential Energy Function for Phospholipids: Criteria for Parameter Optimization and Applications, in "Biological Membranes: A Molecular Perspective from Computation and Experiment" K.M. Merz, Jr. and B. Roux, Eds. Birkhauser, Boston, **1996.**
(20) Lee, S.; Tran, A.; Allsopp, M.; Lim, J. B.; Henin, J.; Klauda, J. B. CHARMM36 United-Atom Chain Model for Lipids and Surfactants. *The Journal of Physical Chemistry B* **2014,** *118* (2), 547–556
(21) Martyna, G.J.; Tobias, D.J.; Klein, M.L. Constant Pressure Molecular Dynamics Algorithms *J. Chem. Phys*. **1994,** *101*(5), 4177-4189
(22) Darden, T.A.; York, D.; Pedersen, L.G. Particle mesh Ewald: An N log(N) Method for Ewald Sums in Large Systems *J. Chem. Phys*. **1993,** *98*, 10089-10092
(23) Feller, S.E.; Zhang, Y.; Pastor, R.W.; Brooks, B.R. Constant Pressure Molecular Dynamics Simulation: The Langevin Piston Method, *J. Chem. Phys.* **1995,** *103*(11), 4613-4621
(24) Zoete, V.; Cuendet, M.A.; Grosdidier, A.; Michielin, O. SwissParam, a Fast Force Field Generation Tool For Small Organic Molecules, *J. Comput. Chem.* **2011,** *32*(11), 2359-2368.
(25) Martínez, L., Andrade, R., Birgin, E. G. and Martínez, J. M. PACKMOL: A package for building initial configurations for molecular dynamics simulations. *J. Comput. Chem.* **2009,** *30*, 2157–2164.
(26) Goetz, A.W.; Williamson, M.J.; Xu, D.; Poole, D.; Le Grand, S.; Walker, R.C. Routine microsecond molecular dynamics simulations with AMBER - Part I: Generalized Born *J. Chem. Theory Comput.* **2012,** *8* (5), 1542-1555
(27) Salomon-Ferrer, R.; Goetz, A.W.; Poole, D.; Le Grand, S.; Walker, R.C. Routine microsecond molecular dynamics simulations with AMBER - Part II: Particle Mesh Ewald *J. Chem. Theory Comput.* **2013,** 9 (9), pp 3878–3888
(28) Le Grand, S.; Goetz, A.W.; Walker, R.C. SPFP: Speed without compromise - a mixed precision model for GPU accelerated molecular dynamics simulations. *Comp. Phys. Comm.* **2013,** *184*, 374-380
(29) Dickson, C. J.; Madej, B. D.; Skjevik, A. A.; Betz, R. M.; Teigen, K.; Gould, I. R.; Walker, R. C. Lipid14: The Amber Lipid Force Field. *Journal of Chemical Theory and*

Computation **2014,** *10*(2), 865–879
(30) Allen, W. J.; Lemkul, J. A.; Bevan, D. R. GridMAT-MD: A Grid-based Membrane Analysis Tool for Use With Molecular Dynamics. *J. Comput. Chem.* **2009,** *30* (12), 1952-1958
(31) Giorgino, T. Computing 1-D Atomic Densities in Macromolecular Simulations: the Density Profile Tool for VMD, *Computer Physics Communications* **2014,** *185*(1), 317–322
(32) Humphrey, W.; Dalke, A.; Schulten, K. VMD - Visual Molecular Dynamics. *J. Molec. Graphics* **1996,** *14,* 33-38
(33) Roe, D.R.; Cheatham, T.E., III; PTRAJ and CPPTRAJ: Software for Processing and Analysis of Molecular Dynamics Trajectory Data *J. Chem. Theor. Comp.* **2013,** 9 (7), pp 3084–3095
(34) Pettersen, E.F.; Goddard TD, Huang CC, Couch GS, Greenblatt DM, Meng EC, Ferrin TE. UCSF Chimera--a visualization system for exploratory research and analysis. *J Comput. Chem.* **2004,** *25*(13), 1605-17.
(35) Marrink, S. J.; Risselada, H. J.; Yefimov, S.; Tieleman, D. P.; de Vries, A. H. The MARTINI force field: coarse grained model for biomolecular simulations. *The Journal of Physical Chemistry B* **2007,** *111*(27),7812-7824.
(36) de Jong, D. H.; Singh, G.; Bennett, W. F. D.; Arnarez, C.; Wassenaar, T. A.; Schaefer, L. V.; Periole, X.; Tieleman, D. P.; Marrink, S. J. Improved parameters for the martini coarse-grained protein force field. *Journal of Chemical Theory and Computation* **2012,** *9*(1), 687-697.
(37) Periole, X.; Cavalli, M.; Marrink, S. J.; Ceruso, M. A. Combining an elastic network with a coarse-grained molecular force field: structure, dynamics, and intermolecular recognition. *Journal of Chemical Theory and Computation* **2009,** *5 (9),* 2531-2543
(38) Hess, B.; Kutzner, C.; Van Der Spoel, D.; Lindahl, E. GROMACS 4: Algorithms for highly efficient, load-balanced, and scalable molecular simulation. *Journal of chemical theory and computation* **2008,** *4*(3), 435-447.
(39) Pronk, S.; Páll, S.; Schulz, R.; Larsson, P.; Bjelkmar, P.; Apostolov, R.; ... & Lindahl, E. (2013). GROMACS 4.5: a high-throughput and highly parallel open source molecular simulation toolkit. *Bioinformatics*, btt055.
(40) Yesylevskyy, S. O.; Schaefer, L. V.; Sengupta, D.; Marrink, S. J. Polarizable water model for the coarse-grained MARTINI force field. *PLoS Computational Biology* **2010,** *6*(6), e1000810.
(41) Arnarez, C.; Uusitalo, J. J.; Masman, M. F.; Ingólfsson, H. I.; de Jong, D. H.; Melo, M. N.; Periole, X.; de Vries, A. H.; Marrink, S. J. Dry Martini, a coarse grained implicit water force field for (bio)molecular simulations, In preparation.

Appendix

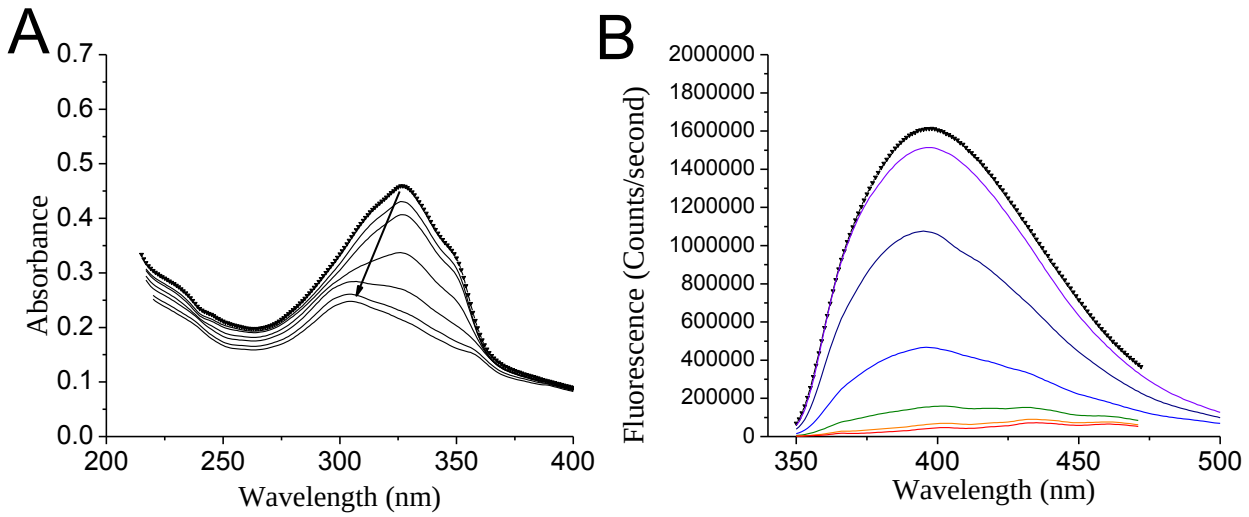

Figure A1 A. UV-Visible absorbance, and **B.** Fluorescence spectrum of 15 uM **+EO$_{C2}$** upon consecutive 1 uL additions of 15 mM TTAB

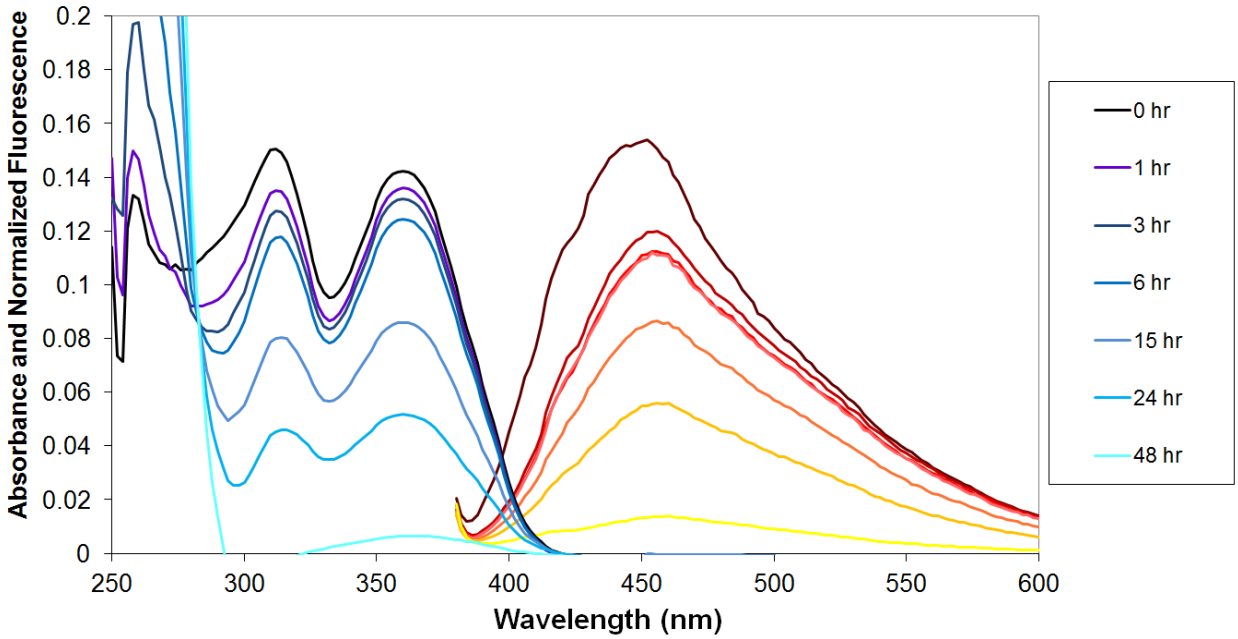

Figure A2. Absorbance and normalized fluorescence of 3.5 µM **+1C** in H_2O under air, with different durations of UVA irradiation.

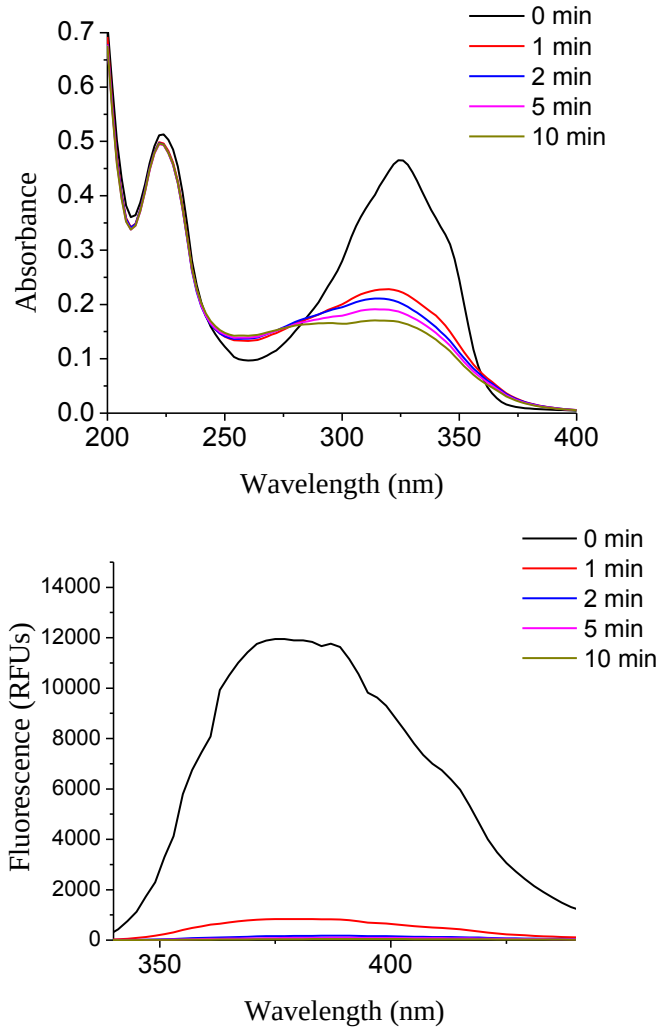

Figure A3. Absorbance and fluorescence of **+EO$_{C2}$** throughout photolysis under UVA irradiation with 10 lamps (5.3 mW-cm^{-2} over 316-400 nm).

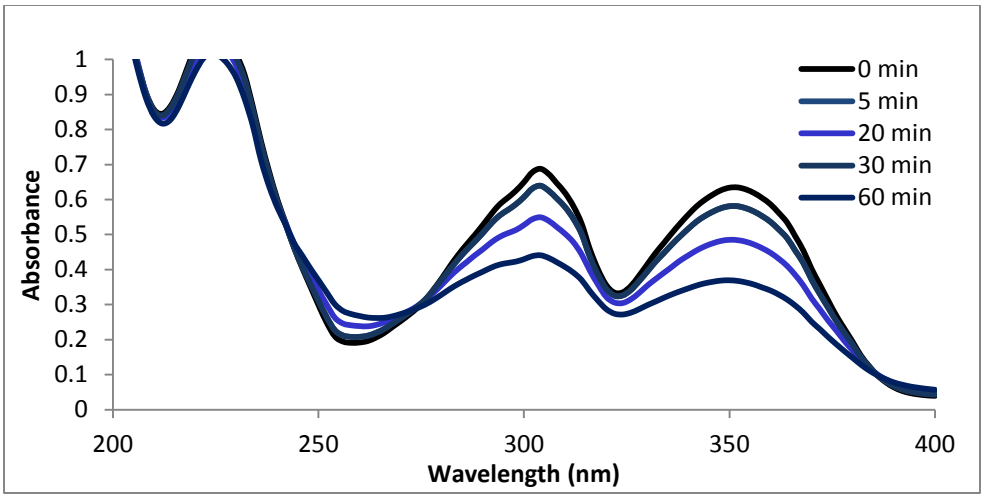

Figure A4. Absorbance of **+1H** throughout the duration of UVA photolysis in 10.4 mM SDS in water

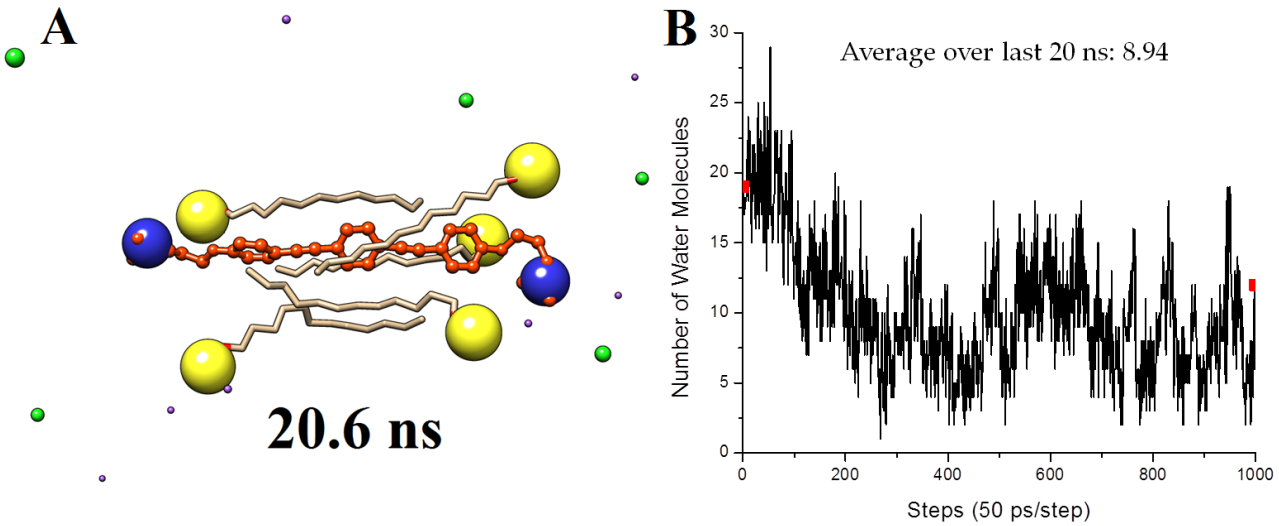

Figure A5. A. Image of complex resulting from 5 SDS molecules simulated with 1 **+EO** molecule **B.** Number of water molecules within 3.4 Angstroms of the backbone of the OPE. The average number of water molecules within 3.4 Angstroms of the OPE Nitrogen atoms is 14.133.

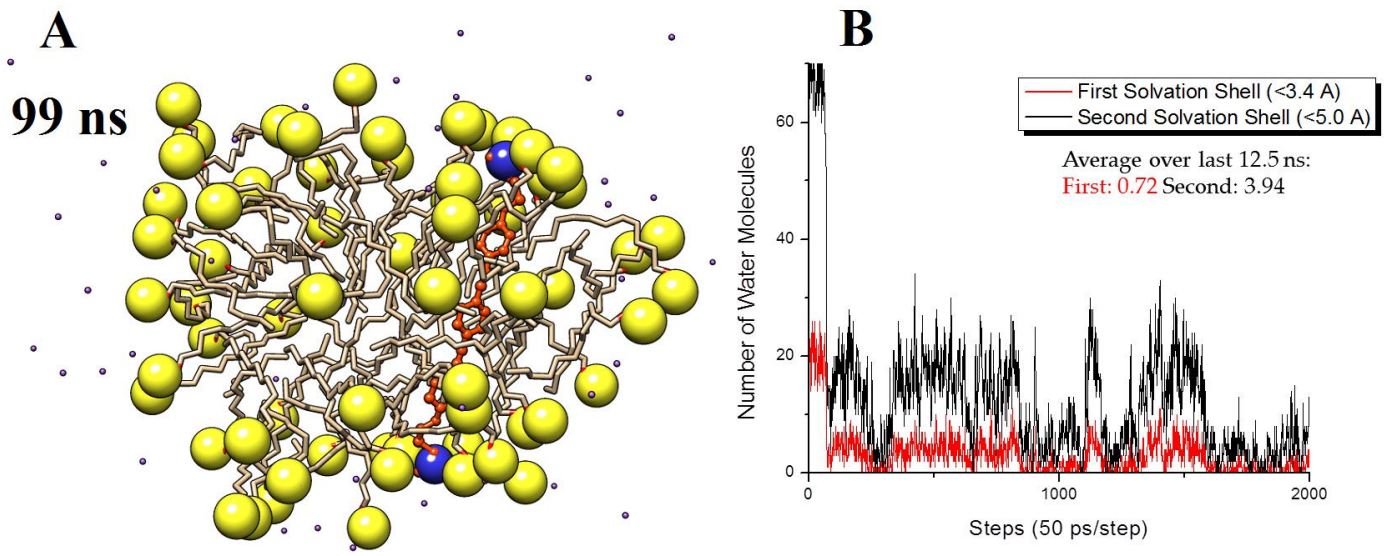

Figure A6. A. Image of **+EO** with an SDS micelle simulated at 303K in water with 0.1M NaCl **B.** Number of water molecules in the first and second solvation shells around the backbone of **EO1** throughout the simulation trajectory. The average number of water molecules in the first solvation shell of the OPE Nitrogen atoms is 9.9, and in the second is 32.5.

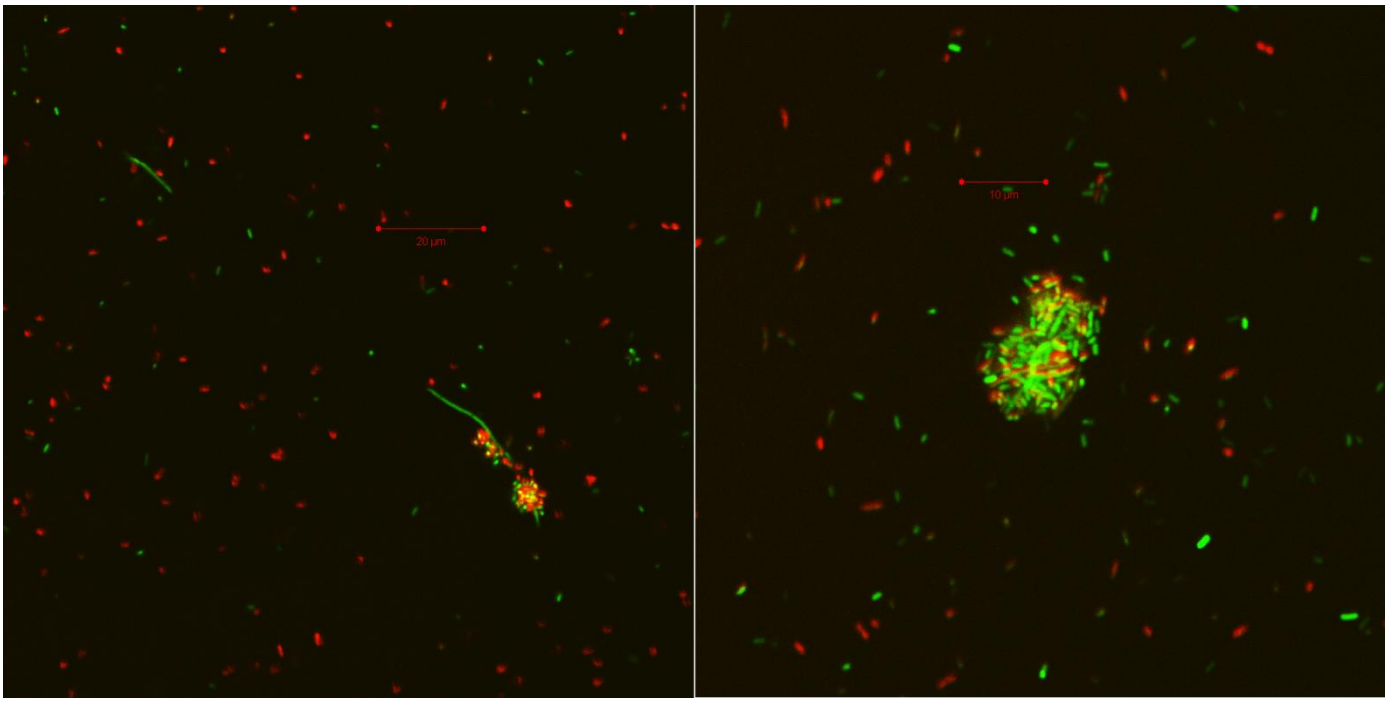

Figure A7. Confocal Fluorescence Microscopy images of E. Coli exposed to 2 hour pre-irradiated **+EO_{C2}-SDS**

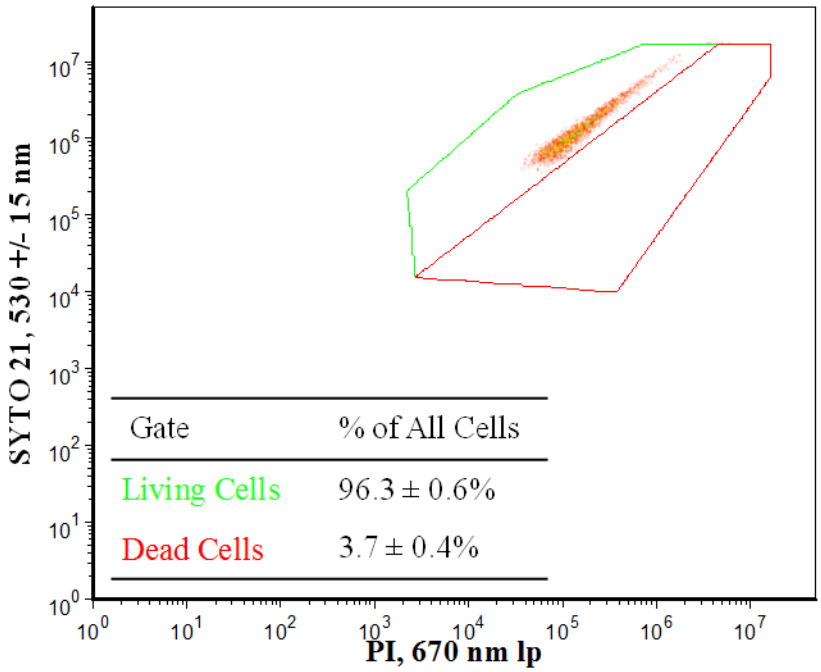

Figure A8. Flow Cytometry Analysis of S. Aureus with 0.33 mM SDS Control

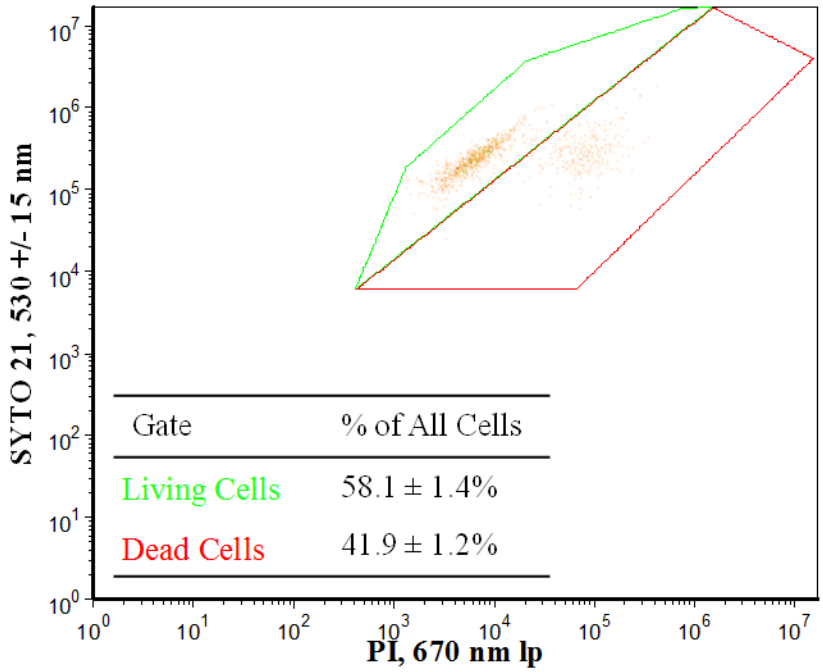

Figure A9. Flow Cytometry Analysis of E. Coli with 40 uM SDS Control

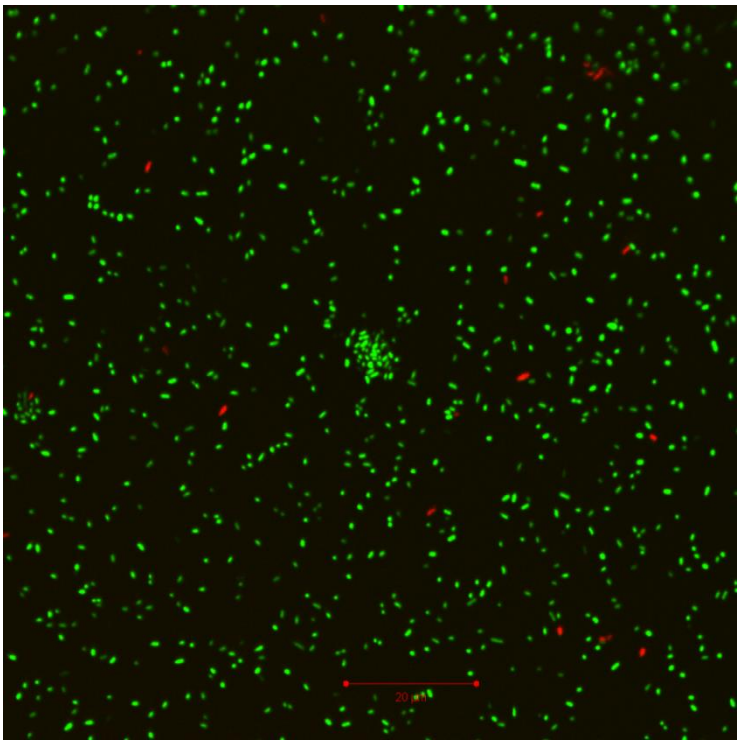

Figure A10. Confocal fluorescence microscope image of the negative control of *E. coli* after 1 hour of UVA irradiation. The "live" stain is SYTO9 in green, and the "dead" stain is propidium iodide in red. The scale bar indicates 20 µm.

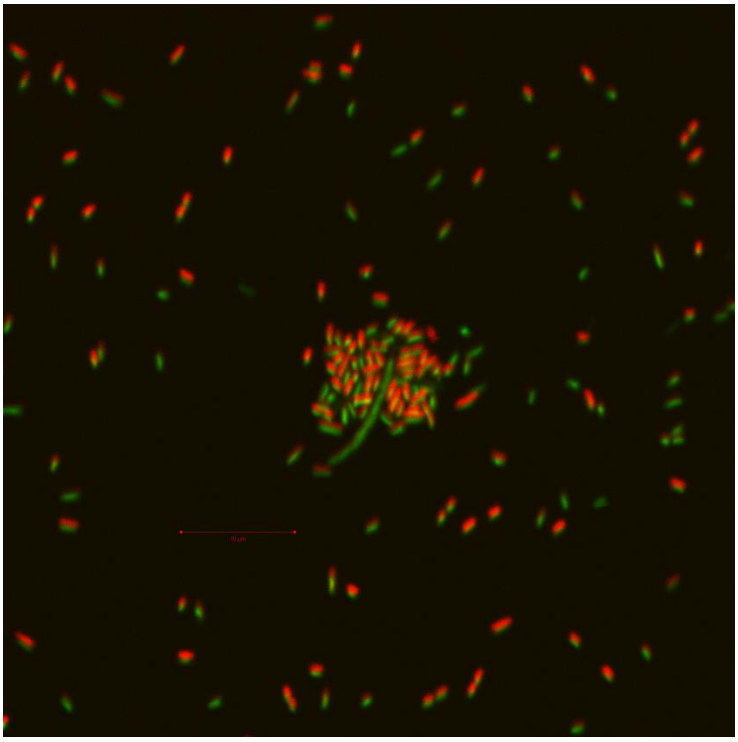

Figure A11. Confocal fluorescence microscope image of *E. coli* exposed to the **-EO**-TTAB complex in the light for an hour. The "live" stain is SYTO9 in green, and the "dead" stain is propidium iodide in red. The scale bar indicates 10 μm.

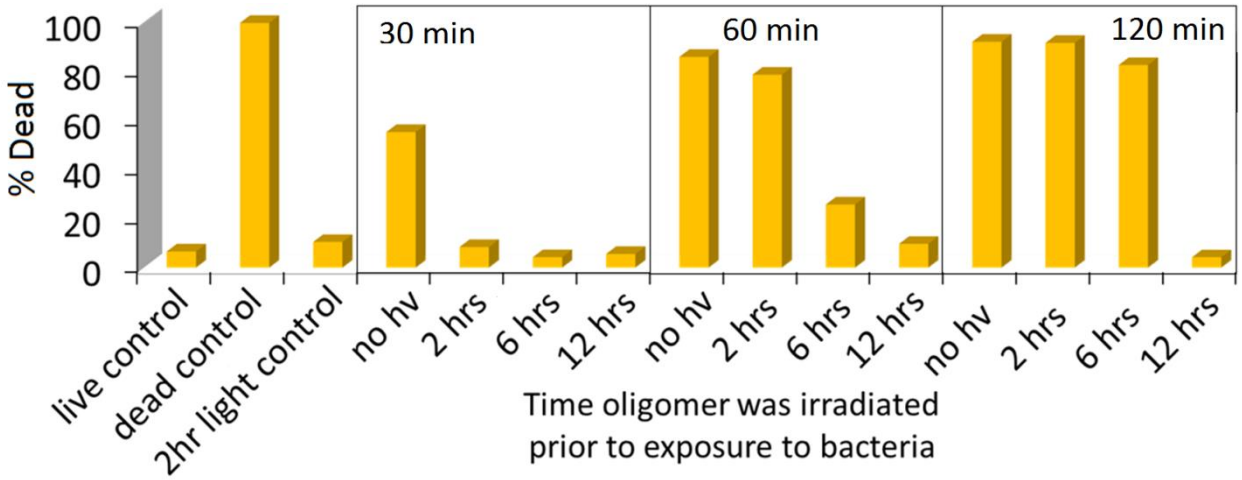

Figure A.12 Biocidal Activity of **+2H** after 0, 2, 6, and 12 hours of UVA irradiation with 30, 60, and 120 minute exposures to *P. aeruginosa* under UVA irradiation.